Imperial College London
Department of Chemical Engineering

Kraft lignin-derived carbon nanofibres as electrodes in aqueous alkaline supercapacitors

A thesis submitted for the degree of Doctor of Philosophy

Philipp Johannes Schlee

April 2020

Declaration of Originality

I, Philipp Johannes Schlee, confirm that the research included within this thesis is my own work or that where it has been carried out in collaboration with, or supported by others, that this is duly acknowledged and my contribution indicated.

April 2020

Acknowledgements

I would like to thank my supervisor, Professor Maria-Magdalena Titirici, for giving me the opportunity to carry out my PhD research in her group. She has been the most amazing mentor; her support and advice have been invaluable to my personal and academic development. Secondly, I would like to thank Per Tomani who launched this project together with Magda and who always kept an eye on this project, even if the organization of Innventia AB, now RISE AB, and his role within it has changed. Furthermore, his knowledge on the complex topic of lignin valorization has been very insightful for me as a rookie. Moreover, I would like to thank Darren and Omid for their help and support throughout my project. Being in continuous contact with lignin experts was of great importance for my progress. A big thank you to all those who have helped me gathering results and analyzing samples for me due to limited access to the respective characterization techniques. I am grateful to Liviu for helping with XPS measurements at the beginning of my PhD and for his advice on XPS data analysis, Rhod for performing nano X-ray tomography of my materials which is tedious, María José and Diego for carrying out temperature programmed desorption measurements. Thank you to my final-year students, Alex, Khalid, Claudia and Pierre who have helped me in preparing samples and sparked good discussions. A special thanks to Kathrin and Servann, who have greatly helped me and given me advice, whenever I got lost at the beginning of my PhD, which is invaluable. Without Servann's expertise and help our lab would not have been running as smoothly. To Maria, who always had a good idea on experimental design and measurement techniques available. Jingyu, who always made work fun and was a great office mate. Sabina, who helped me to gain access to some essential equipment at Queen Mary after the transfer and Linh, for good discussions and XPS and XRD measurements at Queen Mary. Finally, thank you to my parents. They have been the greatest support throughout all my life with their unconditional love and trust. Lastly, I would like to thank Charly for her endless support and encouragement. Her unconditional love and resilience kept me going and I am so grateful for always having her by my side.

Abstract

Kraft lignin emerges as a by-product of the pulp and paper industry on a megaton scale every year. Besides its use as energy source through combustion, alternative uses are sought after as the amount of lignin rises continuously exceeding the energy demand of pulp and paper mills and their capacity to incinerate lignin. Instead of using Kraft lignin as a fuel, it has been shown in this PhD project that hard- and softwood Kraft lignins extracted by the LignoBoost process and refined via fractionation can be used as precursors for the manufacture of electrospun carbon nanofibre (CNF) supercapacitor electrodes. Various routes towards highly nanoporous electrode materials with a unique micro- and macro-morphology were developed. At first, the development of nanoporosity in the lignin fibres was investigated with increasing stabilization temperature in the absence of any additive. Hardwood Kraft lignin inherently develops more nanoporosity than softwood Kraft lignin, which was shown to be caused mainly by the difference in side-chain linkages and functional groups. To further enhance the inherent development of nanoporosity in hardwood Kraft lignin-derived CNFs, activation with CO_2 after carbonization and the addition of $NaNO_3$ in the electrospinning solution were investigated. Softwood Kraft lignin-derived carbon nanofibres were used as electrically conductive scaffolds on which $Ni(OH)_2$ and ZnO were deposited. These composite electrodes were tested in nickel-zinc hybrid capacitors. Finally, CNF electrodes with high mass loadings based on free-standing, lignin-derived CNF electrode stacks were demonstrated. The high-mass loading electrode stacks showed no deterioration in energy and power density compared to the electrodes with ultra-low loadings. This reveals the potential applicability of these novel lignin-derived CNF electrode stacks in commercial supercapacitor cells.

Table of Contents

List of Abbreviations

BDE	Bond dissociation energy
BET	Brunauer, Emmett and Teller
CF	Carbon fibre
CNF	Carbon nanofibre
CP/MAS	Cross-polarized/magic angle spinning solid state
CT	Computed tomography
CV	Cyclic voltammogram
D	Dispersity
DFT	Density functional theory
DP	Degree of polymerization
EDLC	Electric double layer (super-)capacitor
EDX	Energy-dispersive X-ray
FTIR	Fourier transform infrared
GCD	Galvanostatic charge-discharge
HKL	Hardwood Kraft lignin
HSQC	Heteronuclear single quantum correlation
ICP-OES	Inductively coupled plasma optical emission spectroscopy
IL	Ionic liquid
LCC	Lignin-carbohydrate complex
LCF	Lignin-based carbon fibre
LCNF	Lignin-based/-derived carbon nanofibre
LIB	Lithium ion battery
LPP	Lignin property polygon
MS	Mass spectrometry/ mass spectrometric

NIB	Sodium ion battery
NMR	Nuclear magnetic resonance
NZHC	Nickel-zinc hybrid capacitor
PAN	Polyacrylonitrile
PC	Propylene carbonate
PSD	Pore size distribution
RNZB	Rechargeable nickel-zinc battery
RT	Room temperature
SC	Supercapacitor
SEM	Scanning electron microscopy
SKL	Softwood Kraft lignin
SSA	Specific surface area
TEM	Transmission electron microscopy
T_g	Glass transition temperature
TG	Thermogravimetry/ thermogravimetric
TPD	Temperature programmed desorption
XPS	X-ray photoelectron spectroscopy

List of Figures

List of Tables

1. Introduction

1.1. Motivation

Humans living in post-industrialized and newly industrialized countries have become a global geophysical force. Nowadays, we build dams, create new fluvial streams and change the flux of elements, such as N, P, Si, and C, on a global scale.[1] To acknowledge this development, Paul Crutzen and Eugene Stoermer have proposed to introduce a new geological era: "The Anthropocene".[1,2] By defining the new era "Anthropocene", geoscientists have given the ever-growing world population a tremendous responsibility concerning their future on planet Earth. Central to the role of humans in the geosystem is the use of fossil fuels as primary energy source and hence an immense change of the global carbon flux. The combustion of fossil fuels leads to CO_2 emissions accumulating in the atmosphere. Due to the ability of CO_2 to absorb infrared radiation, rising CO_2 levels in the atmosphere trap the heat which otherwise would be emitted to outer space. This phenomenon is known as the greenhouse effect. Therefore, the surge of the CO_2 concentration in the atmosphere leads to an increase of the near-surface temperature which will give rise to a colossal change of the earth system, if not mitigated.[3,4] A global warming of more than 2 °C compared to pre-industrial times will cause a dramatic rise of the sea level, ceasing jet streams and changing ocean currents which in turn will result in droughts, weather extremes and loss of habitable land.[5] In conjunction with the growth of the world population, this would cause migration of climate refugees on an unprecedented scale.[6,7] To prevent these crisis scenarios, most countries in the world have agreed to take measures to limit the rise of the global average temperature to 1.5 °C or at least well-below 2 °C compared to pre-industrial times. This is manifested in the Paris Agreement, which came into effect in 2016. This agreement is a set of norms which 196 countries have agreed to follow in their national policies, which is certainly a big achievement. However, it needs to be noted that the agreement involves no legal binding. Countries that fail to act based on these norms will not face any sanctions.

Not only political decision makers focus increasingly on the mitigation of climate change, but also financial markets adjust. Most recent financial market reports (e.g. by Bloomberg) reveal that sustainable investments rose by 34% (to 30.7 Trillion US Dollars) in 2019 as sustainable strategies and climate change became a leading issue for investors which puts pressure on large businesses to reduce their environmental impact.[8] These changes in political agendas and global investment strategies seem promising, but the most recent data on CO_2 accumulated in the atmosphere published by the World Meteorological Organization are devastating.[3] The rise of global CO_2 emissions has never been as dramatic as in the year 2018 since records began.[3] Currently, the global CO_2 concentration in the atmosphere amounts to 411.8±0.1 ppm, which is about 100 ppm more than 60 years ago (315.9±0.1 ppm) as shown in Figure 1-1.

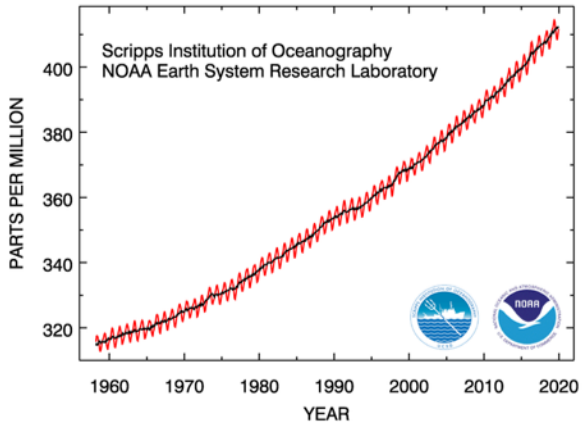

Figure 1-1 Monthly mean carbon dioxide measured at Mauna Loa Observatory, Hawaii, since 1959. The red line represents the monthly mean values. The black line represents the same, after correction for the average seasonal cycle. (source: Dr. Pieter Tans, NOAA/ESRL (www.esrl.noaa.gov/gmd/ccgg/trends/) and Dr. Ralph Keeling, Scripps Institution of Oceanography (scrippsco2.ucsd.edu/))

This tremendous increase implies that the rate of CO_2 emissions is much faster than the rate of its decay. The lifetime of a substantial fraction of atmospheric CO_2 is more than 1000 years.[9,10] Thus, the atmosphere has a limited capacity to accommodate CO_2 without causing the manmade greenhouse effect and the resulting global warming. In order to achieve the 1.5 °C goal set by the Paris Agreement, an absolute maximum of approximately 400 Gt CO_2 can still be emitted.[11,12] Looking at Figure 1-2 it becomes clear that China (~10 Gt CO_2 per annum) and the

USA (~5 Gt CO_2 per annum) alone emit 400 Gt CO_2 in 27 years assuming that their emissions stay constant over this period.

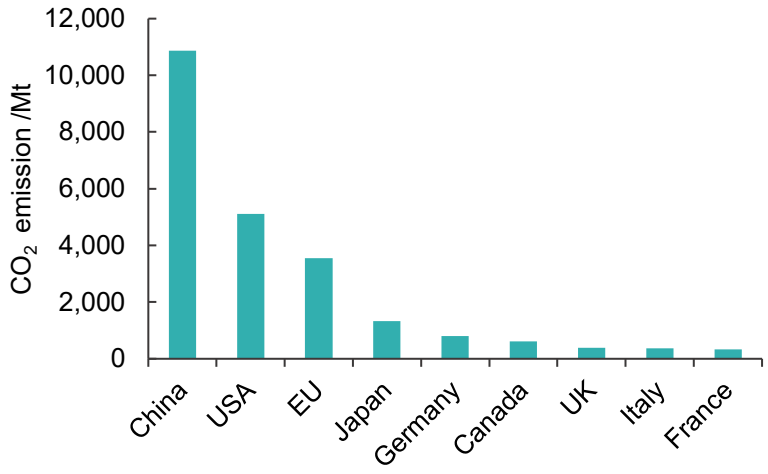

Figure 1-2 CO_2 emissions by country in 2017. (Data taken from Muntean et al.[13])

Figure 1-3 shows the global greenhouse gas emissions (CO_2, CH_4, N_2O) by economic sector. After electricity/power production, agriculture/forestry and industry, transportation accounts for 14% of the global emissions (28% in the EU) which is a major contribution. It is regarded as the most challenging and costly sector to decarbonize (reducing emissions of greenhouse gases).[14] Moreover, this sector shows the highest growth rate of CO_2 emissions in spite of more efficient engines and vehicles (rebound effect).[14] Consequently, the widely used fossil fuel-based combustion engine needs to be replaced by electric motors powered by fuel cells and batteries in order to decarbonize this sector.[15]

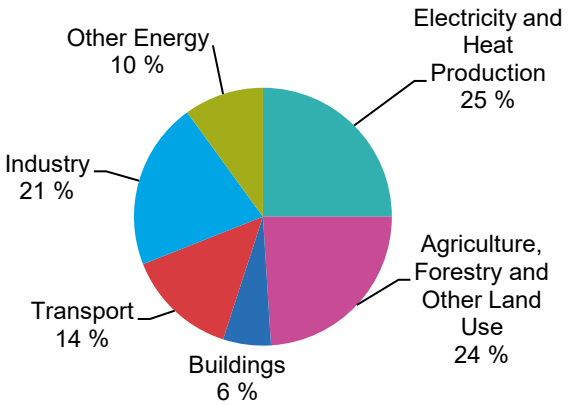

Figure 1-3 Global greenhouse gas emissions by economic sector (source: IPCC, 2014).[16]

The technological bottleneck is to provide onboard energy for the electric motors to the same extent and with the same characteristics (e.g. energy and power density) as fossil fuels. Furthermore, alternative production chains based on renewable resources are necessary in order to reduce the dependence on fossil fuels in the manufacturing of materials. This strategy is termed biorefinery/-economy. It involves the use of renewable raw materials rather than petrochemical precursors in materials synthesis. The aim of this PhD project was to use lignin as the main starting material (precursor) for the production of electrospun carbon nanofibres (CNFs) for mobile energy storage applications (Figure 1-4). Lignin is a major part of the lignocellulosic biomass, such as wood. Wood is a Nature-made composite comprising of three main components: cellulose, hemicellulose and lignin. It is the major base material for papermaking where cellulose is chemically separated from hemicellulose and lignin to produce paper and paperboard from the resulting pulp (cellulose fibres) as shown in Figure 1-4. However, this gives rise to ~55 Mt of degraded lignin as by-product per year of which the majority is currently incinerated to produce excessive heat for the industrial process.[17,18] This does not align with the goal to reduce greenhouse gas emissions and is economically unfavorable.

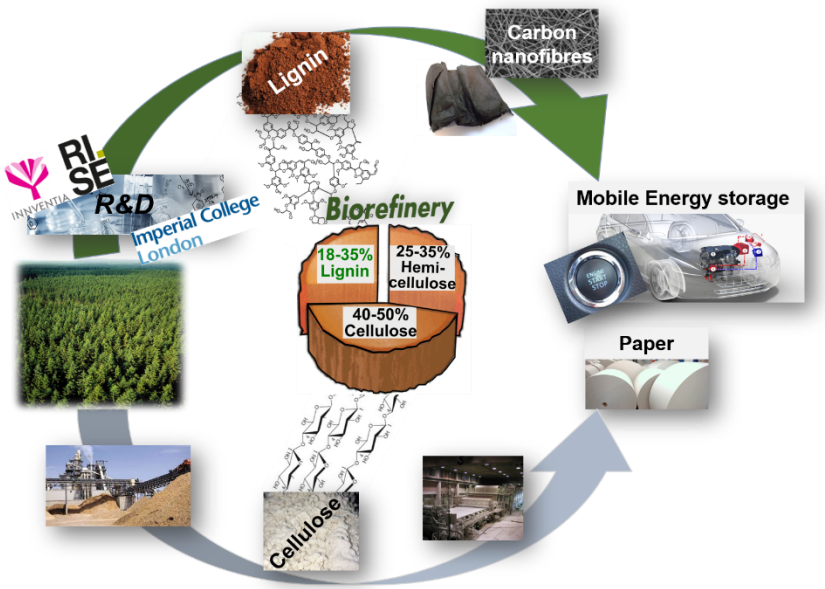

Figure 1-4 Production of electrospun carbon nanofibres from lignin for mobile energy storage applications within the concept of biorefinery.

Cellulose accounts for about half of the dry wood weight as shown in Figure 1-4. The bulk of the other half of the initial base material (wood) is currently discarded as fuel to produce excess of energy in form of heat in the process of papermaking. Additionally, as the production capacities for pulps are increasing, the existing incineration facilities (recovery boilers) reach their maximum capacity leading to an accumulation of lignin in pulp and paper mills, which is costly as it needs to be stored or transported away.[17,19,20] Therefore, the valorization of lignin as precursor for functional materials, chemicals and fuels is currently extensively explored in the pulp and paper industry. The work performed in this PhD thesis is part of this exploration. Generally, the use of lignins can be divided into two main branches: 1) use as a source for low molecular weight chemicals or fuels and 2) use as a macromolecular precursor for materials synthesis (e.g. carbon fibres or bio-plastics) (Figure 1-5).[18,21–23] However, since lignin is an oxygenated polymer formed by combinatorial polymerization, which is altered during the extraction process, it is chemically and structurally inherently different from hydrocarbons (e.g. polyolefins). It can be described as a polymer with a highly crosslinked and complex three-dimensional structure of phenyl propanoid units bonded through various ether bonds (C-O-C) or carbon−carbon (C-C) linkages. Hence, the route towards a direct replacement of fossil hydrocarbons by lignin is often elusive.

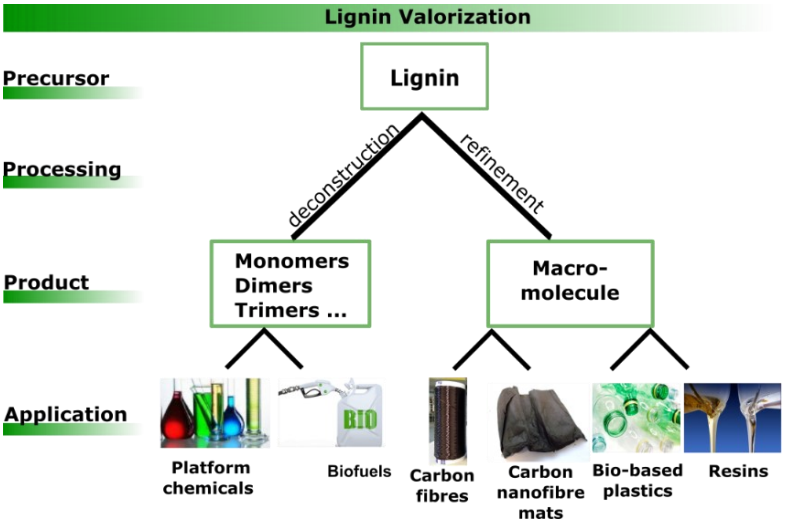

Figure 1-5 Overview of various lignin valorization strategies.

In this work, lignin was used as a renewable starting material in the manufacture of porous lignin-based carbon nanofibres (LCNFs) produced via electrospinning. This approach stands out from the other lignin valorization strategies shown in Figure 1-5 as it does not directly - one-to-one replace an existing product, such as carbon fibres for load-bearing applications or biofuels. The usage of lignin as a macromolecular precursor to produce free-standing CNFs serving as electrodes in energy storage applications without further need of post-processing is an innovative approach. It gives rise to a new class of electrodes with a unique, highly porous micro-morphology. To date, free-standing CNFs are not used in commercially available energy storage devices, such as supercapacitors or batteries, which, however, might change in the future.

1.2. Objectives

The main objectives of this research project were:

- Manufacturing of porous electrospun carbon nanofibres from Kraft lignin via different routes
- Characterization of the resulting materials with focus on the properties relevant for the final application, namely supercapacitors and nickel-zinc hybrid capacitors
- Electrochemical testing of the LCNF electrodes in aqueous alkaline supercapacitors and nickel-zinc hybrid capacitors
- Revealing the advantages of the innovative electrodes based on lignin-derived carbon nanofibres over the traditionally used film coated electrodes based on carbon powder

1.3. Outline

This thesis consists of nine chapters.

Chapter 1 gives a brief introduction to the motivation for lignin valorization, the objectives and the structure of this work.

Chapter 2 introduces various biochemical aspects of lignin and its role in the concept of biorefinery. Moreover, the role of porous carbons in energy storage applications with focus on supercapacitors is discussed.

Chapter 3 comprises the thorough characterization of the lignin precursors used in this work. Additionally, the development of porosity of the lignin fibres is investigated with increasing stabilization temperature.

Chapter 4 describes the process of CO_2 activation of hardwood Kraft lignin-derived carbon nanofibres together with their electrochemical characterization.

Chapter 5 presents the results on $NaNO_3$-activated hardwood Kraft lignin-derived carbon nanofibres together with the electrochemical characterization and compares the results with the previous findings on CO_2-activated carbon nanofibres of the same lignin.

Chapter 6 describes the use of lignin-derived carbon nanofibres as electrically conductive scaffolds decorated with $Ni(OH)_2$ and ZnO particles.

Chapter 7 reveals the possibility of new electrode geometries with high mass loadings that are possible based on free-standing, lignin-derived CNF electrodes.

Chapter 8 gives a summary on the main findings presented in chapters 3, 4, 5, 6 and 7 and concludes this thesis with an outlook for future work based on this research project.

Chapter 9 contains the description of the characterization techniques.

2. Literature review

2.1. Lignin as part of the lignocellulosic biomass

Lignin is next to cellulose and hemicellulose one of the three major components of the lignocellulosic biomass (living plants and plant residues). These three components constitute the plants' cell walls, where lignin is covalently bound to carbohydrates (mainly hemicellulose) forming so-called lignin carbohydrate complexes (LCCs) which surround and occlude the cellulose fibrils.[24–26] Therefore, plant cell walls can be described as a complex composite material serving the plants' protection, structural integrity and water/solute transport, which has been decisive for the evolution of land plants.[27,28] Depending on the plant species, lignin accounts for approximately 15 – 40% of the dry weight of every plant, the polysaccharides, mainly cellulose and hemicellulose, account for the rest.[29] In general, grasses contain less lignin in the cell wall than trees as shown in Figure 2-1. For example, switchgrass consists of 17 – 18% lignin, 32 – 37% cellulose and 26 – 33% hemicellulose.[30]

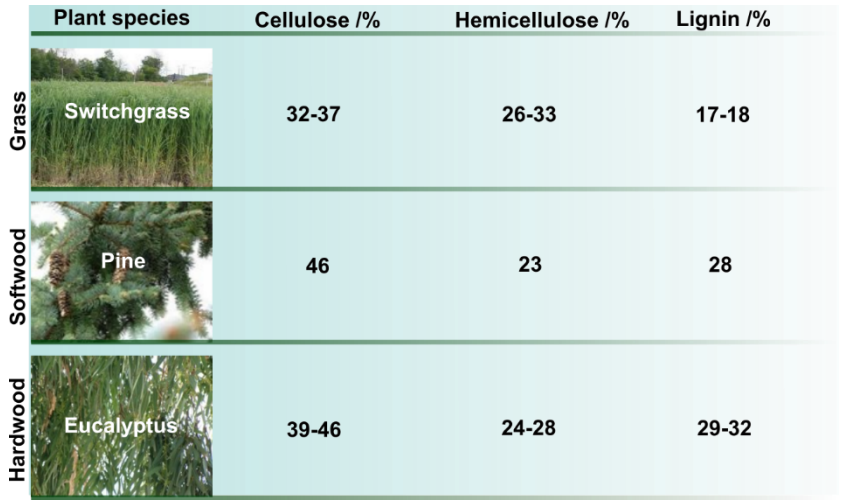

Figure 2-1 Typical biomass composition for various plant species.

In wood, lignin accounts for 18 – 35%, cellulose for 40 – 50% and hemicellulose for 25 – 35% of the dry wood weight depending on the botanical source.[31] In a typical softwood, such as pine, lignin accounts for 28%, cellulose for 46% and hemicellulose for 23% of the dry wood weight.[32]

In a common hardwood, such as eucalyptus, the lignin content is 29 – 32%, the cellulose content is 39 – 46% and the hemicellulose content is 24 – 28% of the dry wood weight.[33]

The compositional variability of wood is not only based on the botanical source. For a specific tree, the distribution of the three main components also varies with tree part (root, stem or branch), type of wood (e.g. normal, tension or compression wood), geographic location, climate, and soil conditions.[31] Since the wood cell wall is hierarchically structured, there are also considerable variations in composition among the different cell wall domains (Figure 2-2). In general, wood cell walls comprise three ultrastructural domains: the middle lamella, the primary wall, and the secondary wall.[34]

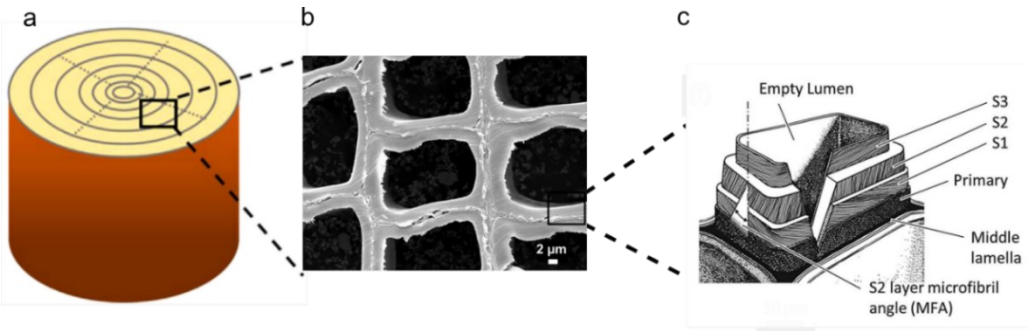

Figure 2-2 Schematic of a tree stem cross-section (a), scanning electron microscope image of wood cells (taken from Agarwal[35]) (b), and a schematic structure of a wood cell wall comprising the secondary cell wall, the primary cell wall and the middle lamella from the lumen outward (reproduced from Jakes et al.[34]) (c).

Most of the lignin is situated in the middle lamella which acts to adhere adjacent cells.[34] The secondary cell wall can be divided into three separate parts (S1, S2, S3) based on the structure and composition of the polymers present.[36] Typically, the S1 layer has the greatest concentration of lignin within the secondary cell wall while the S2 layer contains overall more lignin than the S1 layer because of the greater S2 layer thickness.[37,38] In order to understand the function and synergy of (hemi-)cellulose and lignin, the three components must be considered separately. Cellulose is a glucan polymer consisting of linear chains of 1,4-β-bonded anhydroglucose units. The structure of cellulose is highly organized. Wood cellulose has a degree of polymerization (DP) of at least 9,000 and up to 15,000.

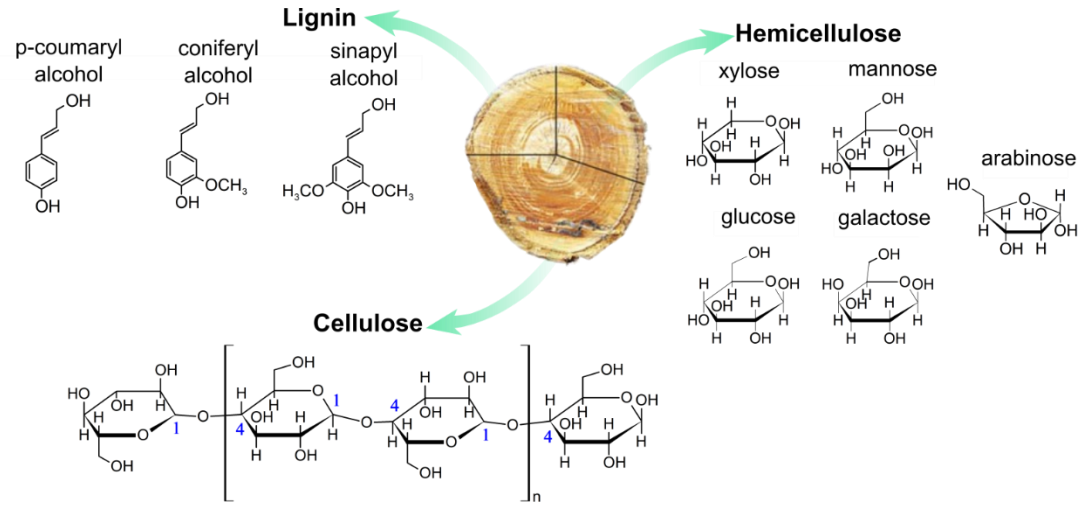

Figure 2-3 Main components of wood: cellulose, hemicellulose and lignin.

Like cellulose, hemicellulose's main chain consists of monosaccharides connected with β-(1,4) glycosidic bonds, although some other bonds can occur. However, hemicelluloses have a relatively low degree of polymerization (DP ≈ 100 – 200) compared to cellulose (DP > 10 000). Additionally, hemicelluloses accommodate a much wider variety of monosaccharides in their chain, namely D-xylose, D-glucose, D-galactose, L-arabinose, D-mannose, and minor amounts of other sugars. Hence, hemicellulose is a heteropolysaccharide consisting of two or more types of hexoses and pentoses.[39] The composition of the hemicelluloses and the resulting lignin-carbohydrate bonding patterns in the LCCs vary with wood type (softwood or hardwood).[40]

The hemicellulose fraction of hardwoods is mainly composed of xylans which are heteropolysaccharides consisting of β-1,4-linked xylose residues with side branches of α-arabinofuranose and α-glucuronic acids.[41] In softwoods only a small portion of the hemicelluloses consists of xylans (10 – 15%).[41] Furthermore, softwood xylans differ from hardwood xylans by the lack of acetyl groups and the presence of arabinose units linked by α-(1,3)-glycosidic bonds to the xylan backbone. Since the hemicellulose in hardwoods exhibits a higher degree of acetylation compared to softwoods, it is much less resistant to acid treatment.[40,42] Moreover, a larger portion of the hemicellulose fraction in softwoods is composed of galactoglucomannan, a hemicellulose, whose backbone is constructed by mannosyl and glucosyl residues giving rise to more

branching compared to xylans.[40,41] The exact covalent bonding patterns between the carbohydrates and lignin in the LCCs are not yet fully understood due to problems during extraction and signal detection.[43] However, the five types of lignin-carbohydrate bonds shown in Figure 2-4 have been suggested.

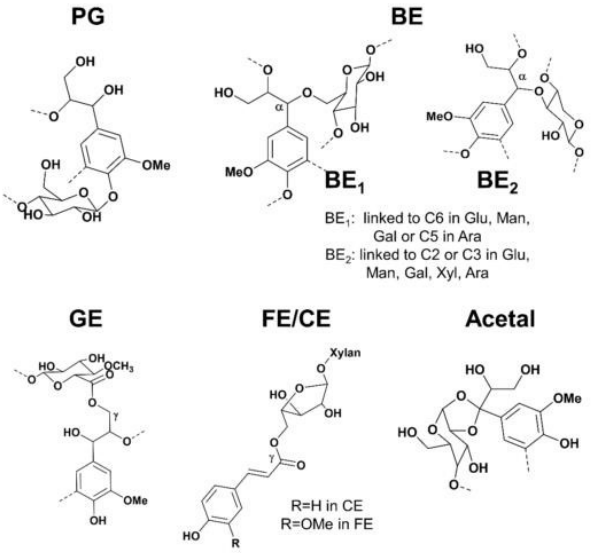

Figure 2-4 Suggested structures of lignin-carbohydrate bonds in woods and grasses. PG=phenyl glycosides, BE=benzyl ethers; GE=y-esters; FE=ferulate esters; CE=coumarate esters (taken from Giummarella et al.[43]).

It was postulated that benzyl ether (BE) bonds are dominant in softwood LCCs, whereas the phenyl glycosidic linkages (PG) are prevalent in hardwood LCCs, whereby the amount of ester linkages greatly varies in different species.[26] Furthermore, it was suggested that the hardwood LCCs consist of a very long polysaccharide chain linked to a few large lignin moieties, whereas the softwood LCCs are composed of small and repeating lignin units bound to the polysaccharide chain yielding complexes with a more branched structure.[26]

Compared to the carbohydrates, lignin is compositionally and structurally fundamentally different as it exhibits no structural regularity and chemical homogeneity, like cellulose, or chemical variability within a narrow range as it is the case for hemicellulose. Lignin shows a very high degree of heterogeneity which results from the biosynthetic pathway that is based on combinatorial radical coupling.[44] The structure and chemical composition of native lignin as found

in the cell wall, called protolignin, are hardly known to date.[44] The reason is that in planta examinations of lignins are extremely challenging and extraction of lignin prior to analysis is inevitably connected with bond cleavage which alters the native lignin structure considerably.[45] Nonetheless, generally accepted is that native lignins in wood may be broadly described as:

three-dimensional amorphous polymers mainly composed of three oxidatively coupled 4-hydroxyphenylpropanoid units differing in their degree of methoxylation.[46,47]

These three so-called monolignols are the p(ara)-hydroxycinnamyl alcohols: p- coumaryl, coniferyl and sinapyl alcohol. The p-hydroxycinnamyl alcohols which are the precursors for the polymerization of lignins are produced in the cytoplasm.[44] They are then transported to the cell wall where the actual polymerization via combinatorial radical coupling takes place.[44] Depending on the botanical source (e.g. hardwood or softwood), these monolignols are present in various ratios as p-hydroxyphenyl (H), guaiacyl (G) and syringyl (S) units in the final lignin polymer (Figure 2-5).[24] Therefore, not only the total amount of lignin found in the cell wall of plants is dependent on the botanical source (Figure 2-1), but also the lignin polymer structure and its chemical composition.

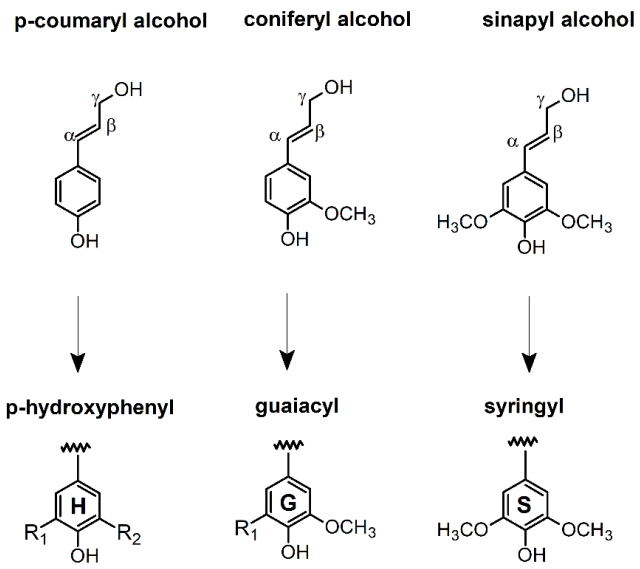

Figure 2-5 Basic building units of lignins which differ in their degree of methoxylation and their corresponding structures in the lignin polymers.

In general, softwoods, like pine or spruce, incorporate almost exclusively guaiacyl (G) units with small amounts of p-hydroxyphenyl (H) units. Lignins in hardwoods, such as eucalyptus, contain both syringyl (S) and guaiacyl (G) moieties together with small amounts of p-hydroxyphenyl (H) units. A crucial step in the lignin biosynthesis is the dehydrodimerization of the monolignols which is catalyzed by oxidative enzymes (O_2-dependent laccase and H_2O_2-dependent peroxidase). This initial dimerization gives rise to three dehydrodimers starting from coniferyl alcohol (softwoods) and only two dimers from sinapyl alcohol (hardwoods) due to the different degree in methoxylation as shown in Figure 2-6.[48] Once these dimers are formed, the key feature of lignification involves coupling reactions between oxidized monolignol radicals and radicals formed on the free phenolic ends of the growing lignin polymer.[48] Moreover, additional possible coupling reactions have been revealed. For instance, the hydroxycinnamyl alcohol radicals can couple at several positions (4-O-, 5-, β-, as well as 1-) in a process that is only under chemical control (e.g. not controlled by proteins or enzymes).[48]

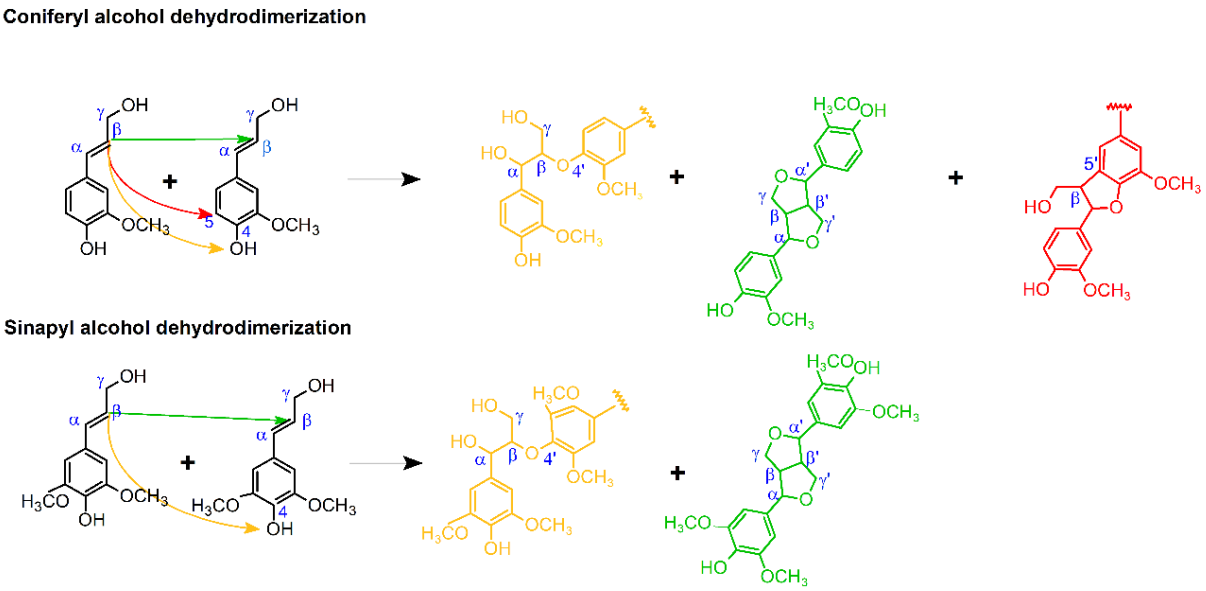

Figure 2-6 The initial dehydrodimerization step starting from coniferyl alcohol (top) typical of softwoods or sinapyl alcohol (bottom) characteristic of hardwoods.

Hence, the process is combinatorial meaning the number of possible outcomes is vast.[47] The actual polymerization step is controlled by chemical/physical conditions involved in any chemical reaction: coupling and cross-coupling propensities, reactant supply, the polysaccharide matrix and other physical/chemical conditions (e.g. pH, temperature, etc.).[44,47]

2.2. Separation and processing of the lignocellulosic biomass components

2.2.1. Lignocellulosic biomass recalcitrance

The recalcitrance of the lignocellulosic biomass towards separation into its components has been shown to scale with the amount of lignin and the type of lignin in the cell wall. For instance, in the production of biofuels from lignocellulosic biomass, it has been demonstrated that biomass digestibility by enzymatic/microbial hydrolysis increases with decreasing lignin content.[49] Thus, for the production of bioethanol from lignocellulosic feedstocks, a pre-treatment step is inevitable to increase the sugar yield from cellulose and hemicellulose via fermentation.[50] Compared to crops or their residues and grasses, wood feedstocks require more severe (pre-)treatment procedures as their lignin content is substantially higher (Figure 2-1). However, wood and forest residues in general are regarded to be the more sustainable route towards biofuels/chemicals as they are not directly linked with the food chain. Moreover, compared to crops and their residues (like rice or wheat straw), wood feedstocks have a considerably lower demand in N-fertilizers and are more space-efficient as they require less floor space (yield per hectare).[51]

Softwoods often have a higher lignin content than hardwoods, where eucalyptus hardwoods constitute an exception (Figure 2-1). However, the hardwood and softwood lignin polymer structures are vastly different. Softwood lignins are mainly composed of guaiacyl units and a small amount of hydroxyphenyl units which gives rise to a more condensed structure (C-C linkages) with higher molar mass, whereas hardwood lignins comprise a ratio of guaiacyl and syringyl units reducing the number of stable C-C linkages accompanied by an increase in more

labile ether bonds (Figure 2-6).[24] Therefore, softwood lignins can be regarded as more recalcitrant than hardwood lignins.

Traditionally, the large-scale use of (hemi-)cellulose in the form of pulp (cellulose fibres) for papermaking and, more recently, for ethanol production for fuels have made it necessary to establish protocols to disintegrate the LCCs and hence separate the carbohydrates from lignin.[18] The lignins that arise from these protocols are called technical lignins in order to distinguish them from the native lignins found in plants (protolignin), as the lignins initially found in the biomass are altered considerably during the separation. Depending on the separation procedure various degrees of modification occur. This contributes to the inherent variability of lignins as feedstocks. Next to the Organosolv process that separates lignin from the carbohydrates by the action of organic solvents (e.g. ethanol) with a catalyst (e.g. H_2SO_4),[52,53] the most prominent separation processes applied to wood feedstocks is the Kraft process, which is described in the following.

2.2.2. The Kraft process

Nowadays, the Kraft process is the most widespread technology for the deconstruction of both hard- and softwoods to produce pulps (cellulose fibres) for the paper and paperboard industry. About 130 million tons of Kraft pulp per year are produced worldwide, which is 80 to more than 90% of the produced chemical pulp depending on the country.[18,54,55] This gives rise to about 50 – 55 million metric tons of lignin in form of the alkaline black liquor.[56] The black liquor is composed of the residual hemicellulose, lignin and inorganics which were separated from the cellulose fibres of the wood raw materials by treating wood with $NaOH_{(aq)}/Na_2S_{(aq)}$ at temperatures between 165 and 175 °C for 1 – 2 hours.[55] 90 – 95% of the lignin in the starting material (various softwoods and hardwoods) can be separated into the black liquor.[57] The remaining high-quality pulp (cellulose fibres) is used for the papermaking process. During the Kraft process lignin is highly modified as it is exposed to strong nucleophiles (OH^- and HS^-) in

the presence of carbohydrates (from hemicellulose) at high temperatures. The reactions taking place in the Kraft process can be divided into two categories: 1) degradation reactions that give rise to the liberation of lignin fragments and ultimately to their dissolution and 2) condensation reactions which increase the molecular size of lignin fragments and may result in their precipitation.[58] These two types of reactions are intimately connected with each other by proceeding via common intermediates.[58] The key intermediate occurring during Kraft pulping is the quinone methide.[59] In the presence of various nucleophiles, such as the hydrosulfide/hydroxide anions and OH groups of the carbohydrates, lignin and released phenolic fragments, the quinone methide undergoes a vast amount of different nucleophilic addition reactions. Thus, altering the initial lignin polymer tremendously. Therefore, Kraft lignins are classified as technical lignins because their structure and chemical composition are very different from native lignins.[59] The degraded and altered lignin dissolved in the alkaline black liquor is commonly combusted in a recovery boiler on site to generate steam and energy (heat) for the pulp and paper mill.[17,60] However, the increasing demands for pulps gives rise to an excess of black liquor which is not used economically as combustion for excess energy generation is neither economically favorable nor environmentally friendly.[19] Therefore, a new strategy in the pulp and paper industry is to extract parts of the lignin (Kraft lignin) from the black liquor to produce value-added products from these lignins.[57] The term "value-added" can be defined as a value higher than combustion of lignin as coal replacement which is estimated to be 10 US$ cents/kg.[61] One process to extract lignin efficiently from the black liquor is the so-called LignoBoost process (Figure 2-7). In the LignoBoost process, lignin is precipitated from the alkaline black liquor by acidification (the preferred acid is CO_2) and filtered as shown in Figure 2-7.[62]

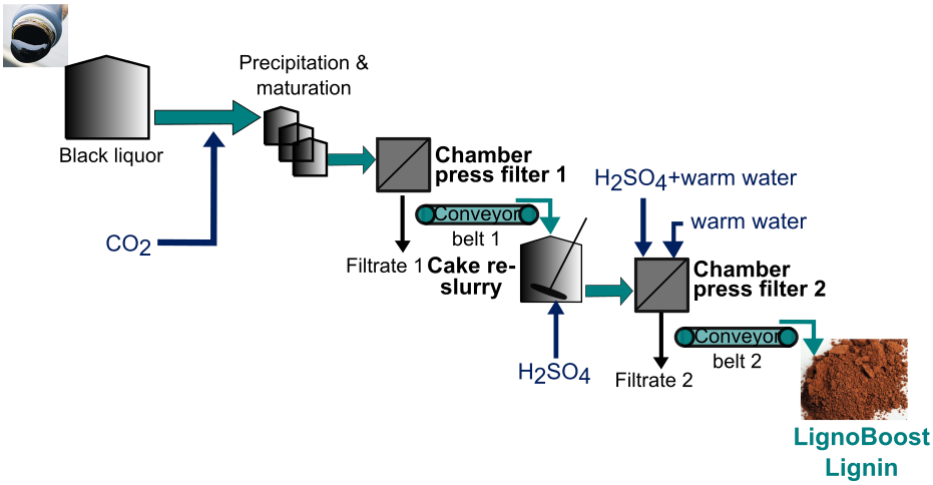

Figure 2-7 Simplified layout of the LignoBoost lignin removal process from the black liquor arising as by-product from the pulp and papermaking redrawn based on the layout presented in 62.

Subsequently, the filter cake is re-dispersed and acidified (H_2SO_4) in order to protonate all types of ionized phenolic lignin structures and carboxylate groups. Hence, the amount of remaining ash (inorganics) in the lignin can be minimized.[57,62] Afterwards, the resulting slurry is filtered and washed by means of displacement washing.[62] The LignoBoost process makes it possible to extract pure (>95%) lignin from the black liquor in Kraft mills.[62] Two commercial plants (Domtar, USA and Stora Enso, Finland) are presently in operation. Peculiar to the Kraft LignoBoost lignins is their quite low sulfur content of about 2% which is covalently bound in the lignin structure and a very low content of carbohydrates and salts compared to other technical lignins.[57] To date, only 2% of the lignin separated in the process of papermaking are used as additives for low-value application (dispersants, binders etc.). However, strategies towards high-value applications of lignin, such as starting material for the production of chemicals, fuels or carbon materials are pursued (biorefinery). The work at hand is part of this endeavor where Kraft LignoBoost lignins are used as precursors for electospun carbon nanofibres utilized in energy storage applications. An overview of the most recent research trends in valorization of lignin within the framework of the biorefinery concept is given in the following section.

2.3. Lignocellulosic biorefinery

The main reason for the deconstruction of lignocellulosic biomass has been to delignify the feedstock to generate revenue from cellulose either by producing paper or more recently ethanol for fuels as shown in Figure 2-8.[18] In this cellulose-centered biorefinery, lignin and hemicellulose are treated as by-products with no attributed use. However, the most recent concept of biorefinery seeks to establish processes where all components of the lignocellulosic biomass are the base of one or several value chains (Figure 2-8).[63,64] This concept has gained momentum in the last decade. Notably, in the pulp and paper industry strategies are adopted to transform traditional pulp and paper mills solely focused on papermaking into bioproduct mills generating revenue not only by papermaking from cellulose, but also from other products based on hemicellulose and lignin. The most recent example of such an endeavor is the bioproduct mill built by the Metsä Group in Äänekoski (Finland), which has been in full operation since August 2018. The bioproduct mill produces tall oil and turpentine oil as products from the mill, which are traditional (bio-)products from Kraft mills.[65]

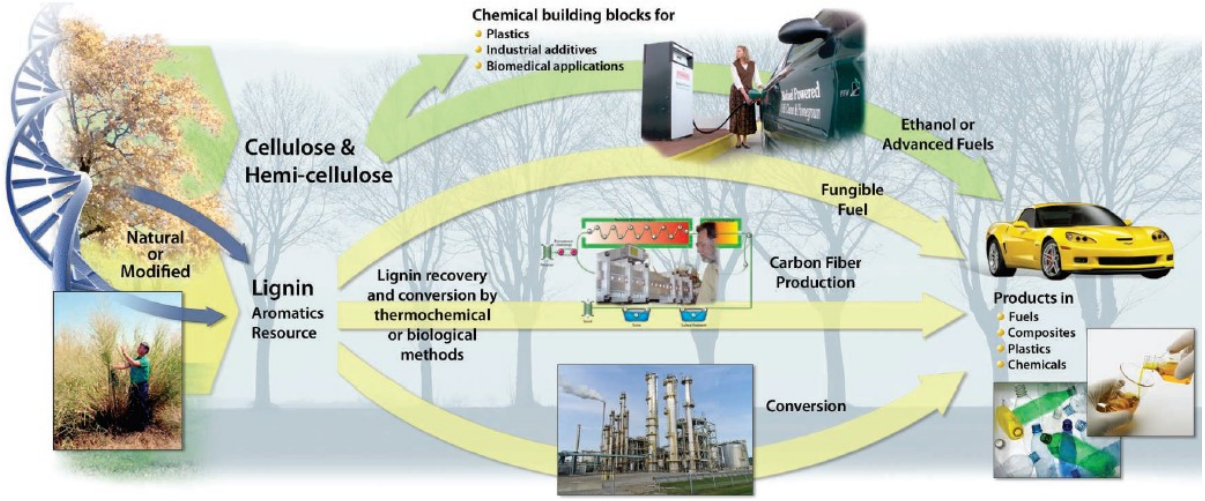

Figure 2-8 Lignocellulosic biorefinery concept involving the production of biofuels from (hemi-)cellulose and carbon fibres, chemicals and fuels from lignins (taken from Ragauskas et al.[29]).

In the future, the Metsä Group plans to expand the product portfolio of the bioproduct mill. For instance, by producing sulfuric acid from odorous sulfur dioxide.[66] The generation of revenue from high-value chemicals or materials from lignin are planned, but in which form and the

timeframe remain unclear. The Domtar pulp and paper mill in the USA, that implemented the LignoBoost process, markets the resulting Kraft lignin (BioChoice® Lignin) advertising it as suitable raw material for adhesives, natural binders, coatings, resins and carbon materials (e.g. carbon fibres). To date, the BioChoice® Lignin is mainly used for R&D (research and development) projects rather than on an industrial scale. Generally, lignins have not found widespread use in the synthesis of functional materials and chemicals/fuels despite of tremendous research and R&D efforts. Even if the bio-macromolecule exhibits a high carbon content and a high degree of aromaticity coupled with a richness in functional groups, its structural and chemical variability are the main obstacles for its use as a precursor for functional materials, chemicals or fuels. Moreover, depending on the separation and refining process the final lignin precursor will differ in its structure (linkages between phenolic building units) and chemical composition. In line with this variability and heterogeneity, a wide range of different strategies towards lignin valorization is pursued. The two main pathways that can be distinguished are the use of lignin as a macromolecule and as a source of low molecular weight compounds which are released by various catalytic depolymerization strategies. The research results of several years in lignin deconstruction have led to the conclusion that technical lignins as by-products of cellulose centered valorization (e.g. pulp and ethanol) are detrimental to lignin valorization.[67] The new concept of lignin-first biomass fractionation is supposed to overcome the trilemma of lignin-hemicellulose-cellulose valorization.[67] Within this concept, lignin valorization is to be considered before the utilization of the carbohydrates to prevent structural degradation of the native lignin as much as possible. In both macromolecular and low molecular weight product streams, it is clear that there is not a single product from native or technical lignins, but a variety of products for which applications need to be found to ensure economic viability. Overall, the economic potential of lignin as a precursor for high-value applications has by far not been exploited. In the following sections, various approaches towards lignin value chains based on macromolecular applications are described.

2.3.1. The use of lignin as a macromolecular precursor

A complementary approach to the deconstruction of lignin into smaller fragments and its conversion to (aromatic) chemicals and fuels is to make use of the macromolecular nature of lignin (e.g. technical lignins). This can either be as precursor for bio-polymer synthesis or as starting material to produce carbons, especially carbon fibres. The latter strategy has been pursued in the work at hand. However, the main issue in exploiting lignin as a macromolecular precursor is the irregular structure of lignin and the heterogeneity depending on feedstock type, separation process and refining strategies applied. Refining is the process of making lignin a reliable (homogeneous) precursor for materials synthesis. It needs to be emphasized that the properties of lignin precursors must be highly controlled in order to produce high-value materials from lignin; in the sense: high value needs high control. Firstly, impurities like inorganics and carbohydrates need to be reduced to a minimum so that lignin purities close to 100% can be achieved. Other heteroatoms or heteropolymer fragments (LCCs) that are covalently incorporated or preserved in the lignin structure during the extraction process must be determined and controlled. For example, during the Kraft process, sulfur is covalently incorporated in the lignin polymer. Secondly, the molar mass distribution (dispersity) should be as narrow as possible which results in a more homogeneous macromolecule than polymeric material with high (poly)dispersity (wide molar mass distribution).[68–70] Isolated lignins obtained by precipitation out of the liquid phase (e.g. black liquor) show high dispersity indices (D) underpinning their heterogenous structure and chemistry caused by both the biosynthesis and the separation/isolation process. Fractionation was shown to split the initially very heterogenous macromolecule lignin into several more homogeneous fractions.[69,71–73] Fractionation can either be implemented in the lignin isolation process by selective precipitation at various pH values and ultrafiltration or it can be applied as post-processing step after isolation of the lignin as solid via solvent fractionation.[71,74] Ultrafiltration is based on size exclusion which is achieved by applying ceramic membranes with variable cut-offs (e.g. 1, 5, and 15

kg/mol) to the lignin-rich liquid phase (e.g. black liquor).[71] One drawback of ultrafiltration is that the initial fraction contains a large number of impurities (inorganics and carbohydrates). Therefore, ultrafiltration needs to be coupled with subsequent isolation and purification steps, like ion exchange. Since the Kraft lignins used in this work were isolated by precipitation based on the LignoBoost process, refining was done as post-processing step through sequential solvent fractionation. In this process, the insoluble lignin fraction is dissolved in organic solvents with varying solubility parameters. In order to ensure economic viability of value chains based on lignin as macromolecule, the emergence of different fractions with distinct properties needs to be considered. This gives the opportunity to establish several value chains from a single lignin via fractionation.

After fractionation of the isolated lignins, the characterization of the lignin fraction used as macromolecular precursor is of great importance in order to ensure reproducibility and to establish precursor-product relationships. To date, this is scarcely performed which is due to the fact that chemical and structural analysis of lignin poses a formidable challenge. To overcome this obstacle, collaborations between lignin chemists and materials scientists need to be established which has been the core of this project in the form of a close collaboration between RISE AB (Kraft lignin) and the Titirici group (carbon materials). The valorization of lignin as macromolecule in form of load-bearing carbon fibres and carbon nanofibres is described in the subsequent sections.

2.3.2. Lignin as precursor for load-bearing carbon fibres

The use of lignin as the precursor for carbon fibres (CFs) suitable for load-bearing applications has a long history initiated in the 1960s at Nippon Kayaku in Japan.[75] This endeavor is still carried on at present, notably by the Oak Ridge National Laboratory in the USA and RISE AB in Sweden as the value potentially generated from lignin-based carbon fibres is higher than for other products, such as lignin-derived resins or surfactants.[76,77] Nowadays, commercial CFs are

mainly used in aerospace, aeronautics, wind energy applications and special sporting goods, but they are not in widespread use even though the demand is high.[76] For example, the automotive industry seeks to reduce vehicle weights to increase fuel efficiency by replacing steel components with carbon fibre reinforced composites.[78,79] However, the main barrier to a widespread use of CFs is the high cost of the carbon fibre production. The high price arises from the precursor that is polyacrylonitrile (PAN).[78] It is produced by polymerization of toxic and cancerogenic acrylonitrile (AN) with a co-monomer (such as methylacrylate) content of up to 5 wt% through a radical polymerization process yielding a semi-crystalline, linear polymer with highly polar nitrile groups (Figure 2-9a).[80–82] Lignin as a low-cost and more benign precursor with its high carbon content (>60 wt%) and a high degree of aromaticity is a promising alternative.[78,83]

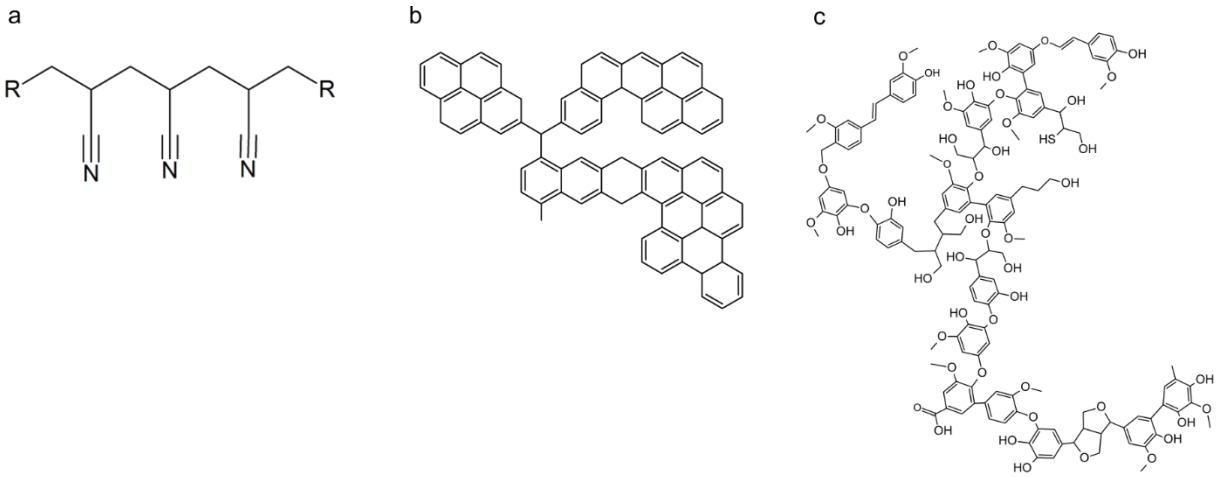

Figure 2-9 The precursors used for the production of carbon fibres: PAN (a), mesophase pitch (b) and lignin based on the lignin model scheme published by Crestini et. al.[59] (c).

Considering the fact that 51% of the total manufacturing cost of carbon fibres is determined by the starting material, lignin is by far more economic than PAN and independent of fossil resources compared to mesophase pitch.[84] However, its highly crosslinked and disordered structure is a major drawback as it impedes the formation of a highly ordered, aligned and dense graphitic structure in the final CFs. Additionally, lignin contains about 30 wt% oxygen that generates voids (defects) during thermal conversion of the biopolymer to carbon fibres. These features are detrimental to the tensile strength and the modulus of the final lignin-based carbon fibres (LCF) as the tensile modulus of CFs was shown to be related to the preferred orientation

of the graphite layer planes along the fibre axis.[85] The tensile strength is dependent on the density and interconnection of defects in the graphitic planes.[85] Therefore, the high degree of structural disorder and oxygenation are the intrinsic barriers to the replacement of commercially available polyacrylonitrile carbon fibres (PAN-CFs) by LCF. To date, LCFs cannot compete with PAN-CFs in terms of tensile strength and Young's (tensile) modulus (Figure 2-10). These are the main two parameters which determine the grade of commercial carbon fibres in load-bearing applications: ultra-high modulus (UHM) (>500 GPa), high modulus (HM) (>300 GPa), intermediate modulus (IM) (>200 GPa), and high tensile strength (HT) (>3 GPa).[82,86] In order to be suitable for carbon fibre reinforced composites in the automotive sector, CFs need to have at least a tensile strength of 1723 MPa and a modulus of 172 GPa.[87] The highest tensile strengths and moduli reported for lignin-based carbon fibres are in the range of 1000 MPa and 100 GPa (Figure 2-10). In particular, the tensile moduli of LCFs do not meet the requirements of the automotive industry. Since the modulus is mainly dependent on the degree of graphitization and preferred orientation of the crystallites along the fibre axis, it is obvious that the intrinsic amorphous and branched structure of lignin is the main obstacle towards commercialization of LCFs. Despite of this fundamental hurdle, the field of research is still quite active due to the potential cost reduction based on the sourcing of the precursor and the manufacturing of CFs from lignin.[83] The overall process chain for both precursors (PAN and lignin) is in principle similar, but the details are different and accordingly various advantages and disadvantages emerge. Firstly, the fibre production from PAN is performed via wet-spinning in a coagulation bath, whereas lignins can be melt-spun. The coagulation bath is typically a mixture of the solvent (e.g. dimethyl sulfoxide, DMSO) and a non-solvent (e.g. water) of the polymer.[88] Low spinning rates are necessary to produce high-quality fibres and additional costs for solvent handling are disadvantageous and add to the high price of PAN-CFs today.[82,88] In contrast, meltspinning of lignin is a solvent-free process and hence industrially attractive. The melted

lignin is extruded into a gaseous atmosphere (e.g. air) through nozzles directed downward, so that the extruded fibres are cooled and solidified.

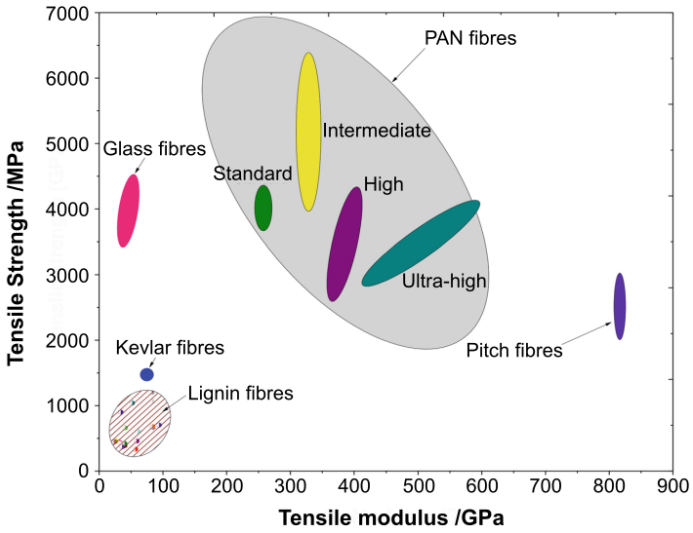

Figure 2-10 Mechanical performance map of carbon fibres from lignin in comparison to synthetic counterparts (adapted version of the one in Ismail et al.[89]).

The solidified fibre is continuously wound onto a spinning spool. After production of the polymer fibre, it needs to be converted to the carbon fibre. This is done in a two-step procedure via heating in air (stabilization) and pyrolysis in an inert atmosphere (carbonization). A third, optional and very energy demanding step is graphitization at a very high temperature of up to 3000 °C in an inert atmosphere to improve the ordering and orientation of the graphitic planes in the direction of the fibre axis.[80] Both PAN and lignin fibres are stabilized at temperatures between 200 and 300 °C to transform the thermoplastic polymers to thermoset materials so that the polymer fibres can be heated to high temperatures during carbonization while maintaining the fibrous shape.[88] The process of stabilization PAN fibres is carried out under tension and at heating rates between 1 and 3 °C/min.[88] It was found that for lignin slow heating rates in the range of 0.01 to 0.5 °C/min are needed to retain the fibre shape without fusing.[90–92] Finally, carbonization converts the polymer fibres to carbon fibres via removal of volatile compounds. Hence, a carbon content well-above 90 wt% can be attained. PAN is usually carbonized up to 1600 °C, which leads to the formation of turbostratic carbon within the fibres.[82] This

turbostratic carbon phase is highly oriented along the fibre axis, but not yet fully graphitic.[82] When heated to temperatures ranging from 1800 to 3000 °C (graphitization), the highly oriented turbostratic carbon structure is converted to a crystalline graphitic structure.[82] The optimum temperatures for the carbonization of lignin are in the range of 1000 – 1200 °C.[91] Higher temperatures lead to lower tensile properties which might be due to an increase in defect density.[91] Graphitization studies conducted on LCFs showed that the formation of a graphitic structure takes place.[93] However, the orientation of the graphitic domains along the fibre axis is poor which explains the rather low tensile moduli.[94]

Even after several decades of intense research efforts, LCFs cannot compete with commercial PAN-CFs in terms of tensile strength and modulus. Therefore, alternative uses of LCFs in composite materials, such as Li ion battery electrodes are considered.[95] Additionally, alternative uses where the mechanical properties are not the main interest, such as activated carbon fibres, have also been considered which will be described in the following.[96,97]

2.3.3. Lignin as precursor for porous carbon nanofibres

The high degree of oxygenation and low structural order along with a high degree of aromaticity with many functional groups (e.g. hydroxyl/methoxy groups) makes lignin a very suitable precursor for the manufacture of porous carbons with good yield. However, the potential economic value is considerably lower than for load-bearing carbon fibres. Additionally, commercial porous (activated) carbon powder is already made from biomass waste (e.g. coconut shells and wood) and hence lignin does not have the merit of being more environmentally friendly than the precursor currently in use.[98–100] Therefore, the production of activated carbons from lignin has not been studied as intensively as load-bearing CFs even if the possibility has been mentioned in the literature.[96,101,102] Only recently, an increasing number of publications focuses on activated carbons from lignin.[20,103–108]

However, the fact that lignin is a macromolecule with numerous polar functional groups rendering it soluble in many common solvents is a property that other biomass (e.g. coconut shells and wood) precursors do not have. Thus, starting from lignin gives the opportunity to manufacture free- and self-standing materials in the form of nanofibre (diameter <1 μm) networks via electrospinning rather than loose powders from other biomass sources.[109] This eliminates post processing steps like slurry, film and electrode preparation needed to immobilize carbon powder in the final application.

Electrospinning involves a syringe loaded with a polymer solution, such as lignin dissolved in dimethyl formamide (DMF) or $NaOH_{(aq)}$ (Figure 2-11). This polymer solution is then ejected by means of a syringe pump into an electrostatic field established between the needle's tip and a grounded metallic collector (e.g. aluminum foil).[110] When the electrostatic force acting on the surface of the liquid overcomes the surface tension, several charged liquid jets emerge from the Taylor cone formed at the needle's tip and are ejected towards the collector.[111] On the way from the needle's tip to the collector the solvent progressively evaporates and the jets start whipping upon further evaporation of the solvent due to the unevenly distributed charges and the resulting repulsion.[112] When the jets reach the collector the majority of the solvent is evaporated and the fibres solidify. A non-woven mat composed of randomly oriented fibres with diameters in the sub-micrometer range (nanofibres) are collected on the grounded metallic foil. Finally, the self-contained and flexible nanofibre mat can be peeled-off the collector and prepared for further processing steps such as stabilization, carbonization and activation. The scalability of electrospinning technical lignins has been demonstrated quite recently by Scion, a research institute located in New Zealand.[113] Compared to the above-mentioned meltspinning of lignin, electrospinning requires less control over the thermal properties of lignins (e.g. low T_g). Thus, it can be taken advantage of the quite high T_g of softwood lignins and high-molar mass hardwood lignin fractions that can be stabilized at high rates of up to 20 °C/min.[84,114] Furthermore, the

electrospinning process is flexible as the solvent for lignin and additives can be chosen to optimize the properties of the final fibres (e.g. porosity, functionality).

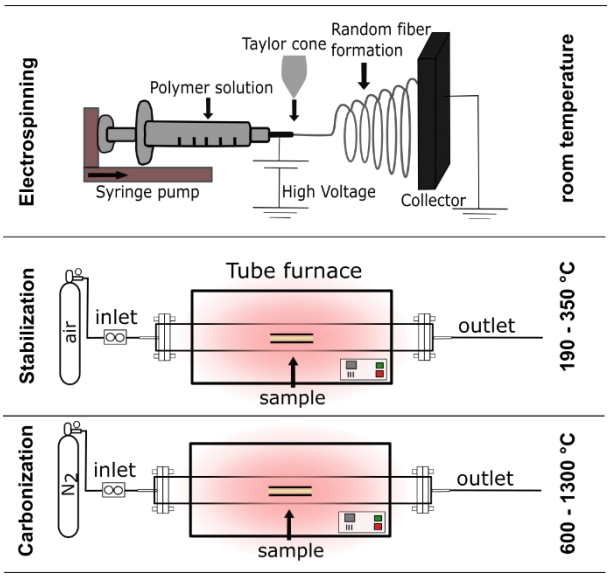

Figure 2-11 The main process steps for the manufacturing of LCNFs via electrospinning and a two-step thermal conversion.

Electrospun lignin-derived carbon nanofibre (LCNF) mats have been investigated for over a decade. First reports of LCNFs from Organsolv lignin via co-axial electrospinning were published by Lallave et al. in 2007 (Figure 2-12).[115] Therein, the authors describe electrospinning of lignin dissolved in ethanol without any additive.[115] By using glycerine as a template hollow fibres were produced.[115] After establishing this electrospinning system the same group proved the flexibility of the process by changing process parameters such as composition of the spinning solution and thermal treatment of the as-spun lignin nanofibres.[109,116–119] Kadla and Kubo showed in a series of papers that strong intermolecular interactions between lignin and polyvinyl alcohol (PVA) and polyethylene oxide (PEO) exist.[120–125] These intermolecular interactions (e.g. hydrogen bonding) have subsequently been demonstrated to facilitate continuous electrospinning of various technical lignins (e.g. Organosolv lignin, Kraft lignin).[126,127] In a subsequent study, lignosulfonate lignin was blended with PAN.[128] The mechanical properties were shown to be best for the 50:50 PAN/lignin blend.[128] Cho et al. showed that electrospinning of fraction-

ated softwood Kraft lignin with PEO and cellulose nanocrystals (CNC) allows to skip the stabilization step in air without fusing of fibres depending on the heating rate during carbonization.[129] Hu et al. reported the production of highly porous electrospun LCNFs via a single-step carbonization/activation process.[130] They showed that using PEO not only facilitates electrospinning of Kraft lignin, but also enables thermal treatment of the fibres without losing structural integrity or fusing.[130]

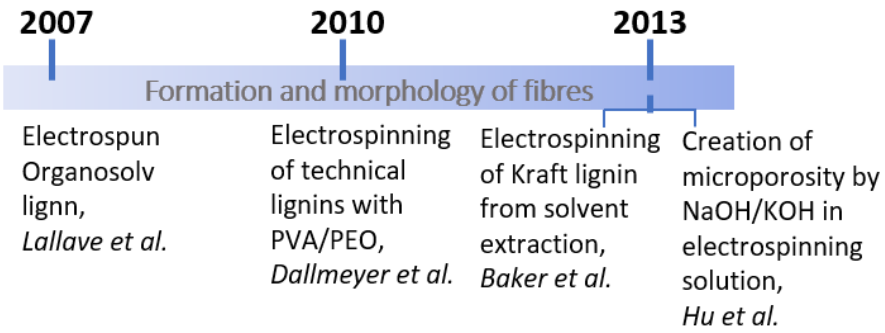

Figure 2-12 Timeline with the key publications on electrospinning lignin with the main focus on the formation and morphology of the resulting fibres.

Additionally, they demonstrated that incorporating small amounts (alkali hydroxide/lignin ratios of 0.1, 0.3 and 0.5) of NaOH in the electrospinning solution creates both micro- and mesoporosity, whereas by adding KOH, mainly microporosity was created.[130] Hosseinaei and Baker described a procedure in which a commercial lignin can be purified and fractionated by solvent extraction to give a lignin with a high T_g (e.g. 185 °C) that can be electrospun without any additive in a solvent mixture of DMF and methanol and rapidly converted to carbon nanofibres.[84]

After this first wave of publications on lignin-derived carbon nanofibres which was mainly concerned with the formation and morphology of fibres, the first application-based publications of LCNFs appeared in 2013 (Figure 2-13). Choi et al. fabricated PAN/Kraft lignin-based carbon nanofibres with various weight ratios of PAN to lignin for high-power lithium ion battery (LIB) anodes.[131] They ground the fibrous mats into granular material and coated it onto a copper foil used as current collector.[131] These electrodes were then tested as anodes in half cells against

lithium metal.[131] The authors showed that the manufactured carbon nanofibres exhibited almost the same exceptionally high rate capability regardless of the lignin content.[131] However, the initial irreversible capacities were higher for the carbon nanofibres with lignin than for the purely PAN-based fibres.[131] In the same year, Wang et al. published an article about the use of lignin-derived fused electrospun carbon fibrous mats as free-standing anodes in LIBs.[132] The authors prepared a PEO-Organosolv lignin blend by electrospinning, carbonized these mats directly and finally annealed them in the presence of urea to increase the nitrogen content which improved the electrical conductivity.[132] The maximum specific capacity was 445 mAh/g at 0.1 A/g.[132] Hu et al. tested supercapacitors (SCs) based on sub-micrometer activated LCNFs in aqueous 6 M KOH electrolytes.[133] They fabricated the LCNFs by their previously established recipe with PEO as co-polymer and KOH as activation agent in the spinning solution.[133] The authors did not use the LCNF mats as free-standing electrodes, but prepared dispersions of them via sonication to deposit them on a nickel foam as current collector.[133]

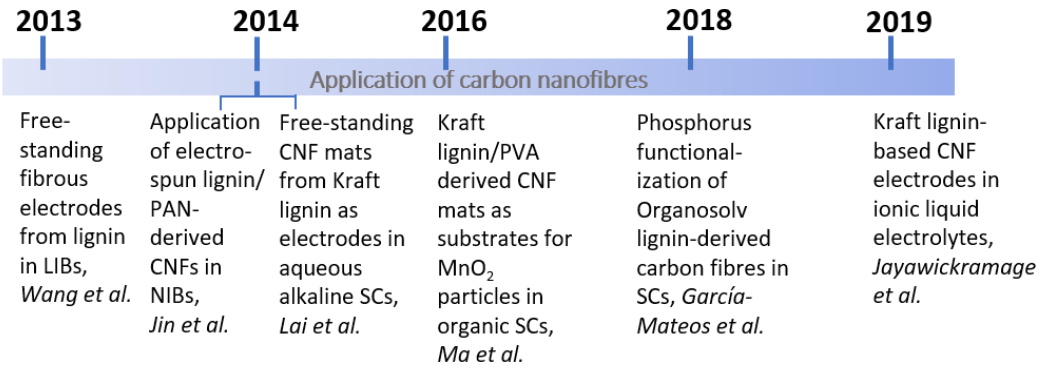

Figure 2-13 Timeline with the key publications on electrospun lignin-derived carbon nanofibres with the main focus on their application in energy storage.

Notably, the KOH activated LCNFs showed high specific gravimetric capacitance (344 F/g) with low mass loading (1.8 mg/cm^2) at 10 mV/s.[133] With increasing active material loading (10 mg/cm^2) and increasing scan rate (50 mV/s) the performance decreased to a still high value of 196 F/g and a high areal capacitance of 0.55 F/cm^2.[133] Lai et al. published an article on free-standing and mechanically flexible mats from Kraft lignin-derived electrospun carbon nano-fibres as electrodes.[134] Their spinning solutions contained Kraft lignin-PVA blends dissolved

in water with a mass ratio of Kraft lignin/PVA being 70/30.[134] After stabilization in air at 220 °C and carbonization in N_2 at 1200 °C, the researchers used the electrospun LCNF mats as electrodes in supercapacitors without further processing.[134] They tested the LCNFs in two-electrode supercapacitor cells in 6 M KOH electrolyte. However, their maximum capacitance values were considerably lower (64 F/g at a current density of 0.4 A/g) than the ones reported by Hu et al., even if they were tested in the same electrolyte.[133,134] More recently, PAN/lignin-based CNFs were also used in high-voltage (3.5 V) SCs operating with an ionic liquid as electrolyte exhibiting a high specific capacitance of 128 F/g and an energy density of 59 Wh/kg.[135] Jin et al. were the first to report the application of electrospun lignin/PAN derived carbon nanofibres in sodium ion batteries (NIBs).[136] The authors used commercially available hardwood lignosulfonate lignin and dissolved various mass ratios of it with PAN in DMF.[136] After stabilization at 250 °C for 1 h in air and carbonization at temperatures ranging from 800 to 1300 °C in N_2, they used the LCNF mats without further modifications as anodes in NIB half cells with sodium metal as the counter electrode.[136] The best results were obtained for blends with equal amounts of PAN and lignin carbonized at 1300 °C.[136] This material showed a reversible capacity of 292.6 mAh/g with an initial coulombic efficiency of 70.5% at a current density of 0.02 A/g.[136] In 2015, Ma et al. used straw lignin as precursor for electrospinning lignin-PAN blends dissolved in DMF.[137] Rather than focusing on the application of the LCNF mats they investigated the lignin precursor (Figure 2-14). The authors characterized four lignins by elemental analysis and chose a straw lignin for the fabrication of LCNFs because of its low sulfur and high carbon content.[137] After electrospinning, they converted the lignin nanofibres to CNFs via stabilization at 280 °C and carbonization at different temperatures (600, 700, 800, 900, 1000 °C) in N_2.[137] Regardless of the carbonization temperature, a low degree of graphitization was determined for all samples by X-ray diffraction and Raman scattering.[137] Jeon et al. investigated the dependence of the porosity in the final carbon material on the type of lignin. Additionally, they tested

the performance of the lignin-derived carbon powder in symmetric two-electrode supercapacitors (SCs) using 1 M H_2SO_4 as electrolyte.[103] The authors compared three lignins (Kraft and Organosolv lignins) which differed in their weight average molar masses (1098, 1710, 2596 g/mol). They showed that the molar mass plays a major role in the development of porosity and the electrochemical performance of the lignin-derived carbon powder.[103]

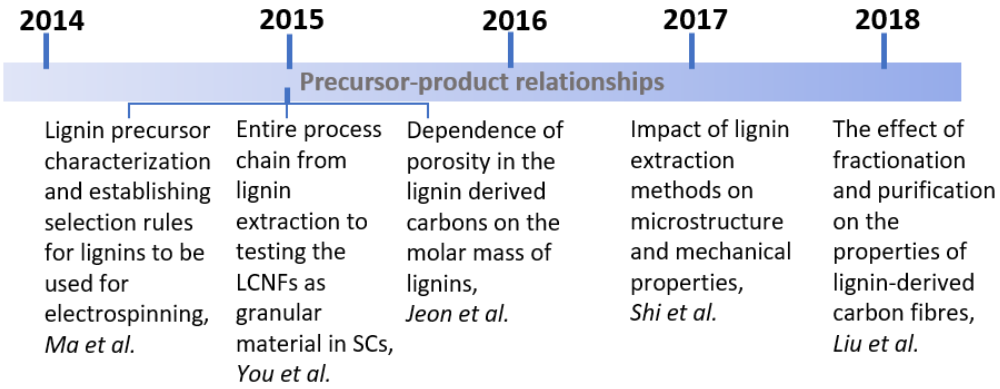

Figure 2-14 Timeline with the key publications on precursor (lignin)-product (carbon fibres) relationships in electrospinning lignin.

The maximum capacitance (114 F/g and 79 F/g at 5 mV/s and 100 mV/s) was achieved by the carbon material derived from the lignin with the lowest molar mass.[103] The authors related this to the degree of graphitization and porosity which were highest for this material.[103] You et al. published a work in which they describe the entire process chain from lignin extraction (birch wood via Organosolv treatment) to testing the LCNFs as granular material in symmetric SCs.[138] The authors have electrospun the Organosolv lignin in a solvent mixture of acetic acid and tetrachloromethane with hexamine which accelerated the stabilization in air at 250 °C.[138] The stabilized fibres were then carbonized at 1000 °C for 1 h in N_2. Finally, the LCNFs were activated at 900 °C with steam.[138] The activated LCNFs were then slurry coated on an aluminum foil and tested in symmetric two-electrode supercapacitors (SCs) using 1 M $TEABF_4$ (tetraethylammonium tetrafluoroborate) dissolved in PC (propylene carbonate) as electrolyte.[138] Since the SCs were charged and discharged up to 3 V, the measured capacitance of 133 F/g (at 1 A/g) translated into a high gravimetric energy density of 42 Wh/kg.[138] These promising results were

correlated with the high surface area of 2185 m^2/g with pore sizes in the range of 0.5 – 1.3 nm determined for this material.[138] In 2017, Shi et al. investigated the impact of the molar mass of different lignins obtained by various extraction methods on the microstructure and mechanical properties of lignin-based carbon fibres.[139] They concluded that a high molar mass with a narrow molar mass distribution is the key factor for preparing CNFs from lignins. Liu et al. showed similar trends in 2018 by preparing CFs from lignin/PAN blends with lignins with varying molar mass distributions dependent on the fractionation conditions.[74]

Besides investigating LCNFs as sole active material, research was also directed towards employing them as electrically conductive scaffolds for the deposition of metal particles. This gives the opportunity to increase the energy density. Ma et al. manufactured flexible LCNF mats by electrospinning aqueous solutions of Kraft lignin and PVA in order to use them as conductive substrates for MnO_2.[140] After stabilization and carbonization, MnO_2 was deposited in a separate step by immersing a LCNF mat into aqueous $KMnO_4$ solutions at 65 °C for four hours.[140] The resulting composite electrodes were then used in symmetric SCs in an organic electrolyte.[140] The maximum performance of 83.3 F/g, 84.3 Wh/kg, and the maximum power density of 5.72 kW/kg was achieved by the composite electrode with an equal mass ratio of MnO_2 to carbon.[140]

Porous carbons find application in the fields of gas capture and storage, filtration (sorbents) and energy storage.[21,104,141–143] As presented in this section, the use of lignin as precursor for porous CNFs has been studied in various contexts with different focal points. The work at hand is a contribution to the effort of producing porous, functional CNFs from well-characterized Kraft lignins towards free-standing and eventually flexible supercapacitors. These energy storage devices will be the topic of the final section of the literature review.

2.4. Porous carbons in mobile energy storage

Carbons are widely used in various energy storage technologies and applications due to their physical and chemical versatility.[144,145] For instance, the most widespread electrochemical energy storage system, namely Li ion batteries, relies on carbon (graphite) anodes.[146–148] Fuel cells and metal air batteries also heavily rely on carbon materials as active material or support of electrocatalysts.[149,150] Finally, electric double layer supercapacitors constitute another more rapid form of energy storage in which highly porous carbon materials play a crucial role by providing surface sorption sites for charge storage/accomodation.[145,151,152]

2.4.1. Supercapacitors in the context of energy storage

Supercapacitors, also called ultracapacitors or electrochemical capacitors, are energy storage devices that provide higher power (>10 kW/kg), but lower energy densities (~5 Wh/kg) than the widely used Li ion batteries (~150 – 200 Wh/kg) and Ni-metal hydride (~60 Wh/kg) batteries as shown in the Ragone plot displaying power versus energy density (Figure 2-15). Thus, supercapacitors are the devices of choice when power pulses are needed (e.g. engine cranking), whereas Li ion batteries can provide electrical energy continuously over hours due to their higher energy density.[145] The different characteristics of both devices arise from the fundamentally different charge storage mechanisms.

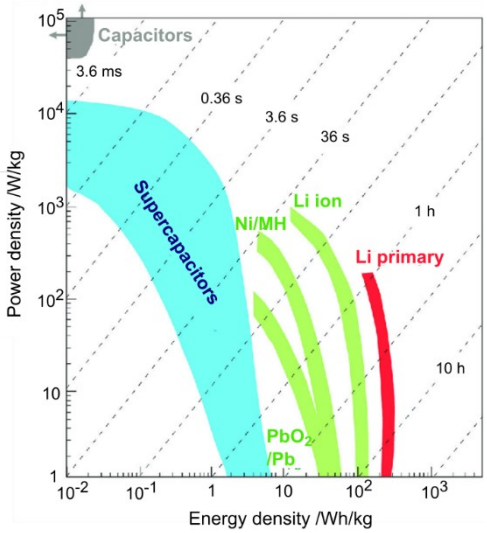

Figure 2-15 Ragone plot modified based on the version published by Simon et al.[153]

Energy storage for both devices can be understood as accommodation of charge (ions) at a certain cell potential (voltage). The higher the voltage (U) and the greater the amount of charge (Q) stored the more energy is stored.

Li ion batteries store charges indirectly via de-/intercalation of Li ions into Li host materials at 3 – 4 V. Most widely used are metal oxides as cathode and graphite as anode.[146] The de-/intercalation is a bulk reaction which changes the cathode and anode materials chemically and structurally involving several phase transitions accompanied by volume changes.[147]

Conversely, supercapacitors in their most original form store charges directly via electrostatic ad-/desorption of ions from the electrolyte on the surface of two oppositely polarized electrodes forming a so-called electric double layer at each of them. During charging and discharging, no chemical or structural changes are induced in the electrode materials. This fundamental difference in charge storage mechanism gives rise to very different specifications and hence both devices should be regarded as complementary rather than replaceable.[154] The degree of reversibility and thus the cycle life of SCs solely relying on the electrostatic ad-/desorption of ions on electrically polarized surfaces is much higher compared to batteries.[154] Moreover, the maximum power output of SCs is by orders of magnitude higher than the one of batteries due to the fact that no bulk chemical changes are associated with charging and discharging. However, both the amount of charges that can be stored and the operating voltage are considerably lower in SCs than in batteries and hence their energy density is lower.[152] The fundamental difference in charge storage mechanism is reflected in the charging and discharging profiles (voltage vs. time-plot) of the two devices (Figure 2-16). For Li ion batteries, the voltage is a smooth function of time only with a gentle slope, whereas for (super-)capacitors the voltage is a linear function of time.[155] As more charges are accumulated on the surface of the electrode during charging of a SC, increasingly more work has to be done against the already accumulated charges which

leads to progressively rising voltage in the charging process and vice versa during discharging.[155,156] Conversely, for LIBs the progressively increasing charge is being added at a quite constant (slowly decreasing) voltage U.

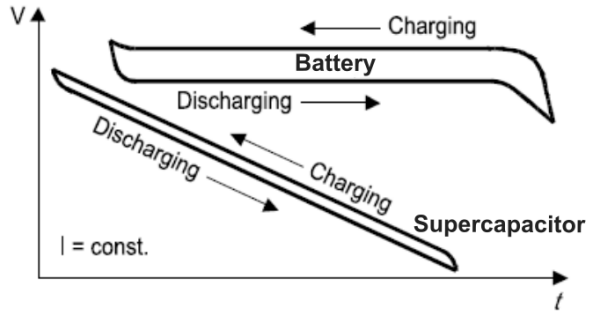

Figure 2-16 Idealized charge and discharge profiles of a battery and supercapacitor at a constant current.

Consequently, the Gibbs energy, G, stored in a SC based on electrostatic ad/desorption of ions is $G = ½ \cdot Q \cdot U$ compared to $G \cong Q \cdot U$ in a battery.[155] Since the invention and commercialization of the earliest supercapacitors that were solely based on the above-mentioned charge storage mechanism, new strategies have been pursued to increase the energy density of these devices. The different variations starting from the basic electric double layer supercapacitor (EDLC) will be described in the following.

2.4.1.1. Electric double layer capacitors

The electric double layer (super-)capacitor (EDLC) is the most original form of supercapacitor based on electrostatic ad-/desorption of the electrolyte ions on the surface of two oppositely polarized electrodes. This leads to the formation of electric double layers at the electrode-electrolyte interfaces. The earliest EDLC based on porous carbon electrodes has been patented, but not commercialized, by Becker at General Electric in 1957.[157] It was not further considered by industry or academia until 1970, when Standard Oil filed another patent on "Electrolytic capacitor having carbon paste as electrodes" which it sold to Nippon Electric Corporation where it was further developed and successfully marketed.[158,159] It was not until the 1990s that EDLCs emerged from a niche product to a widely used energy storage device in hybrid vehicles where they have been used within brake energy regeneration and start-stop systems.[160,161] To date,

electrodes still consist of activated carbon pastes coated on aluminum current collectors as described in these early patents.[145] Nowadays, the most widespread electrolytes are organic (e.g. tetraethylammonium tetrafluoroborate in acetonitrile or propylene carbonate). However, there are also EDLCs commercially available that use aqueous electrolytes for very high power applications.[159,162] The principal difference between the aqueous and organic electrolyte-based devices is the electrochemical stability window (ESW), which is 1.23 V for aqueous electrolytes and 2.5 – 2.7 V for organic electrolytes.[152] Ionic liquids (ILs) with ESWs of up to 6 V have been proposed as a possible strategy to increase the energy stored in an EDLC.[152,163] Increasing the operating cell voltage is a promising pathway to increase the energy as the stored energy in an EDLC rises with the square of the cell voltage meaning doubling the voltage results in a four-fold increase of the energy (equation I). However, ILs suffer from drastically reduced maximum power at room temperature, safety issues and high manufacturing costs.[152,159]

$$E = \frac{1}{2} \cdot C \cdot U^2 \qquad \textbf{(I)}$$

Where E = energy [Ws], C = capacitance [F], U = cell voltage [V]

The capacitance is defined as the amount of charge (Q) accumulated on the electrodes' surfaces per potential difference (V) applied. The capacitance (unit: Farad, F) is mainly dependent on the accessible surface area (A) and the dielectric constants (ε_r) of the electrolyte and the double layer thickness (d).

$$C = \frac{Q}{U} = \frac{\varepsilon_r \cdot \varepsilon_0 \cdot A}{d} \qquad \textbf{(II)}$$

Where C = capacitance [F], Q = charge [C], U = voltage [V];
ε = dielectric constant of electrolyte (r) and vacuum (0) [As/Vm], A = accessible surface area [m^2], d = double layer thickness [m]

In addition to the energy stored in a supercapacitor, the second main characteristic is the maximum power (P_{max}), which is the rate of energy released per unit time. P_{max} is determined by the resistance of the internal components of a SC cell such as current collectors, electrode materials,

the electrolyte and the separator. It can be measured via the equivalent series resistance (ESR) to which all the previously mentioned resistances contribute.

$$P_{max} = \frac{U^2}{4 * ESR} \quad \textbf{(III)}$$

Where P_{max} = maximum power [W], U = voltage [V], ESR = equivalent series resistance [Ω]

In industry, capacitance, energy and power are given as absolute values for a certain supercapacitor type, whereas in materials science where different materials are to be compared, energy, power and the capacitance are normalized either by weight (gravimetric) or by volume (volumetric) of the electrodes tested. This gives rise to the units Wh/kg or Wh/cm^3 for energy density, W/kg or W/cm^3 for power density and F/g or F/cm^3 for the specific capacitance used throughout this thesis. Since there are two electrode-electrolyte interfaces in one EDLC cell at which double layer formation occurs upon charging (polarization of the electrodes), the total cell capacitance (C_{cell}) is calculated as a series of capacitances (equation IV).

$$\frac{1}{C_{cell}} = \frac{1}{C_+} + \frac{1}{C_-} \quad \textbf{(IV)}$$

Where C_{cell} = cell capacitance [F], C_+/C_- = capacitance on positively/negatively polarized electrode [F]

Hence, if $C_+ = C_- = C_e$ it follows equation (V).

$$C_{cell} = \frac{C_e}{2} \leftrightarrow 2 * C_{cell} = C_e \quad \textbf{(V)}$$

Where C_{cell} = cell capacitance [F], C_e = capacitance of the individual electrode [F]

Dividing the last expression in equation (V) by the weight or volume of one electrode (positive electrode) in the SC cell gives the gravimetric/volumetric capacitance. However, it is more representative of the entire SC cell to consider the weight of both electrodes (total active carbon in the cell) which leads to equation (VI) used here.

$$C_{cell} = \frac{C_{active}}{4} \leftrightarrow 4 * C_{cell} = C_{active} \quad \textbf{(VI)}$$

Where C_{cell} = cell capacitance [F], C_{active} = capacitance of the total active carbon in the cell [F]

Other than testing different electrolytes in order to optimize energy and power densities, a key parameter to optimize is the porous carbon structure and chemistry to maximize the cell capacitance. This can only be done in the context of a certain electrolyte as every electrolyte type (aqueous, organic or IL) and different electrolytes of one type require different pore structures and surface chemistries. For instance, it was shown that the maximum capacitance can be attained by matching the pore sizes to the unsolvated ion sizes in the electrolyte.[164,165] Different models exist to describe the electric double layer in a porous system filled with electrolyte. Based on earlier models published by Helmholtz and Gouy and Chapman, Stern described two different regions of ion distribution at the electrode-electrolyte interface: 1) the so-called compact or Stern layer and 2) the diffuse layer.[166] In the compact region, ions from the electrolyte are strongly adsorbed by the electrode, whereas in the diffuse layer further away from the electrode there is a continuous distribution of ions in solution arising from thermal motion.[166] Hence, the overall double layer capacitance consists of both compact and diffuse layer capacitance.[166] Since the carbon electrode materials are highly porous, the double layer charging becomes considerably more complex.[152] To describe the double layer formation in highly porous structures on a microscopic level, Huang et al. established a model based on density functional theory (DFT) combined with experimental data.[167] In their model, the authors take into account curvatures of pore walls by introducing additional terms in equation (II). They found an improved correlation of their model to experimental data by applying the curvature terms for pores with sizes of 2 – 50 nm (mesopores) and <2 nm (nanopores).[167] Assuming that the mesopores were cylindrical, the authors modelled that the solvated ions enter the pores and approach the pore walls of the cylindrical pore to form an inner cylindrical arrangement of the adsorbed ions generating an electric double-cylinder capacitor (Figure 2-17a).[167]

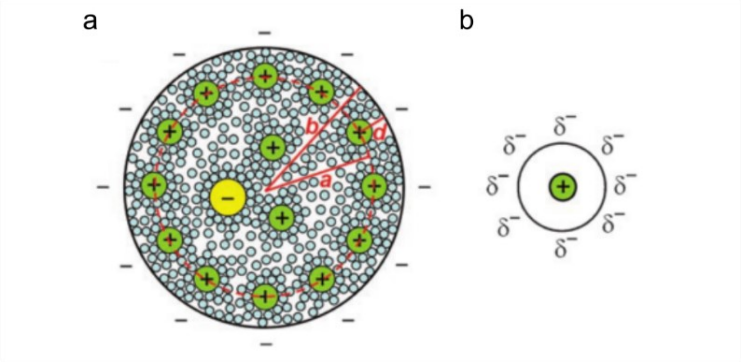

Figure 2-17 Schematic diagrams of a negatively charged mesopore with cations approaching the pore wall to form an electric double-cylinder capacitor with radii b and a for the outer and inner cylinders, respectively, separated by a distance d (a) and a negatively charged nanopore with cations lining up to form an electric wire-in-cylinder capacitor (b) (taken from Huang et al.[167]).

In nanopores, however, the width of pores is drastically reduced and hence the solvated or desolvated ions line up to form a single line of ions (an electric wire-in-cylinder capacitor) (Figure 2-17b).[167] Next to the new insights into the geometry of the electric double layers in nanopores, the dynamics of charging of electric double layer capacitors was studied by in operando nuclear magnetic resonance (NMR) spectroscopy and molecular dynamics (MD) simulations.[165,168] It was shown that upon polarization of the carbon electrodes, the charging mechanisms involve a variety of processes rather than only simple counter-ion (anion on positive electrode) adsorption. Since the pores contain ions (counter and co-ions) even in the uncharged (unpolarized) state, counter-ion adsorption, ion exchange, and co-ion desorption illustrated in Figure 2-18 take place upon polarization of pores in the carbon electrode that were initially filled with electrolyte.[165,168] The ion exchange charging mechanism was found to be the most prominent mechanism by in situ characterization techniques, whereas pure counter-ion adsorption has not been observed to date.[168,169] Next to the pore size effect, pore connectivity and the overall pore size distribution were shown to be important, particularly for achieving high power densities.[170] Hierarchical porous carbons exhibiting a large fraction of micropores (<2 nm) with a fair amount of well-connected mesopores facilitating ion transport seems to be the optimum for high capacitance and good rate capabilities.[170]

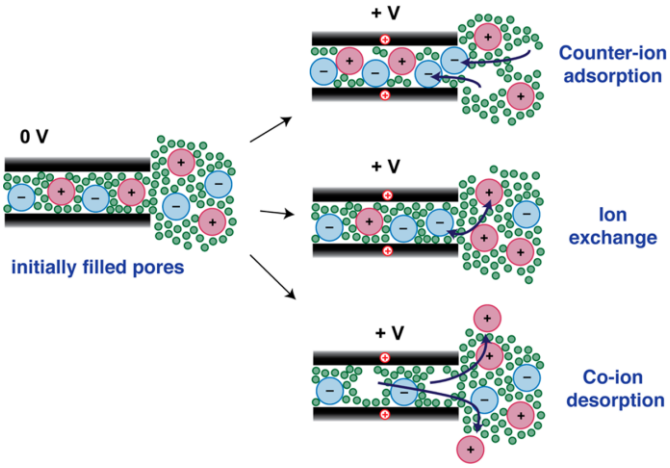

Figure 2-18 Possible charging mechanisms for pores initially filled with electrolyte: counter-ion adsorption, ion exchange, and co-ion desorption (taken from Forse et al.[168]).

Depending on the starting precursor, the strategy to achieve this pore structure are highly variable. Starting from biomass (e.g. wood) or biomass components (e.g. lignin) yields inherent pore creation during pyrolysis creating highly porous structures as biomass precursors are oxygenated and often have a hierarchical pore structure, which may be preserved during conversion to carbon materials.[171] Conversely, starting synthesis from fossil hydrocarbon precursors gives rise to dense and ordered carbon materials as fossil carbon sources are almost oxygen-free and structurally more ordered than biomass precursors (e.g. mesophase pitch versus lignin, Figure 2-9). In order to increase the porosity, chemical and physical activation procedures, soft and hard templating are applied.[172,173] For chemical activation dehydrating salts like KOH and $ZnCl_2$ and for physical activation steam or $CO_{2(g)}$ at high temperature (700 – 900 °C) are commonly used.[172,173] These two methods affect both micropores and mesopores. Soft and especially hard templating mainly affect the mesopore structure.[174,175] Consequently, in academia templating strategies are often coupled with chemical or physical activation to attain hierarchical pore structures.[176] However, activated carbons produced on an industrial scale are prepared via chemical or physical activation starting from biomass (e.g. wood, coconut shells) or fossil carbon sources (e.g. petroleum coke, pitch, synthetic polymers) as templating

strategies are too costly.[177,178] An overview of capacitances measured for various carbon materials in different electrolytes is shown in Table 2-1.

Table 2-1 Gravimetric capacitance values for various carbon materials in different electrolytes.

	Capacitance /F/g		
Electrode material	**Aqueous**	**Organic**	**Ionic liquid**
Activated carbons	100-200[145]	100-150[145]	100-150[179]
Templated carbons	120-350[180]	120-135[152]	150[152]
Carbon nanotubes	20-180[145,172]	20-80[152]	20-45[181]

Depending on the type of electrolyte, differences in terms of surface chemistry need to be considered, too. In organic and IL electrolytes, which operate at high voltages, it is important that the number of oxygen groups (e.g. carboxylic acid groups) is kept at a minimum as these functional groups were shown to be unstable at high voltages (>2.0 V).[182,183] Fossil precursors are more suitable than biomass ones due to the lower degree of oxygenation. However, in aqueous systems, oxygen or nitrogen functional groups can improve the performance considerably.[184] Firstly, polar functional groups make carbon materials more hydrophilic and hence more accessible to the aqueous electrolyte.[172] Secondly, certain functional groups were shown to interact with ions not only via the electrostatic ad-/desorption mechanism, but also through an additional charge storage mechanism, namely pseudo-capacitance, which is described in the following section.

2.4.1.2. Pseudo-capacitors

Pseudo-capacitance is a charge storage mechanism distinctly different from the electrostatic ad-/desorption of ions on the electrodes' surfaces as an electrochemical charge transfer (redox process) takes place.[152] Hence, pseudo-capacitors incorporate a charge storage mechanism based on rapid and reversible near-surface redox reactions unlike diffusion limited bulk redox reactions in batteries.[152] It occurs together with the previously described EDLC behavior. To account for this new charge storage mechanism, the term 'pseudo'-capacitor/capacitance was

coined by Conway.[152,155] Transition metal oxides, such as RuO_2, MnO_2 and PbO_2, have been used to add pseudo-capacitance and hence increase the energy density of SCs. Moreover, the cell design was modified so that the positive electrode was pseudo-capacitive, whereas the negative electrode purely based on the electrostatic ad-/desorption of ions (asymmetric EDLC). Thus, the cell capacitance could be almost doubled compared to a symmetric EDLC device.[152] However, additional costs for the materials and their manufacture has limited their use to niche markets (e.g. military applications).[185] Moreover, carbon materials with oxygen and nitrogen functional groups on their surface show reversible charge transfer reactions in aqueous media.[172] For instance, oxygen functionalized carbon materials also show pseudo-capacitive behavior especially in acidic media.[144,186] Notably, the protonation and deprotonation of quinone/hydroquinone groups in the carbon structure give rise to an additional charge transfer reaction (Figure 2-19a).[187] This well-known redox reaction for oxygen functional groups has also been demonstrated with lignin-derived carbon materials.[188] Furthermore, pyrone-like structures (combination of non-neighboring carbonyl and ether oxygen atoms at edge of graphene layers) have been proposed to be redox active. After the irreversible protonation of the carbonyl group by an acid pre-treatment a formal positive charge on the ether oxygen is created rendering it electrochemically active (Figure 2-19b).[187,189,190] Generally, the pseudo-capacitive behavior in basic electrolytes (e.g. $KOH_{(aq)}$) is not as well-understood as in acidic media. It was shown that increasing oxygenation of the carbon electrodes results in a higher affinity towards alkali and alkaline earth metal ions, such as K^+ or Ca^{2+}, contributing to an increase in capacitance.[191]

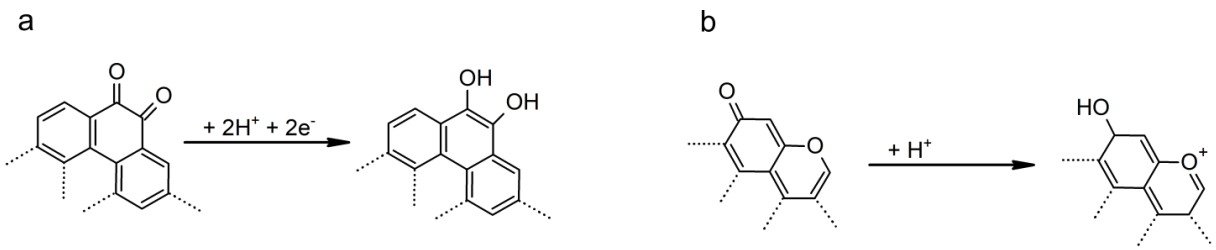

Figure 2-19 The reduction/oxidation of quinone/hydroquinone groups (a), pyrone activation protonation of the carbonyl group by an acid treatment (b).

Another strategy towards boosting the energy density of SC devices is to couple a battery electrode with a supercapacitor electrode in a so-called hybrid-capacitor cell.[192]

2.4.1.3. Hybrid capacitors

In order to increase the energy density even more, hybrid capacitors are being developed and have been commercialized already.[193,194] Instead of either increasing the voltage window or the charge storage capacity of the supercapacitor, both can be achieved at the same time with the concept of hybrid capacitors. Within this concept, the positive electrode is a highly porous carbon electrode, whereas the negative electrode is chosen to be an intercalation compound such as graphite or a transition metal oxide.[193] The electrolytes used in hybrid capacitor cells are usually organic, such as lithium hexafluorophosphate ($LiPF_6$) dissolved in propylene carbonate (PC). Thus, the hybrid capacitor consists of an EDLC electrode and a de-/intercalation battery electrode together with organic electrolytes similar to the ones used in pure battery devices. In general, two types of hybrid capacitors can be distinguished differing in the choice of the electrode materials. There are 1) carbon-carbon hybrid cells where both electrodes are made of carbon materials, like activated carbon as the positive and graphite as the negative electrode and 2) carbon-transition-metal-oxide cells where the negative electrode is composed of a transition metal oxide and the positive electrode of activated carbon. The carbon-carbon hybrid cell type is less expensive and based on facile materials, but in order to achieve high coulombic efficiencies and maximum cell potential the graphite negative electrode needs to be pre-doped with the ion (e.g. Li^+) to be used in the final cell. In the hybrid cell type with a transition metal oxide as negative electrode material, the pre-doping step is dispensable, but the preparation of the electrode material is more sophisticated and hence more expensive.[192,193,195,196] Coupling EDLC electrodes with de-/intercalation electrodes gives rise to significant advantages compared to the original battery or EDLC cells.[193] Firstly, the Li ion de-/intercalation occurs in the negative electrode at a shallower state of charge which means that less severe structural and

chemical changes are induced in the material than in the corresponding pure battery cell. Additionally, rather than solely relying on the Li ion for charge shuttling between the two electrodes both cations and anions are used in a hybrid capacitor cell. The cation (e.g. Li^+) undergoes intercalation and deintercalation on the negative electrode (e.g. graphite) and the anion (e.g. PF_6) is ad-/desorbed on the porous positive electrode (e.g. activated carbon). This leads to higher charge storage capacity at higher operating voltage (3.8 – 4.0 V) compared to organic electrolyte based EDLCs.[193,195] However, the power density is reduced through the limited rate capability of the negative electrode.[197] To date, energy densities exceeding 100 Wh/kg at low power densities of 0.06 kW/kg and energy densities of up to 50 Wh/kg at 10 kW/kg have been reported.[198] This is a ten-fold improvement in energy density compared to organic EDLCs.[192,198]

2.4.2. Supercapacitor cell design – towards new device geometries

Independent of the type of electrochemical storage device, the overall electrochemical cell consists of two electrodes, which are separated by an electrically insulating but ion permeable separator soaked in liquid electrolyte.[145] The electrodes in supercapacitors or batteries are in general thin coatings of active material (e.g. activated carbon) on metallic current collectors.[199] Before coating, the surface of the current collector is etched and modified by a coating with conductive carbon in order to improve the adhesion of the active material.[159] The active material is mixed with a binder and a conductive additive (carbon nanotubes or carbon black) to form a slurry that can be coated with a controlled thickness, rolled, and dried to form a porous electrode (Figure 2-20). The thickness of the electrode in commercial devices ranges from 100 to 300 µm with a high porosity of 65 – 75% and densities of 0.7 to more than 0.9 g/cm^3.[154,159,199]. In particular for supercapacitors, the state-of-the-art electrode manufacturing is costly and the resulting SC cells and cell modules (several cells in series or parallel) are bulky.[160] Both factors hinder the replacement of oversized batteries by SCs in full electric and hybrid vehicles.[160] Self-supported active materials in the form of electrospun nanofibres prepared from lignin could

drastically reduce the processing steps and hence costs for electrode preparation compared to activated carbon powder produced from for example coconut shells.

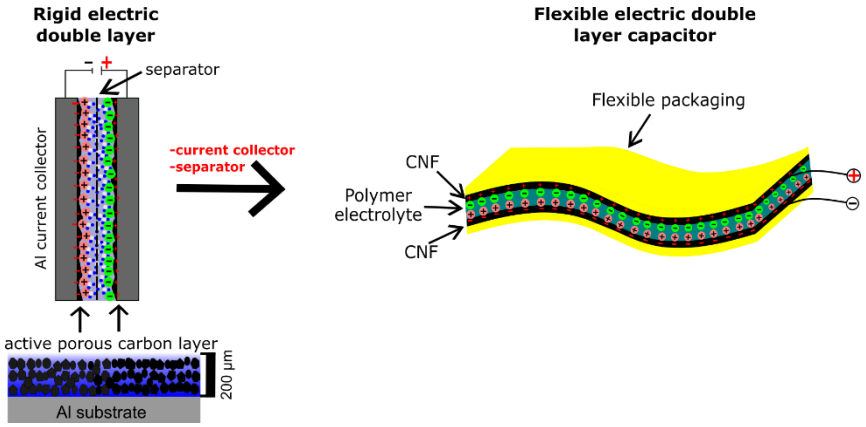

Figure 2-20 SC cells with film coated carbon powder-based electrodes (left) and with free-standing and flexible CNF electrodes as electrodes in conjunction with a polymer electrolyte (right).

Self-supported, which is termed ‘free-standing’ in this thesis, and flexible electrodes do not require metallic substrates (Figure 2-20). Thus, multiple process steps like current collector preparation, particle sizing and slurry coating could be omitted through the new electrode design. In conjunction with a polymer electrolyte, the free-standing CNF mats may also be suitable electrodes for the next generation energy storage devices that will be flexible and wearable.[200]

3. Lignin-based carbon nanofibres from softwood and hardwood Kraft lignin

3.1. Introduction

In this chapter, the preparation and characterization of the two types of Kraft lignins used for the manufacture of lignin-derived carbon nanofibres (LCNFs) throughout this research project are described. Additionally, the thermal conversion of the lignin precursor fibres to carbon nanofibres (CNFs) and their characterization are presented. Finally, the capacitive performance in aqueous alkaline supercapacitors was tested. Literature focusing on the relation between the structure and chemistry of a lignin precursor and the resulting materials' properties is scarce, to date. Since lignin is not a well-established ("off-the-shelf") chemical compound, but inherently a loosely defined precursor, it is crucial to characterize the lignin used as starting material to understand its structural and chemical features. A model workflow (Figure 3-1) was created, whereby the properties of the initial lignin precursor are linked with the properties of the resulting carbons by the thorough preparation and characterization of the lignin precursor. Therefore, this work is a contribution to finding relationships between certain structural and chemical features of Kraft lignins and the properties of the resulting product (here: LCNFs). The reactions taking place during the Kraft process yielding new structural arrangements (building units and linkages) and chemical compositions have been the focus of several research works in the past.[59,201–203] In particular, advanced spectroscopic and rigorous analytical methods give more and more insights into the wealthy structural arrangements of various Kraft lignins.[59,202,204] These insights have been proven useful on the route towards low molecular weight compounds via catalytic depolymerization of lignin.[22,23,205] It was found that the higher the number of C-C linkages in the lignin structure the less successful the depolymerization; whereas the presence of a large number of more labile arylglycerol-β-O-4 aryl ether linkages (β-O-4 ether bonds) has been shown to facilitate the deconstruction of lignin enormously.[201,205,206]

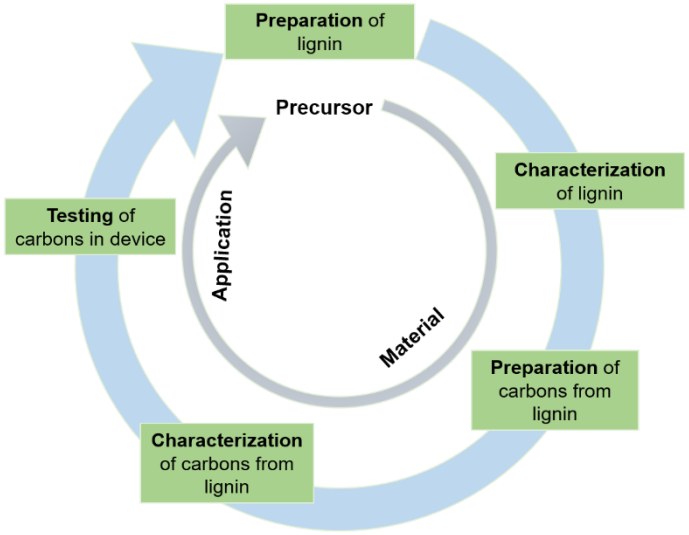

Figure 3-1 Workflow for the use of lignin as a precursor for carbon materials.

The different linkages and structural arrangements were also investigated in the use of lignin as a macromolecular precursor for the production of carbon fibres.[90,207,208] Braun et al. investigated the structural and chemical changes of meltspun fibres during oxidative thermostabilization of hardwood Kraft lignin.[92] Reactions occurring during thermostabilization in air increase the molar mass and the degree of crosslinking and hence the glass transition temperature (T_g).[92] It was found that the homolytic cleavage of the α-O-4 and β-O-4 ether bonds takes place first during oxidative thermostabilization.[92,209] This can be explained by the lower bond dissociation energies (BDEs) of the ether bonds (α-O-4: ~55 kcal/mol, and β-O-4: ~65 kcal/mol) compared to the various C-C bonds (~72 – 110 kcal/mol).[209–213] The bond homolysis yields radical intermediates such as phenethyl and phenoxy radicals which undergo a series of rearrangement, elimination and oxidation reactions.[92,212] The scission of methoxy groups was shown to occur only at high temperatures (>280 °C) during oxidative thermostabilization.[92] Furthermore, the influence of different thermostabilization conditions on the properties of the final carbon fibres was investigated by several authors.[129,207,214] The authors focused on optimizing the process of oxidative thermostabilization of lignin fibres which is regarded to be one of the bottlenecks towards commercialization of lignin-based carbon fibres. It was found that for meltspun lignin fibres slow heating rates in the range of 0.01 to 0.5 °C/min are needed in order to attain a thermoset

lignin and hence retain the fibre shape and properties.[90,91] Various soft- and hardwood LCNFs were tested in supercapacitors operating in different electrolytes and cell configurations.[119,134,215] To date, a clear inference concerning the reasons for superior performance of one lignin compared with another is out of reach.

Herein, a eucalyptus hardwood Kraft lignin (HKL) is compared with a pine/spruce softwood Kraft lignin (SKL) in the manufacture of porous electrospun CNFs. These are then used as free-standing electrodes in supercapacitors without further modifications. As mentioned in the literature review of this thesis, 'free-standing' electrodes are defined as self-supported carbon electrodes that do not require a polymeric binder, a conductive additive and additional metallic substrates. HKL is composed of a greater number of more labile β-O-4 ether linkages than SKL. It is shown that the preparation of functional CNFs with different porosities is governed by the abundance of linkages and functional groups of the lignin precursors in combination with the thermostabilization temperature. This translates into differently performing materials in aqueous alkaline supercapacitors.

3.2. Preparation and characterization of the two lignin precursors

Throughout the project two different Kraft lignins were used as precursors to produce LCNFs. Both the preparation (extraction and refining) of the Kraft lignins and the characterization were carried out by RISE AB (Research Institutes of Sweden). Both lignins were derived from industrial black liquors. The hardwood eucalyptus lignin was obtained from a black liquor provided by the ENCE (Energía y Celulosa) pulp mill (Huelva, Spain). The lignin was isolated by the LignoBoost process (described in the literature review) and dried at 80 °C under vacuum for about 24 h. Sequential solvent extraction was used to produce a suitable lignin fraction for electrospinning (Figure 3-2). The solvent extraction method is a modified version of the method described by Baker, Hosseinaei and Mörck, Yoshida and Kringstad.[114,216] At first, the dry lignin (1000 g) was extracted with deionized water by rapidly stirring in 10 L water at 60 °C for 2 h

(Figure 3-2). The suspension was cooled to room temperature and then filtered. The recovered air-dried solid was dried at 80 °C under vacuum for about 12 h. Subsequently, the lignin was extracted with dichloromethane by stirring in 10 L solvent at room temperature for 2 h. Afterwards, the sample was filtrated and the solid recovered on the filter and extracted using methanol (1:10 solid to liquid ratio, room temperature, 4 h). The extract solution was then filtered, and lignin from the filtrate was isolated using a rotary evaporator. The isolated lignin was dried in a vacuum oven at 80 °C for 12 h. The final yield for this fraction used as the precursor for electrospinning was 52.3%. A softwood (pine/spruce mixture) Kraft lignin was obtained from the LignoBoost demonstration plant (Bäckhammer, Sweden). The lignin was dried at 80 °C under vacuum for about 12 h. As shown in Figure 3-2, the dry lignin (1000 g) was first extracted with methanol, by rapidly stirring in 10 L methanol at room temperature for 2 h. The sample was filtrated and the solid recovered on the filter was then extracted using a 70/30 v/v mixture of methanol and dichloromethane (1:10 solid to liquid ratio, room temperature, 4 h). The extract solution was then filtered and the lignin from the filtrate was isolated using a rotary evaporator.

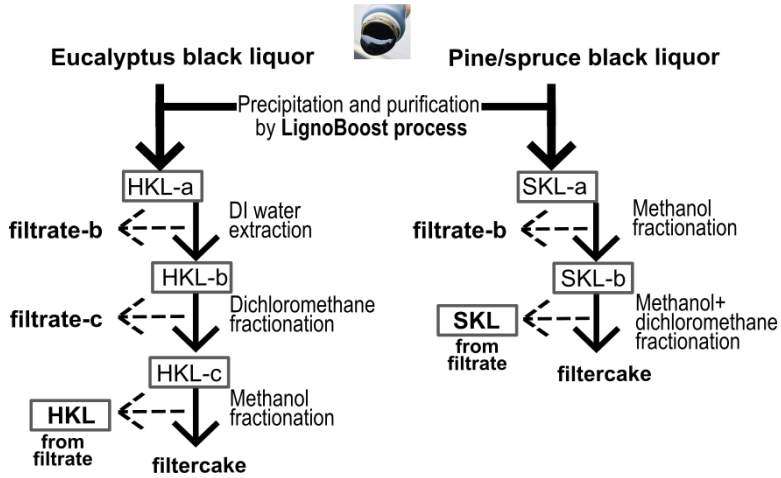

Figure 3-2 Flow chart revealing the differences in the fractionation procedure of the two lignins, HKL and SKL.

The isolated lignin was dried in a vacuum oven at 80 °C for 12 h. The final yield for this fraction was 42.5%. The two lignin fractions (HKL and SKL) used for electrospinning were thoroughly characterized in order to reveal structural and chemical differences. The purities of HKL and

SKL were determined by several standard protocols for lignins. The ash content was determined by combustion of the lignin sample at 575 °C. The compositional analysis was performed by a two-step acid hydrolysis and measurement of lignin and carbohydrate content. The lignin content was measured as acid soluble and acid insoluble lignin by gravimetric method and UV spectroscopy. The carbohydrate content was measured using high-performance liquid chromatography (HPLC).[217–220]

Additionally, elemental analysis with an elemental analyzer and trace metal analysis were performed by inductively coupled plasma optical emission spectroscopy (ICP-OES).[221] The oxygen content was calculated as 100% minus the sum of C, H, N, S and ash content. The amounts of inorganic and organic impurities of HKL and SKL are very low indicated by the low ash (HKL: 0.27 wt% and SKL: 0.09 wt%) and carbohydrate (HKL: 0.40 wt% and SKL: 0.31 wt%) content. The sulfur content of HKL and SKL are 2.1 wt% and 1.3 wt%, respectively. Sulfur is a common impurity in Kraft lignins arising from the $Na_2S_{(aq)}$ used as a delignifying agent in the Kraft process. The results of the elemental analysis can be seen in Table 3-1.

Table 3-1 The chemical compositions of HKL and SKL determined by elemental analysis with the standard deviations given in brackets.

Component	HKL /%	SKL /%
C	62.20(8)	65.7(2)
H	5.56(1)	5.89(4)
N	0.17(1)	0.18(3)
O*	29.70	26.76
S	2.10(2)	1.32(2)

** The oxygen content was calculated as 100% minus the sum of C, H, N, S, and ash.*

The results of the trace metal analysis by ICP-OES are shown in Figure 3-3. The main impurity besides sulfur are the alkali metals Na and K with concentration well below 1 wt% (10^4 ppm).

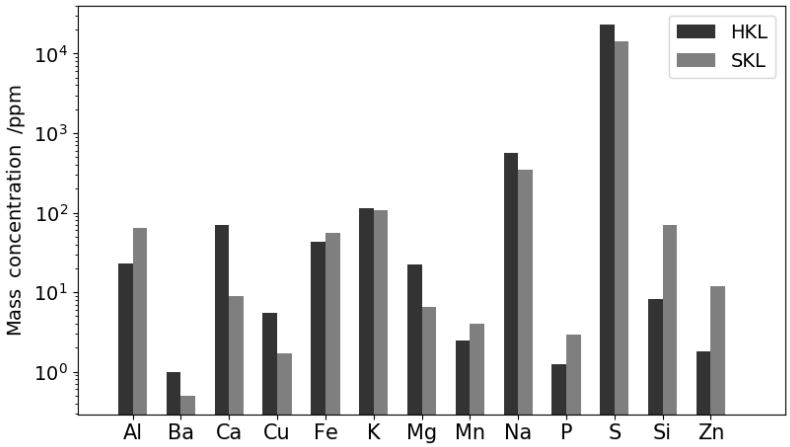

Figure 3-3 Trace metal content of HKL and SKL determined by ICP-OES.

The purity can be determined by subtracting the carbohydrate and ash content from the dry weight of lignin. For both lignins the purity is higher than 99% (HKL: 99.3% and SKL: 99.6%). This renders the two lignins comparable. Hence, certain properties of the carbons can be related to structural and chemical features of the lignin precursor. Nuclear magnetic resonance (NMR) spectroscopy is nowadays the most important and powerful tool to characterize structural features of lignins. Besides the common one-dimensional (1D) proton (^{1}H) or carbon (^{13}C) NMR measurements, two- (2D) and even three- (3D) dimensional NMR experiments are performed.[45,59,202,222,223] A very useful and widely applied 2D NMR technique is the heteronuclear single quantum correlation (HSQC) NMR which is based on correlating a carbon's chemical shift in one dimension with the proton chemical shift of its attached proton in a second dimension via pulse NMR sequencing (^{13}C-^{1}H 2D HSQC NMR).[45,224] Consequently, an improved signal dispersion compared to single 1D ^{1}H or ^{13}C NMR is achieved. The ^{13}C-^{1}H 2D HSQC NMR spectra of HKL and SKL are shown in Figure 3-4. In the aromatic region of HKL (Figure 3-4a), signals of syringyl (S) and guaiacyl (G) units are found as expected for hardwood lignins.[24,225] However, signals related to guaiacyl units, especially C_2–H_2 (G_2) and C_6–H_6 (G_6), are very weak which may indicate a low amount of guaiacyl units or condensation in guaiacyl units. Moreover, signals related to oxidized syringyl (S_{ox}) moieties can be identified which result from the Kraft delignification process.[203]

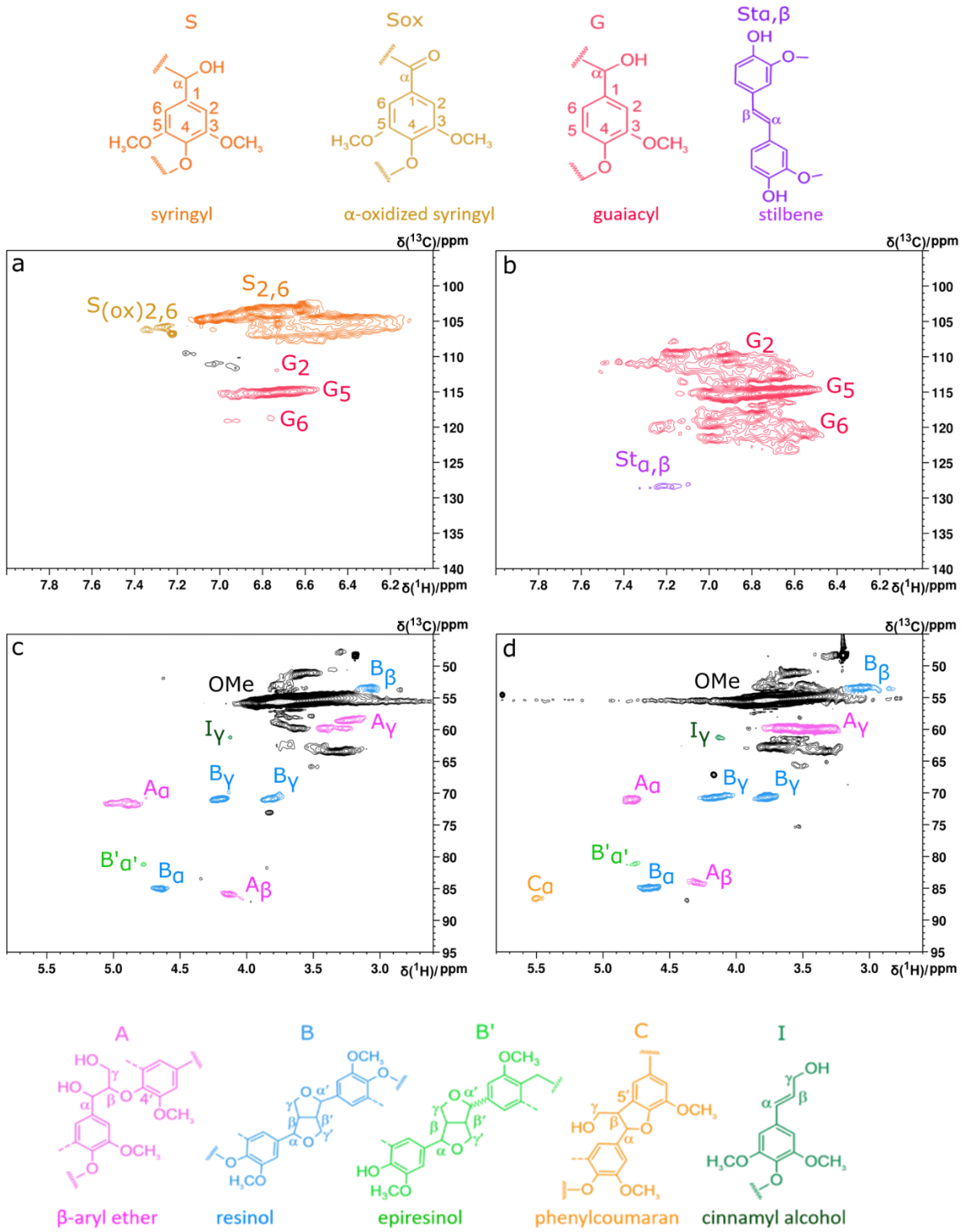

Figure 3-4 Aromatic (top) and side-chain (bottom) regions of the ^{13}C–^{1}H (HSQC) spectra of HKL (a and c) and SKL (b and d) together with the signal assignments.

SKL exhibits very pronounced signals of G (G_2, G_5, G_6) units in the aromatic region (Figure 3-4b) typical of softwood lignins.[24,225] Additionally, signals related to stilbenes were identified (C_α–H, C_β–H) in the spectra of SKL. These are generated from phenylcoumaran units (β-5 linkages),[59] which (C_α–H) were detected in the side-chain region of SKL (Figure 3-4d), but are absent in HKL (Figure 3-4c). Signals related to resinols, epiresinol units and cinnamyl alcohol were found in the side-chain regions of both HKL and SKL (Figure 3-4c,d).

For the development of nanoporosity during heat treatment, the side-chain region of lignins is of great importance. The main linkages determined by 2D HSQC NMR spectroscopy are presented as percentages based on the total number of linkages in Scheme 3-1. The most pronounced difference between the two Kraft lignin precursors is the percentage of β-O-4 ether bonds. In HKL, 63.3% of all linkages are β-O-4 ether bonds, whereas in SKL 35.0%. Conversely, the number of more stable C-C bonds in the resinol, epiresinol and phenylcoumaran structures are higher in SKL than in HKL (Scheme 3-1). The different percentages of β-O-4 ether to C-C bonds can be interpreted as an indicator for the stability of the side chain which is substantially lower in HKL (more β-O-4 ether bonds) than in SKL (more C-C bonds). Next to the abundance of different linkages in the lignin side chain, a second important factor is the type and abundance of hydroxyl groups present in the lignin polymers. The hydroxyl groups are important in the formation of inter-/ and intramolecular hydrogen bonding in lignin.[125]

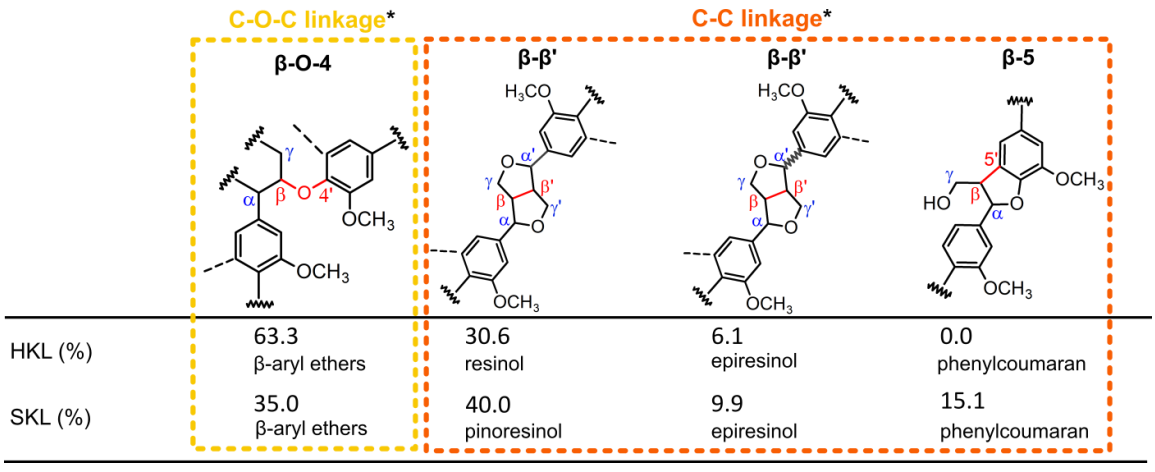

Scheme 3-1 Comparative quantification of linkages based on volume integrals of the 2D HSQC NMR signals (*linkages are categorized based on the strongest bonds directly connecting two aromatic units).

Aliphatic hydroxyl groups can form intermolecular hydrogen bonds and thus limit fusibility of lignin while phenolic hydroxyl groups provide higher thermal mobility to lignin.[125,226,227] These intermolecular interactions are of great importance in the oxidative thermostabilizing step as they control the rate of stabilization and crosslinking in the lignin. The distribution of OH groups was investigated by quantitative ^{31}P NMR spectroscopy.[228,229] 2-chloro-4,4,5,5-tetramethyl-1,3,2-dioxaphospholane (TMDP) is used to phosphitylate the hydroxyl groups in lignin according to the method introduced by Argyropoulos and co-workers.[228,230] The ^{31}P NMR spectra with signal assignments and the corresponding hydroxyl-group distribution of HKL and SKL are presented in Figure 3-5 and Scheme 3-2, respectively. From the ^{31}P NMR spectra of HKL and SKL, the total amount and the distribution of hydroxyl groups in the lignins can be determined by integration of the peak areas. The total number of hydroxyl functional groups in SKL is with 5.35 mmol/g only slightly lower compared to HKL (5.41 mmol/g). However, the distribution of the hydroxyl groups is different. From the OH-group distributions shown in Scheme 3-2, it is obvious that HKL is composed of a mixture of phenolic guaiacyl (G) and syringyl (S) moieties and a minor amount of p-hydroxyphenyl (H) units. The SKL precursor contains exclusively G and a minor amount of H moieties, which is consistent with the results from 2D HSQC NMR spectroscopy.

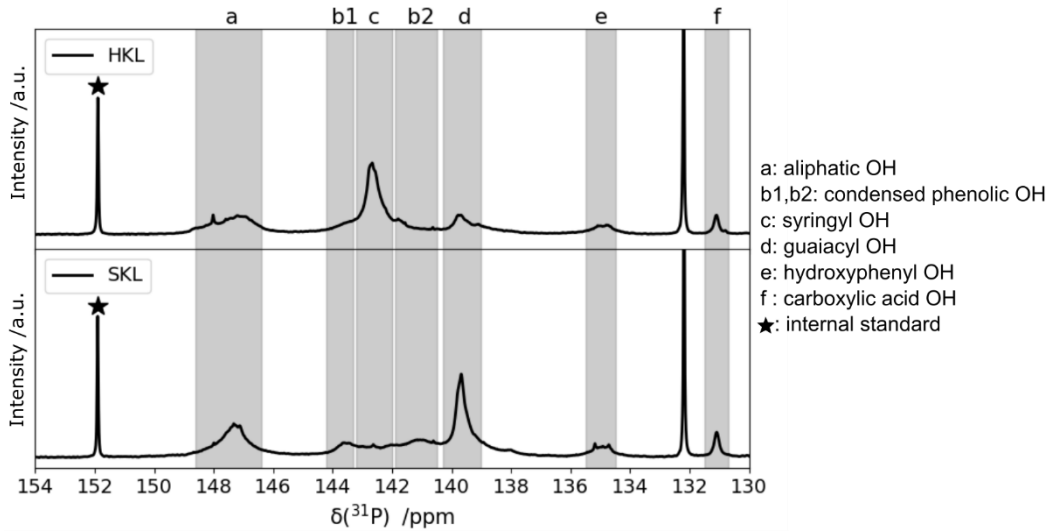

Figure 3-5 ^{31}P NMR spectra of HKL (top) and SKL (bottom) with signal assignments. The star indicates the signal of the internal standard (N-hydroxy-5-norbornene-2,3-dicarboxylic acid imide).

Another very important difference is the abundance of condensed phenolic moieties in lignin polymers. SKL contains considerably more of these phenolic units which is in line with the higher degree of condensation, which means a larger number of C-C linkages, in SKL shown by 2D HSQC NMR spectroscopy (Scheme 3-1). Furthermore, there are more aliphatic OH groups in SKL compared to HKL which means SKL can potentially be stabilized at higher heating rates and at lower temperatures than HKL.[231]

	Carboxylic	Hydroxyphenyl	Guaiacyl	Syringyl	Condens. phenolic	Aliphatic
		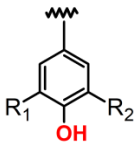	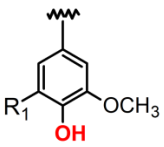	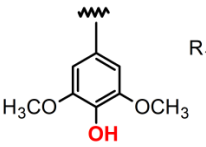	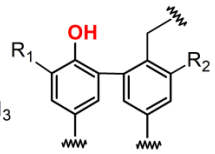	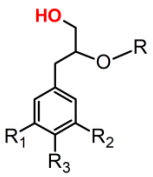
HKL (%)	7.2	2.6	15.6	37.7	13.7	23.2
SKL (%)	5.4	3.0	32.5	0.0	26.0	33.2

Scheme 3-2 Distribution of hydroxyl functional groups in the HKL and SKL precursors determined by ^{31}P NMR spectroscopy.

The elevated content of carboxylic acid groups in HKL contributes to a lower thermal stability.[232] In addition to the differences in structural features and functional groups, the molar mass of the two lignins, which was determined by gel permeation chromatography (GPC), is also an important property. HKL has a weight average molar mass of 1900 g/mol (M_w) and SKL a molar mass of 8600 g/mol (M_w). The dispersity (D = weight average molar mass/number average molar mass = M_w/M_n) is elevated for SKL (2.8) compared to HKL (1.5). Overall, D of both lignins is low due to the fractionation process applied which effectively eliminates lower molar mass fractions.[114,216,233] The glass transition temperature (T_g) of HKL is 154 °C which is lower than the one of SKL (184 °C). The difference in T_g arises from the differences in molar mass, structure, namely number/type of linkages between different building units, chemical composition (C-content) and functional groups (hydroxyl groups). Thus, it is a highly convoluted property which is very important in determining the applicability of different lignins for various

processing strategies. For instance, the lignins used here exhibit a high T_g (HKL: 154 °C, SKL: 184 °C) which renders them unsuitable for meltspinning, but highly suitable for electrospinning.

Lignin characterization is a formidable challenge as a vast number of properties need to be determined to fully characterize a lignin sample. In order to visualize the most important properties, a diagram termed 'Lignin Property Polygon (LPP)' was developed that visualizes certain properties for both lignin samples in a concise way (Figure 3-6a). This is especially useful in order to compare two lignins relative to each other or to examine batch-to-batch reproducibility of one type of lignin. In the LPP, each corner of a polygon is assigned to one property (e.g. molar mass) from which a line (the axis) is drawn to the center of the LPP which serves as origin of each axis. The number of properties considered can be variable depending on the field of application. The LPP with eight properties (octagon) of HKL and SKL is shown in Figure 3-6 together with a pyramid chart revealing the dependence of the T_g on the purity and chemical composition, the structural units/linkages and the functional groups.

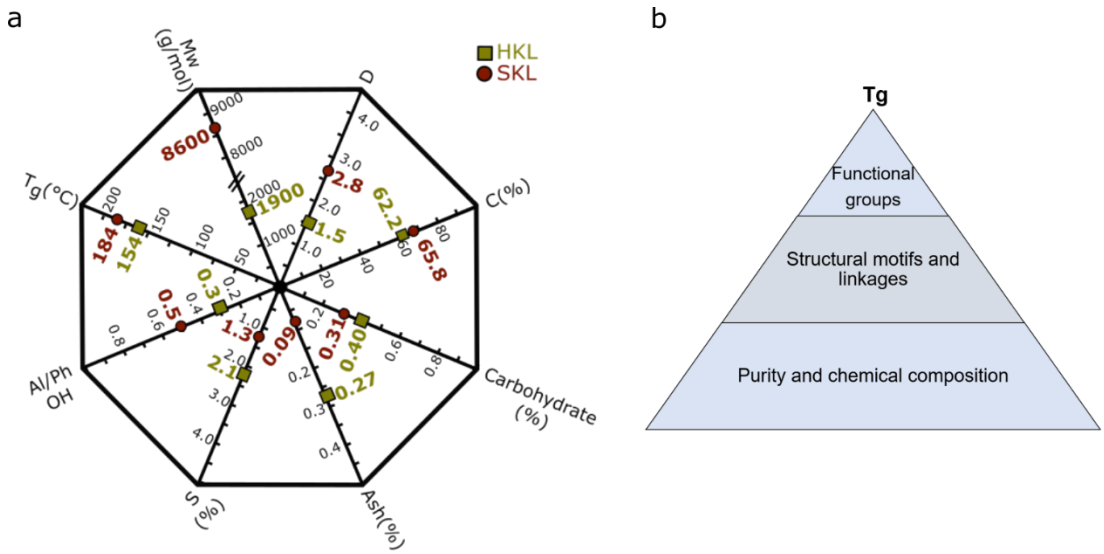

Figure 3-6 LPP showing eight important properties: carbon (C), carbohydrate, ash and sulfur (S) content, ratio of aliphatic to phenolic OH groups (Al/Ph OH), weight average molar mass (M_w), dispersity (D) and glass transition temperature (T_g) of HKL and SKL (a), pyramid chart revealing the dependence of the T_g on various sets of properties (b).

The thorough investigation of the two fractionated Kraft lignin precursors shows that both HKL and SKL are of high purity and have a narrow molar mass distribution. HKL is a S-rich precursor with a lower number of C-C bonds and a lower molar mass compared to SKL. HKL also has a considerably lower number of aliphatic OH groups and a lower carbon content than SKL. Consequently, the T_g of HKL (154 °C) is lower than the one of SKL (184 °C). These structural and chemical differences will have profound effects on the processability of the two lignins and the properties of the resulting carbon nanofibres. In the following section, the preparation and characterization of carbon nanofibre mats via electrospinning of polymer solutions of HKL and SKL are described.

3.3. Preparation and characterization of the lignin-based carbon nanofibres

The precursor solutions for electrospinning contained either 50 wt% eucalyptus hardwood Kraft lignin (HKL) dissolved in dimethyl formamide (DMF) (VWR) and methanol (v/v = 80/20) or 47 wt% pine/spruce softwood Kraft lignin (SKL) dissolved in DMF. These solutions were typically sonicated for 90 min, repeatedly shaken for a few minutes and finally stirred for several days in a sealed glass vial until homogeneous solutions were obtained. For one electrospinning run, a plastic syringe was loaded with the electrospinning solution and discharged at a rate of 0.5 ml/h with a single syringe infusion pump. Additionally, a high voltage (17 kV) between the syringe needle and a rotating collector was applied with a transformer (Glassmann high voltage inc., USA). The collector consisted of an aluminum foil wrapped around a plastic bottle that in turn was mounted on an overhead stirrer. This collector was placed 13 cm away from the needle's tip and the rotating speed was adjusted to 72 rpm. In order to control humidity at 30% (±5%), electrospinning was carried out in a room with an air conditioning system.

After electrospinning, the as-spun lignin nanofibre mats were converted to CNF mats by a two-step thermal treatment: 1) stabilization under an air flow (500 ml/min) and 2) carbonization under a nitrogen flow (500 ml/min) in a quartz tube (outer diameter: 80 mm) furnace. For the

stabilization series, the lignin nanofibre mats were stabilized at 190 °C, 250 °C, 310 °C and 340 °C for 15 min, where the ramp between room temperature (RT) and 50 °C was 5 °C/min and the one between 50 °C and the corresponding stabilization temperature was 0.5 °C/min. Subsequently, the stabilized nanofibre mats were carbonized at a fixed temperature of 800 °C for 120 min, where the ramp between RT and 110 °C was 5 °C/min and the one between 110 °C and target temperature was set to 3 °C/min.

3.4. Results and discussion

Stabilizing HKL and SKL at the same heating rate (0.5 °C/min), but different stabilization temperatures (190, 250, 310, 340 °C), gives the opportunity to investigate the influence of the starting precursor and stabilization temperature on the development of porosity and oxygen functional groups in the final LCNFs. To follow the structural and chemical changes upon oxidative stabilization, ^{13}C CP/MAS NMR (cross-polarized/magic angle spinning solid state NMR) spectroscopy, thermogravimetry (TG) equipped with a mass spectrometry (MS) system (TG-MS) and Fourier transform infrared (FTIR) spectroscopy were used. It was found that a stabilization temperature of 190 °C is insufficient to stabilize HKL under the chosen conditions (heating rate/ dwell time). It melted and formed a brittle film upon carbonization at 800 °C in N_2, whereas SKL was stable during carbonization and retained the fibre shape (Figure 3-10). From ^{13}C CP/MAS NMR spectroscopy, it is evident that hardly any structural changes occurred in HKL and SKL at such a low stabilization temperature. However, in SKL the aliphatic C-H region (0 – 40 ppm) changed slightly together with the formation of carboxylic acid groups (~180 ppm) indicating that even at 190 °C oxidation of the SKL side chain took place. TG-MS clearly shows that the extent of this reaction is small as the amount of gaseous products detected is low (Figure 3-7b). At a temperature of 250 °C, both lignins could be stabilized without fusing. For both HKL and SKL, C_2H_5/CHO (m/e=29), C_2H_3 (m/e=27), H_2O (m/e=18), OH (m/e=17) and CH_3 (m/e=15) were detected. Additionally, increasing amounts of CO_2 (m/e=44) were

measured for both lignins with an onset at 220 °C. The signal-to-noise ratios of all signals recorded by TG-MS are lower for SKL compared to HKL indicating that crosslinking reactions take place to a lesser extent in SKL. This is in line with the more rigid (C-C bond rich), hence less reactive, side chain of SKL and lower amount of methoxy groups.[209,234] The TG-MS signals of HKL are sharp with distinct maxima, whereas the ones of SKL are very broad covering a wider temperature range which may be explained by the much higher molar mass (Figure 3-6) imposing more diffusional constraints on the volatile products. Moreover, the side chain of SKL is composed of bonds with BDEs that cover a broad range.[232] In the ^{13}C CP/MAS NMR spectra of both lignins (Figure 3-7a,b) a decrease in intensity in the aliphatic C-H (0 – 40 ppm) and aliphatic C-C region (65 – 97 ppm) can be seen after stabilization at 250 °C. Furthermore, a shoulder emerging between 158 and 174 ppm indicates formation of ester/anhydride linkages. These are clear indicators that crosslinking took place.

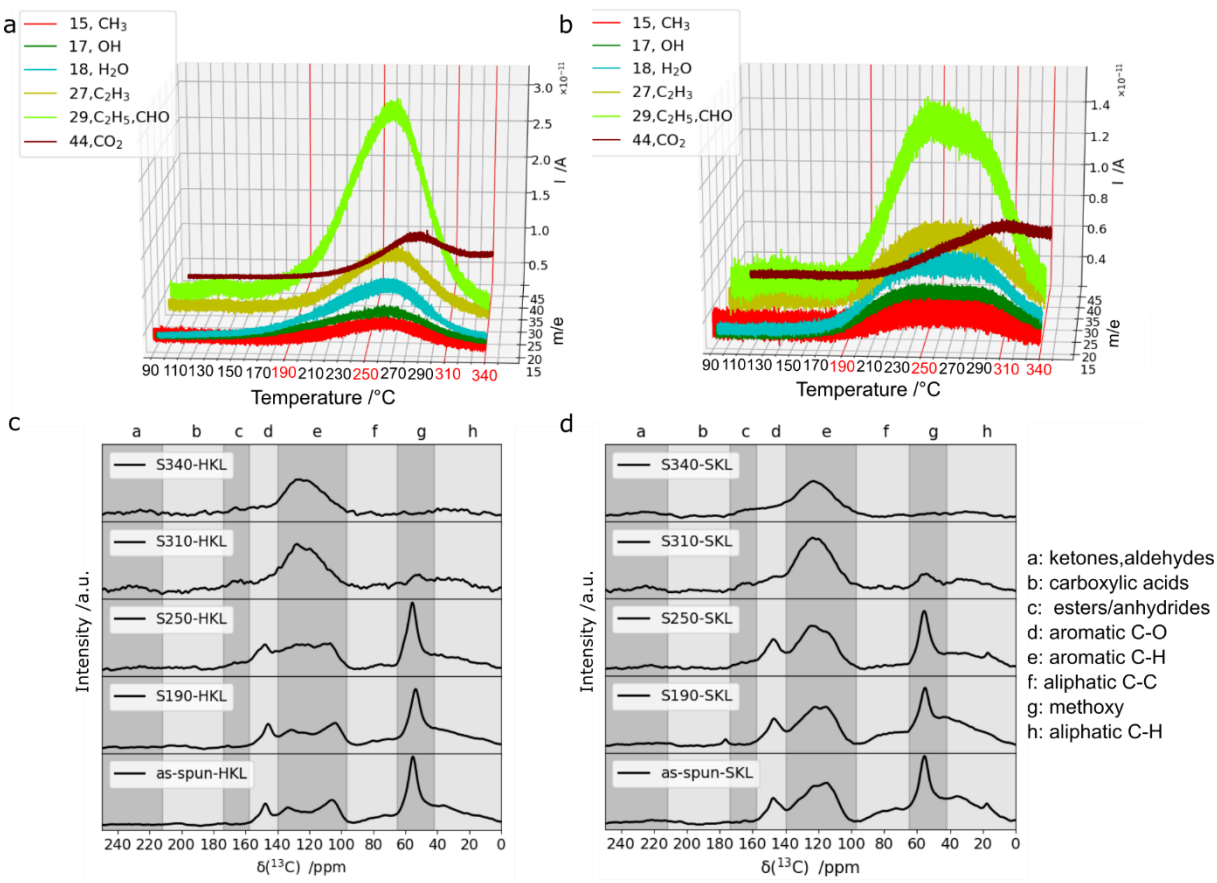

Figure 3-7 TG-MS signals recorded during stabilization of HKL (a) and SKL (b) and ^{13}C CP/MAS NMR spectra of as-spun fibres and after stabilization of HKL (c) and SKL (d) at different temperatures.

At 310 °C, the drastic decrease in intensity of the signal between 42 and 65 ppm indicates that the scission of methoxy groups took place.[92] Additionally, the signal between 140 and 158 ppm indicative of aromatic C-O bonds disappeared in both lignins and the signals for ester/anhydride linkages are more pronounced than at 250 °C. Hence, the degree of crosslinking in both lignins is enhanced. The TG-MS data shows that at 310 °C the amount of volatile products decreased more sharply for HKL than for SKL.

After stabilization at 340 °C, there are hardly any structural changes discernible in the ^{13}C CP/MAS NMR spectra. The signal between 40 and 65 ppm disappears completely which indicates that the scission of methoxy groups is complete. Additionally, the signal indicative of anhydride and ester linkages is weakened again pointing at an increase in C-C linkages and no additional crosslinking by anhydride and ester linkages at such high temperatures. This observation is in line with the low amounts of volatile products detected by TG-MS. Only the trend of signals for CO_2 are reversed. The signal shows a maximum at about 280 °C for HKL and at about 300 °C for SKL and stays at a constant level between 310 and 340 °C for both lignins. In this high temperature region, it can be expected that C-C bonds in the resinol (epiresinol and pinoresinol) and phenylcoumaran structures are affected. For instance, the β-5' bond in the phenylcoumaran units only present in SKL was shown to be among the strongest bonds in lignins with a BDE calculated to be 110 kcal/mol or more.[209] Breaking these more stable bonds under an air flow results in CO_2 as volatile product explaining the reverse trend of the CO_2 signal in TG-MS. Therefore, stabilization in this temperature region involves increasing degradation and decreasing crosslinking of lignin.

This is also confirmed by the corresponding weight loss traces of HKL and SKL plotted between 90 °C and 340 °C in Figure 3-8. The percentages in the graphs are based on the initial weight, which was 12 mg. It is obvious that the weight loss upon stabilization at temperatures exceeding 250 °C increases considerably. HKL shows a much higher weight loss than SKL. HKL loses 63.5% of the initial weight upon stabilization at 340 °C (residual weight: 36.5%).

The weight loss of SKL amounts to 44.9% at the same stabilization temperature (residual weight: 55.1%). The differences in weight loss between the two lignins are in line with the differences in the side-chain linkages and functional groups. Since SKL contains more stable C-C linkages, fewer methoxy groups together with a higher total carbon content, its T_g and hence its thermal stability is higher.

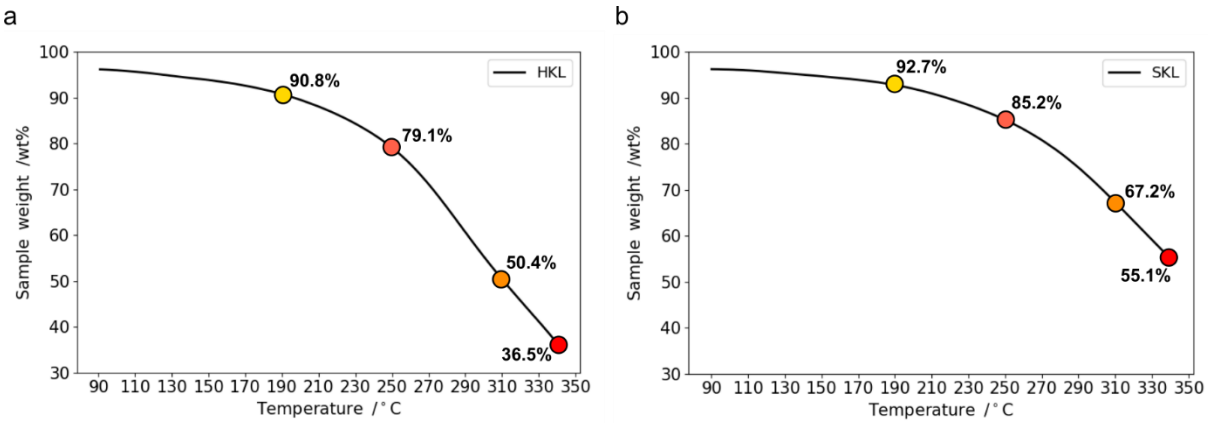

Figure 3-8 Weight loss traces of HKL (a) and SKL (b) upon stabilization in air.

Complementary to ^{13}C CP/MAS NMR spectroscopy, Fourier transform infrared (FTIR) spectroscopy was carried out for the as-spun and stabilized samples. The spectra of HKL and SKL are shown in Figure 3-9. The two weak bands between 3000 and 2800 cm^{-1} (zone a) assigned to aliphatic C-H bonds and to the C-H stretching of aromatic methoxy groups decrease with increasing stabilization temperature.[235] The band disappears completely at a stabilization temperature of 250 °C for HKL. However, SKL still shows very weak residual intensity of this band. At a stabilization temperature of 310 °C, the band also disappears in the spectrum of SKL. In the region between 1710 and 1880 cm^{-1} (zone b and c) corresponding to anhydride linkages (1880 – 1810 cm^{-1}), unconjugated carbonyl groups (1700 – 1750 cm^{-1}), aliphatic esters (1722 cm^{-1}) and aromatic esters (1770 cm^{-1}), an increase in intensities with increasing stabilization temperature can be observed for both lignins.[235,236] However, at a low stabilization temperature of 190 °C, the change in intensity of these bands are negligible, which indicates that no substantial crosslinking reactions took place.

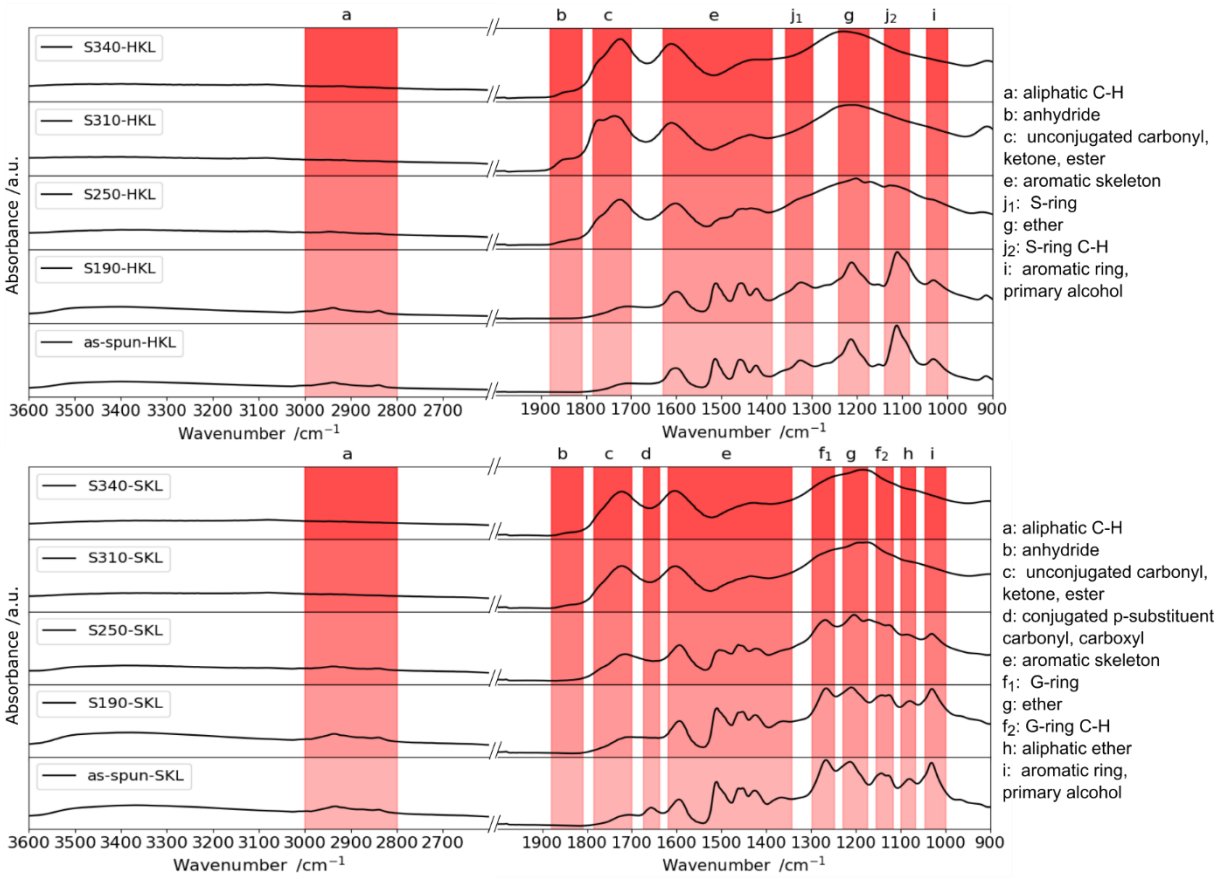

Figure 3-9 FTIR spectra of the as-spun and stabilized samples derived from HKL (top) and SKL (bottom).

This is consistent with the ^{13}C CP/MAS NMR and TG-MS data. However, a slight decrease in intensity in the region of conjugated carbonyl groups (1675 – 1639 cm^{-1}, zone d) and a concomitant increase in intensity of the unconjugated carbonyl, ketones, and ester bands (1700 – 1785 cm^{-1}, zone c) can be observed for SKL. Upon stabilization at 250 °C, a new, weak band appears at 1850 cm^{-1} in the spectrum of HKL which corresponds to the formation of anhydride linkages. This band is not yet observed for SKL at this temperature. However, the intensity of the band between 1700 – 1785 cm^{-1} (zone c) increases for both lignins indicating oxidation of the side chain. Upon stabilization at 310 °C, both lignins show an increase in intensity of the band characteristic of anhydride linkages (1850 cm^{-1}) and unconjugated carbonyl, ketones, and ester groups between 1700 and 1785 cm^{-1} (zone c). At a stabilization temperature of 340 °C, the intensity of the band assigned to anhydride linkages (1850 cm^{-1}) decreases slightly for HKL and remains unchanged in the spectrum of SKL. This is in line with the TG-MS data which

showed that CO_2 is the main product arising from HKL and SKL indicating the cleavage of more stable C-C bonds (degradation) rather than formation of new bonds (crosslinking). In addition, the weight loss during stabilization shown in Figure 3-8 reveals substantial weight losses at 340 °C which supports the conclusion of excessive stabilization (polymer degradation). The FTIR spectra of SKL, however, remain unchanged between 310 and 340 °C, which underpins its higher thermal stability and recalcitrance due to the higher number of C-C linkages, lower amount of methoxy groups and higher carbon content resulting in a higher T_g. The four aromatic skeleton vibrational modes between 1343 and 1619 cm^{-1} (zone e) gradually disappear in both lignins with increasing temperature, whereas the one at around 1600 cm^{-1} (aromatic ring stretch) gradually increases in intensity, indicating a higher degree of condensation (C-C bonds).[237] The lignin specific bands: G-ring (zone f_1, f_2) for SKL and S-ring (zone j_1, j_2) for HKL merge with increasing temperature which can be explained by the loss of the substituents (methoxy and hydroxyl groups).[237] Additionally, the band indicative of ether bonds in the region of 1230 – 1174 cm^{-1}, the band characteristic of aliphatic ethers (zone h) only observed in SKL and the band of primary alcohol of the aromatic units (zone i) all merge into one very broad absorption band upon rising stabilization temperature. This occurs at a temperature of 250 °C for HKL. In SKL, it is observed at 310 °C due to its lower reactivity.

After stabilization at different temperatures in air, all samples were carbonized at 800 °C for 120 min. Scanning electron microscopy (SEM) images of the resulting LCNFs can be seen in Figure 3-10. The overall micro-morphology is similar for HKL- and SKL-derived LCNFs. Both consist of a randomly entangled nanofibre network. The average fibre diameters for the samples stabilized at 190 °C and 250 °C are similar (HKL: 460±115 nm; SKL: 470±109 nm). As the temperature is increased the LCNFs derived from HKL show substantially smaller diameters compared to their low-temperature counterparts. The LCNFs based on HKL stabilized at 340 °C have an average diameter of 280±69 nm.

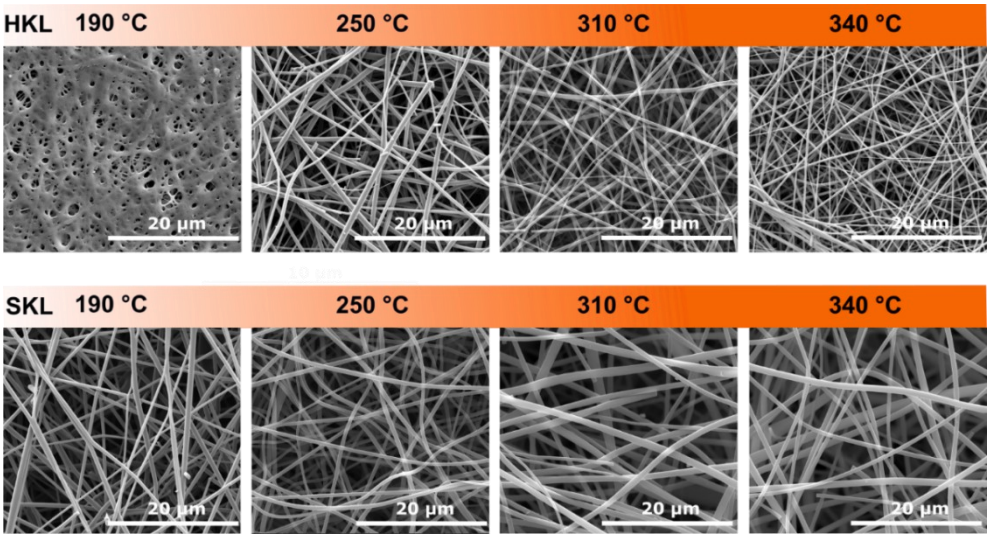

Figure 3-10 SEM micrographs of the carbonized HKL (top) and SKL (bottom) CNFs stabilized at different temperatures.

This effect is not observed for the LCNFs derived from SKL which show no significant change in fibre diameter over the entire temperature range. All average fibre diameters including standard deviations are shown in Table 3-2.

Table 3-2 Average diameters and densities of LCNFs derived from HKL and SKL.

	HKL		SKL	
Stabilization temperature /°C	Average fibre diameter /nm	Density (carbonized) /g/cm^3	Average fibre diameter /nm	Density* (carbonized) /g/cm^3
190	n.d.	n.d.	477 ± 109	0.19
250	460 ± 115	0.17	471 ± 106	0.15
310	371 ± 89	0.13	470 ± 106	0.11
340	280 ± 69	0.13	469 ± 105	0.11

**average value of 10 samples (weight of electrodes with circular shape with d = 1.0 cm).*

The Raman spectra of the LCNFs stabilized at various temperatures are shown in Figure 3-11. Both the D (1322.6 cm^{-1}) and G band (1595.8 cm^{-1}) characteristic of disordered carbons can be observed for all samples.[238] The 2D band (~2700 cm^{-1}) indicating graphene layers (2D ordering) are hardly discernible.[238] Moreover, the spectra of the LCNFs derived from HKL and SKL show hardly any changes in terms of position or intensity with increasing stabilization temperatures, which was reported in the literature previously.[239] Hence, the structure of the resulting

CNFs is disordered and does not change substantially with increasing stabilization temperature. This is also indicated by the I(D)/I(G) ratios given in Figure 3-11, where the intensities are determined by the peak heights of the D and G bands. The values range from 1.20 to 1.35 which is only a slight variation. Therefore, the overall disordered carbon structure does not change upon increase of the stabilization temperature.

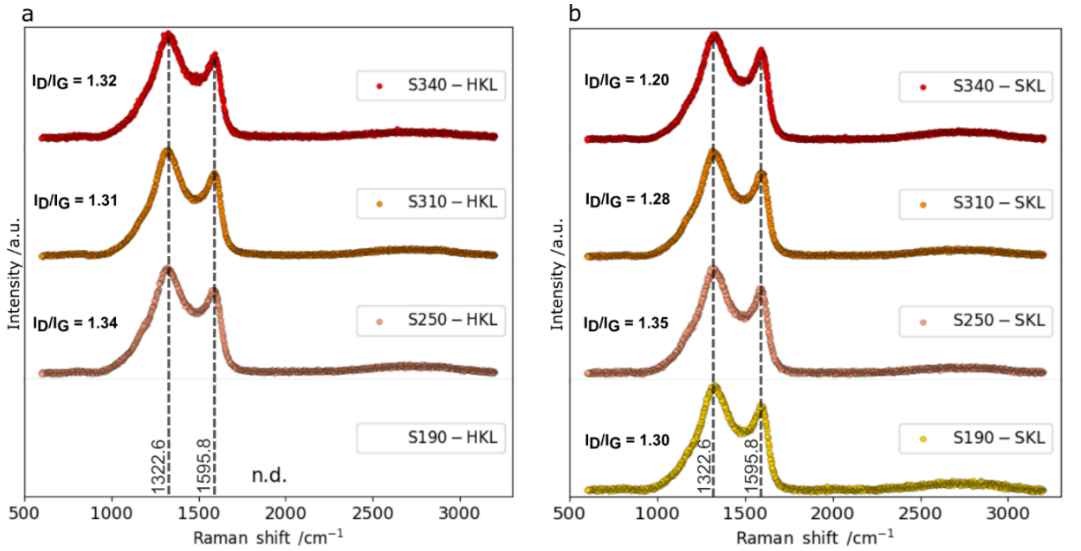

Figure 3-11 Raman spectra of the carbon nanofibres derived from HKL (a) and SKL (b) stabilized at different temperatures.

The micro-morphology and carbon structure are not expected to affect the electrochemical performance in electric double layer supercapacitors. The two main factors influencing the capacitive performance of the LCNFs are the accessible surface area and the surface functional groups.[184,240]

The development of the nano- (<2 nm) and mesoporosity (2 – 50 nm) with increasing stabilization temperature is shown in Figure 3-12. Complementary, Figure 3-13 shows the N_2 and CO_2 gas sorption isotherms of both HKL- and SKL-based LCNFs from which the pore size distributions and the specific surface areas were derived. The overall specific surface area values (m^2/g) and the corresponding pore size distributions upon increasing the stabilization temperature are considerably different for both lignins. For HKL, the specific surface area derived from nitrogen sorption increases linearly with rising stabilization temperature from 250 °C to

340 °C (Figure 3-12b). From the pore size distributions shown in Figure 3-12a, it becomes clear that the increase is accompanied by pore widening which leads to a rise in the specific surface area.

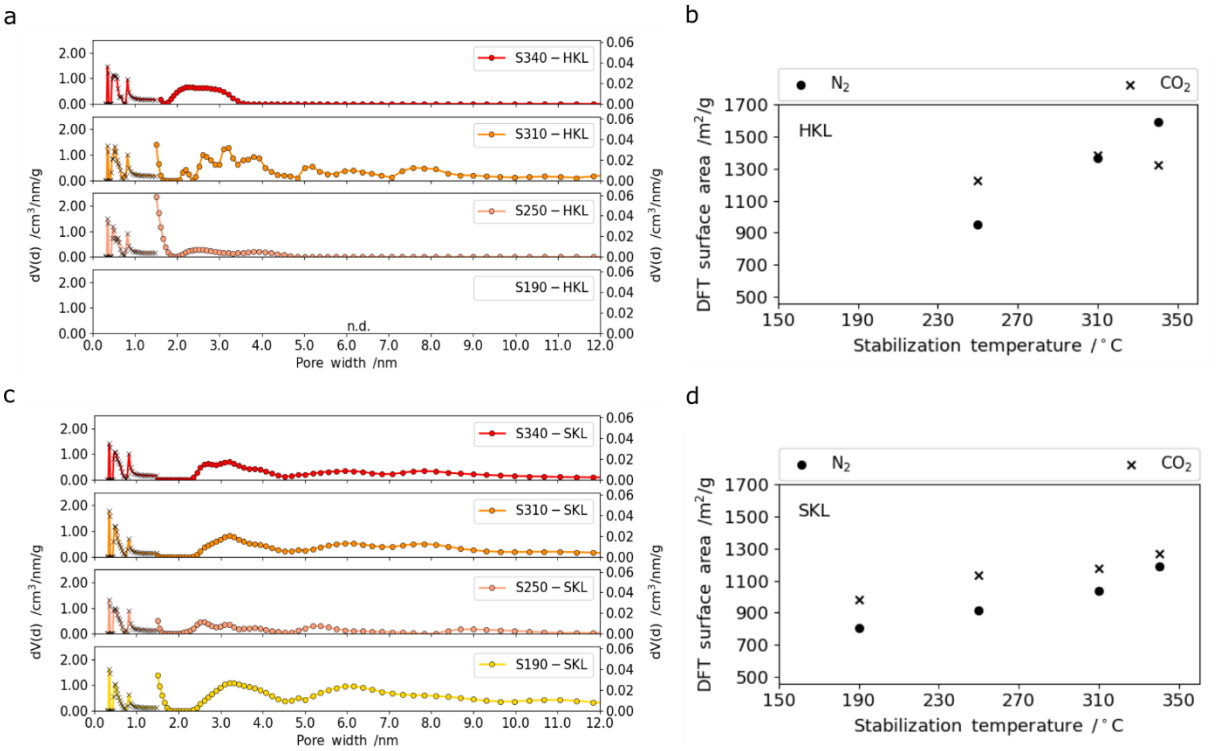

Figure 3-12 Pore size distributions of HKL- (a) and SKL- (c) derived LCNFs with increasing stabilization temperatures from bottom (190 °C) to top (340 °C) (traces with cross-shaped (x) symbols are derived from CO_2 sorption and circle-shaped symbols from N_2 sorption measurements), development of the DFT surface areas with increasing stabilization temperatures for HKL (b) and SKL (d).

When stabilized at 250 °C (major crosslinking event), the majority of pores is within a very narrow range of around 1.5 nm in diameter as measured by N_2 sorption (Figure 3-12a). Upon increasing the stabilization temperature to 310 °C, which was shown to result in the scission of methoxy groups and further crosslinking reactions, a more open pore structure with bigger nano- and mesopores (1.5 – 5 nm) is created. At the same time, the porosity in the (sub-)nanometer range probed by CO_2 sorption measurements increases, too. The latter is assigned to the crosslinking reactions that give rise to a dense polymeric framework. Increasing the stabilization temperature further to 340 °C changes the pore size distribution derived from the N_2 sorption measurement so that mainly mesopores between 2 and 5 nm are present.

This correlates well with the ^{13}C CP/MAS NMR and TG-MS data which showed that no cross-linking reactions took place at 340 °C, but the cleavage of rigid C-C bonds releasing CO_2. This can be considered as pre-activation step that leads to increasing pore diameters of the pre-existing (sub-)nanopores, which is also confirmed by CO_2 sorption measurements. The specific surface areas derived from these measurements show that stabilization at lower temperatures involving crosslinking reactions contribute to an increase in number of pores with diameters below 1 nm. However, the fibres stabilized at 340 °C (no crosslinking) show no increase in the (sub-)nanopore surface area. This will have implications on the capacitive performance in symmetric supercapacitors operating with $KOH_{(aq)}$ as electrolyte. Turning to SKL subjected to the same stabilization conditions a different trend can be observed. The difference in crosslinking degree upon oxidation arising from the more rigid (C-C -rich) structure and higher molar mass of SKL affects the development of porosity. Overall, the specific surface areas determined for SKL are lower than the ones for HKL. This is a direct consequence of the difference in linkages in the side chain and number of functional groups (e.g. methoxy groups). For SKL, both specific surface areas determined from N_2 (nano- and mesopores) and CO_2 ((sub-)nanopores) sorption measurements increase nearly in a linear fashion with rising stabilization temperature.

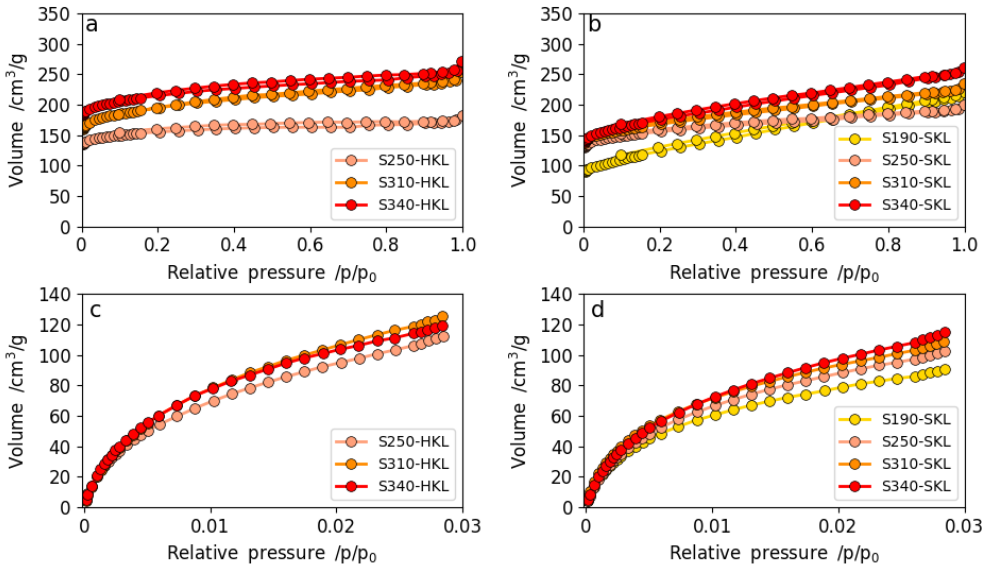

Figure 3-13 N_2 sorption isotherms of LCNFs derived from HKL (a) and SKL (b) and CO_2 adsorption isotherms of LCNFs derived from HKL (c) and SKL (d).

This indicates that the pore widening effect caused by polymer degradation is by far less present in SKL. The observation is in line with the TG-MS data which shows that between 310 °C and 340 °C minor crosslinking and degradation reactions take place giving rise to a slight increase in both (sub-)nanometer and mesopores. At a very low stabilization temperature of 190 °C, which did not lead to major structural changes in the polymer, both mesopores and nanopores are present. Stabilization at 250 °C results in a densification of the polymeric framework through major crosslinking reactions and hence leads to a narrower pore size distribution with a reduced number of mesopores in the resulting LCNFs. This is analogous to HKL which indicates that the denser polymer network created by the crosslinking reactions (most intense at 250 °C) for both lignins yield narrow pore size distributions in the final LCNFs. As SKL is stabilized at higher temperatures (310 and 340 °C), which involves scission of methoxy groups and cleavage of more stable C-C bonds together with further crosslinking reactions, the mesoporosity increases (pore size: 2-5 nm) together with an increase in (sub-)nanoporosity. Overall, the less reactive SKL with a more rigid C-C rich side chain shows a gradual increase in porosity with rising stabilization temperature, whereas the more reactive HKL composed of more ether bonds in the side chain and more methoxy groups shows tremendous changes upon stabilization in a narrow temperature range between 250 and 340 °C. As the two lignins are stabilized, two types of reactions can be distinguished, namely crosslinking and degradation. The former leads to an increase in (sub-)nanoporosity, the latter to an increase in mesoporosity and larger nanopores (>1 nm). Depending on the type of lignin these reactions take place to different extent and over different temperature ranges. The oxygen content on the LCNF surface dependent on the stabilization temperature of HKL and SKL was determined by temperature programmed desorption (TPD) and X-ray photoelectron spectroscopy (XPS). The total oxygen content of both types of lignins determined by TPD varies only slightly between 4 and 6 wt% over the entire temperature range (Figure 3-14).

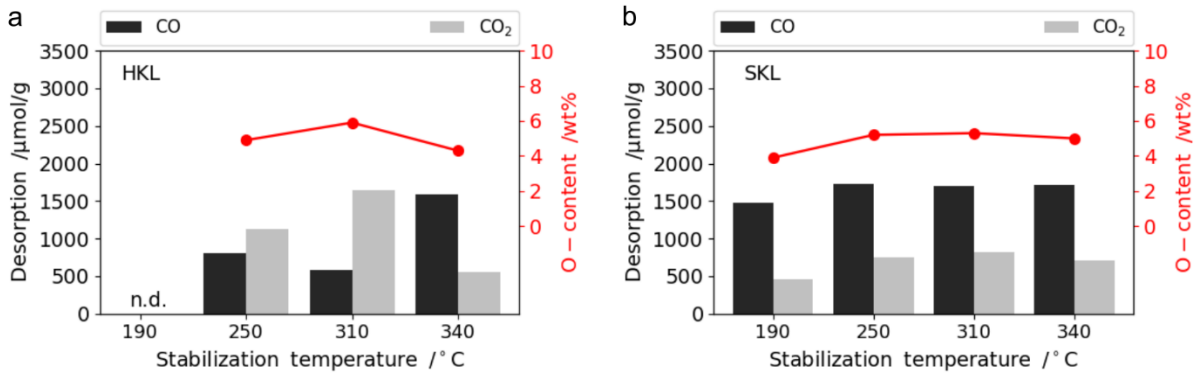

Figure 3-14 The bar chart indicates the total amount of desorbed CO and CO_2 from TPD measurements dependent on the stabilization temperature for HKL (a) and SKL (b). The red line graph shows the total oxygen content in wt% derived from the sum of CO and $2 \cdot CO_2$ desorbed from the samples.

Hence, the stabilization temperature does not have a major impact on the oxygen content of the carbonized fibres. The only notable variation is the type of oxygen functional groups in HKL. Stabilized at 310 °C, HKL contains more CO_2 desorbing, whereas at 340 °C more CO desorbing O-functional groups. This will have an impact on the cyclability as it was shown that CO_2 desorbing functional groups are less stable in aqueous alkaline electrolytes.[241] The total oxygen content determined by XPS is lower than by TPD as only the first nanometers of the sample's surface are probed, whereas TPD is a bulk technique accessing oxygen functional groups in deep pores.

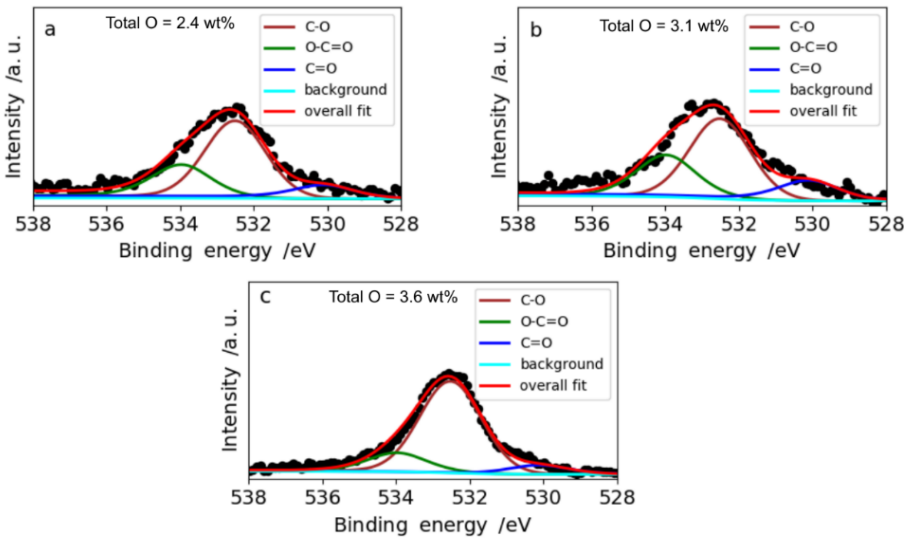

Figure 3-15 Deconvolutions of the O1s peaks from XPS of S250-HKL (a), S310-HKL (b), S340-HKL (c).

Nonetheless, the overall trend, that the total oxygen content does not substantially change with increasing stabilization temperature, is also confirmed by XPS. For the LCNFs derived from HKL stabilized at 250 °C and carbonized at 800 °C (S250-HKL), the total oxygen content amounts to 2.4 wt% and the main oxygen functional groups are of C-O-ether type (>60% of the total O content). S310-HKL shows an increase in C=O (21% of the total O content) and O-C=O (28% of the total O content) groups as also suggested by TPD, which showed an increase of CO_2 desorbing functional groups. As the stabilization temperature is increased further to 340 °C, the amount of C=O (8% of the total O content) and O-C=O (16% of the total O content) groups on the LCNF surface decrease again in line with the results of TPD. The LCNFs derived from SKL stabilized at various temperatures do not show the same change of the type of oxygen functionality with increasing temperature (Figure 3-16). The main oxygen functionality of all SKL-derived LCNFs is of C-O type (>60% of the total O content) which is consistent with TPD showing a majority of CO desorbing functional groups (Figure 3-14).

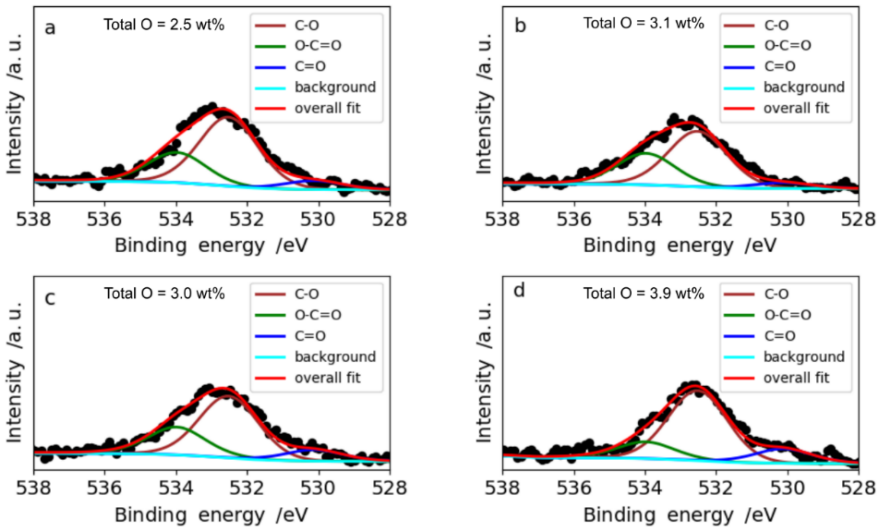

Figure 3-16 Deconvolutions of the O1s peaks from XPS of S190-SKL (a), S250-SKL (b), S310-SKL (c), S340-SKL (d).

As already mentioned above, the C-O oxygen functional groups are more stable than C=O and O-C=O groups and hence are more favorable for the long-term stability of electrodes. The LCNFs derived from HKL and SKL stabilized at different temperatures and carbonized at

800 °C for 120 min under nitrogen atmosphere were used as free-standing electrodes in supercapacitors. The measurements were carried out in symmetric two-electrode supercapacitor cells in 6 M $KOH_{(aq)}$ electrolyte. The cyclic voltammograms measured at 10 mV/s and 500 mV/s are shown in Figure 3-17 for HKL and in Figure 3-18 for SKL-derived LCNFs. S250-HKL shows the rectangular voltammograms characteristic of electric double layer supercapacitors at slow and high scan rate. Similarly, the cyclic voltammograms of S310-HKL and S340-HKL have a rectangular shape, but they also show signs of an irreversible process close to the maximum voltage of 1.2 V at low scan rate (10 mV/s) related to electrolyte decomposition. This process is not present at high scan rates, which implies it is rate dependent. However, for slow rates the cut-off voltage will need to be 1 V in practical supercapacitors. At 500 mV/s, it is also apparent that the rate capability of S310-HKL and S340-HKL is higher than for S250-HKL as the cyclic voltammogram of S250-HKL has curved edges at 500 mV/s, whereas S310-HKL and S340-HKL keep the rectangular shape. This can be related to the more open pore structure created by stabilization at higher temperatures involving both crosslinking and degradation reactions.

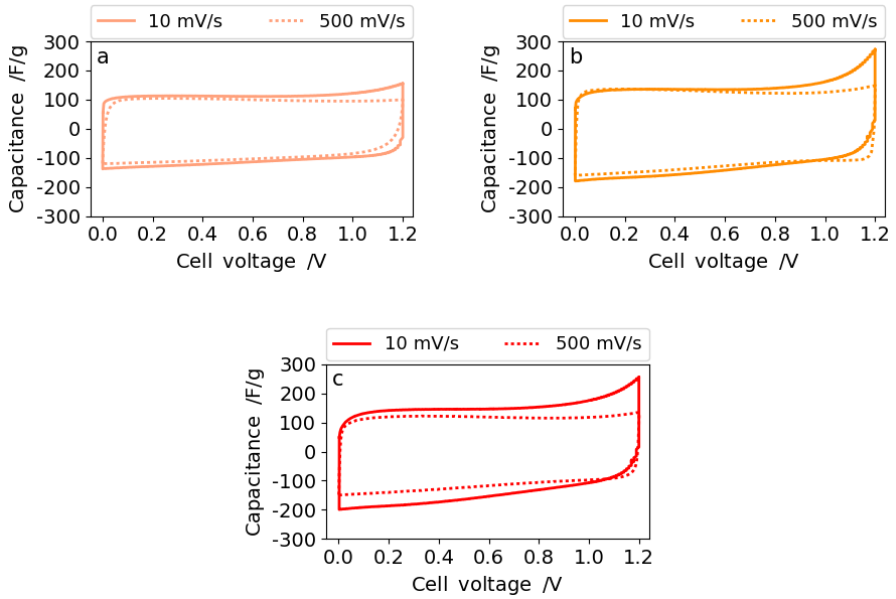

Figure 3-17 Cyclic voltammograms of S250-HKL (a), S310-HKL (b), S340-HKL (c) at 10 and 500 mV/s.

S190-SKL and S250-SKL show both lower rate capability (non-rectangular shape of voltammograms) and lower overall capacitance (area enclosed by the voltammograms) compared to HKL-derived LCNFs. S190-SKL shows a much lower capacitance than S250-SKL. However, it keeps the rectangular shape of the voltammogram at higher rates, whereas S250-SKL shows a dramatic drop of its capacitance measured at a low scan rate. This correlates well with the difference in pore size distributions of both samples. S190-SKL consists of both (sub-)nanoporosity and mesopores as no crosslinking reactions took place, S250-SKL underwent crosslinking reactions and hence has a much narrower pore size distribution. Porous materials with pore sizes in a narrow range are less accessible by the ions in the electrolyte and thus give rise to low rate capabilities as observed here. Upon stabilization at higher temperatures (310 and 340 °C), a more open pore structure was created by both crosslinking and degradation reactions analogously to HKL (Figure 3-13). This gives rise to a leap in both overall capacitance and rate capability of the SKL-derived LCNFs (Figure 3-18).

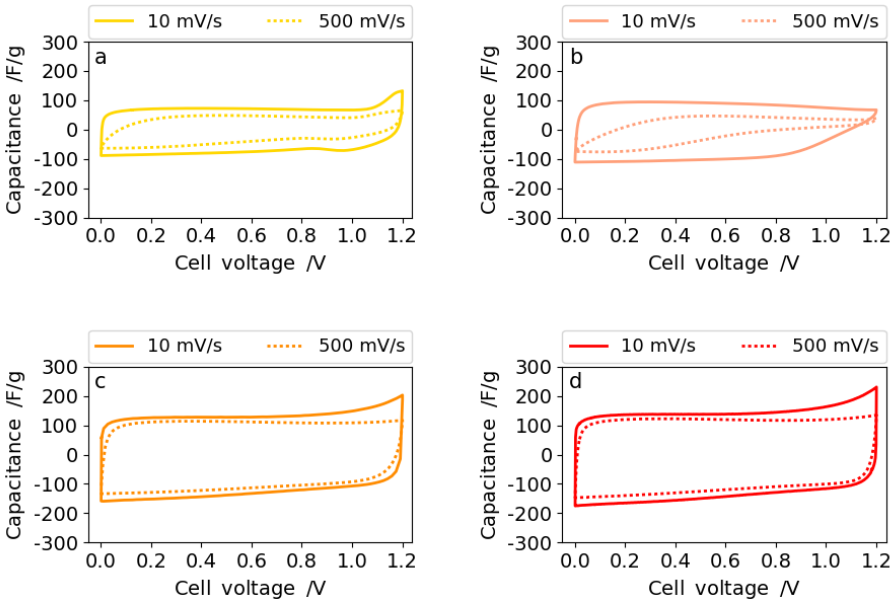

Figure 3-18 Cyclic voltammograms of S190-SKL (a), S250-SKL (b), S310-SKL (c), S340-SKL (d) at 10 and 500 mV/s.

The resulting trends of capacitance with increasing current densities derived from galvanostatic charge-discharge (GCD) measurements may be seen in Figure 3-19. Comparing the two lignins

it is obvious that HKL is more capacitive and shows a higher rate capability than SKL. This can be related to the higher specific surface area and enhanced accessibility of the nanoporosity (Figure 3-13). This, in turn, arises from the more labile side chain which creates accessible nanoporosity at low stabilization temperatures by crosslinking reactions. Additionally, at higher stabilization temperatures the scission of methoxy groups, which are more abundant in HKL, together with further crosslinking creates both (sub-)nano- and mesoporosity. However, at a stabilization temperature of 340 °C pore widening by cleavage of C-C bonds is detrimental to the capacitive performance in 6 M $KOH_{(aq)}$. Conversely, SKL shows increasing specific surface area in both the (sub)nanometer and mesopore range as the stabilization temperature is increased. This is assigned to the more rigid side chain that gives rise to crosslinking reactions even up to 340 °C leading to enhanced (sub-)nanoporosity rather than the pore widening effect. At low temperatures, S190-SKL and S250-SKL show very low capacitance and rate capability as revealed by cyclic voltammetry (Figure 3-18).

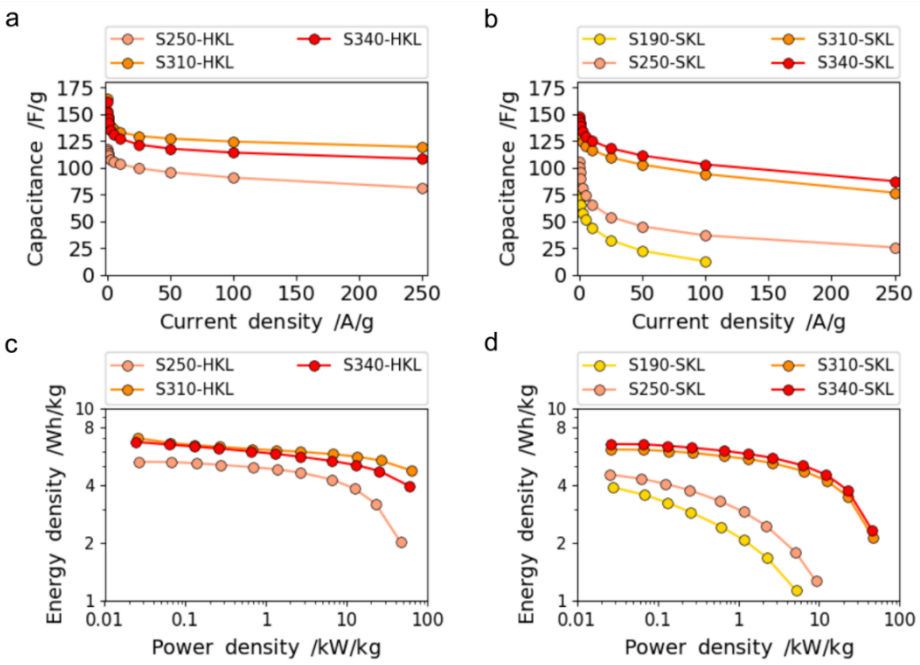

Figure 3-19 Specific gravimetric capacitance of HKL- (a) and SKL-derived LCNFs (b) as a function of current density and the corresponding Ragone plots for HKL- (c) and SKL-derived LCNFs (d).

A leap in capacitive performance can be observed by the scission of methoxy groups in conjunction with crosslinking reactions creating enhanced (sub-)nanoporosity at 310 °C. This is analogous to HKL. S340-SKL shows a small increase in capacitance consistent with the additional increased (sub-)nanoporosity rather than pore widening. In Figure 3-20a and b, galvanostatic charge-discharge (GCD) traces measured at 1 A/g are shown. All of them have a triangular shape characteristic for EDLCs. The capacitance retention after 6000 cycles at 10 A/g is shown in Figure 3-20c,d as relative value (in percent) and as absolute value (in F/g). All samples show good capacitance retention with over 90%. S250-HKL and S340-HKL show retentions of even more than 95% which makes the difference between S310-HKL and S340-HKL in terms of capacitive performance only marginal after 6000 cycles. This might be related to the difference in the type of oxygen functional groups determined by TPD and XPS. S190- and S250-SKL show capacitance retentions of even more than 100% after 6000 cycles which can be assigned to a wetting effect which arises from cycling the material repeatedly.

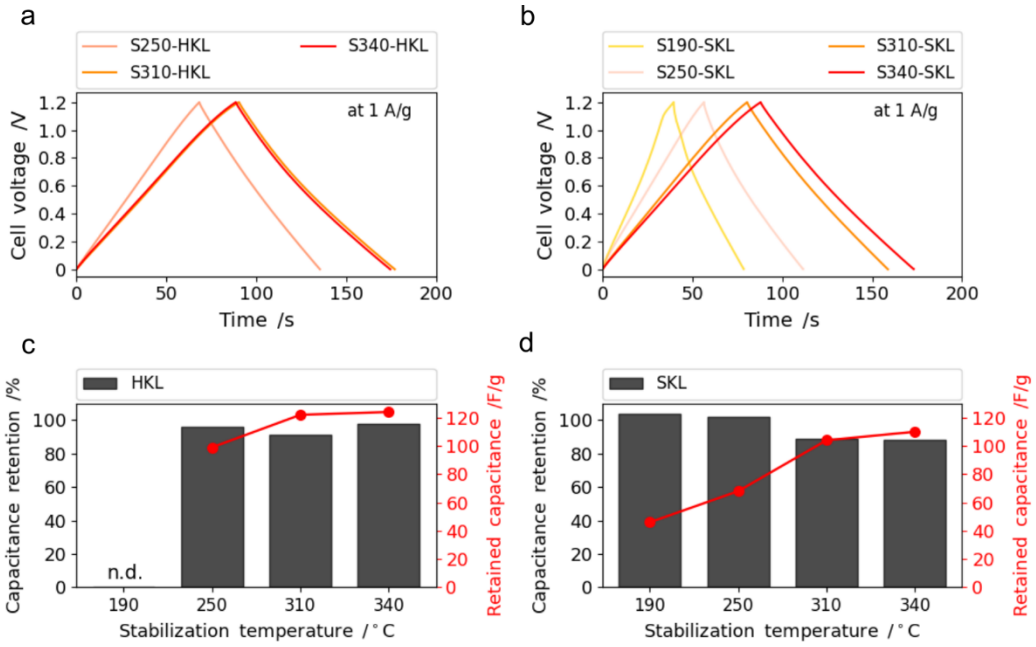

Figure 3-20 Galvanostatic charge-discharge traces of HKL (a) and SKL (b) at 1 A/g and the capacitance retention after 6000 cycles at 10 A/g as percentage in form of a bar chart and as absolute values (red curves) for HKL (c) and SKL (d).

This proves the low accessibility of existing (sub-)nanoporosity, which improves with the number of cycles. S310- and S340-SKL show capacitance retentions of more than 90% and hence the improved capacitive performance caused by the difference in stabilization temperature is retained even after 6000 cycles. Finally, impedance spectroscopy was carried out. The resulting Nyquist plots can be seen in Figure 3-21a,b. It is apparent that HKL-derived LCNFs show lower resistances than SKL-based LCNFs and oxidative thermostabilization at high temperatures (310 and 340 °C) decreases the resistance. Moreover, the diffusion part in the medium frequency range (after the semi-circle) decreases considerably for SKL and slightly for HKL with increasing stabilization temperature which supports the improved pore accessibility with increasing stabilization temperature mentioned before. The imaginary capacitance (C'') plotted as a function of frequency (Figure 3-21c,d) derived from impedance spectroscopy confirms this observation.

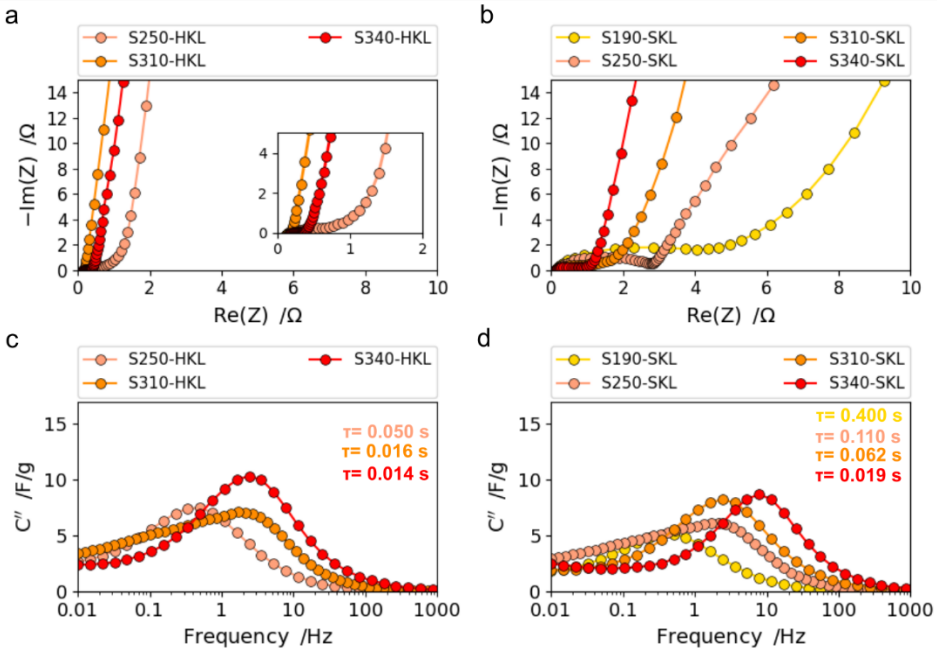

Figure 3-21 Nyquist plots of the LCNFs derived from HKL (a) and SKL (b) and the imaginary capacitance versus frequency plots for the LCNFs derived from HKL (c) and SKL (d).

Herein, the maximum imaginary capacitance is located at the relaxation frequency, f_R, determining the characteristic time constant according to $\tau = (2\pi f_R)^{-1}$.[242] In general, the higher the time constant the lower the rate capability.[242] The time constants determined for HKL-derived

LCNFs are lower than for SKL-based LCNFs (Figure 3-21c,d) and stabilization at high temperature (310 and 340 °C) decreases the time constants as more accessible (sub-)nanoporosity is created via both crosslinking and degradation reactions during stabilization (Figure 3-21c,d).

3.5. Conclusion

Two Kraft lignins were shown to develop different porosities when subjected to increasing stabilization temperatures before carbonization. The differences in side-chain linkages have a profound effect on the development of porosity during heat treatment and this in turn affects the performance of the resulting lignin-based CNFs used as free-standing supercapacitor electrodes. Upon stabilization, two types of reactions occur: 1) crosslinking and 2) degradation. Depending on the type and number of the structural motifs and functional groups, these reactions occur to a different extent and in different temperature windows yielding different porosities. HKL with more β-O-4 ether bonds, more methoxy groups and lower molar mass undergoes crosslinking reactions at 250 °C yielding a very narrow pore size distribution in the (sub-)nanometer range. At 310 °C, both crosslinking and degradation reactions occur, which yields both nano- and mesopores. At 340 °C, mainly degradation reactions (C-C cleavage) take place that lead to a widening of pre-existing nanopores which is detrimental to the capacitive performance. SKL, with fewer β-O-4 ether bonds, but more C-C bonds, fewer methoxy groups and higher molar mass undergoes both crosslinking and degradation reactions over the temperature range of 250 – 340 °C. Both types of reaction occur to a lesser extent in SKL. Therefore, SKL shows far less pore widening and develops less specific surface area than HKL. The sample with the most suitable porosity (both nano- and mesopores) and hence best capacitive performance as free-standing electrode in supercapacitors was prepared by stabilizing HKL at 310 °C and carbonization at 800 °C. It shows a specific gravimetric capacitance of 164 F/g at 0.1 A/g and 119 F/g at 250 A/g with a capacitance retention of more than 90% after 6000 cycles.

4. CO_2 activation of hardwood Kraft lignin-derived carbon nanofibres

4.1. Introduction

In this chapter, the CO_2 activation of electrospun hardwood Kraft lignin-derived (HKL) fibres is described. By stabilization in air, carbonization in N_2 and additional activation with CO_2, free-standing, porous lignin-based carbon nanofibres (LCNFs) were produced. Activated carbons are commonly produced either via chemical or physical activation processes.[243] Chemical activation involves the use of alkali metals in form of KOH and NaOH or acids, such as nitric (HNO_3), sulfuric (H_2SO_4) or phosphoric (H_3PO_4) acid.[104,180,243] Furthermore, carbonates, such as Na_2CO_3, K_2CO_3 or $KHCO_3$, are used to enhance the effect by creating a partially oxidizing atmosphere within the carbon matrix arising due to the thermal decomposition of carbonates which produces carbon dioxide gas.[244,245] Additionally, dehydrating agents, such as $ZnCl_2$, are frequently used.[20] The impregnation or physical mixing of the activating agents with the precursor material enables carbonization and activation in one step. However, chemical activation is a rather inefficient process as high activating agent to carbon ratios of two-to-one or three-to-one are often applied and the resulting activated carbons need to be cleaned after activation by extensive washing. Physical activation is a more resource-efficient process as it involves the reaction of an oxidizing gas, such as carbon dioxide or steam, with the already carbonized material at elevated temperatures to create porosity.[243] During the CO_2 activation step, the creation of porosity is based on the Boudouard reaction with the overall stoichiometry:[243,246,247]

$$C_{(s)} + CO_{2(g)} \rightleftharpoons CO_{(g)} + C[O]$$

Herein, C[O] is a surface oxygen complex formed by the reaction of solid carbon with gaseous CO_2 at elevated temperatures.[246] The Boudouard reaction is strongly endothermic and hence highly temperature dependent.[248] The equilibrium of the reaction is effectively shifted towards the right side (gasification of solid carbon) at temperatures exceeding 700 °C.[249]

CO_2 activation of carbon materials to produce activated carbons for various applications has been described in the literature.[250] In comparison with chemical activation (e.g. by KOH), which creates both nano- and mesoporosity, CO_2 activation was reported to be very efficient in widening pre-existing nanoporosity.[180] CO_2 activation was also utilized in several works to create porosity in lignin-derived chars.[251] It was found that rather long reaction times were needed to achieve a substantial increase in pore volume.[251] For instance, Rodríguez-Mirasol et al. activated eucalyptus Kraft lignin (powder) at 850 °C for 20 h.[252] The resulting carbons were highly porous 1853 m^2/g with a maximum micropore (< 2 nm) volume of 0.57 cm^3/g.[253] The same authors also investigated the reactivity of eucalyptus Kraft lignin and showed that with rising inorganic content (e.g. Na) the reactivity towards CO_2 and hence the development of porosity increases.[252] Saha et al. prepared mesoporous carbons from a pre-crosslinked hardwood lignin gel which was activated via physical and chemical routes.[254] Both physical and chemical activation enhanced the mesoporosity along with a significant increase in microporosity (< 2 nm).[254] Consequently, the gravimetric capacitance measured in a three-electrode set-up increased from 77.1 F/g for the non-activated carbon to 102.3 F/g for the CO_2-activated carbon.[254] In the following, the preparation of electrospun hardwood Kraft lignin-derived fibre mats is described. The as-spun, free-standing HKL fibre mats composed of randomly entangled fibres were converted to carbon nanofibre mats by a two-step procedure (stabilization and carbonization). Finally, one batch of LCNFs was CO_2-activated to enhance the nanoporosity and hence the capacitive performance in an electric double layer supercapacitor (SC).

4.2. Preparation of CO_2-activated LCNFs

The precursor solutions for electrospinning contained 50 wt% fractionated eucalyptus hardwood Kraft lignin (RISE AB, Stockholm) dissolved in DMF (VWR). For one electrospinning run, a plastic syringe (Plastipak luer-lock, 5 ml) was loaded with 2 ml of the solution. The syringe was discharged at a rate of 1 ml/h with a single syringe infusion pump (KDS-100-CE, KD

Scientific). A high voltage (17 – 18 kV) between the syringe needle (gauge = 22, Hamilton) and the rotating collector was applied with a transformer (Glassmann high voltage inc., USA). Electrospinning was carried out in a room with an air conditioning system to control humidity at 30% (±5%). After electrospinning, the as-spun lignin fibres were converted to carbon nanofibres by a two-step thermal treatment: 1) stabilization in air (300 ml/min) and 2) carbonization in N_2 (300 ml/min) in a quartz tube furnace (OTF-1200X, MTI). The as-spun lignin fibres were stabilized at 250 °C for 15 min, where the ramp between RT and 50 °C was 10 °C/min and the one between 50 and 250 °C was 0.5 °C/min. Subsequently, the stabilized fibres were carbonized at 900 °C for 30 min, where the ramp was 3 °C/min. Additionally, some of the LCNFs were further activated at 800 °C with CO_2 (200 ml/min) for 60 min. The heating rate was set to 5 °C/min.

4.3. Results and discussion

Despite the low molar mass of the lignin precursor (M_w = 1900 g/mol) compared with other polymer fibres (e.g. polyacrylonitrile, M_w = 150,000 g/mol), fibre formation during electrospinning was achieved without any additional synthetic high molar mass polymer (e.g. polyethylene oxide or polyvinyl alcohol) dissolved in solution as shown in the SEM micrographs in Figure 4-1.[255] The formation is attributed to strong intermolecular interactions via hydrogen bonding and π-π-interactions between the lignin macromolecules in solution. Hence, the molar mass is increased at high polymer concentrations in solution. The resulting fibre mats consist of randomly entangled fibres with cylindrical shape. The as-spun fibres have an average diameter of 769 nm (Table 4-1) which is quite large compared to other studies suggesting that intermolecular interactions must take place.[256,257] Additionally, the high polymer concentration in the solution (50 wt%) and the lack of additives (salts or co-polymers), which generally decrease fibre diameters, give rise to fibres with relatively large diameters.[256,258] After stabilization at 250 °C in air, the overall fibre morphology does not change (no fusing of fibres). Carbonization

of the stabilized fibres at 900 °C leads to a decrease of about 100 nm to 567 nm. The additional activation step does not lead to a further decrease in fibre diameter (Table 4-1).

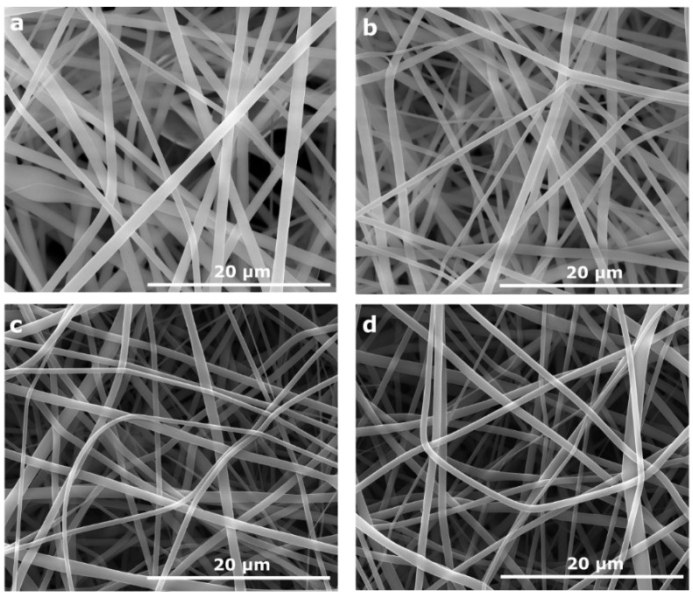

Figure 4-1 As-spun fibres produced from a pure Kraft lignin electrospinning solution (a), stabilized fibres (b), carbonized fibres (non-activated) (c), and activated for 60 min in CO_2 (d).

Instead, the porosity increases dramatically which is discernible in the single fibre morphology analyzed by transmission electron microscopy (TEM) (Figure 4-2).

Table 4-1 Average diameters of fibres and yields at all stages of the process chain.

Fibre type	Average fibre diameter /nm	Standard deviation /nm	Yield /%
As-spun	769	258	-
Stabilized	656	152	79
Carbonized	567	132	42 (overall: 33.1)
CO_2-activated	566	177	75 (overall: 25.0)

It is obvious that the non-activated fibre (Figure 4-2a) is dense, whereas the CO_2-activated fibre contains a large number of pores and hence appears less dense (Figure 4-2b). Additionally, selected area electron diffraction (SAED) was carried out. Considering the short (30 min) carbonization time, low carbonization temperature (900 °C) and the lack of structural order in the lignin precursor a low degree of graphitization is expected. This is confirmed by SAED shown

in Figure 4-2c. The rings in the diffraction pattern, however, indicate the presence of disordered few-layer graphene sheet stacks.[259] This may be explained by the high degree of aromaticity in lignin.[23] The additional one-hour treatment at 800 °C in CO_2 yields partially graphitized domains in the carbon structure (Figure 4-2d).

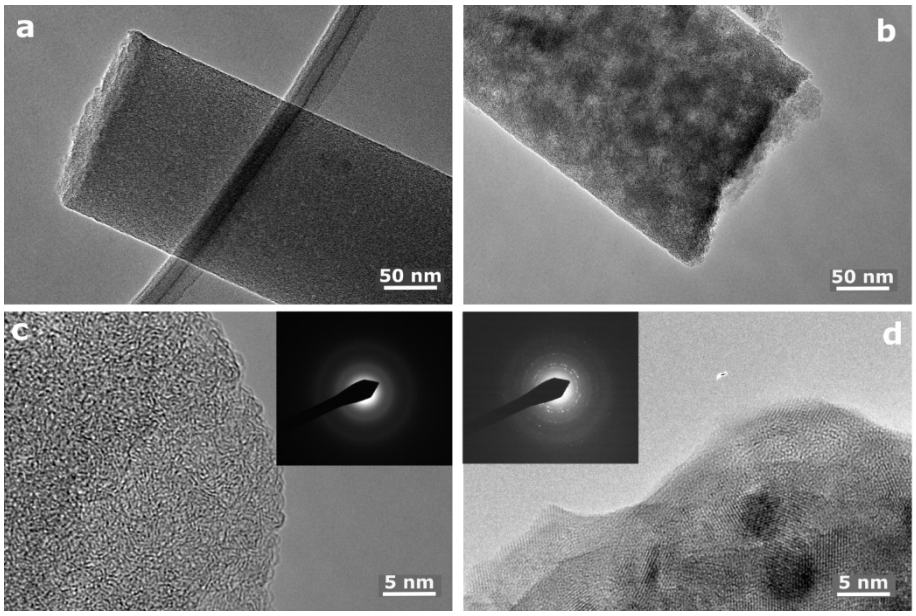

Figure 4-2 TEM image of a non-activated LCNF (a), a CO_2-activated LCNF (b); electron diffraction of selected area on a non-activated (c), a CO_2-activated fibre (d).

In addition to the diffraction rings, there are diffraction spots superimposed indicative of polycrystalline domains in the fibre. This might be assigned to a 'leaching' effect through CO_2 activation that exposes ordered domains which might be hidden in the dense matrix of the non-activated fibres. Another possible explanation for the formation of these ordered domains upon CO_2 activation may be the reduction of evolving CO gases by the carbon matrix which could lead to the deposition of ordered carbon on top of the parent disordered carbon.

The Raman spectra of the non-activated and CO_2-activated samples in Figure 4-3 show both D and G bands, indicating disordered carbon structures which was also concluded from the TEM micrographs. The spectra were fitted by using Breit-Wigner-Fano (BWF), Pseudo-Voigt and

Gauss components. Moreover, the crystallite sizes were calculated from the intensity ratios between the D ($I(D)$) and G ($I(G)$) bands, whereby $C(\lambda)$ = 8.3 nm for λ = 633 nm, as reported by Herdman.[260]

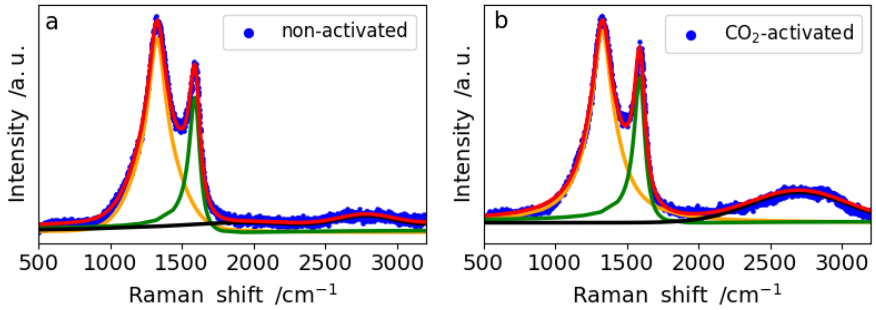

Figure 4-3 Normalized Raman spectra of the non-activated (a) and CO_2-activated (b) sample after baseline correction. Each spectrum was fitted using Breit-Wigner-Fano (orange), Pseudo-Voigt (green) and Gauss (black) components.

The intensities were determined by the peak heights, which is suitable for mainly amorphous/disordered carbons.[260,261] The crystallite size was then estimated by:

$$L_a = C(\lambda) \cdot \frac{I(G)}{I(D)}$$

The peak positions and the intensities (peak heights) were determined by fitting all spectra using the OriginPro 9.1 suite. The fitting results are given in Table 4-2. The ratios between the D band ($I(D)$) and G band ($I(G)$) only slightly deviate with the additional CO_2 activation step. However, the intensity of the 2D band, which is the D overtone, changes. This indicates that the number of graphene domains (multi or single layer) in the sample increased with the additional activation step, which is consistent with the TEM analysis.[238]

Table 4-2 Fitting parameters of the G, D and 2D band positions and estimated crystallite size L_a derived from the Raman spectra.

Sample	D band /cm^{-1}	G band /cm^{-1}	2D band /cm^{-1}	*I(D)/I(G)*	*L_a* /nm
Non-activated	1328.3(0)	1597.1(3)	2787.(4)	1.44	5.76
CO_2-activated	1328.8(3)	1590.4(3)	2701.(2)	1.34	6.19

The results of the CO_2 and N_2 gas sorption experiments are shown in Figure 4-4a and b. The results clearly indicate that the CO_2 activation yields enhanced porosity as the amount of adsorbed CO_2 and N_2 rises dramatically after activation.

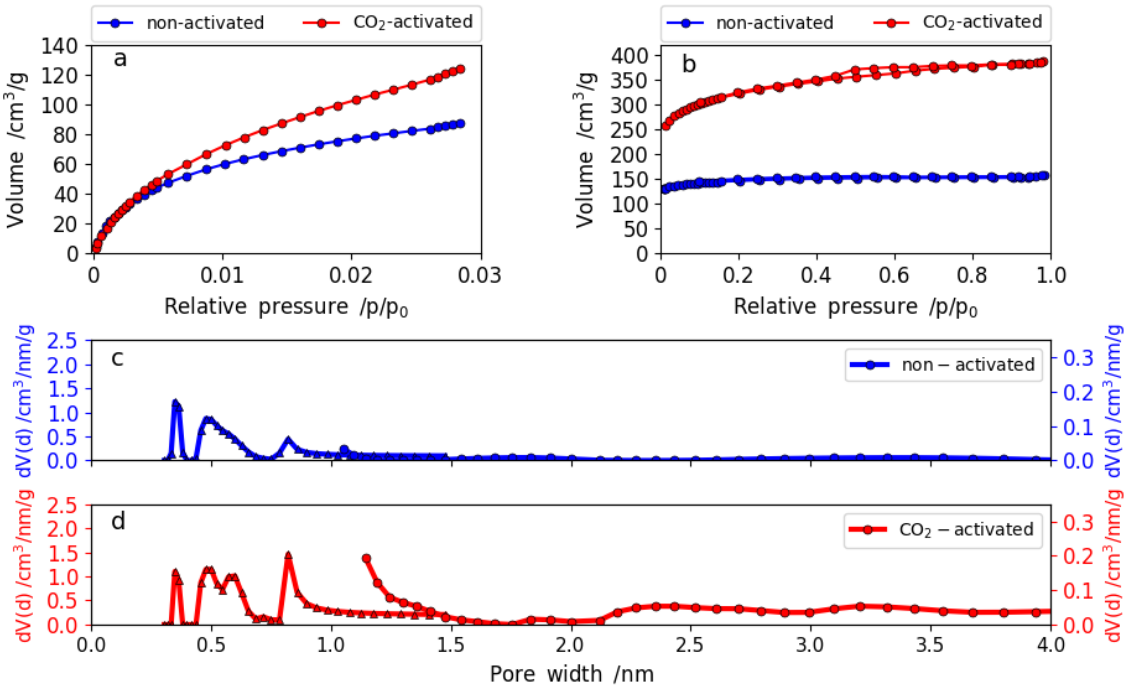

Figure 4-4 CO_2 adsorption isotherms of the non-activated (blue) and CO_2-activated (red) LCNFs (a), N_2 ad-/desorption isotherms of the non-activated (blue) and CO_2-activated (red) LCNFs (b), pore size distributions calculated by DFT based on the adsorption isotherms of: non-activated (c) and CO_2-activated (d) LCNFs, circles indicate points derived from N_2 sorption and triangular symbols from CO_2 sorption.

From both N_2 and CO_2 sorption measurements, pore size distributions (PSDs) were generated by density functional theory (DFT) models (NLDFT for CO_2 sorption and QSDFT for N_2 sorption) implemented into the gas sorption analyzer software (ASiQwin, version 3.0).[262] The resulting PSDs calculated by DFT based on the adsorption isotherms indicate that the non-activated sample contains a considerable amount of (sub-)nanopores (<1 nm) (Figure 4-4c). This was anticipated as the lignin precursor contains approximately 30 wt% of oxygen as shown in the previous chapter about lignin characterization and a high degree of disorder, hence a low packing density.[263] The additional CO_2 activation effectively creates both meso- (2 – 50 nm) and nanopores (<2 nm) (Figure 4-4d). This might take place by widening of the pre-existing (sub-)nanopores and additional creation of new (sub-)nanopores. This explanation is supported

by the fact that the CO_2 activation did not lead to a decrease in the fibre diameter (Table 4-1). Hence, the CO_2 activation might take place in the existing nanopore space rather than uniformly on the external fibre surface. The increased porosity is also manifested in the values of specific surface area shown together with the adsorbed gas volumes in Table 4-3.

Table 4-3 Overview of BET and DFT specific surface area (SSA) and pore volumes (pore vol.) derived from the N_2 and CO_2 gas sorption experiments.

	N_2 sorption					CO_2 sorption			
Sample	BET* SSA/ m^2/g	DFT SSA/ m^2/g	Total pore vol./ cm^3/g	Pore vol. <2nm/ cm^3/g	Pore vol. fraction <2nm/ %	DFT SSA/ m^2/g	Pore** vol./ cm^3/g	Pore vol. <0.8nm / cm^3/g	Pore vol. fraction <0.8nm / %
Non-activated	676	576	0.220	0.208	95	944	0.275	0.188	68
CO_2-activated	1204	1144	0.552	0.385	70	1412	0.472	0.263	56

*rel. pressure range used: 0.007 – 0.034

**pore volume of pores with diameters in the range of 0.30 – 1.48 nm

Upon CO_2 activation, the specific BET (Brunauer, Emmett and Teller) and DFT surface areas increase (Table 4-3). From the N_2 sorption measurements, it is apparent that pore widening through CO_2 activation took place as the fraction of pores with diameters smaller than 2 nm decreased from 95% (non-activated) to 70% (CO_2-activated). A similar trend can be observed for the (sub-)nanometer pores with diameters smaller than 0.8 nm probed by CO_2 sorption measurements. After CO_2 activation, the fraction of pores with diameters smaller than 0.8 nm decreased from 68% for the non-activated to 56% for the CO_2-activated LCNFs.

The oxygen content on the LCNF surface was determined by temperature programmed desorption (TPD) and X-ray photoelectron spectroscopy (XPS). The TPD spectra are shown in Figure 4-5. In general, the non-activated and CO_2-activated samples have very similar desorption rates of both CO and CO_2. Overall, both samples desorb more CO (2562 and 2635 μmol/g) than CO_2

(860 and 896 µmol/g) (Table 4-4). From this, the total oxygen content was determined to be 6.9 wt% for the non-activated and 7.1 wt% for the CO_2-activated LCNFs.

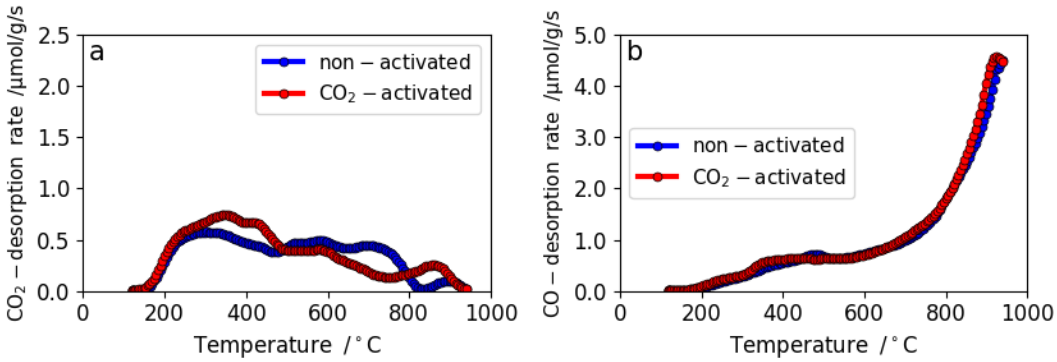

Figure 4-5 TPD spectra: CO_2 desorption rates (a) and CO desorption rates (b) of the non-activated (blue) and CO_2-activated LCNFs (red).

The evolution of CO_2 arises from carboxylic groups and their derivatives, such as lactones and anhydrides, whereas CO is associated with the decomposition of carbonyl groups, ethers and hydroxyl groups (e.g. phenols) groups.[144,264,265] It was shown that the CO-desorbing oxygen groups have a positive effect on the capacitance in electric double layer capacitors in alkaline electrolytes, whereas the CO_2-desorbing oxygen groups are less stable and hence detrimental.[241] From ^{31}P NMR and $^{13}C–^{1}H$ (HSQC) NMR presented in the previous chapter, it is clear that the HKL precursor is rich of hydroxyl groups (especially: syringyl, aliphatic, guaiacyl and condensed phenolic groups) and ether bonds (especially: β-O-4 ether bonds). As determined by TPD, these types of oxygen functional groups are preserved in a reduced quantity upon thermal treatment (6.9/7.1 wt% compared to 30 wt% initially).

Table 4-4 Amount of desorbed CO_2 and CO and the resulting oxygen content determined by TPD measurements.

Sample	Amount of CO_2 / µmol/g	Amount of CO/ µmol/g	Amount of O/ µmol/g	Oxygen content /wt%
Non-activated	860	2562	4282	6.9
CO_2-activated	896	2635	4427	7.1

The XPS spectra shown below (Figure 4-6) indicate that the main oxygen functional groups in both the non- and CO_2-activated sample are ether groups which corresponds to CO desorption in TPD. However, C=O and O-C=O functional groups were determined as well, although in a smaller quantity, which can be seen in the C1s high resolution XPS spectra in Figure 4-6a and b.

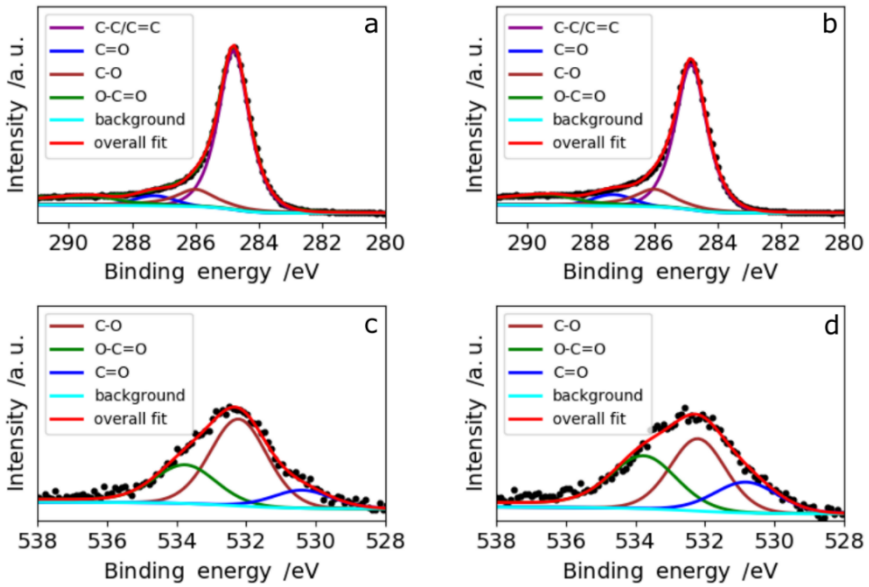

Figure 4-6 Deconvolution of the C1s peak of the non-activated (a) and CO_2-activated (b) LCNFs and deconvolution of the O1s peak of the non-activated (c) and CO_2-activated (d) LCNFs.

Additionally, the difference in total oxygen content of the non- and CO_2-activated LCNFs from XPS is 1.3 wt% (Table 4-5) and hence only slightly higher than from TPD. This can be explained by the fundamental difference of the two methods. XPS probes only the first nanometers of the samples whereas TPD probes the bulk of the samples.[90]

Table 4-5 Overview of the surface chemistry: C, O, N, S and Na content of the LCNFs based on XPS.

Sample	C /wt%	O /wt%	N /wt%	S /wt%	Na /wt%
Non-activated	92.52	5.39	1.18	0.90	0.00
CO_2-activated	91.31	6.69	0.95	0.95	0.10

The nitrogen (N), sulfur (S) and sodium (Na) content on the fibre surface were determined by XPS in addition to the carbon (C) and oxygen (O) content (Table 4-5). The amount of these

elements arising from the Kraft process (e.g. sulfur and sodium) and the natural environment (nitrogen) are low. After the thorough characterization of the non-activated and CO_2-activated LCNFs, the capacitive performance in a supercapacitor operating with 6 M $KOH_{(aq)}$ electrolyte is tested. The LCNFs were used as free-standing electrodes after carbonization/activation without any further processing in a two-electrode symmetric supercapacitor (SC) device. Cyclic voltammetry at different scan rates was carried out with the non-activated and CO_2-activated LCNF electrodes in 6 M $KOH_{(aq)}$ (Figure 4-7). All voltammograms show the rectangular shape typical of electric double layer charge storage.[145,184] The CO_2-activated sample shows a slight curvature indicating pseudocapacitive contribution of the oxygen functional groups.[191] The absence of the contribution in the non-activated sample is assigned to the non-accessibility due to lacking porosity as the oxygen content only marginally changed upon CO_2 activation. The voltammograms reveal that the increased porosity in the CO_2-activated LCNFs translates into elevated capacitances. At low scan rates (5 and 50 mV/s), the difference between non-activated and CO_2-activated LCNFs is less pronounced.

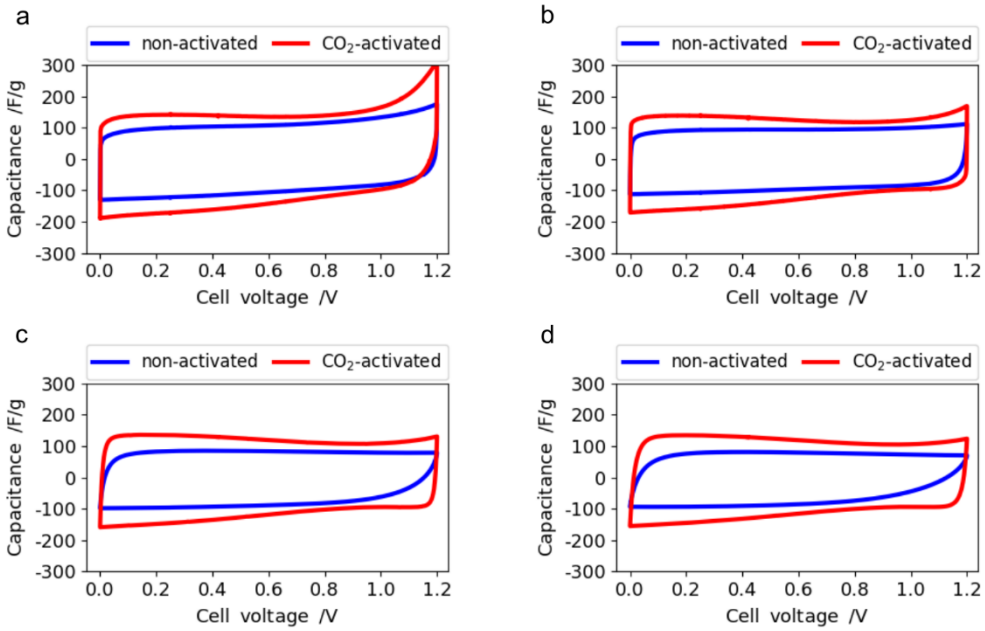

Figure 4-7 Cyclic voltammograms at scan rates of 5 (a), 50 (b), 500 (c) mV/s and 1 V/s (d) of the non-activated (blue) and CO_2-activated (red) LCNF electrodes.

But the CO_2-activated LCNFs show signs of an irreversible process close to 1.2 V, which is less present in the voltammogram of the non-activated LCNFs.

Tang et al. showed recently that carbon edge sites terminated by hydrogen and oxygen-functional groups might be the main cause for carbon corrosion at high voltage.[182] As shown by TEM and Raman, the CO_2-activated LCNFs comprise more of these sites compared to the non-activated LCNFs created by the physical activation procedure and the concomitant carbon leaching/re-deposition. At high scan rates of 500 mV/s and 1 V/s (Figure 4-7c,d), the voltammograms of the non-activated sample have a deformed shape indicating limited pore accessibility and hence lower capacitance. This is well-explained by the gas sorption experiments which revealed that the short pyrolysis at 900 °C for 30 min effectively creates (sub-)nanopores, but hardly any meso- (2 – 50 nm) or larger nanopores (1 – 2 nm) as can be seen in the pore size distributions in Figure 4-4c.

The galvanostatic charge-discharge (GCD) curves at 0.25 A/g shown in Figure 4-8a exhibit the symmetric triangular shapes typical of EDLCs. As for the voltammograms, the GCD curve of the CO_2-activated sample shows a slight curvature indicating the contribution from oxygen functional groups. The dependence of the specific gravimetric capacitances on the current density was derived from the GCD curves at various current densities to investigate the rate capabilities (Figure 4-8a). Clearly, the CO_2 activation increases both the specific gravimetric capacitance, which is 155 F/g at 0.1 A/g, and the overall rate capability (113 F/g at 250 A/g) which can be assigned to the increased nano- and mesoporosity (Table 4-3). The capacitance values attained are well-comparable with other recent reports on lignin-derived composite CFs (64 F/g, 83.3 F/g).[134,140] The leap in performance upon CO_2 activation is also shown in the corresponding Ragone plot in Figure 4-8c. Both energy and power density of the CO_2-activated LCNFs are considerably higher than the ones of the non-activated LCNFs. The difference between the samples is especially pronounced at a high power density (high rates). The non-activated LCNFs retain only 1.2 Wh/kg at 41 kW/kg, whereas the CO_2-activated LCNFs still achieve

4 Wh/kg at 52 kW/kg. This can be assigned to the presence of mesoporosity and improved accessibility to the stable CO-desorbing oxygen functional groups in the CO_2-activated sample. Finally, the cyclability test (Figure 4-8d) at 5 A/g over 6000 cycles shows an interesting trend. The CO_2-activated LCNFs exhibit a typical slight capacitance decay with increasing cycle number (94% retention after 6000 cycles). Contrarily, the non-activated LCNFs show a slight increase in capacitance with cycle number. This is unusual and can be assigned to the low degree of pore accessibility and hence low pore penetration by the electrolyte.

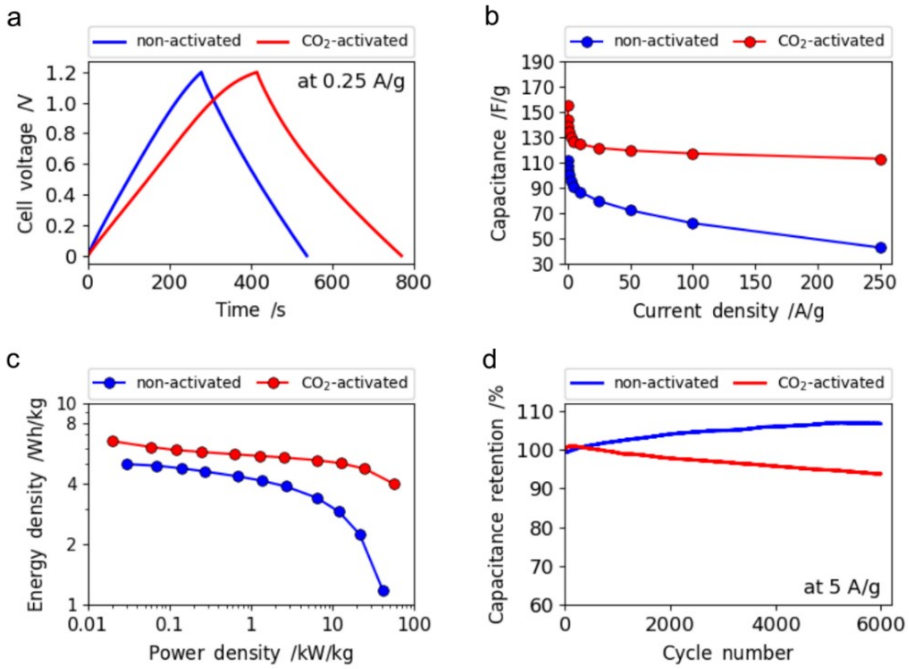

Figure 4-8 Charge-discharge curves at 0.25 A/g (a), dependence of the specific gravimetric capacitance on the current density (b), Ragone plot (c) and capacitance retention over 6000 cycles at a current density of 5 A/g (d).

However, with time (increasing cycle number), a slight improvement in the wettability by repetitive cycling is observed. The correlation between the mainly (sub-)nanoporous PSD with low degree of accessibility and the electrochemical performance is striking in this case. The imaginary capacitance (C'') plotted as a function of frequency derived from impedance spectroscopy confirms this observation (Figure 4-9c). The maximum imaginary capacitance is located at the relaxation frequency, f_R, determining the characteristic time constant according to

$\tau = (2\pi fR)^{-1}$.[242] In general, the higher the time constant the lower the rate capability.[242] For the non-activated LCNFs, f_R = 0.68 Hz, whereas for the CO_2-activated LCNFs, f_R = 14.5 Hz. Hence, the non-activated LCNFs exhibit an elevated time constant of 0.23 s compared to the CO_2-activated LCNFs (0.011 s). Furthermore, the Nyquist plot presented in Figure 4-9a shows that the non-activated LCNF electrode gives rise to a bigger semi-circle and hence a higher resistance than the CO_2-activated LCNF electrode.

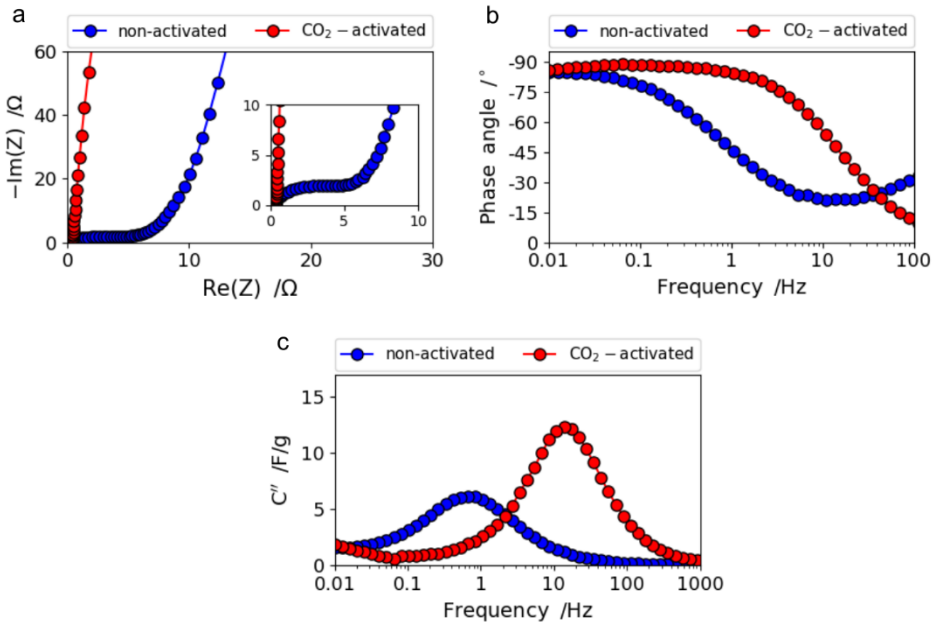

Figure 4-9 The Nyquist plot (a), Bode phase angle plot (b), imaginary capacitance vs. frequency dependencies (c) of non-activated (blue) and CO_2-activated (red) LCNF electrodes.

In the Bode phase angle plot (Figure 4-9b), it is obvious that the CO_2-activated LCNFs preserve the ideal value of -90 ° (fully capacitive) towards higher frequencies compared to the non-activated LCNFs confirming the higher rate capability of the LCNFs by CO_2 activation.

Due to the low density of activated carbon materials in general and of activated carbon fibre networks in particular, the consideration of the areal capacitance and volumetric energy/power density is of great importance. The difference in areal capacitance among the samples is similar to the specific gravimetric capacitance. However, the overall difference is less substantial (Figure 4-10).

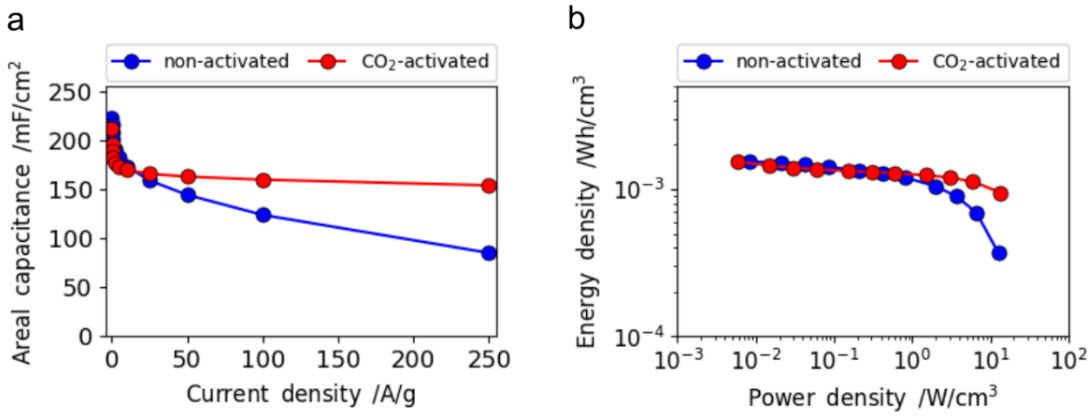

Figure 4-10 Areal capacitance as a function of current density (a), Ragone plot in volumetric measures (b).

This is also true for the Ragone plot in volumetric measures. This can be explained by the fact that the density of the LCNF networks is reduced by CO_2 activation (Table 4-6) which affects the volumetric measures negatively (Table 4-6).

Table 4-6 Data of the electrode weights and area and resulting mass loadings of the electrodes.

Sample	Weight /mg	Area /cm^2	Mass loading /mg/cm^2
Non-activated	0.78	0.785	0.994
CO_2-activated	0.61	0.785	0.777

Overall, the CO_2 activation is still beneficial in terms of rate capability as shown in Figure 4-10a and b. This comparison proves the importance of considering both gravimetric and volumetric measures for energy and power densities. The issue will be further considered in the following chapter describing the salt activation of lignin-based carbon nanofibres from hardwood Kraft lignin. In this chapter, it was shown that it is possible to produce highly capacitive LCNF electrodes from fractionated eucalyptus Kraft lignin with high purity. The fibre formation from this low molar mass polymer (1900 g/mol, D = 1.5) in the absence of any synthetic, high molar mass polymer is attributed to strong intermolecular interactions via hydrogen bonds between ether bonds (e.g. β-O-4) and hydroxyl groups (e.g. aliphatic) and π-π interactions (various phenolic moieties) in the electrospinning solution at high lignin concentration (50 wt%). Through stabilization in air, carbonization in a N_2 atmosphere and activation with CO_2, it is possible to

produce highly capacitive, free-standing carbon nanofibre electrodes from eucalyptus Kraft lignin without any additive. The combination of high oxygen and carbon content and the high degree of aromaticity of the lignin precursor translates into nanoporous, oxygen functionalized carbon nanofibres with good yield (33% after carbonization and 25% after CO_2-activation). The hydroxyl and ether groups of the initial precursor are preserved in a reduced quantity as beneficial oxygen functional groups in the final LCNFs.

4.4. Conclusion

Physical activation based on the reaction of CO_2 as oxidizing gas with carbon was used to improve the capacitive performance of hardwood Kraft lignin-based carbon nanofibres. These LCNF mats possess mainly CO-desorbing oxygen functional groups in TPD, which proved to be beneficial when tested as free-standing electrodes in aqueous alkaline supercapacitors. Consequently, the CO_2-activated LCNF electrodes showed a high specific gravimetric capacitance of 155 F/g at 0.1 A/g, excellent rate capability with 113 F/g at 250 A/g and a good capacitance retention of 94% over 6000 cycles when tested in 6 M $KOH_{(aq)}$ electrolyte. It can be concluded that lignin itself is a promising precursor to produce nanoporous, oxygen functionalized carbon fibres via a three-step thermal treatment (stabilization, carbonization and activation). The resulting LCNF mats can be used without further processing steps as free-standing electrodes in aqueous alkaline supercapacitors. However, the CO_2 activation process has a negative impact on the volumetric energy density. Therefore, the leap in performance observed in gravimetric measures is preserved to a much lower degree in volumetric ones. At high rates, the CO_2-activated LCNFs still outperform the non-activated LCNFs even in volumetric measures. However, at low current densities (up to 25 A/g), the difference in capacitance and hence energy density becomes miniscule. Consequently, the densification of these nanofibre networks used as free-standing electrodes needs to be achieved to improve the capacitive performance of the activated LCNF electrodes in volumetric measures. This will be addressed in the following chapter.

5. $NaNO_3$ activation of hardwood Kraft lignin-derived carbon nanofibres

5.1. Introduction

As described in the previous chapter, next to physical activation through $CO_{2(g)}$ or steam, chemical activation by alkali metal salts is another effective strategy to produce high surface area carbon materials.[177] This route is explored for hardwood Kraft lignin-derived (HKL) carbon nanofibres (LCNFs) in this chapter. The resulting LCNFs are then used as free-standing electrodes in aqueous alkaline supercapacitors (SCs). An efficient way to take advantage of alkali metal catalyzed gasification is to use the hydroxides (here: NaOH) as aqueous solvents in electrospinning of lignin. In this work, $NaNO_3$ was added in various quantities to the electrospinning solutions to further enhance the chemical activation by decomposition of $NaNO_3$ during carbonization:[266,267]

$$2\ NaNO_{3(s)} \xrightarrow{380°C} 2\ NaNO_{2(s)} + O_{2(g)}$$

$$4\ NaNO_{3(s)} \xrightarrow{>800°C} 2\ Na_2O_{(s)} + 5\ O_{2(g)} + 2\ N_{2(g)}$$

Thus, the activation agent can be incorporated in the electrospinning process and thus activation takes place in the thermal conversion process (activation by decomposition) rather than in a separate process step as in physical activation. However, after electrospinning and the thermal conversion (carbonization), an additional washing step with hot water (80 °C) is required to remove residual activating agents and by-products, such as $Na_2O_{(s)}$. Another important advantage of incorporating the chemical activation agent in the electrospinning step is that, the mixing of the activating agent with the polymer takes place in solution. The mixing on a molecular level ensures a more homogeneous distribution and stronger interactions than by physical mixing of pre-formed materials, such as coal, wood or coconut shells. When lignin is solubilized in an alkaline medium the hydroxyl groups are ionized.[57,268] Thus, the Na^+ ions provided through NaOH and $NaNO_3$ in solution will be bound to the solubilized lignin fragments

by coulombic interactions which is illustrated in Figure 5-1.

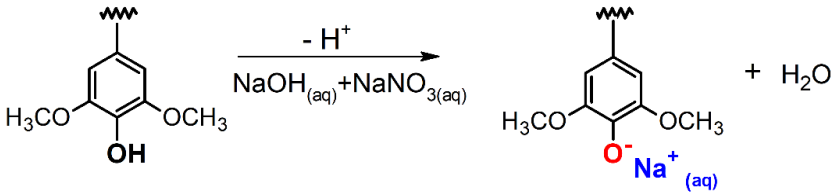

Figure 5-1 Ionization of lignin in a $NaOH/NaNO_3$ solution and interaction of the ionized phenolic moieties with Na^+ ions. The same principle applies to the aliphatic hydroxyl groups in lignin.

The reaction mechanism of activating carbon materials by NaOH was studied thoroughly in the past.[243,269–271] It has been suggested that the activation of carbon by alkali metal hydroxides occurs via the following general reaction:

$$6\ NaOH_{(s)} + 2\ C_{(s)} \xrightarrow{\Delta\ (>700\ ^\circ C)} 2\ Na + 3\ H_{2(g)} + 2\ Na_2CO_{3(s)}$$

Therefore, high activating-agent-to-carbon ratios need to be applied to create porosity effectively. Most commonly, activating-agent-to-carbon ratios of two-to-one or three-to-one are used.[269–271] In the activation of carbons, a solid-solid or liquid-solid redox reaction takes place involving the reduction of the alkali metal hydroxide and the concomitant oxidation of the carbon material, which creates porosity.[271] Additionally, the decomposition of functional groups in the carbon structure at elevated temperatures (>700 °C) leads to CO, CO_2 and H_2 evolution and hence yields porosity.[243] In the previous chapters, the latter was shown to be of great significance during carbonization of the Kraft lignins used as precursors throughout this project. The oxidative salt, $NaNO_3$, serves not only as an additional activating agent, but it also controls the lignin fibre diameter and incorporates oxygen functional groups. Furthermore, the charge density in the electrospinning solution is increased by $NaNO_3$, hence the fibre packing density in the final LCNF electrodes can be tailored. Therefore, the addition of $NaNO_3$ to the electrospinning solution greatly affects both the specific gravimetric and volumetric energy and power densities when used as free-standing electrodes in aqueous alkaline supercapacitors (SCs).

5.2. Preparation of $NaNO_3$-activated LCNFs

The solutions for electrospinning contained polyethylene oxide (PEO) with an weight average molar mass of 600,000 g/mol and eucalyptus hardwood Kraft lignin with a weight average molar mass of 1900 g/mol in a weight ratio of PEO/lignin of 0.14 dissolved in 1 M $NaOH_{(aq)}$. The total amount of polymer in solution was 12 wt%. 10, 30 and 50 mol% of $NaNO_3$ with respect to NaOH in the solvent were added to the polymer solution in form of a 0.7 g/ml $NaNO_{3(aq)}$ solution. The resulting $NaNO_3$/lignin weight ratios are given in Table 5-1.

Table 5-1 $NaNO_3$/polymer weight ratios in the electrospinning solutions.

Sample	$NaNO_3$ /mol %	$NaNO_3$/polymer
N0	0	0.000
N10	10	0.059
N30	30	0.179
N50	50	0.299

The samples prepared from the various solutions are abbreviated according to the amount of $NaNO_3$ in solution as N0, N10, N30 and N50. These solutions were stirred for three hours and then stored in sealed glass vials overnight without stirring before electrospinning. For electrospinning, a plastic syringe was loaded with 4 ml of the electrospinning solution. The syringe was discharged at a rate of 1 ml/h with a syringe pump (Pump 33 DDS Dual Drive System, Harvard Apparatus, USA). Additionally, a high voltage (20 – 25 kV) between the syringe needle (gauge = 23) and the collector, which was an aluminum foil (24 × 24 cm), was established with a transformer (Glassmann high voltage inc., USA). In order to control the humidity (at 10%), electrospinning was carried out in a glovebox (Plas-labs, USA). After electrospinning, the as-spun lignin fibre mats were converted to carbon nanofibre mats in a one-step thermal treatment by direct carbonization in forming gas (5 mol% H_2 in N_2) without the need of a separate stabilization step due to the co-polymer PEO which forms hydrogen bonds with the lignin in solution.

In addition, PEO provides additional oxygen which promotes crosslinking during the thermal conversion in the nitrogen atmosphere.[272] For the direct carbonization, the fibre mats were heated to 800 °C for 2 h with a heating rate of 3 °C/min. Finally, the carbonized mats were washed in a water bath at 80 °C for 1 h and subsequently dried overnight at 120 °C to remove residual salts and activation agents.

5.3. Results and discussion

The as-spun lignin fibres with various concentrations of $NaNO_3$ in the electrospinning solution are shown in Figure 5-2. The packing density of the fibres within the mats rises considerably with increasing $NaNO_3$ concentration in the electrospinning solution, as can be seen in Figure 5-2. The void space (macropores >50 nm) between the fibres in sample N0 (Figure 5-2a) gradually decreases with increasing amount of $NaNO_3$ in N10 (Figure 5-2b) and N30 (Figure 5-2c) and is smallest for N50 (Figure 5-2d).

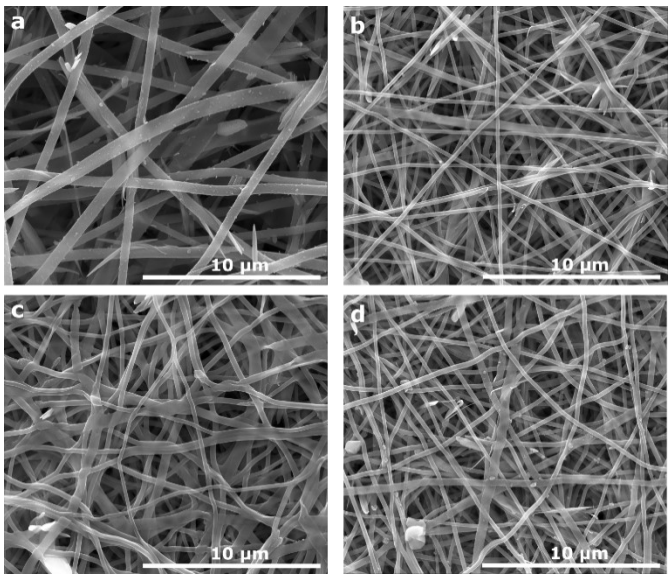

Figure 5-2 The as-spun Kraft lignin fibres with 0 (a), 10 (b), 30 (c), and 50 (d) mol% of $NaNO_3$ added to the electrospinning solution.

The effect of $NaNO_3$ on the fibre packing density in the nanofibre network is especially pronounced when considering the difference between N0 and N10, with 0 and 10 mol% of $NaNO_3$. Furthermore, the average fibre diameter decreases upon the addition of $NaNO_3$ to the electrospinning solution. The smallest average diameter of 182 nm was measured for the fibres of

sample N10, as shown in Table 5-2. With increasing amounts of $NaNO_3$ in solution, the average fibre diameter seems to slightly increase again for N30 (241 nm) and N50 (255 nm), while still being much smaller than the one of the pristine (N0) fibres (478 nm). This can be observed more clearly when looking at the single fibre morphology which changes gradually from cylindrically shaped fibres to more band-like fibre morphologies (Figure 5-2). The fibre thinning upon the addition of salts in electrospinning solutions was also described in several publications previously and was attributed to the increase of charge density in the solution and thus enhanced elongation of the electrospinning jets.[256,273] Furthermore, the non-linear decrease in average fibre diameter at high salt concentrations was previously attributed to an excess of charge density on the collector and hence incomplete splitting of the electrospinning jet.[274,275]

Table 5-2 Average diameters of the as-spun and carbonized fibres. Additionally, the average area density of the carbonized samples is given as a measure for the increase in fibre packing density.

Sample	Average fibre diameter (as-spun) /nm	Average fibre diameter (carbonized) /nm	Average area density* (carbonized) /mg/cm^2
N0	478 ± 89	331 ± 42	0.51
N10	182 ± 26	163 ± 42	0.69
N30	241 ± 42	201 ± 38	0.77
N50	255 ± 60	188 ± 38	1.03

* *average value of 10 samples (weight of electrodes with circular shape with a diameter of 1 cm)*

After direct carbonization, the trend of fibre thinning and fibre network densification observed for the as-spun fibre mats is maintained (Figure 5-3). This is also confirmed by the area density of the carbonized nanofibre mats reported in Table 5-2. Furthermore, the average fibre diameter decreased further for all samples during carbonization. The change in average diameter between as-spun and carbonized fibres is greatest (>100 nm) for N0. Nano X-ray computed tomography (CT) was carried out by Dr. Rhodri Jervis at University College London (UCL) to visualize the carbonized electrospun mats in 3D. Figure 5-4 shows a 3D rendering and a greyscale *xy* orthoslice of the reconstructed X-ray CT volume of the carbonized N0 sample where the *xy*

plane shown in Figure 5-4b and c is the plane in which the fibres are deposited, growing the thickness of the mat with time in the *z*-direction.

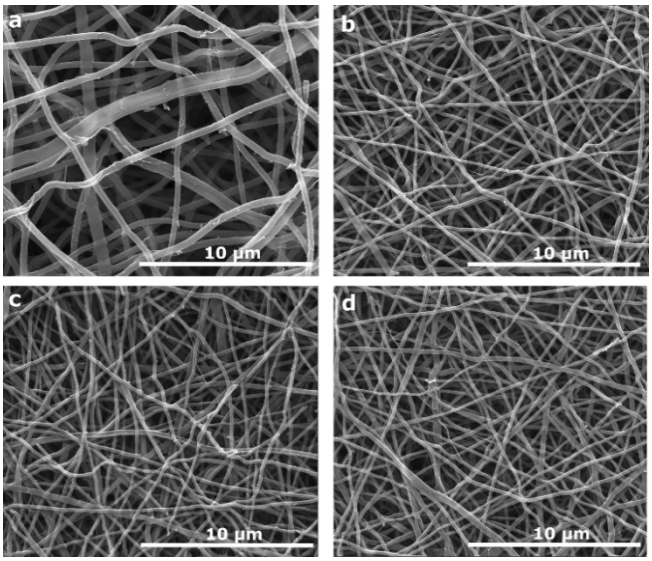

Figure 5-3 The LCNFs prepared with 0 (a), 10 (b), 30 (c), 50 (d) mol% of $NaNO_3$ in the electrospinning solution.

The lab CT system produced a pixel resolution of 63.15 nm providing clear images and good contrast for the N0 fibres. However, upon treatment with $NaNO_3$, the reduction in fibre diameter is large enough that the resolution limits of the CT instrument were reached. From SEM, the fibre diameters for the $NaNO_3$ treated samples are on the order of two to three voxels on average, and thus there is not sufficient detail in the scan to infer accurate information.

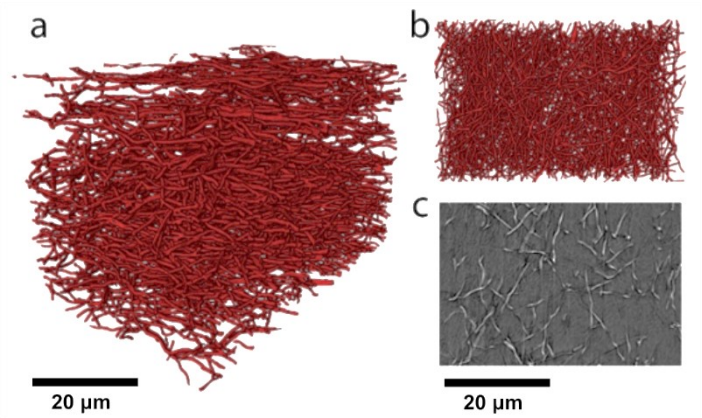

Figure 5-4 X-ray CT of the carbonized N0 sample showing 3D renderings of the reconstructed volume (a and b) and the 'xy' face, the plane of deposition of fibres, (right) in 3D (b) and an orthoslice of the greyscale data from the center of the volume (c). Images were obtained with a voxel size of 63.15 nm.

Hence, only larger fibres or nodes from the junctions of multiple fibres are visible at this resolution (Figure 5-5). Nevertheless, it is clear from the images of the N50 sample in Figure 5-5 that there is a densification of the mat and a decrease in macroporosity upon $NaNO_3$ treatment, from 96% in the case of N0 and 76% for N50, although there is a large error associated with the latter number.

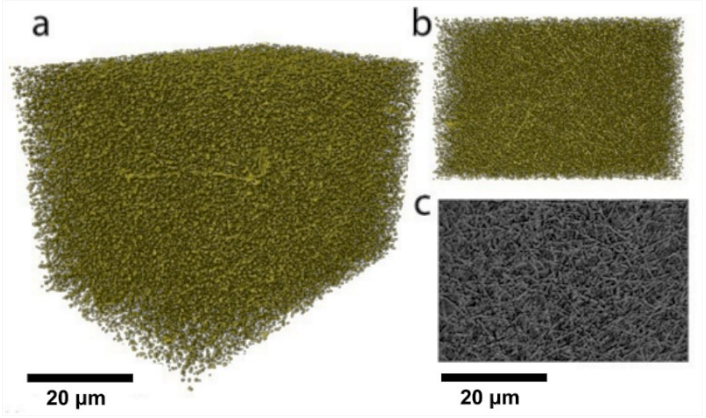

Figure 5-5 X-ray CT of the carbonized N50 sample showing 3D renderings of the reconstructed volume (a and b) and the 'xy' face, the plane of deposition of fibres, (right) in 3D (b) and an orthoslice of the greyscale data from the center of the volume (c).

In addition to the morphological 2D and 3D analysis of the entire nanofibre network, the change of the single fibre morphology was investigated by transmission electron microscopy (TEM). The TEM micrographs show some interesting features on the fibre surfaces (Figure 5-6).

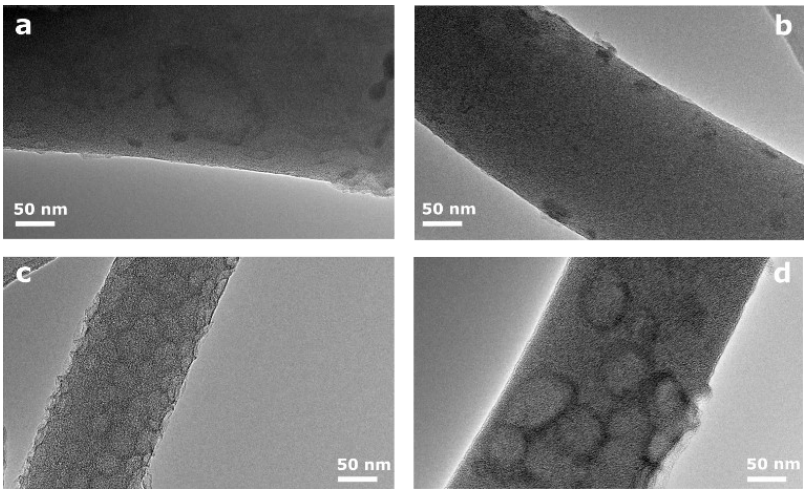

Figure 5-6 TEM micrographs of the LCNFs prepared with 0 (a), 10 (b), 30 (c) and 50 (d) mol% of $NaNO_3$ in the electrospinning solution.

Upon addition of large amounts of $NaNO_3$ (Figure 5-6c and d), the LCNFs exhibit a much higher degree of morphological heterogeneity than N0 and N10. This is manifested in an onset of ordering of ring-like domains on the fibre surface with the addition of 30 and 50 mol% of $NaNO_3$ in solution (Figure 5-6c and d). The XPS data given in Table 5-3 clearly indicates very low amounts of Na and N on all LCNFs which means the features seen on the fibres are no salt impurities (e.g. remaining $NaNO_3$ or Na_2CO_3). Instead, these ring-like domains might indicate where the activating salts were located before decomposition which has led to an enhanced ablation and rearrangement of the carbon matrix in this region.

The Raman spectra of the four samples (N0, N10, N30, N50) show both D and G bands, indicating a disordered carbon structure (Figure 5-7).[261,276,277] Upon addition of $NaNO_3$, the degree of disorder increases slightly indicated by an increase in I_D/I_G ratio (Figure 5-7). The intensities were determined by the peak heights which was suggested to be more suitable for highly disordered carbons than the peak areas.[260,261]

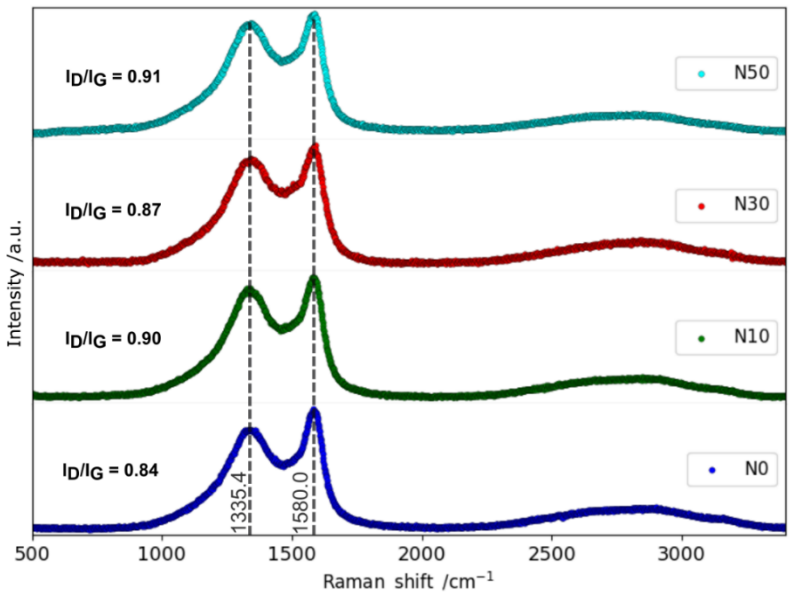

Figure 5-7 Normalized Raman spectra of N0, N10, N30, N50 after baseline correction.

The oxygen content with increasing amount of $NaNO_3$ was determined by XPS (Figure 5-8 and Table 5-3). Counterintuitively, the oxygen content is slightly lower for N10 (7.0 wt%) than for the pristine sample, N0 (8.9 wt%), which might be explained by the fact that with the addition

of a small amount of $NaNO_3$ the porosity and fibre morphology are modified quite significantly. These changes might lead to a shadowing of the surface oxygen groups in narrow nanopores which are not probed by XPS due to its low penetration depth.[144] The XPS data indicates that the nanofibre surface is free from any residual salts or other impurities. Additionally, it indicates a very low sulfur content which is a result of extensive refinement of the Kraft lignin via the LignoBoost process and sequential solvent fractionation.

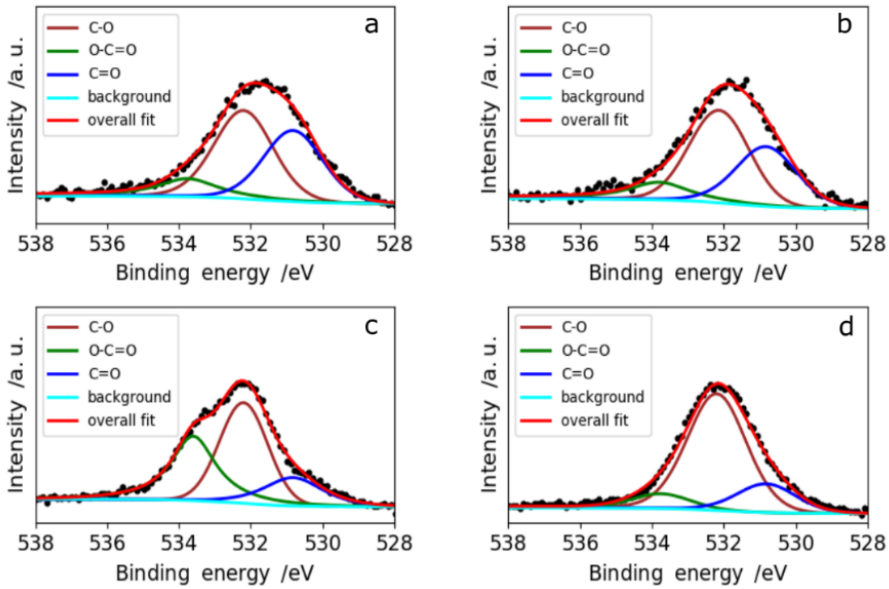

Figure 5-8 Deconvolution of the O1s narrow scan of N0 (a), N10 (b), N30 (c) and N50 (d).

From the deconvolution of the O1s peak in XPS, it is clear that C-O is the most abundant functional group in all samples. The samples N0 and N10 prepared with low amounts of $NaNO_3$ in the electrospinning solution show more C=O functional groups (N0: 39.2% and N10: 34.7%) than N30 and N50 with 17.0% and 17.7%, respectively. For N30, an elevated number (36.2%) of O-C=O functional groups was determined as shown in Figure 5-8c. Furthermore, the oxygen content of the LCNFs was determined by temperature programmed desorption (TPD). Compared to the results from XPS, the changes in oxygen content with increasing amounts of $NaNO_3$ in the electrospinning solution are less substantial. This can be explained by the fact that TPD probes the bulk oxygen content, whereas XPS only the first nanometers of the sample's surface.

Table 5-3 Overview of the surface chemistry: C, O, N, S and Na content of the LCNFs derived from XPS.

Sample	C /wt%	O /wt%	N /wt%	S /wt%	Na /wt%
N0	90.1	8.9	0.3	0.5	0.2
N10	91.5	7.0	0.8	0.3	0.3
N30	85.7	13.1	0.6	0.4	0.2
N50	86.0	12.8	0.7	0.2	0.2

Moreover, the reducing atmosphere (5 mol% H_2 in N_2) during the carbonization step effectively removes the oxygen functionalities arising from the $NaNO_3$ decomposition. This is especially true for the samples N10 and N30. N50 shows a clear increase in both CO_2 and CO desorption. Consequently, the total amount of oxygen increases from 2.9 wt% for N0 to 4.5 wt% for N50 (Figure 5-9). This indicates that the reducing condition during carbonization is not sufficient to remove the surplus of oxygen functional groups anymore. All samples desorb more CO than CO_2 which is consistent with the data derived from XPS which showed that C-O is the main functional group. In particular, the pronounced increase of CO desorption determined for N50 is in line with the results from the deconvolution of the O1s peak of this sample.

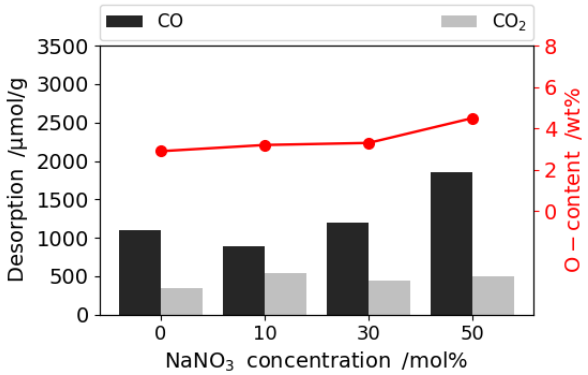

Figure 5-9 The bar chart indicates the total amount of desorbed CO and CO_2 from TPD measurements. The red line graph shows the total oxygen content in weight percent derived from the sum of CO and $2 \cdot CO_2$ desorbed from the samples.

The isotherms of the N_2 sorption experiments are shown in Figure 5-10a. The results clearly indicate that the increasing amount of $NaNO_3$ translates into increasing porosity as the volume

of adsorbed N_2 rises with increasing amount of $NaNO_3$ in the electrospinning solution (Figure 5-10a). Within the experimental error, a linear correlation with a R^2 value of 0.97 between the $NaNO_3$ content and the DFT surface area derived from the N_2 adsorption could be found, which can be seen in Figure 5-10b.

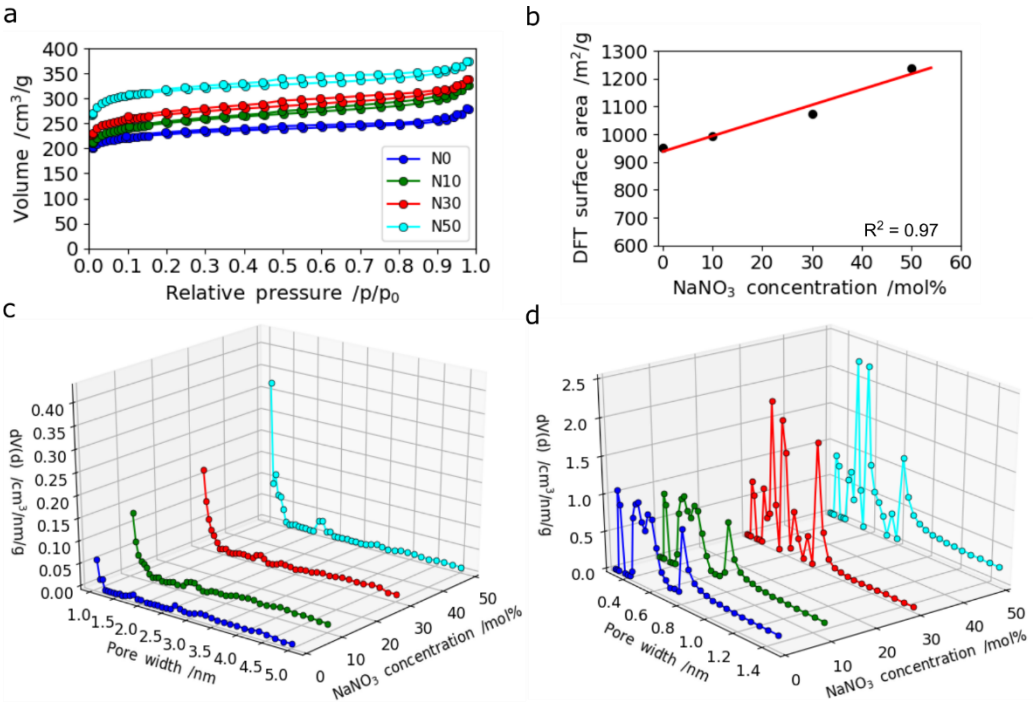

Figure 5-10 N_2 sorption isotherms of all four samples (a), correlation of DFT-derived surface area and $NaNO_3$ content (b), PSDs calculated by DFT (QSDFT (slit pore/cylindrical pore) model) based on the adsorption isotherms of N_2 (c) and PSDs from CO_2 adsorption measurements (NLDFT, non-localized DFT method) (d).

The pore size distributions (PSDs) calculated by Quenched Solid State Density Functional Theory (QSDFT) implemented into the gas sorption analyzer software (ASiQwin, version 3.0) show that the addition of the oxidizing agent, $NaNO_3$, creates slightly bigger pores around 1.0 and 1.4 nm. For the sample N50, even a small hump at around 2.2 nm is observed in the PSD (Figure 5-10). However, the PSDs of all samples are very narrow. A closer look at the PSDs within the narrow (sub-)nanopore region using CO_2 adsorption (Figure 5-10d) shows that, while N0 and N10 have similar (sub-)nanoporous pore size distributions (<1 nm), the PSDs of N30 and N50 are markedly different showing an increase in pore volume between 0.4 and 0.6 nm as indicated by two sharp and distinct peaks at 0.5 and 0.6 nm in the PSDs. This suggests that even

at high salt concentrations no agglomeration and hence formation of enlarged pores takes place, but rather a fine and homogeneous distribution of the activating salt translates into an enhancement of the (sub-)nanoporosity.

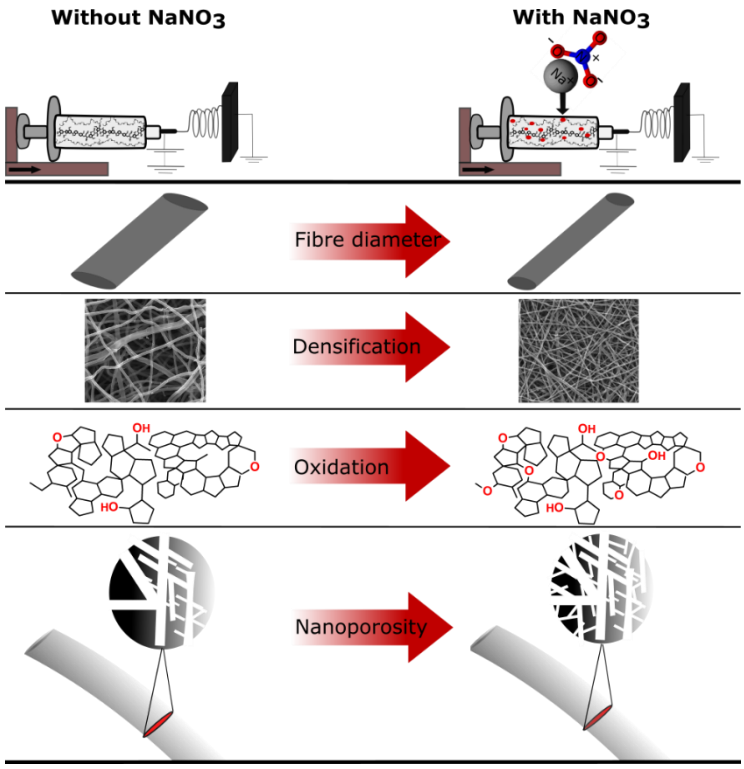

Scheme 5-1 Summary of the effects of $NaNO_3$ in the electrospinning solution determined by various characterization techniques.

The controlled oxidation by the addition of $NaNO_3$ and the subsequent reduction during carbonization of the LCNFs results in an increase in fibre packing density as shown by CT and SEM, controlled oxygen functionalization shown by TPD and XPS and an increase in (sub-)nanoporosity analyzed by gas sorption measurements (Scheme 5-1). This will have a great impact on the overall performance of the LCNFs in aqueous alkaline supercapacitors. The capacitive performance of the LCNFs as free-standing electrodes in symmetric two-electrode supercapacitors was evaluated in Swagelok-type cells using an aqueous alkaline electrolyte (6 M $KOH_{(aq)}$). To evaluate the capacitive performance of the free-standing LCNF electrodes derived from eucalyptus hardwood Kraft lignin in SCs, cyclic voltammograms (CVs) at various

scan rates were recorded. These reveal a similar behavior of all four samples for low (5 mV/s) and mid-level (50 mV/s) scan rates as shown in Figure 5-11a and b, respectively.

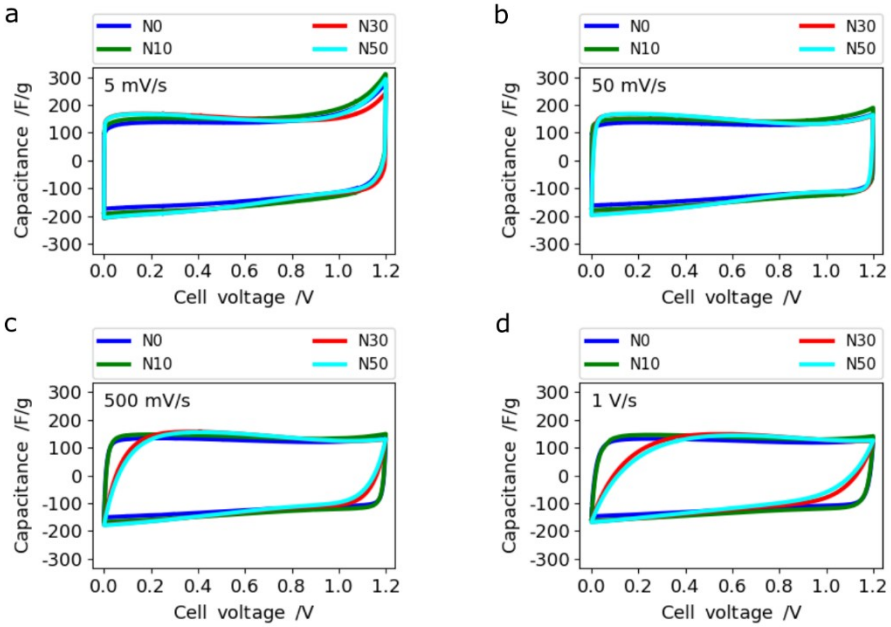

Figure 5-11 Voltammograms at 5 (a), 50 (b), 500 (c) mV/s and 1 V/s (d) of all four samples measured in 6 M $KOH_{(aq)}$.

However, the CVs of N30 and N50 show a slight curvature and hence higher capacitance values at low and mid-level scan rates which might arise from the contribution of the oxygen functional groups in combination with the elevated (sub-)nanoporosity. A reaction mechanism for the contribution of oxygen groups in alkaline media remains to be elucidated. However, enhanced hydrophilicity and ion affinity are the two main contributions most commonly described for oxygen-rich carbons tested in alkaline media.[186,191] At high and very high scan rates of 500 mV/s (Figure 5-11c) and 1 V/s (Figure 5-11d), N0 and N10 keep a rectangular shape of the voltammograms, whereas N30 and N50 exhibit a deformed shape which indicates a lower accessibility of the (sub-)nanometer pores.[187]

Therefore, the samples synthesized with no or low $NaNO_3$ content (N0 and N10) reveal a better rate capability compared with N30 and N50. This is also supported by the impedance data shown in Figure 5-12. The Nyquist plot in Figure 5-12a shows an enlarged semi-circle for N30 and N50 (low rate capability) compared to N0 and N10 (high rate capability) as a result of the

increase in the number of oxygen functional groups, the rise in (sub-)nanopores within the LCNFs and increase of the fibre packing density (decrease in macroporosity).[278,279] In the Bode phase angle plot (Figure 5-12b), the frequency responses of N0, N10, N30 and N50 show that N0 and N10 preserve the ideal value of -90 ° (fully capacitive) towards higher frequencies indicating higher rate capability than N30 and N50. The imaginary capacitance (C'') plotted as a function of frequency confirms this observation (Figure 5-12c). Herein, the maximum imaginary capacitance is located at the so-called relaxation frequency, f_R, determining the characteristic time constant according to $\tau = (2\pi f_R)^{-1}$. In general, the lower the time constant the higher the rate capability.[242] For N0 and N10, f_R = 7.7 Hz and for N30 and N50, f_R = 1.7 Hz. Hence, N0 and N10 show a smaller time constant of 0.02 s than N30 and N50 (0.095 s). The combined CV and impedance analyses clearly reveal that the increase in oxygen groups in N30 and N50, the enhancement of (sub-)nanoporosity and the densification of the LCNF network give rise to a lower rate capability, but higher capacitance values at low rates.

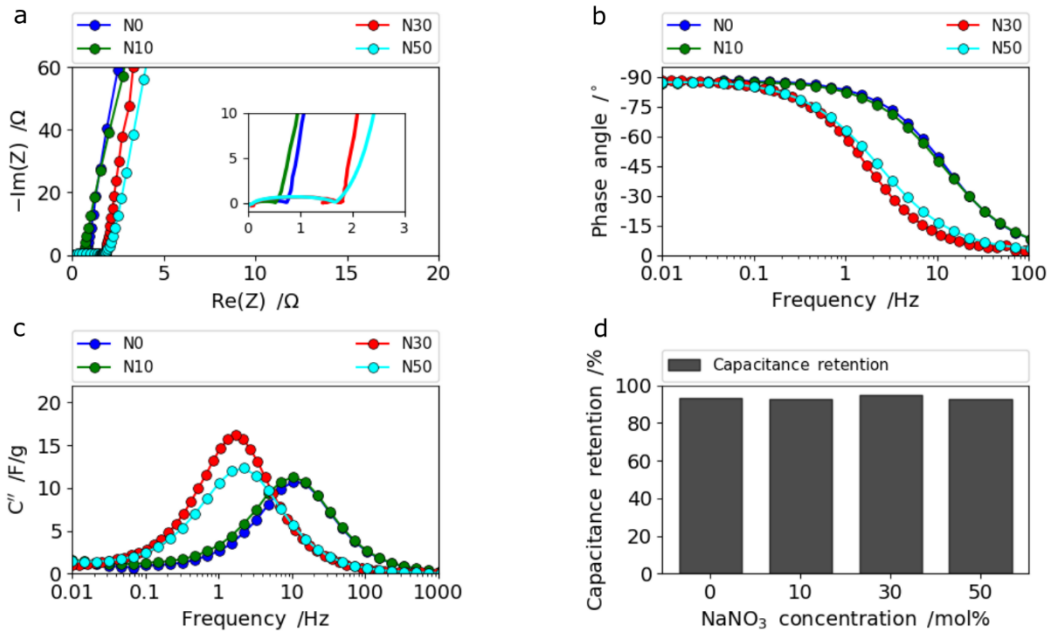

Figure 5-12 The Nyquist plots (a), Bode phase angle plots (b), imaginary capacitance vs. frequency plot (c) and cyclability data (d) of all four samples.

Lower rate capabilities due to oxygen functionalization and due to pores smaller than 1 nm were also reported in previous works on carbon based supercapacitors.[184,274,280–282] The capacitance retention of more than 92.8% after 6000 cycles for all samples, which is shown in Figure 5-12d, indicates good cyclability regardless of the $NaNO_3$ content in the electrospinning solution supporting the previous observations that CO-desorbing oxygen functional groups in TPD are stable in aqueous alkaline electrolytes.[241]

The rate capability was investigated in more detail by galvanostatic charge-discharge (GCD) measurements at various current densities. In Figure 5-13a and b, the dependence of specific gravimetric and areal capacitance values on the current density are presented. The direct comparison of the gravimetric and areal capacitance reveals the role of densification. In Figure 5-13a, all results are normalized by the electrode weights (F/g) meaning the densification and the resulting increase in electrode weights of the CNF electrode is not taken into account. Hence, the trend already derived from cyclic voltammetry and impedance spectroscopy can also be deduced from the GCD measurements (Figure 5-13a).

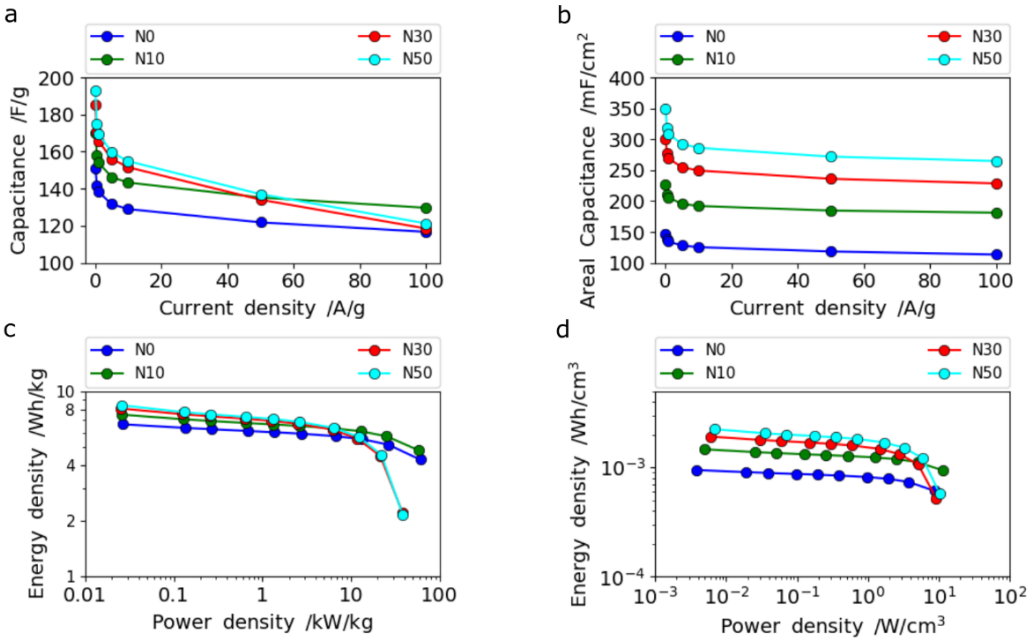

Figure 5-13 Dependence of the specific gravimetric capacitance on the current density for all four samples (a), dependence of the specific areal capacitance on the current density for all four samples (b), Ragone plot in gravimetric measures (c) and Ragone plot in volumetric measures (d).

The samples produced with large amounts of $NaNO_3$ in the electrospinning solution (N30 and N50) show a lower rate capability than the ones with no or small amounts of $NaNO_3$ (N0 and N10). More explicitly, at current densities of up to 50 A/g (medium rate), the specific gravimetric capacitance increases with increasing amount of $NaNO_3$ and a maximum gravimetric capacitance of 192 F/g at 0.1 A/g was obtained for N50. At high current densities (charge and discharge rates) exceeding 50 A/g, N10 with a low number of oxygen functional groups, a moderate increase in (sub-)nanoporosity and fibre packing density shows excellent rate capability. Determining the areal capacitance factors in the positive effect of fibre network densification. Consequently, the values for the specific areal capacitance (mF/cm^2) show even more pronounced differences among the samples (Figure 5-13b). At low rates, the areal capacitance can be more than doubled from 147 mF/cm^2 (N0) to 350 mF/cm^2 (N50). At high rates, this leap in areal capacitance is preserved as the increase in packing density, oxygen functionality and (sub-)nanoporosity are all factored in. The Ragone plots in gravimetric and volumetric measures, shown in Figure 5-13c and d, reveal the tuneability between high power and high energy density based on the $NaNO_3$ content in the electrospinning solution. N30 and N50 contain an increased number of oxygen functional groups, (sub-)nanoporosity and have a higher fibre packing density and hence operate as high energy density materials (up to 8.4 Wh/kg) at low power (2.6 W/kg). N0 and N10 contain small amounts of surface oxygen and less (sub-)nanopores and have a lower fibre packing density. Consequently, N0 and N10 operate as high-power density materials (up to 60 kW/kg). The same trend as for the gravimetric energy and power densities can be observed in terms of volumetric energy density (Figure 5-13d). However, as the fibre network densification is considered, N30 and N50 compare well with N0 and N10. Only at very high power densities exceeding 9.0 W/cm^3, N0 and N10 outperform N30 and N50 (Figure 5-13d). N10 exhibits a high power density of 11.6 W/cm^3 with an energy density of $14.7 \cdot 10^{-4}$ Wh/cm^3, whereas N50 delivers the highest energy density with $22.5 \cdot 10^{-4}$ Wh/cm^3 and a max-

imum power density of 10.3 W/cm^3. Simply by varying the amount of $NaNO_3$ in the electrospinning solution and subsequent reduction (5 mol% H_2 in N_2) during carbonization, the resulting electrode specifications can be tailored towards high energy (high $NaNO_3$ content) or high power (low $NaNO_3$ content) applications.

5.4. Conclusion

Eucalyptus hardwood Kraft lignin-derived carbon nanofibre electrodes were prepared by chemical activation embedded in the electrospinning and carbonization process steps. The specific gravimetric capacitance of the LCNF electrodes could be increased from 151 to 192 F/g in 6 M $KOH_{(aq)}$ at a low current density of 0.1 A/g via the two-step procedure of oxidative electrospinning ($NaNO_3$) and reducing carbonization (5 mol% H_2 in N_2). Moreover, the method allows doubling of the loading per electrode via fibre network densification with the addition of $NaNO_3$, which allows the areal capacitance to more than double from 147 mF/cm^2 in the absence of $NaNO_3$ to 350 mF/cm^2 with the maximum amount of $NaNO_3$ in the electrospinning solution with good capacitance retention of 92.8% after 6000 cycles. Thus, the low volumetric energy density normally associated with CNF electrodes could be greatly improved from 949 µWh/cm^3 to 2245 µWh/cm^3. Compared to the physical activation of eucalyptus Kraft lignin-derived CNF electrodes, chemical activation by addition of $NaNO_3$ to the electrospinning solution has two advantages as revealed in this chapter. Firstly, the number of process steps can be reduced. While CO_2-activated LCNFs were prepared by a four-step procedure (electrospinning, stabilization, carbonization and CO_2 activation), the $NaNO_3$-activated LCNFs could be produced by a three-step process: electrospinning, carbonization and cleaning. However, the input of chemicals is higher for preparing the $NaNO_3$-activated LCNFs than for the CO_2-activated ones. Secondly, the weight loss induced by CO_2 activation decreases the density of the resulting LCNF networks which is detrimental to the volumetric energy and power densities as

shown in the previous chapter. $NaNO_3$ activation, however, has the opposite effect. The addition of $NaNO_3$ to the electrospinning solution yields a decrease of the macro-pore space in between the individual fibres in the LCNF network and hence leads to an increase in density. Concomitantly, $NaNO_3$ activation leads to an increase of the nanoporosity within the fibres. Therefore, this activation procedure is beneficial for both volumetric and gravimetric energy/power densities. However, the resulting electrode loadings (maximum 1.03 mg/cm^2) are still below the ones of commercial supercapacitors (8 – 10 mg/cm^2) implying that the void space (macropores) in the LCNF network is still substantial. By measuring the apparent and skeletal density of a nanofibre mat, a shrinking factor, κ, can be introduced as a simple measure for space efficiency of the LCNF network. The apparent density is determined by measuring the weight of a piece of nanofibre mat with known dimensions (e.g. circular disk with known diameter and thickness). The skeletal density can directly be determined via helium pycnometry. With these values the shrinking factor, κ, collapses the apparent macro-structure of the nanofibre network with void space mathematically into a structure without voids while keeping the original aspect ratio. Obviously, the closer κ is to 1 the denser the CNF network. For a CNF network with circular shape it can be derived as follows:

$$\rho(\text{apparent}) \cdot \kappa = \rho(\text{skeletal})$$

$$\frac{m}{\pi \cdot \left(\frac{d \cdot \kappa}{2}\right)^2 \cdot z \cdot \kappa} = \rho(\text{skeletal})$$

$$\frac{m}{\frac{\pi \cdot d^2 \cdot \kappa^2 \cdot z \cdot \kappa}{4}} = \rho(\text{skeletal})$$

$$\frac{m}{\frac{\pi \cdot d^2 \cdot z}{4}} = \rho(\text{skeletal}) \cdot \kappa^3$$

$$\sqrt[3]{\frac{4 \cdot m}{\pi \cdot d^2 \cdot z \cdot \rho(\text{skeletal})}} = \kappa$$

With:

- m = weight of electrode in g
- d = apparent diameter in cm
- z = apparent thickness in cm
- ρ(skeletal) = skeletal density determined by He pycnometry (2.26 g/cm^3) or assumed (density of graphite 2.3 g/cm^3).
- κ = shrinking factor (dimensionless quantity)

Of course, the sole difference between ρ(skeletal) and ρ(apparent) gives a measure of the void space. However, it gives no direct insight into the degree of space efficiency. With κ determined, the diameter and thickness of the collapsed CNF network (without voids) can be recalculated keeping the original aspect ratio (Figure 5-14). This gives a direct measure of the space efficiency.

Table 5-4 Calculation of the shrinking factor and the resulting collapsed geometry for N0 and N50.

	Apparent geometry					**Collapsed geometry**	
Sample	m /mg	d /cm	z /µm	ρ(skeletal) /g/cm^3	**κ**	d /cm	z /µm
N0	0.4004	1.0	60	2.26	**0.335**	0.335	20.1
N50	0.8086	1.0	60	2.26	**0.423**	0.423	25.4

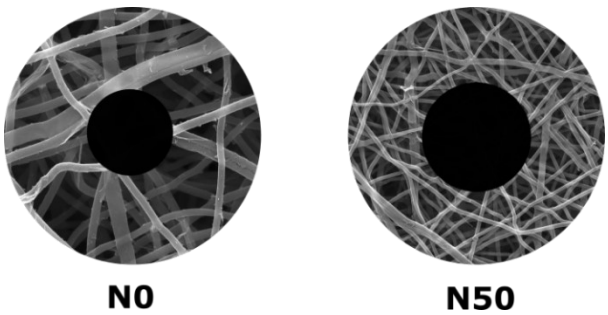

Figure 5-14 Illustration of the effect of densification by the addition of $NaNO_3$ to the electrospinning solution. The black filled circle indicates the collapsed geometry.

For N0, the original (apparent) geometry of a disk with a diameter of 1 cm and a thickness of 60 µm yields a collapsed (void-free) geometry with a diameter of 0.335 cm and a thickness of 20.1 µm. For N50, a collapsed geometry with a diameter of 0.423 cm and a thickness of 25.4 µm was calculated (Table 5-4). The black filled circle in Figure 5-14 indicates the collapsed geometry of both samples. It can be concluded that even if a considerable degree of densification of the fibre network could be achieved by addition of $NaNO_3$ in the electrospinning solution, there is still a substantial void volume incorporated in the CNF network of N50. The main obstacle to implement electrospun fibre electrodes for energy storage applications is their vast amount of void space and hence ultra-low density. This issue will be further addressed towards the end of this thesis.

6. Softwood Kraft lignin-derived carbon nanofibres in nickel-zinc hybrid capacitors

6.1. Introduction

In this chapter, softwood Kraft lignin-derived carbon nanofibres (LCNFs) are used as electrically conductive scaffolds on which nickel hydroxide ($NiOH_2$) and zinc oxide (ZnO) particles were deposited. These composite electrodes were then used to build an aqueous alkaline nickel-zinc hybrid capacitor (NZHC). This energy storage device takes advantage of both the electric double layer capacitance emerging from the (sub-)nanoporosity of the LCNFs and the redox reactions of rechargeable nickel-zinc batteries (RNZBs). RNZBs have gained renewed interest due to their lower cost, higher safety and rate capability compared to the widely used lithium ion batteries (LIBs).[283] The elevated rate capability is caused by the use of an aqueous electrolyte with high ionic conductivity (600 mS/cm) in RNZBs rather than an organic electrolyte used in LIBs (10 mS/cm).[161,284–286] In comparison to other aqueous battery systems, such as lead acid or nickel metal hydride batteries, RNZBs can operate at higher voltages (up to 1.73 V) and hence provide high energy and power densities.[283] The quite high operating voltage in an aqueous medium is a consequence of the high cathodic working potential of Ni and low anodic working potential of Zn and hence high cell potential.[287,288] However, the limited cycle life of RNZBs (less than 500 cycles) arising from changes in morphology and shape of the zinc electrode after repeated charging and discharging impeded their development until quite recently.[289–291] The instability of the zinc anode in aqueous alkaline electrolytes leads to dendrite formation and capacity loss.[289] The issues related to the zinc anode are a consequence of the high solubility of the zinc discharge product (ZnO) in aqueous alkaline electrolytes ($KOH_{(aq)}$).[289,292,293] The ZnO anode material dissolves in the KOH solution to form a soluble zincate ($Zn(OH)_4^{2-}$) ion. During the charging process the zincate ion is then reduced to zinc metal:

1) $$Zn + 4\,OH^- \underset{\text{charging}}{\overset{\text{discharging}}{\rightleftharpoons}} Zn(OH)_4^{2-} + 2e^-$$

2) $Zn(OH)_4^{2-} \underset{\text{charging}}{\overset{\text{discharging}}{\rightleftharpoons}} ZnO + 2OH^- + H_2O$

The cathode reaction is described as follows:

3) $2NiOOH + 2H_2O + 2e^- \underset{\text{charging}}{\overset{\text{discharging}}{\rightleftharpoons}} 2Ni(OH)_2 + 2OH^-$

Therefore, the overall cell reaction can be described as:

4) $Zn + 2NiOOH + H_2O \underset{\text{charging}}{\overset{\text{discharging}}{\rightleftharpoons}} ZnO + 2Ni(OH)_2$

In order to suppress the dissolution and shape change of the zinc anode during cycling, various salts, such as fluorides (KF) and carbonates (K_2CO_3), were added to the KOH based electrolyte so that the concentration of OH^- ions in solution could be reduced.[294,295] Recently, it was shown that a 3D porous ('sponge'-like) morphology of the zinc electrode instead of the commonly used dense sintered zinc electrode improves the cycling performance tremendously.[296] Moreover, it was demonstrated that a dense zinc electrode can be stabilized by preparing zinc-carbon composites.[289] For instance, as shown by Frackowiack in 1995, the addition of 5% acetylene black significantly inhibits dissolution of a sintered pellet of zinc. Additionally, the oxidation products remain in the interior of the electrode owing to the adsorbent properties of acetylene black.[297] However, the achieved cycle number was still far below 500 cycles.[297] Combining both the merits of adding carbon to the zinc anode and a 3D porous ('sponge'-like) electrode morphology can be achieved by depositing ZnO particles on electrospun carbon nanofibres. The use of ZnO (discharge product) as sole active material instead of metallic Zn was shown to improve the cycle life further because ZnO can be regarded as a buffer for the loss of active material via the zincate ion formation during repeated cycling.[298] Several authors prepared such carbon-ZnO or carbon-$Ni(OH)_2$ composites via electrodeposition on commercial carbon fibre felts which are nowadays manufactured from polyacrylonitrile and hence costly.[299–302] Nanostructured carbons, such as carbon nanotubes which are energy – intensive

to produce were also used as substrates.[303] In the work at hand, softwood Kraft lignin-derived carbon nanofibre (LCNF) networks are used as electrically conductive scaffolds. The highly porous micro-morphology of the LCNF network is of great use to accommodate the redox active material without loss of its accessibility as it provides a three-dimensional and highly connected pore structure which was visualized by nano X-ray CT in chapter 5. Moreover, the deposition via precipitation based on the hydrolysis of urea was carried out rather than electrodeposition. The precipitation of metal salts from aqueous solutions via the hydrolysis of urea at elevated temperatures has been described as early as 1937 by Willard and Tang.[304] The slow hydrolysis of urea yields ammonia and carbon dioxide which leads to a gradual increase of the pH controlling the precipitation of hydroxides from the solution.[304,305] Therefore, the homogeneous alkalization in solution results in a more homogeneous coverage of the fibres compared to electrodeposition which physically deposits the metal precursor on the fibres via coulombic attraction. The carbon nanofibres used as substrates for the deposition were prepared as described in chapter 3 of this thesis. The preparation of the ZnO-LCNF and $Ni(OH)_2$-LCNF composites is described in the following section.

6.2. Preparation of $Ni(OH)_2$- and ZnO-LCNFs

For the deposition of $Ni(OH)_2$ or ZnO on the LCNF substrates, 10 ml of a 0.1 M solution with either nickel chloride hexahydrate ($NiCl_2 \cdot 6H_2O$) or zinc acetate dihydrate ($Zn(CH_3COO)_2 \cdot 2H_2O$) was prepared and heated to 90 °C and 70 °C, respectively. When the respective temperature was reached, 2.924 ml of a 9 M $urea_{(aq)}$ solution were added (acting as a precipitation agent) and the solution was shaken for one minute. Afterwards, the SKL-derived LCNFs stabilized at 250 °C and carbonized at 700 °C were added to the solution. In order to ensure complete wetting of the LCNF network and to allow the solution to penetrate the carbon nanofibre network fully, the vial filled with the solution and the LCNFs was sealed and evacuated. After several (typically three) evacuation and backfill cycles, the air trapped in the LCNF

network could be removed and instead be filled with the respective precursor solution. After this, the LCNF mat was fully immersed into the solution. In the case of the $Ni(OH)_2$ deposition, the LCNF mat was left for 55 min at 90 °C in solution. The $Zn(OH)_2$ deposition proceeded for 40 min at 90 °C. After the deposition, the samples were removed from the vial and washed with deionized water in a beaker to terminate the precipitation reaction by the resulting cooling and dilution and in order to clean the sample from any residual salts. Finally, the $Ni(OH)_2$-LCNFs were dried at 70 °C for one hour and the $Zn(OH)_2$-LCNFs were annealed at 300 °C for one hour to convert the deposited zinc hydroxide to ZnO.

6.3. Results and discussion

The morphology of the pristine, Ni-LCNFs ($Ni(OH)_2$ deposited on LCNFs) and the Zn-LCNFs (ZnO deposited on LCNFs) are shown in Figure 6-1a, b and c, respectively.

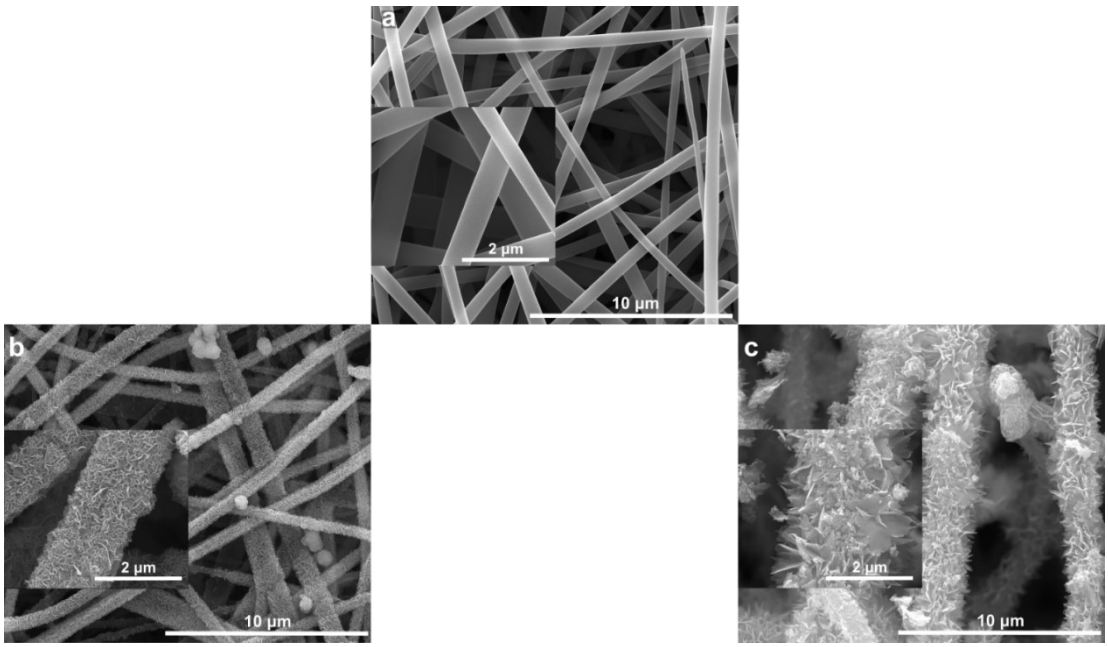

Figure 6-1 SEM micrographs of the pristine LCNFs (a), the Ni-LCNFs (b), and the Zn-LCNFs (after calcination) (c).

It can be observed that the $Ni(OH)_2$ (Figure 6-1b) and the ZnO (Figure 6-1c) particles could be deposited homogeneously on the pristine LCNFs (Figure 6-1a) by the precipitation method applied. The size of the ZnO particles is considerably larger than the one of the $Ni(OH)_2$ depositions. This can be attributed to the additional heat treatment at 300 °C that was used to transform

$Zn(OH)_2$ to ZnO which also leads to a growth of the particles. In addition, the solubility of the two metal precursor salts is different, where $NiCl_2 \cdot 6H_2O$ has a much higher solubility of 2540 g/l than $Zn(CH_3COO)_2 \cdot 2H_2O$ (430 g/l).[306,307] Since both metal precursor solutions were prepared and treated in a similar way, it is obvious that the state of (over-) saturation and thus precipitation is reached much earlier in the case of zinc acetate dihydrate. Therefore, both particle and crystallite growth proceed over a longer period yielding larger particles and crystallites of Zn-LCNFs. The TEM micrographs presented in Figure 6-2 confirm this reasoning.

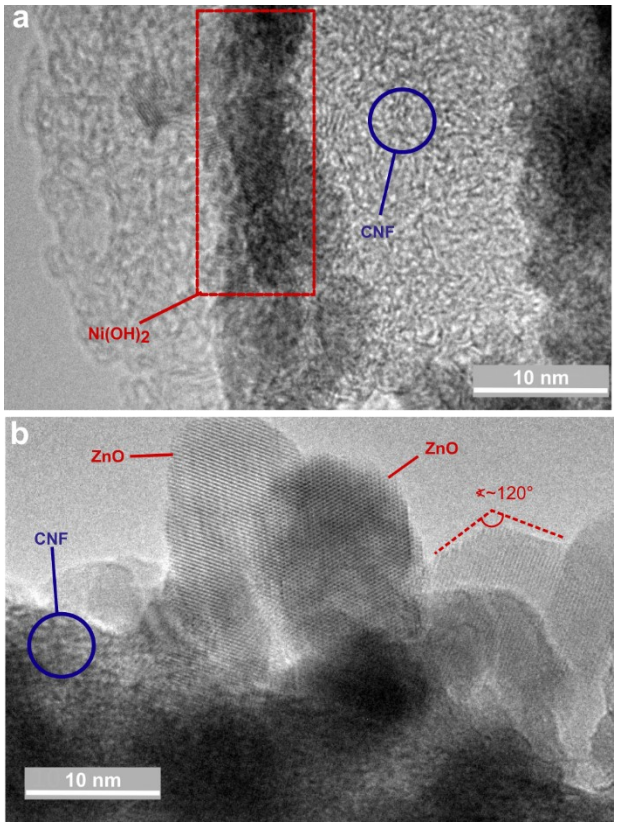

Figure 6-2 TEM micrographs of a Ni-LCNF (a) and a Zn-LCNF (b).

The polycrystalline precipitates of $Ni(OH)_2$ on the Ni-LCNFs (Figure 6-2a) are considerably smaller than the large polycrystalline ZnO particles on the Zn-LCNFs (Figure 6-2b). In the case of the Zn-LCNF, even the hexagonal crystal morphology characteristic of the hexagonal wurtzite structure of ZnO was formed (Figure 6-2b) implying a high degree of crystallinity. The difference in crystallite size is also apparent in the diffractograms based on the width of the

reflections arising from $Ni(OH)_2$ and ZnO. The full width at half maximum (FWHM) of the reflections in a diffractogram is dependent on the average crystallite size.

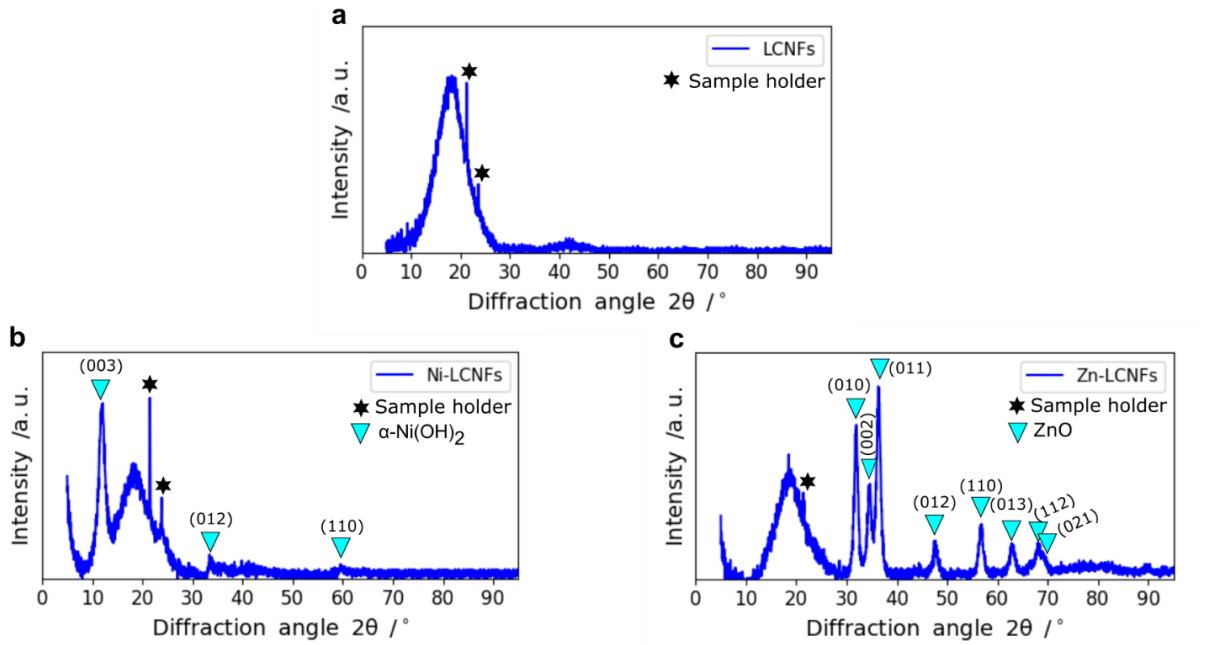

Figure 6-3 Diffractograms of the pristine LCNFs (a), Ni-LCNFs (b) and Zn-LCNFs (c).

Hence, the average crystallite size can be estimated by using the Scherrer equation:[308]

$$L = \frac{K \cdot \lambda}{FWHM \cdot \cos(\theta)}$$

L is the average crystallite size, K is the formfactor (0.9), λ is the wavelength (CuKα = 0.15406 nm), FWHM is the full width at half maximum and θ the diffraction angle. The pristine LCNFs show a broad peak between 10 and 25 ° and a very small increase in intensity at around 40 °, which is indicative of disordered carbon consisting of few-layer graphene or disordered graphitic domains. The non-crystalline, disordered carbon structure is a direct consequence of the high degree of disorder of the amorphous lignin polymer. The Ni- and Zn-LCNFs show peaks of crystalline phases superimposed on the signals related to the LCNFs. The three reflections in the diffractogram of the Ni-LCNFs can be assigned to the α-phase of $Ni(OH)_2$ which is closely related to the more common/stable β-phase of $Ni(OH)_2$.[305] It was reported before that

the presence of urea consistently yields the α-phase instead of the β-phase due to the intercalation of its decomposition products (e.g. OCN^- and CO_3^{2-} ions) into the $Ni(OH)_2$ interlayers.[309,310] The average crystallite size derived from the well-resolved (003) reflection at 11.924 ° is 5.9 nm (Table 6-1). The diffractogram of Zn-LCNFs indicates that the hexagonal wurtzite phase of ZnO was formed. The average crystallite size determined from the (010) reflection at 31.896 ° is 10.2 nm. The difference in crystallite size of Ni- and Zn-LCNFs is consistent with the TEM imaging (Figure 6-2).

Table 6-1 Values used for the calculation of the average crystallite sizes derived from XRD.

Material	Position 2θ /°	FWHM /°	L /nm
Ni-LCNFs	11.924	1.343	5.9
Zn-LCNFs	31.896	0.877	10.2

Energy-dispersive X-ray (EDX) spectroscopic measurements were carried out on the pristine LCNFs, Ni-LCNFs and Zn-LCNFs in order to determine the elemental composition. The average of three measurements per sample are shown in Table 6-2. From the atomic ratios of the metal (Ni, Zn) and oxygen (O), it is clear that the LCNFs were oxidized in the process of depositing $Ni(OH)_2$ and ZnO. Since the Ni/O-ratio determined by EDX is 0.31, but its theoretical value is 0.50, as apparent from the molar ratios in the molecular formula. A similar discrepancy of the Zn/O-ratio between the EDX results (0.55) and the molecular formula (1.0) was found for ZnO.

Table 6-2 Elemental composition determined by EDX (average value of three measurements per sample).

Element	pristine LCNF	Ni-LCNF	Zn-LCNF
C /at%	94.1	78.4	33.4
O /at%	5.9	16.5	43.1
Ni /at%	0.0	5.1	0.0
Zn /at%	0.0	0.0	23.5
Total /at%	100.0	100.0	100.0

Therefore, it can be assumed that the LCNFs were oxidized as the initial oxygen content of the pristine LCNFs of 5.9 at% does not account for the differences between theoretical and measured stoichiometries of the Ni and Zn-LCNFs. Furthermore, X-ray photoelectron spectra of the Ni-LCNFs and Zn-LCNFs were measured, which can be seen in Figure 6-4.

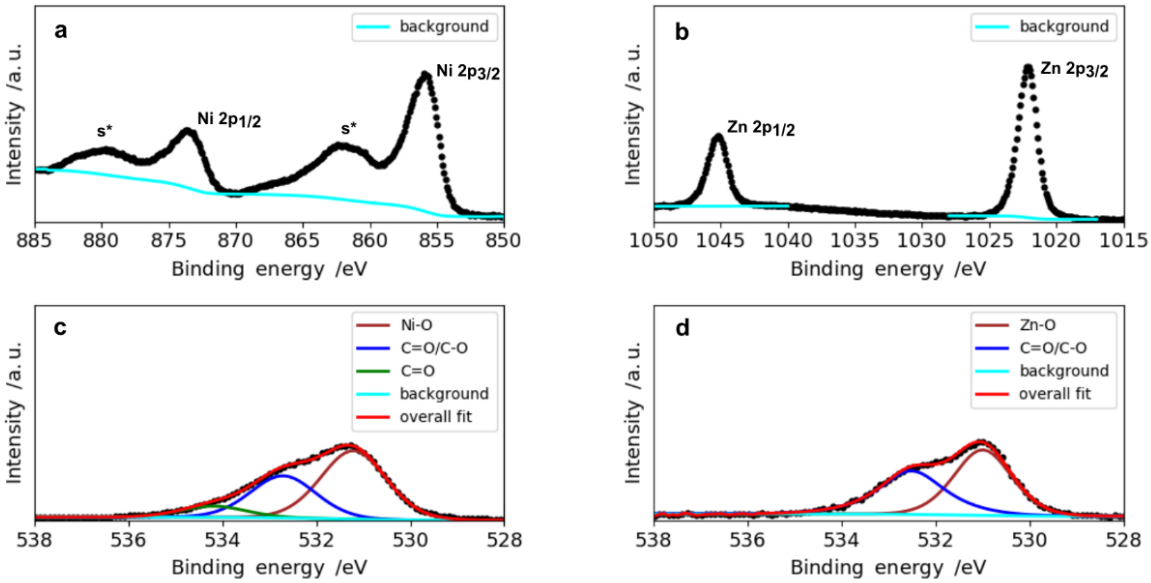

Figure 6-4 XPS spectra: Ni 2p of Ni-LCNFs, s* indicates the satellite peaks of Ni $2p_{1/2}$ and Ni $2p_{3/2}$ (a), Zn 2p spectrum of Zn-LCNFs (b) and the O1s peak of Ni-LCNFs (c) and Zn-LCNFs (d).

Even if there is a considerable overlap of the oxygen bonded to carbon and the oxygen bonded to the metal (Ni-O or Zn-O), it has been suggested in the literature that the majority of the oxygen content arising from Ni-O and Zn-O can be assigned to the intensity at approximately 531 eV and the intensity at higher binding energies to C=O/C-O. However, there might be a considerable overlap giving rise to uncertainties in deriving the contributions of metal bonded oxygen and carbon bonded oxygen to the total intensity of the O1s peak.[311] Based on the O1s peak deconvolutions, shown in Figure 6-4a and b, 56 at% of the total oxygen content determined by XPS can be assigned to Ni-O in the Ni-LCNF and 55 at% can be attributed to Zn-O in the Zn-LCNFs. Combining this data with the oxygen content determined by EDX (Table 6-2) yields improved metal/carbon ratios: Ni(5.1 at%)/O(16.5 at%·0.56 = 9.24 at%) = 0.55 (theoretical: 0.50) and Zn(23.5 at%)/O(43.1 at%·0.55 = 23.7 at%) = 0.99 (theoretical: 1.0).

The influence of the deposited particles on the (sub-)nanoporosity of the LCNFs was investigated by N_2 and CO_2 sorption measurements shown in Figure 6-5.

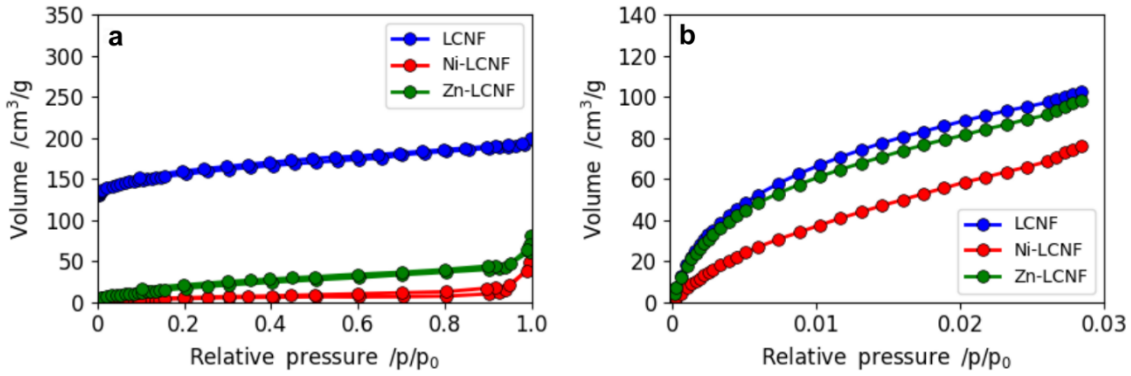

Figure 6-5 N_2 sorption isotherms (a) and CO_2 adsorption isotherms (b) of the pristine LCNFs, the Ni- and the Zn-LCNFs.

Interestingly, the influence of the deposition of particles on the mesoporositiy (pore diameter: 2 – 50 nm) and macroporosity (>50 nm) determined by N_2 sorption and the (sub-)nanoporosity measured by CO_2 sorption (<2 nm) is different. The N_2 isotherms indicate a drastic drop of adsorbed gas for both Ni- and Zn-LCNFs compared to the pristine LCNFs (Figure 6-5a). The resulting BET (Brunauer, Emmett and Teller) surface area determined for the Zn-LCNFs (74 m^2/g) is slightly larger than the one determined for the Ni-LCNFs (24 m^2/g). However, both are very low compared to the one of the pristine LCNFs (591 m^2/g). This suggests that the pores are filled and/or pore entrances are blocked by the metal oxide/hydroxide particles on the LCNFs. However, the (sub-)nanometer pores were not filled by the particles as the CO_2 adsorption isotherms indicate. From the CO_2 adsorption isotherms which probes solely the (sub-)nanometer pores due to the different measurement conditions (rel. pressure and temperature), it is apparent that the drop in volume of adsorbed gas upon metal particle deposition is much less substantial for the Zn-LCNFs than for the Ni-LCNFs. This might be explained by the crystallite size and the resulting particle size that were shown to be much smaller for the Ni-LCNFs than for the Zn-LCNFs. Therefore, the $Ni(OH)_2$ particles can fill small nanopores much more effi-

ciently than the bigger ZnO particles (>5 nm). Consequently, the DFT surface areas of the pristine sample (1131 m^2/g) and Zn-LCNFs (1110 m^2/g) are similar and the one determined for the Ni-LCNFs considerably smaller (743 m^2/g).

After the thorough characterization of the composite electrodes, electrochemical tests were performed, whereby the Ni-LCNFs served as the cathode and the Zn-LCNFs as the anode operating with 1 M $KOH_{(aq)}$ as electrolyte. The loadings of $Ni(OH)_2$ and ZnO were each approximately 10 wt%. Hence, the final device assembled herein will not be called nickel-zinc battery, but nickel-zinc hybrid capacitor (NZHC), as the electric double layer charge storage contribution is still present to a substantial extent. This is discussed in more detail further below. The cyclic voltammograms indicate the difference between a symmetric supercapacitor assembled with the pristine LCNFs (LCNF-SC) and the NZHC composed of Ni- and Zn-LCNF electrodes operating in the same electrolyte (Figure 6-6a).

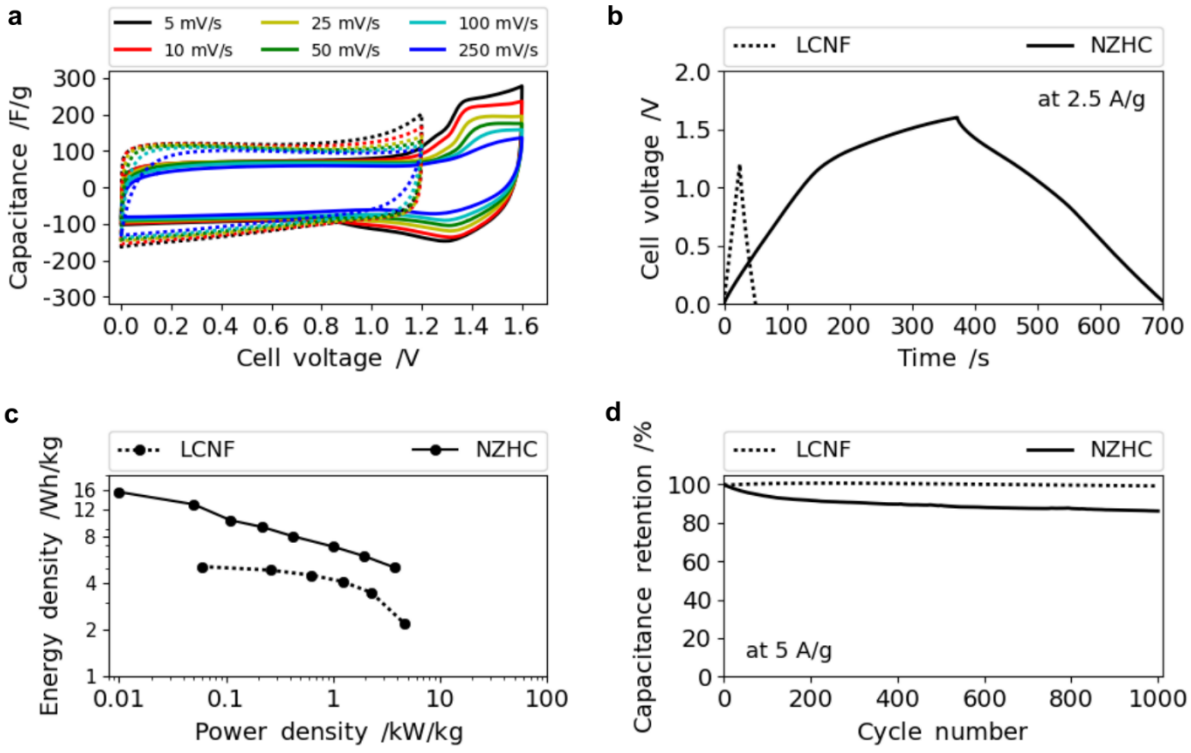

Figure 6-6 Cyclic voltammograms at various scan rates for a SC composed of pristine LCNFs (dashed line) and a NZHC (solid lines) (a), charge-discharge traces of a SC assembled with pristine LCNF electrodes (dashed) and a NZHC (solid line) (b), Ragone plot of a LCNF-SC and a NZHC (c) and cyclability of both a LCNF-SC and a NZHC at 5 A/g (d).

The gravimetric units are normalized based on the total mass of the electrodes (LCNFs + redox active materials). Compared to the LCNF-SC, the NZHC can operate at a higher voltage (cut-off 1.6 V) and it shows increased charge storage capacity due to the redox activity of the $Ni^{II/III}$ and $Zn^{0/II}$ redox pairs. In addition, it is apparent that a considerable fraction of the initial double layer capacitance arising from the (sub-)nanoporosity of the pristine LCNFs is retained between 0 and 1.1 V, which is consistent with the gas sorption data (Figure 6-5). This can also be observed in Figure 6-6b, where the charge-discharge profiles of the LCNF-SC and the NZHC at a current density of 2.5 A/g are shown. Up to 1.1 V, a linear change of the voltage with time can be observed in the charge-discharge profile. This is characteristic for electric double layer capacitors. Above 1.1 V, a curved plateau region is indicative of the redox activity of $Ni^{II/III}$ and $Zn^{0/II}$. The contribution of the electric double layer charge storage (Q(C)) and the Ni/Zn redox mechanism (Q(Ni/Zn)) are dependent on the scan rate as shown in Figure 6-7. Herein, the voltammograms of the NZHC at a slow scan rate of 5 mV/s (Figure 6-7a) and a high scan rate of 250 mV/s (Figure 6-7b) are shown indicating various contributions to the total capacity

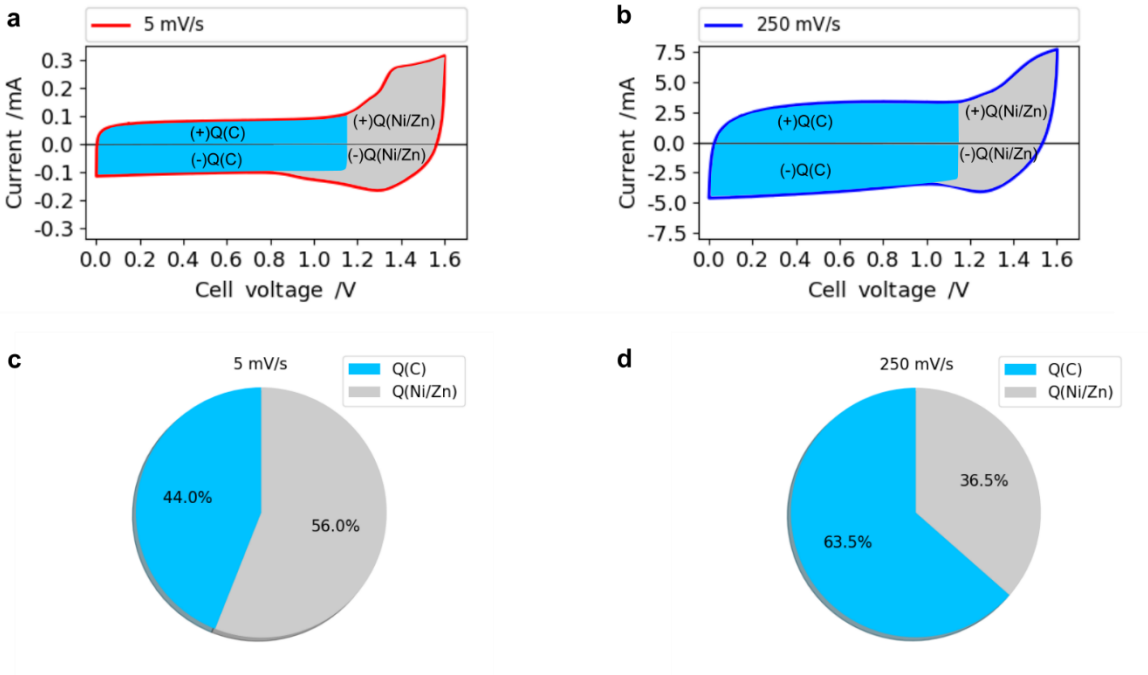

Figure 6-7 Voltammograms of the NZHC at 5 mV/s (a) and 250 mV/s (b) with the various contributions to the total capacity and the percentages of the charge storage arising from the porous LCNFs (Q(C)) and the nickel zinc redox reactions (Q(Ni/Zn)) at 5 mV/s (c) and 250 mV/s (d).

enclosed by the voltammograms. It is obvious that the double layer capacity contribution (Q(C)) increases with increasing scan rate and the one of the Ni/Zn redox charge mechanism (Q(Ni/Zn)) decreases. The exact values determined by integrating the areas attributed to the different charge storage mechanisms are presented in Table 6-3. It needs to be mentioned that there is an uncertainty as to where exactly the area of the electric double layer contribution terminates and where the one of the Ni/Zn redox activity begins. This cannot be fully elucidated as electric double layer and redox mechanism always overlap.

Table 6-3 Charge (Q) and charge fractions (Q fractions) derived from dividing and integrating the area enclosed by the voltammograms.

	5 mV/s		250 mV/s	
Contribution	Q /mC	Q fraction /%	Q /mC	Q fraction /%
(+)Q(C)	15.6	20.9	13.5	29.2
(-)Q(C)	17.2	23.1	15.9	34.1
Total(C)	**32.8**	**44.0**	**29.4**	**63.5**
(+)Q(Ni/Zn)	23.6	31.7	9.51	20.6
(-)Q(Ni/Zn)	18.1	24.3	7.35	15.9
Total(Ni/Zn)	**41.7**	**56.0**	**16.86**	**36.5**
Total	74.5	100.0	46.26	100.0

However, the area enclosed above 1.1 V was fully assigned to the Ni/Zn redox charge storage mechanism as this region would not be viable without the Ni/Zn mechanism. At 5 mV/s, 56 % of the total charge stored can be assigned to the Ni/Zn charge storage mechanism and the residual 44% to the electric double layer mechanism (Table 6-3). At 250 mV/s, only 36.5% of the total charge stored arises from the Ni/Zn redox reaction and 63.5% from the electric double mechanism. Redox reactions are charge transfer reactions at the interface of the electrode and electrolyte and hence diffusion controlled/limited. In addition, they involve bond breaking and new bond formation in the bulk electrode material which is highly rate dependent. Therefore, the charge storage via the redox reactions is drastically reduced at such high scan rates. The electric double layer mechanism is based on physical ad-/desorption on electrically polarized surfaces and hence a much faster process because no charge transfer and no bulk chemical

reactions occur. The NZHC takes advantage of both mechanisms. This translates into an increased energy and power density compared to the pristine LCNFs as shown in the Ragone plot (Figure 6-6c). At low power densities of 0.01 – 0.1 kW/kg, the energy density of the NZHC is four (16 Wh/kg) to three times (12 Wh/kg) the one of the LCNF-SC. Between 0.1 and 1 kW/kg, the energy density of the NZHC still shows a two-fold increase compared to the LCNF-SC. Even at a high power density of 5 kW/kg, the energy density of the NZHC is still greater than the one of the LCNF-SC. In Figure 6-6d, the capacitance retention upon repeated charging and discharging over 1000 cycles can be seen. Here, the LCNF-SC outperforms the NZHC, which could be expected as the pure electric double layer charge storage mechanism is a highly reversible process compared to the bulk chemical redox reactions taking place in the NZHC. Nonetheless, the NZHC retains 86% of the initial capacity after 1000 cycles of repeated charging and discharging (Figure 6-6d) which is promising. The coulombic efficiency shown for the first 250 cycles of a fresh cell in Figure 6-8a confirms that irreversible side reactions take place during cell operation as it never reaches 100% (fully reversible).

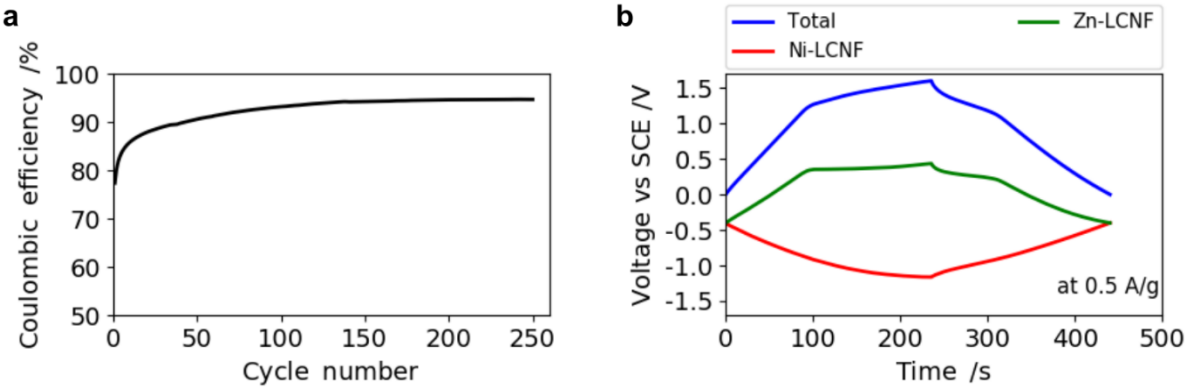

Figure 6-8 Coulombic efficiency shown for the first 250 cycles of a fresh (un-cycled) NZHC cell (a) and the voltage-time profiles measured versus a saturated calomel reference electrode (SCE) for the anode (Zn-LCNF) and the cathode (Ni-LCNF) and the total cell voltage (b).

After the activation (up to 100 cycles), the coulombic efficiency stays constant at 95% (at 5 A/g).

In order to gain more insights into the cause of the decreased coulombic efficiency, a third reference electrode was inserted into the NZHC cell. This allows for the measurement of the voltage-time profiles of the individual electrodes independent of each other as both electrodes are referenced to the unpolarizable reference electrode (saturated calomel electrode, SCE). This is not possible without a reference electrode as then only the total cell voltage can be measured. At 0.5 A/g, the coulombic efficiency is 89% which is even lower than at 5 A/g (95%) as the redox reactions are generally more prominent at low charge-discharge rates due to diffusion limitations at high rates that limit the extent to which the reversible and irreversible reactions take place. Looking at the charge and discharge traces of the Ni-LCNF and the Zn-LCNF (Figure 6-8b), it is obvious that the irreversible side reactions take place at the Zn-LCNF electrode as the charge-discharge profile is asymmetric (charging time is longer than discharging time). This might arise from the irreversible dissolution of the ZnO into the electrolyte during charging by the mechanism described in the introduction of this chapter. The charge-discharge profile of the Ni-LCNF is symmetric and shows almost identical charging and discharging time. In order to further stabilize the Zn-LCNF electrode, it will be necessary to increase the loading of ZnO relative to the loading of the Ni-LCNF electrode in order to lower the depth of discharge on the Zn-LCNF electrode and hence decrease the loss of material during repeated charging and discharging.[289]

6.4. Conclusion

Softwood Kraft lignin-derived carbon nanofibres were used as electrically conductive scaffolds on which nickel hydroxide ($NiOH_2$) and zinc oxide (ZnO) particles were deposited via urea assisted precipitation. These composite electrodes were then used to build an aqueous alkaline nickel-zinc hybrid capacitor. The NZHC shows improved energy and power density compared to the pristine LCNF-SC. At low power densities of 0.01 – 0.1 kW/kg, the energy density of the NZHC is 16 and 12 Wh/kg which is a four to three-fold increase compared to the pristine

LCNF-SC. Between 0.1 and 1 kW/kg, the energy density of the NZHC still shows a two-fold increase compared to the LCNF-SC. Since the loading of redox active species was kept quite low here (10 wt%), there is still a considerable contribution of the electric double layer charge storage mechanism to the overall capacity. In the future, it needs to be focused on optimizing the loadings of the redox active material. The ratio of ZnO to $Ni(OH)_2$ in the NZHC needs to be optimized so that there is two to three times more ZnO in the NZHC cell than $Ni(OH)_2$ in order to lower the depth of discharge of the Zn-LCNF electrode and hence decrease the loss of material during repeated charging and discharging.[289] Furthermore, the overall loadings of ZnO and $Ni(OH)_2$ need to be increased so that a higher overall energy density can be reached (up to 50 Wh/kg). Finally, the addition of salts to decrease the solubility of ZnO in the aqueous alkaline electrolyte should be considered.[295] All in all, the approach to use LCNFs as electrically conductive scaffolds to deposit redox active species on the LCNFs via precipitation is promising and will widen the scope of application of LCNFs considerably.

7. Free-standing electrode stacks

7.1. Introduction

The advantage of creating free-standing LCNF electrodes consisting of randomly entangled nanofibres via electrospinning over traditional carbon powder electrodes is demonstrated herein. The electrodes in commercially available supercapacitors and batteries are thin coatings of active material (e.g. activated carbon) on metallic current collectors.[199] This requires the surface of the current collector to be etched and modified by a coating with conductive carbon in order to improve the adhesion of the active material.[159] Furthermore, the active material is mixed with inactive materials, such as a binder and a conductive additive, to form a slurry that can be coated with a controlled thickness, rolled and dried to form an electrode. The thickness of the electrodes in commercial devices ranges from 100 to 300 μm.[154,199] The density of the coated films ranges from 0.7 to more than 0.9 g/cm^3 and mass loadings of 8 to 10 mg/cm^2 per electrode.[154,159] As outlined in chapter 4, the low density of activated LCNFs prevents them from being used as alternative to the above-mentioned film coated electrodes because the attained loading is very low (~0.78 mg/cm^2). As described in chapter 5, the densification of the fibre network is possible by addition of salts in the electrospinning solution. However, the maximum achieved electrode loading (1.03 mg/cm^2) is still not sufficient when compared to the loadings of commercial electrodes. Manufacturing lignin-based nanofibres via electrospinning results in planar networks of randomly entangled LCNFs covering a large area (10s of centimeters) with a layer thickness of about 60 μm (0.006 centimeters). Therefore, another strategy to increase the mass loading per electrode pursued herein was to stack several layers of LCNFs on top of each other rather than to optimize further the in-plane density (parallel to the fibre axis). The unique macro- and micro- morphology of the nanofibre network gives rise to two properties that are of great importance for the successful stacking of several LCNF layers on top of each other:

1) The resulting nanofibre networks are self-standing as produced.
2) The resulting nanofibre networks are compressible in the z-direction (perpendicular to the fibre axis).

Property 1) is the prerequisite for the efficient stacking as without the self-/free-standing feature, the active material (in form of carbon powder) would need to be immobilized by a binder together with the addition of a conductive additive. Hence, stacking of several layers would add up to 20 wt% of inactive material (binder and conductive additive) with each new layer. In the case of free-standing LNCF networks, each layer adds exclusively active material to the electrode. The compressibility mentioned as property 2) is also a unique feature arising from the LCNF network. Based on this feature, it is clear that each layer of about 60 µm thickness added to the electrode will not contribute 100% of its thickness to the electrode stack. The preparation and the electrochemical characterization of the electrode stacks are described in the following two sections.

7.2. Electrode stack preparation

All stack cells were assembled with the hardwood Kraft lignin-derived CNFs stabilized at 310 °C and carbonized at 800 °C as described in chapter 3. A sketch of a symmetric supercapacitor Swagelok-type cell assembled with a single layer electrode and a LCNF stack electrode can be seen in Figure 7-2a. A stack of eleven layers resulted in a stack thickness of 460 µm. Assuming a constant single layer thickness of 60 µm with a uniform fibre density, a stack of eleven layers would result in a stack thickness of 660 µm, if the material was incompressible. There might be an error associated with this reasoning by assuming a uniform fibre density of all layers which is challenging to achieve by the electrospinning technique which produces randomly entangled nanofibres. However, as shown in Figure 7-1c, the overall electrode density indeed increases by about 83% from a single layer electrode (0.12 g/cm^3) to the largest electrode stack (0.22 g/cm^3). The densities and thicknesses were measured in the dry state before

cell assembly, as the pressure in the Swagelok-type cell could not be controlled precisely. Hence, the comparability of the thicknesses of electrodes with different loadings would be flawed after the electrochemical measurements.

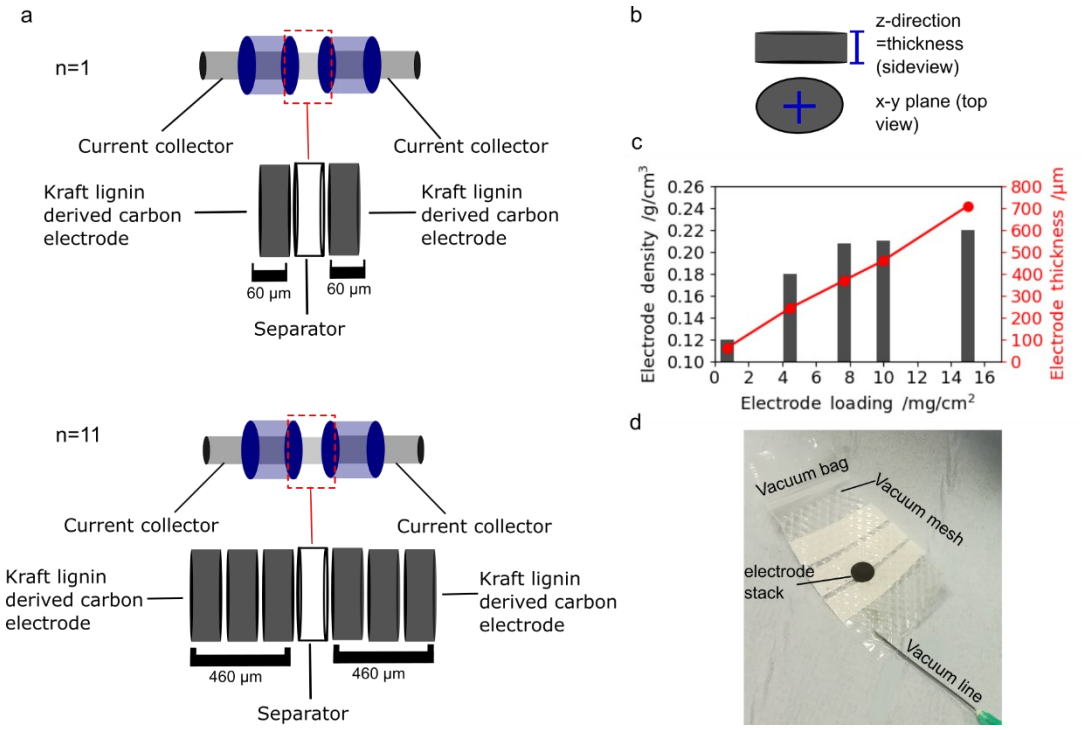

Figure 7-1 Swagelok-type cell illustrating a single (n=1) layer electrode cell (top) and an electrode stack cell (n=11) (a), illustration of directions/orientations of a single layer fibre network (b), relation of electrode density, thickness and mass loading (c) and photograph of the experimental set-up for vacuum infiltration of the electrode stacks (d).

However, it could be noted that, after vacuum infiltration and after cell disassembly, the stacks were considerably thinner (by about 30%). This can be assigned to the compression by the vacuum and by the pressure exerted during the electrochemical measurement. The set-up with which the electrode stacks were vacuum infiltrated with the electrolyte solution (6 M $KOH_{(aq)}$) can be seen in Figure 7-1d.

7.3. Electrochemical characterization

After the electrode preparation, the electrode stacks were tested in the same Swagelok-type cells as the single layer electrodes that were the subject of the previous chapters. The rise in equivalent series resistance derived from direct current measurements (ESR_{DC}) with increasing

electrode thickness/loading was determined by galvanostatic charge discharge (GCD) measurements at a constant current density of 25 A/g. The ESR_{DC} can be determined from the IR drop (V) of the charge-discharge traces indicated in Figure 7-2a for 10 and 15 mg/cm^2 electrode stacks and the applied current (A):

$$ESR_{DC} = \frac{\text{IR drop}}{I}$$

Where ESR_{DC} = equivalent series resistance derived from a constant current measurement [Ω], IR drop = voltage drop at the beginning of charging and discharging cycle [V], I = current [A]

It is obvious that with increasing loading and electrode thickness the ESR_{DC} rises. However, the values for the ESR_{DC} compare well with the ones of commercial devices which range from 20 to 700 mΩ depending on supplier and cell type.[162,312]

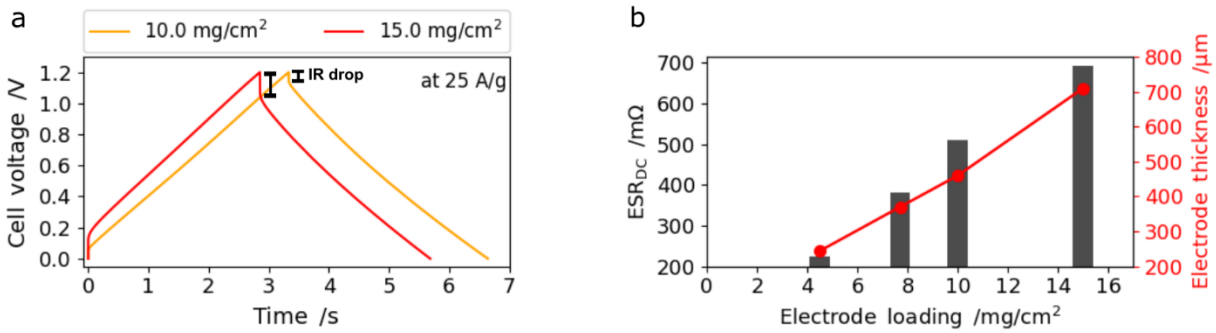

Figure 7-2 Charge-discharge traces of an electrode stack with 10 and 15 mg/cm^2 loading (a) and the determined ESR_{DC} and the electrode thicknesses of all electrode stacks (b).

Only at a very high loading of 15 mg/cm^2 the ESR_{DC} is close to 700 mΩ (Table 7-1). In Figure 7-3, the cyclic voltammograms of the electrode stacks with various loadings are shown.

Table 7-1 Overview of the electrode loadings, thicknesses, IR drops and currents and the resulting ESR_{Dc} for all electrodes determined at 25 A/g.

Loading /mg/cm^2	Thickness /µm	IR drop /V	Current /A	ESR_{DC} /mΩ
4.5	244	0.0120	0.0536	223.9
7.7	370	0.0350	0.0918	381.3
10.0	460	0.0583	0.1142	510.5
15.0	710	0.1271	0.1831	694.2

At low and medium scan rates of 5 and 50 mV/s, all electrodes show the typical rectangular shape, where the electrode stacks with high loadings show a higher degree of irreversibility close to 1.2 V at very low scan rates. This might be due to electrolyte decomposition close to 1.2 V which is not apparent at 50 mV/s. However, in low-rate applications, the operating voltage needs to be limited to 1 V. At high (500 mV/s) and very high scan rates (1 V/s), all voltammograms are slightly deformed, but up to 10 mg/cm^2, the electrode stacks are still capacitive as indicated by the large area enclosed by the voltammograms. However, the electrode stack with the maximum loading of 15 mg/cm^2 shows a considerably decreased capacitance compared to lower scan rates.

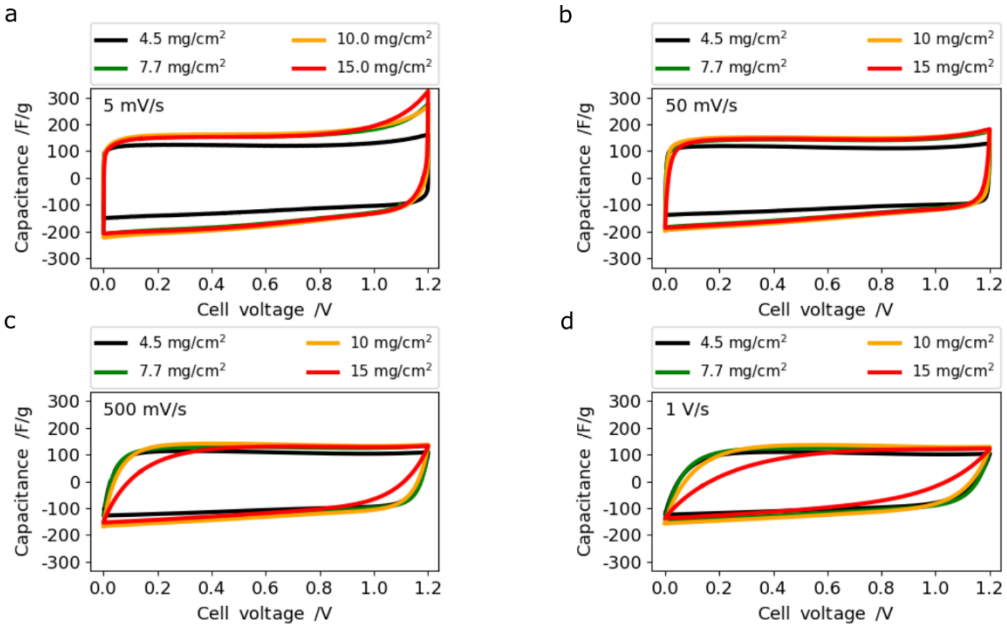

Figure 7-3 Voltammograms at 5 (a), 50 (b), 500 mV/s (c), and 1 V/s (d) of all four samples measured in 6 M $KOH_{(aq)}$.

The gravimetric and areal capacitances derived from GCD measurements are shown as a function of the applied current density in Figure 7-4a and b. With increasing electrode loadings, the gravimetric capacitance rises. However, the electrode stack with the maximum loading of 15 mg/cm^2 shows a decreased capacitance at high rates which was also shown by cyclic voltammetry (Figure 7-3d). The trend of increasing performance with rising electrode loading is contrary to the results published on film coated electrodes which usually report a considerable

drop of capacitance with increased mass loadings.[143,313] The different trend can be explained by the unique macro- and micro- morphology of the LCNF network which is highly accessible to the electrolyte. The vacuum infiltration technique applied here takes advantage of the open structure by filling it effectively with the electrolyte. As the stack thickness grows, the spreading of the vacuum in the nanofibre network is enhanced and hence the pore wetting improved. Consequently, the capacitive performance can be slightly improved and a drop in capacitance with increasing loading can be avoided. The areal capacitance (Figure 7-4b) shows an even more distinct difference between the samples as the areal capacitance scales solely with the amount of active material in the cell neglecting the weight and volume differences. The Ragone plots in gravimetric and volumetric measures shown in Figure 7-4c and d reveal that the power density /rate capability decreases as the electrode loading increases. This can be explained by the increase in ESR_{DC} shown in Figure 7-2b.

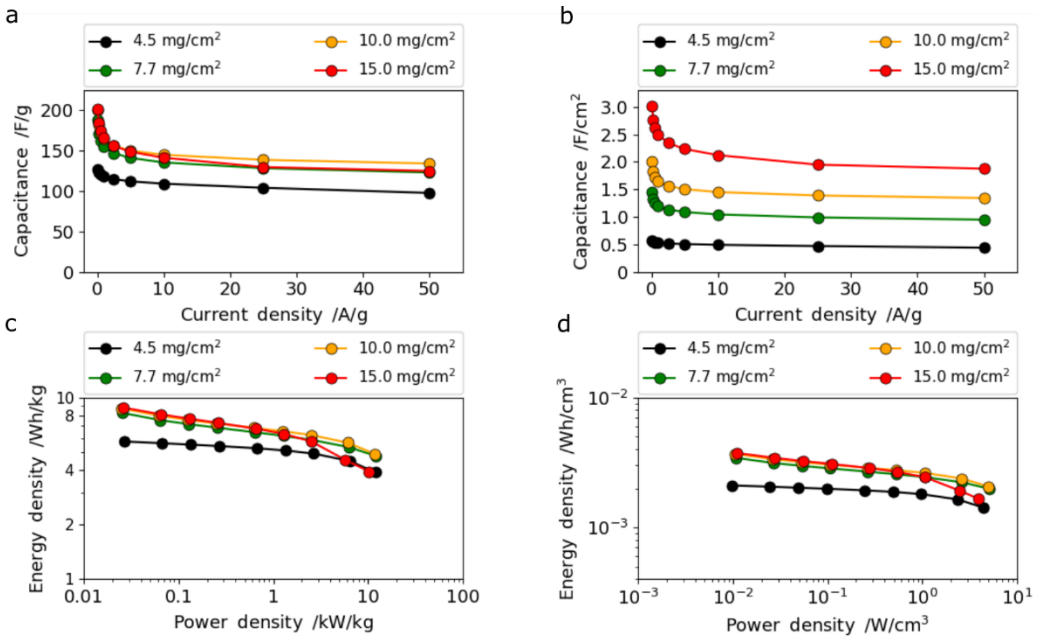

Figure 7-4 Dependence of the specific gravimetric capacitance on the current density for all four samples (a), dependence of the specific areal capacitance on the current density (b), Ragone plot in gravimetric measures (c) and Ragone plot in volumetric measures (d).

However, considering the fact that the electrode mass loadings were increased by a factor of more than ten compared to single layer electrodes (~0.78 mg/cm^2) which were described in the

previous chapters, the here achieved energy and power densities are very promising. The sample with 10 mg/cm^2 loading shows a maximum gravimetric energy density of 8.7 Wh/kg at low power density 0.03 kW/kg and 4.9 Wh/kg at a maximum power density of 11.6 kW/kg. In volumetric measures the electrode stack shows an energy density of $36.9 \cdot 10^{-4}$ Wh/cm^3 at $10.6 \cdot 10^{-6}$ W/cm^3. The impedance data shown in Figure 7-5 sheds light on the possible mass transport issue identified for the sample with the maximum loading of 15 mg/cm^2.

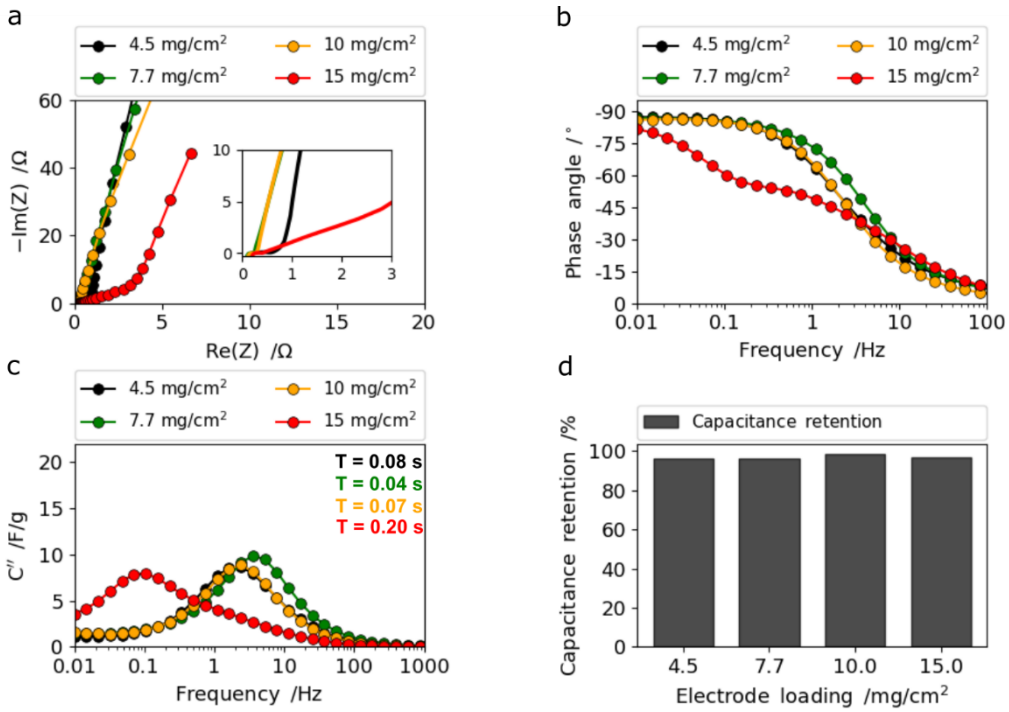

Figure 7-5 The Nyquist plots (a), Bode phase angle plots (b), imaginary capacitance vs. frequency plot (c) and capacitance retention after 6000 cycles (d) of all four samples.

In the Nyquist plot in Figure 7-5a, the line with an angle of approximately 45 ° to the Re(Z) axis is indicative of mass transfer limited processes in the micro-/mesoporous carbon electrode.[242] This is confirmed by the Bode phase angle plot in Figure 7-5b which shows the phase angle as a function of frequency. A phase angle of -90 ° means ideally capacitive behaviour. All electrodes reach this state at low frequency and keep this phase angle up to ~0.5 Hz except the electrode stack with the maximum loading of 15 mg/cm^2. It rapidly decreases to a phase angle of -60 ° at a frequency of 0.1 Hz and drops further to -45 ° at 3 Hz. This is characteristic of electrodes with low rate capability. Furthermore, the relaxation frequency at the maximum

of the imaginary part of the capacitance determines the time constant which is another measure for the rate capability of electrodes in supercapacitors.[242] It is clear that the electrode stack with the maximum mass loading has a much lower rate capability than the other electrodes as the time constant is more than doubled (0.20 s) compared to the electrode stacks composed of fewer layers and hence lower mass loadings (0.04 – 0.08 s). The electrode stack with a mass loading of 10 mg/cm^2 has a time constant of 0.07 s, which is comparable to the one of the single-layer electrode of the same material (0.016 s) presented in chapter 3. Regardless of the mass loading, all electrode stacks retain more than 96% of the initial capacitance after 6000 cycles at 10 A/g as shown in Figure 7-5d which proves the stability of the electrode stacks.

7.4. Conclusion

Herein, the scalability of electrospun LCNFs as electrodes in aqueous alkaline supercapacitors was demonstrated on the basis of the best-performing material in chapter 3 (S310-HKL). However, the route towards carbon nanofibre electrodes with high mass loading can be applied to any free-standing CNF network. In order to achieve industrially applicable electrode loadings of 10 mg/cm^2, two properties that are unique to LCNF networks were shown to be of great importance: 1) free-standing as produced and 2) compressible perpendicular to the fibre axis. Therefore, by stacking several layers of LCNFs on top of each other and subsequent vacuum infiltration with the electrolyte (6 M $KOH_{(aq)}$), electrode stacks with 10 mg/cm^2 could be produced without deterioration of their performance (energy and power density) compared to electrodes of the same material with low loadings. This is very promising as this possibility renders the class of materials investigated in this PhD project applicable to commercial supercapacitor cells. The most applicable electrochemical cell designs used commercially for the free-standing LCNF stack electrodes would be coin cells and pouch cells. These types of cells are assembled by pressing the negative and positive electrode against each other which is analogous to the Swagelok-type cells used to test materials in this project.

8. Conclusion and future work

In this project, it was shown that it is possible to manufacture electrospun carbon nanofibres from both hardwood and softwood Kraft lignin (LCNFs) based on a deep understanding of structural and chemical features of the Kraft lignin precursors. The resulting LCNFs served as free-standing electrodes in aqueous alkaline supercapacitors, whereby the LCNFs were either used as sole active material based on their high specific surface area or as electrically conductive scaffolds which functioned as both the active material and the substrate for redox active materials (here: $Ni(OH)_2$ and ZnO). The resulting composite electrodes could then be used as positive and negative electrodes in a nickel-zinc hybrid capacitor (NZHC).

The two Kraft lignins used in this project were shown to develop different porosities when subjected to increasing stabilization temperatures before carbonization without any additive. It could be shown that the differences in side-chain linkages and functional groups of the two precursors have a profound effect on the development of nanoporosity during heat treatment. This in turn affects the performance of the resulting lignin-based CNFs used as free-standing supercapacitor electrodes. Upon stabilization, two types of reactions occur: 1) crosslinking and 2) degradation. Depending on the nature of the side chains in the lignins, these reactions occur to a different extent and in different temperature windows yielding different porosities. HKL with more β-O-4 ether bonds, more methoxy groups and lower molar mass undergoes cross-linking reactions at 250 °C yielding a very narrow pore size distribution in the (sub-)nanometer range. At 310 °C, both crosslinking and degradation reactions occur which yields both nano- and mesopores. At 340 °C, mainly degradation reactions (C-C cleavage) take place that lead to a widening of pre-existing nanopores which is detrimental to the electrochemical performance. SKL, with fewer β-O-4 ether bonds, but more C-C bonds, fewer methoxy groups and higher molar mass undergoes both crosslinking and degradation reactions over the temperature range of 250 – 340 °C. However, both types of reactions occur to a lesser extent and hence SKL develops less nanoporosity. Stabilizing HKL at 310 °C yielded the most suitable porosity (both

nano- and mesopores) after carbonization and hence the best performance as free-standing electrodes in supercapacitors. It showed a specific gravimetric capacitance of 164 F/g at 0.1 A/g and 119 F/g at 250 A/g with a capacitance retention of more than 90% after 6000 cycles.

To further enhance the inherent development of nanoporosity in HKL-derived CNFs, activation with CO_2 after carbonization and via the addition of $NaNO_3$ in the electrospinning solution were investigated. The CO_2-activated HKL CNFs showed a high specific gravimetric capacitance of 155 F/g at 0.1 A/g, an excellent rate capability with 113 F/g at 250 A/g and a good capacitance retention of 94% after 6000 cycles when tested in 6 M $KOH_{(aq)}$ electrolyte. Therefore, it can be concluded that lignin itself is a promising precursor to produce nanoporous, oxygen functionalized carbon fibres via a three-step thermal treatment (stabilization, carbonization and activation). However, the CO_2 activation process has a negative impact on the volumetric energy density. Therefore, the leap in performance observed in gravimetric measures is preserved to a much lower degree in volumetric ones.

The second strategy to enhance the development of nanoporosity in HKL-derived CNF electrodes was to add $NaNO_3$ as an activating agent to the electrospinning solution. The specific gravimetric capacitance of the LCNF electrodes could be increased from 151 F/g without $NaNO_3$ to 192 F/g with $NaNO_3$ in 6 M $KOH_{(aq)}$ at a low current density of 0.1 A/g via the two-step procedure of oxidative electrospinning ($NaNO_3$) and reducing carbonization (5 mol% H_2 in N_2). Moreover, the method allows doubling of the mass loading per electrode via fibre network densification by the addition of $NaNO_3$. This allows the areal capacitance to more than double from 147 mF/cm^2 in the absence of $NaNO_3$ to 350 mF/cm^2 with $NaNO_3$ with a good capacitance retention of 92.8% after 6000 cycles. Thus, the low volumetric energy density normally associated with electrospun CNF networks could be greatly improved from 949 µWh/cm^3 to 2245 µWh/cm^3. Compared to the CO_2 activation of eucalyptus hardwood Kraft lignin-derived CNF electrodes, chemical activation by addition of $NaNO_3$ to the electrospinning solution has two advantages. Firstly, the number of process steps can be reduced. While CO_2-activated

LCNFs were prepared by a four-step procedure (electrospinning, stabilization, carbonization and CO_2 activation), the $NaNO_3$-activated LCNFs could be produced by a three-step process: electrospinning, carbonization and cleaning. However, the input of chemicals is higher for preparing the $NaNO_3$-activated LCNFs. Secondly, the weight loss induced by CO_2 activation decreases the density of the resulting LCNF networks which is detrimental to the volumetric energy and power densities. $NaNO_3$ activation has the opposite effect. The addition of $NaNO_3$ to the electrospinning solution yields a decrease of the macro-pore space in between the individual fibres in the CNF network and hence leads to an increase in density. Concomitantly, $NaNO_3$ activation causes an increase of the nanoporosity within the fibres. Therefore, this activation procedure is beneficial for both volumetric and gravimetric energy/power densities. However, the resulting electrode loadings (maximum 1.03 mg/cm^2) are still below the ones of commercial supercapacitors (8 – 10 mg/cm^2) implying that the void space (macropores) in the CNF network is still substantial.

Instead of using the LCNFs as sole active material in a electrochemical energy storage device, softwood Kraft lignin-derived carbon nanofibres were used as electrically conductive scaffolds on which $Ni(OH)_2$ and ZnO were deposited. These composite electrodes were tested in a nickel-zinc hybrid capacitor (NZHC). The NZHC showed an improved energy and power density compared to the pristine LCNF-SC. At low power densities of 0.01 – 0.1 kW/kg, the energy density of the NZHC is 16 and 12 Wh/kg which is a three- to four-fold increase compared to the pristine LCNF-SC. Between 0.1 and 1 kW/kg, the energy density of the NZHC still shows a two-fold increase compared to the LCNF-SC. Since the loading of redox active species was kept quite low (10 wt%), there is still a considerable contribution of the electric double layer charge storage mechanism to the overall capacity.

Finally, electrodes with high mass loadings (mg/cm^2) based on free-standing, lignin-derived CNF electrode stacks were produced, which reveals the applicability of these novel CNF electrodes in commercial cells. In order to achieve industrially applicable electrode loadings of

10 mg/cm^2, two properties, that are unique to LCNF networks, were shown to be of great importance: 1) free-standing as produced and 2) compressible perpendicular to the fibre axis. Therefore, by stacking several layers of LCNFs on top of each other and subsequent vacuum infiltration with the electrolyte (6 M $KOH_{(aq)}$), electrode stacks with 10 mg/cm^2 could be produced without deterioration of their capacitive performance compared to electrodes of the same material with low loadings. This is very promising as this strategy renders the class of materials investigated in this PhD project applicable to commercial supercapacitor cells. The most applicable commercial cell types for the free-standing LCNF electrode stacks are coin cells and pouch cells.

The work at hand shall be regarded as a launch pad for the use of Kraft lignin-derived carbon nanofibres in energy storage applications. In the future, the scalability of the electrospinning of Kraft lignin should be explored. In addition, three key aspects need to be considered during the process of up-scaling: 1) intrinsic, 2) extrinsic properties and 3) component performance.

1) Intrinsic properties:
   - Density
   - Thickness
   - Fibre diameter
   - Porosity
   - Chemical composition (e.g. hetero-atoms and functional groups)

2) Extrinsic (stimulated/induced) properties:
   - Light absorption (color, texture)
   - Sound absorption
   - Fluid uptake
   - Electrical/thermal conductivity
   - Mechanical properties

3) Component performance:
   - Supercapacitor electrode
   - Battery electrode

- Catalytic substrate
- Filter material
- Functional textiles

Finally, electrospinning of Kraft lignin should be coupled with other valorization strategies, such as catalytic depolymerization or meltspinning. The commercially available LignoBoost lignin could then be divided into low molar mass fractions suitable for depolymerization or meltspinning. Electrospinning can make use of the residual high molar mass fraction to produce high-value products, such as supercapacitor or battery electrodes, which was demonstrated in the PhD project at hand.

9. Materials and methods

9.1. Lignin characterization

The thorough lignin characterization was performed by the analytical laboratory at RISE AB in Stockholm. The data visualization and interpretation were done by the PhD candidate in close collaboration with the co-supervisors at RISE AB, Darren Baker (until 2018) and Omid Hosseinaei (since 2018).

9.1.1. Ash and carbohydrate content of the lignins

The ash content and composition of the extracted lignin samples were determined using standard methods.[217–220] The ash content was determined by combustion of the lignin samples at 575 °C. The compositional analysis was performed by a two-step acid hydrolysis and the measurement of the lignin and carbohydrate content. Extracted lignin samples were hydrolyzed at 121 °C in an autoclave with 0.4 M sulfuric acid according to the standard procedure SCAN-CM 71:09. The solubilized monosaccharides were quantified using an ion chromatograph coupled to a pulsed amperometric detector (IC-PAD). The lignin content was measured as acid soluble (ASL) and acid insoluble lignins by ultra-violet (UV) spectrophotometry and by gravimetry, respectively. The acid-insoluble residue (AIR) was determined gravimetrically according to TAPPI T222 om-11. The acid-soluble residue was measured by UV spectrophotometry at 205 nm. Ultra-pure water was used as a reference and for the dilution of the hydrolyzate. The content of the acid-soluble residue was calculated using the absorption coefficient 111 g/(l·cm).

$$\mathrm{AIR} = \frac{\mathrm{m}}{\mathrm{M}} \cdot 1000\ \mathrm{mg/g}$$

Where m = dry weight of the residue [g], M = dry weight before acid hydrolysis [g]

$$\mathrm{ASL} = \frac{\mathrm{A} \cdot \mathrm{D} \cdot \mathrm{V}}{\mathrm{a} \cdot \mathrm{b} \cdot \mathrm{M}} \cdot 1000\ \mathrm{mg/g}$$

Where A = absorption at 205 nm, D = dilution factor, V = volume of the filtrate [l] (0.029 l), a = extinction coefficient of lignin [g/(l·cm)] (111 g/(l·cm)), b = cuvette path length [cm] (1 cm), M = dry weight of lignin before acid hydrolysis [g]

$$\text{Total lignin content} = \mathrm{AIR} + \mathrm{ASL}$$

9.1.2. Elemental composition

The organic content of the lignins was measured using a PerkinElmer 2400II CHNS/O combustion elemental analyzer. The absolute content of C, H, N and S were measured. The oxygen content was calculated as 100% minus the sum of C, H, N, S, and ash.

9.1.3. Inorganic elemental contents

Inductively coupled plasma – optical emission spectroscopy (ICP-OES) was used to characterize the metal and inorganic contents of the lignins. The elements quantified are Al, Ba, Ca, Cu, Fe, K, Mg, Mn, Na, P, S, Si and Zn. A PerkinElmer Optima 8300 inductively coupled plasma – optical emission spectrometer was used to determine the metals and inorganic contents of the lignin. The samples were wet digested in a microwave digestor with concentrated nitric acid prior to the volumetric work-up and the measurement.

9.1.4. Determination of the molar mass

The molar mass distribution was determined by size exclusion chromatography (SEC) using a Water SEC system equipped with UV (set at 280 nm) and refractive index (RI) detectors. Two PSS MCX columns (1000 and 100000 Å) were connected in series. The mobile phase was a pH 12 buffer solution at a flow rate of 0.5 ml/min. The lignin sample was dissolved in $NaOH_{(aq)}$ solution (pH = 13.5) and diluted to a suitable concentration with the mobile phase. The injection volume was 100 µL. The SEC system was calibrated using polystyrene standards with molar masses in the range of 891 to 780000 g/mol.

9.1.5. Determination of the glass transition temperature

The glass transition temperature (T_g) was determined in triplicate by using a sample weight of approximately 3 mg using a Q2000 (TA Instruments, USA) differential scanning calorimeter (DSC). Each specimen was heated under a nitrogen flow (50 ml/min) at a rate of 20 °C/min from 25 °C to 150 °C and held at that temperature for five minutes, to remove any remaining moisture, then cooled to 25 °C and again heated to 220 °C at the same heating rate. The second trace was used for the calculation of the T_g.

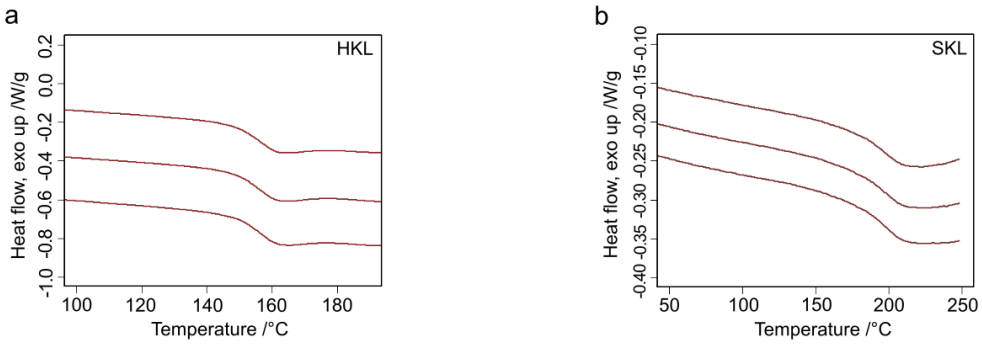

Figure 9-1 Triplicate DSC curves of HKL (a) and SKL (b) where the second trace was used to determine the glass transition temperature. The scales of the y-axes are different to facilitate the observation of the transition.

9.1.6. NMR spectroscopy

^{1}H-^{13}C 2D heteronuclear single quantum correlation (HSQC) nuclear magnetic resonance (NMR) spectroscopy was performed using a Bruker Avance III 400 MHz NMR spectrometer equipped with a 9.4 T magnet and with a broadband PFG 5 mm probe at room temperature (25 °C). For 2D (HSQC) spectroscopy, 100 mg of lignin were dissolved in 0.75 ml of DMSO-d_6. NMR spectra were recorded using the Bruker's "hsqcetgpsisp2.2" pulse program (adiabatic-pulse) with 1.5 s pulse delay. The number of transients was 64 and 256 time increments and were recorded in the ^{13}C dimension. The $^{1}J_{CH}$ used was 145 Hz. Data processing and analysis were performed using Bruker's Topspin 4.0. The central solvent peak was used as an internal reference (δ_C/δ_H 39.5/2.49 ppm) and the HSQC cross-signals were assigned by correlation with literature databases.[59,202,203,314,315] For relative quantification of the side-chain linkages, signal

integration of the C_α–H_α correlations of the interunit linkages were used as they are well-separated (no overlap with other signals).

Hydroxyl groups were measured using quantitative ^{31}P NMR spectroscopy after derivatization of lignin with 100 µL of 2-chloro-4,4,5,5-tetramethyl-1,3,2-dioxaphospholane (TMDP).[228,229] The lignin sample (30 mg) was dissolved in dimethyl formamide/pyridine (1:1 v/v) and mixed with 100 µL of a solution of *N*-hydroxy-5-norbornene-2,3-dicarboxylic acid imide (20 mg/ml) and chromium(III) acetylacetonate (5 mg/ml) as internal standard and relaxation agent, respectively. ^{31}P NMR spectra were acquired using an inverse-gated decoupling pulse sequence with a 90 ° pulse angle, 10 s relaxation delay and 512 scans.

9.2. Characterization of the stabilized and carbonized lignin-derived fibres

9.2.1. Thermogravimetric and mass spectrometric (TG-MS) analysis

The TG-MS analyses were performed on a NETZSCH TG 209F1 Libra TGA instrument coupled with a QMS 403 D Aëolos (Netzsch) mass spectrometer. 12 mg samples were heated with a rate of 0.5 °C/min from 50 to 340 °C in an open Al_2O_3 crucible under a 40 ml/min air flow. The volatile products from the TG furnace were transported to the detector through a 1.5 m transfer line (heated at 190 °C).

9.2.2. Fourier Transform Infrared (FTIR) spectroscopy

FTIR spectra were acquired through attenuated total reflectance Fourier transform infrared (ATR FTIR) spectroscopy on a Tensor27 (Bruker) equipped with a ZnSe single crystal. Each spectrum was averaged over 32 scans at a resolution of 4 cm^{-1} between 4000 and 900 cm^{-1}. Before each measurement, a background scan was carried out.

9.2.3. ^{1}H-^{13}C cross-polarization/magic angle spinning (CP/MAS) nuclear magnetic resonance (NMR) spectroscopy

All experiments were performed on a Bruker Avance III HD spectrometer equipped with an 11.7 T magnet ($\nu_0(^1H)$ = 500.13 MHz and $\nu_0(^{13}C)$ = 125.76 MHz). A Bruker 2.5 mm double

channel magic angle spinning (MAS) probe and a spinning speed of 12 kHz were used for all experiments. ^{1}H magic angle spinning (MAS) NMR spectra were acquired with a rotor-synchronized Hahn echo pulse sequence with optimized 90° and 180° pulse lengths of 2.25 and 4.5 μs, respectively. ^{1}H longitudinal relaxation time constants (T_1) were measured with a saturation-recovery experiment and recycle delays were set to five times the T_1. ^{13}C spectra were acquired using the ^{1}H-^{13}C variable-amplitude cross polarization pulse sequence. The ^{1}H 90° pulse length was 2.6 μs, 60 kHz of spin-locking power was used, and 50 kHz SPINAL-64 ^{1}H decoupling was applied during acquisition. Optimized contact times are shown in Table 9-1. Chemical shifts were referenced relative to tetramethylsilane (δ_{iso} = 0 ppm) using adamantane as a secondary reference ($\delta_{iso}(^{1}H)$ = 1.85 ppm, $\delta_{iso}(^{13}C)$ = 38.57 ppm).

Table 9-1 Experimentally optimized ^{1}H-^{13}C CP/MAS NMR acquisition parameters.

Sample	^{1}H T_1 /s	Recycle delay /s	Contact time /μs
as-spun -SKL	0.366	1.830	500
S190-SKL	0.683	3.415	500
S250-SKL	0.239	1.197	1000
S310-SKL	0.101	0.505	250
S340-SKL	0.071	0.353	450
as-spun-HKL	0.390	1.950	500
S190-HKL	0.418	2.091	700
S250-HKL	0.213	1.065	1000
S310-HKL	0.052	0.209	250
S340-HKL	0.029	0.143	300

9.2.4. Scanning electron microscopy (SEM) and energy dispersive X-ray (EDX) spectroscopy

The lignin and carbon nanofibre morphologies were characterized using a FEI Inspect F scanning electron microscope with an accelerating voltage of 20 kV. Carbonized fibre samples were gold coated for 30 s prior to imaging. Fibre diameter distributions were generated from SEM

images using the ImageJ software package (U.S. National Institutes of Health). The diameters are reported as the mean and standard deviation based on measurements of 100 fibres. Energy-dispersive X-ray spectroscopy was carried out with an INCA Xact detector from Oxford Instruments.

9.2.5. Transmission electron microscopy (TEM)

TEM images were recorded with a JEOL 2010 operated at 200 kV. The fibre samples were cut and ground in order to be dispersed in ethanol (~ 1 mg/mL), then dropped onto a copper grid with holey carbon mesh (TAAB, Holey Carbon Film 300 Cu) and left at room temperature for drying before loading onto the TEM sample holder.

9.2.6. X-ray computed tomography (CT)

X-ray nano-CT was performed on the point of triangular samples of the LCNF mats glued to a pin, and by selecting a scanning region that was fully internal, but as close to the point of the triangle as possible. A lab-based nano-CT instrument (Zeiss Xradia Ultra 810, Carl Zeiss Inc.) was used in phase contrast mode, containing a rotating Cr anode source set to an accelerating voltage of 35 kV. The beam was quasi-monochromatized at the Cr-Kα emission line of 5.4 keV by a capillary condenser, illuminating the sample with a hollow cone beam focused on the sample, with a Fresnel zone plate as the objective element creating a magnified image on a 1024 × 1024-pixel charge-coupled device (CCD) detector. The insertion of a Au phase ring in the back focal plane of the objective shifts the undiffracted component of the beam resulting in negative Zernike phase contrast. Large field-of-view mode with a pixel binning of 1 was used yielding a pixel size of about 63 nm and a field-of-view of about 65 μm. The sample was rotated through 180 ° with radiographs collected at discrete angular intervals amounting to 1601 projections, each of 40 s exposure. The radiographic projections were then reconstructed with a proprietary reconstruction software (XMReconstructor, Carl Zeiss Inc.) using a parallel beam reconstruction algorithm. The grey-scale reconstructed volume was then segmented into a binary image

using the Avizo Fire software (Thermo Fisher Scientific, Waltham, MA, USA) to designate pixels as either ‘fibre’ or ‘pore’ materials by thresholding based on their greyscale value on a cropped data set resulting in a volume of 650×650×1000 pixels, or slightly more than 10 × 104 μm^3. Avizo Fire was also used for 3D visualisation. The ’Beat‘ plug in of ImageJ35 was used to calculate the continuous pore size distribution on a binned data set (325×325×500 pixels) and also applied to the fibre phase for the original data set.

9.2.7. Gas sorption measurement

The surface areas and pore size distributions of the carbonized fibre mats were determined by N_2 and CO_2 ad-/desorption measurements at -196 °C and 0 °C, respectively, using an Autosorb iQ (Quantachrome Instruments, US). The samples were degassed at 200 °C for 16 h under vacuum (0.27 Pa) prior to analysis. Pore size distributions were generated by non-local density functional theory (NLDFT) for CO_2 sorption and quenched solid state DFT (QSDFT, cylindrical/spherical pore model) for N_2 sorption. The models were implemented in the gas sorption analyzer software (AsiQwin version 3.0, Quantachrome). Discrepancies between the measured and modeled isotherms were always below 1% (fitting error), which was determined by the software.

9.2.8. Raman spectroscopy

Raman spectra were recorded on a Renishaw inVia Reflex spectrometer system equipped with a laser working at 633 nm and less than 20 mW. The use of a 100x objective (Olympus) provided a focus spot of about 1 µm diameter. Raman spectra were collected in the range of 500 cm^{-1} to 3200 cm^{-1} with a spectral resolution of approximately 2 cm^{-1} using a grating of 1800 grooves/mm and a thermoelectrically cooled CCD detector (Synapse, 1024 x 256 pixels). The spectral positions were calibrated against the Raman band of Si (520.7 ± 0.4 cm^{-1}) before and after the sample measurements.

9.2.9. X-ray diffraction (XRD)

X-ray diffraction (XRD) was carried out with a Panalytical X'Pert Pro diffractometer equipped with Ni-filtered Cu Kα radiation (λ_1=1.5406 Å and λ_2=1.5444 Å) and an X'Celerator multi-strip detector. The data was collected in the 2θ range from 5° to 95° using a scan rate of 1°/min. Data interpretation (background determination and peak indexing) was performed with the X'Pert HighScore Plus software (Malvern Panalytical).

9.2.10. Chemical characterization - X-ray photoelectron spectroscopy (XPS) and temperature programmed desorption (TPD)

The surface chemistry of the carbon nanofibres was analyzed by XPS using a Thermo Scientific Kα spectrometer with an AlKα monochromatic source (1486.6 eV) using a spot size of 100 μm and a multidetection analyzer under a residual pressure of 5×10^{-8} mbar. TPD experiments were carried out in a TGA-DSC instrument (TA Instruments, SDT Q600 Simultaneous) coupled to a mass spectrometer (Thermostar, Balzers, GSD 300 T3) by heating the samples (~ 4 mg) up to 950 °C (heating rate: 20 °C/min) under helium atmosphere (flow rate: 100 ml/min). The thermobalance was purged for 2 h under helium atmosphere prior to the heating of the sample. The calibration of the equipment for H_2O, CO and CO_2 evolved gases was carried out using the decomposition of a calcium oxalate (99.999%, Sigma Aldrich) standard.

9.2.11. Helium pycnometry

Helium gas displacement pycnometry was carried out with an AccuPyc 1330 V2.04N system (Micromeritics) in order to determine the skeletal density of the LCNFs. The resulting skeletal density was determined as an average value of ten consecutive measurements. The sample weight was 8 mg and the sample cell volume was 3.044 cm^3. Prior to the measurement, the sample cell was calibrated.

9.3. Electrochemical characterization

The Kraft lignin-derived carbon nanofibres were tested as electrodes in symmetric supercapacitor (SC) cells. Most measurements were performed in a two-electrode set-up consisting of two similar carbon electrodes (symmetric SC type). A third reference electrode (saturated calomel reference electrode) was inserted in the cell during the measurement, where indicated in the text. The SCs were assembled in a Swagelok-type cell. It consisted of a perfluoralkoxy-polymer (PFA) cell body and Hastelloy C276 heat resisting alloy rods which was connected to a SP300-potentiostat (Biologic, France). An image of the cell set-up can be seen in Figure 9-2. 6 M $KOH_{(aq)}$ was used as the electrolyte and standard glass microfibre filter as the separator (Whatman, GE Healthcare Life Sciences, UK, Grade GF/D). Before the actual measurements, the cells were galvanostatically charged and discharged for 500 cycles at 5 A/g to ensure good wetting of the electrodes with the electrolyte. Subsequently, cyclic voltammetry and galvanostatic charge-discharge with potential limitation (GCD) measurements were carried out at different rates. Impedance spectroscopy was conducted at open circuit potential and with an amplitude of 5 mV in a frequency range of 10 mHz to 1 MHz. Finally, the capacitance retention was measured at a current density of 10 A/g for 6000 cycles.

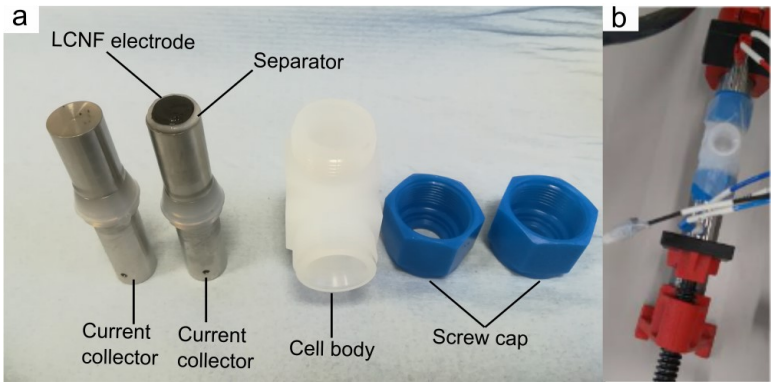

Figure 9-2 Cell components of the Swagelok-type cells used in this project (a) and assembled Swagelok-type cell connected to the galvano-/potentiostat (b).

Capacitance calculation:

$$C\ [F/g] = \frac{4 * Q * 3.6}{(dU - IR) * m_{cell}}$$

Where Q = discharge capacity [mAh] determined by EC Lab software, dU = potential difference [V], IR = IR drop measured in the discharge curves [V], m_{cell} = total weight of carbon in the supercapacitor cell [g]

Energy density calculation (gravimetric):

$$E\ [Wh/kg] = \frac{0.5 * Q * U}{m_{cell}}$$

Where Q = discharge capacity [Ah], U = potential window [V], m_{cell} = total weight of carbon in the supercapacitor [g]

Power density calculation (gravimetric):

$$P\ [W/kg] = \frac{0.5 * Q * U}{t * m_{cell}}$$

Where Q = discharge capacity [Ah], V = potential window [V], m_{cell} = total weight of carbon in the supercapacitor [g], t = discharge time [s]

The capacitance, energy and power densities in volumetric measures were calculated analogously except that "m_{cell}" was replaced by "V_{cell}" in cm^3. The areal capacitance (F/cm^2) was calculated by replacing "m_{cell}" by the electrode's cross-sectional area "A_{cell}" in cm^2.

10. References

1 J. Grotzinger and T. Jordan, in *Allgemeine Geologie*, Springer Spektrum, 2017, pp. 621–640.

2 P. J. Crutzen and E. F. Stoermer, *Glob. Chang. Newsl.*, 2000, **41**, 17–18.

3 The World Meteorological Organization, *WMO Greenh. Gas Bull.*, 2019, **15**, 1–8.

4 T. M. L. Wigley, V. Ramaswamy, J. R. Christy, J. R. Lanzante, C. A. Mears, B. D. Santer and C. K. Folland, *U.S. Clim. Chang. Sci. Progr. - Exec. Summ.*, 2006, 1–14.

5 W. Steffen, J. Rockström, K. Richardson, T. M. Lenton, C. Folke, D. Liverman, C. P. Summerhayes, A. D. Barnosky, S. E. Cornell, M. Crucifix, J. F. Donges, I. Fetzer, S. J. Lade, M. Scheffer, R. Winkelmann and H. J. Schellnhuber, *Proc. Natl. Acad. Sci. U. S. A.*, 2018, **115**, 8252–8259.

6 F. Biermann and I. Boas, *Environ. Sci. Policy Dev.*, 2008, **50**, 8–17.

7 M. R. Allen, O. P. Dube, W. Solecki, F. Aragón-Durand, W. Cramer, S. Humphreys, M. Kainuma, J. Kala, N. Mahowald, Y. Mulugetta, R. Perez, M. Wairiu and K. Zickfeld, in *Global Warming of 1.5°C. An IPCC Special Report on the impacts of global warming of 1.5°C above pre-industrial levels and related global greenhouse gas emission pathways, in the context of strengthening the global response to the threat of climate change,* 2018, pp. 49–91.

8 E. Chasan, Global Sustainable Investments Rise 34 Percent to $30.7 Trillion, https://www.bloomberg.com/news/articles/2019-04-01/global-sustainable-investments-rise-34-percent-to-30-7-trillion , (accessed 27 April 2020).

9 D. Archer, H. Kheshgi and E. Maier-Reimer, *Global Biogeochem. Cycles*, 1998, **12**, 259–276.

10 F. Cherubini, G. P. Peters, T. Berntsen, A. H. Strømman and E. Hertwich, *GCB Bioenergy*, 2011, **3**, 413–426.

11 J. A. Lowe and D. Bernie, *Philos. Trans. R. Soc. A*, 2018, **A376**, 1–13.

12 IPCC, in *Contribution of Working Groups I, II and III to the Fifth Assessment Report of the Intergovernmental Panel on Climate Change*, Geneva, 2014, pp. 1–12.

13 M. Muntean, D. Guizzardi, E. Schaaf, M. Crippa, E. Solazzo, J. G. J. Olivier and E.

Vignati, in *EUR 29433 EN, Publications Office of the European Union, Luxembourg*, 2018.

14 R. Sims, R. Schaeffer, F. Creutzig, X. Cruz-Núnez, M. D'Agosto, D. Dimitriu, M. J. Figueroa Meza, L. Fulton, S. Kobayashi, O. Lah, A. McKinnon, P. Newman, M. Ouyang, J. J. Schauer, D. Sperling and G. Tiwari, in *Climate Change 2014: Mitigation of Climate Change. Contribution of Working Group III to the Fifth Assessment Report of the Intergovern- mental Panel on Climate Change*, Cambridge University Press, Cambridge, U.K. and New York, NY, USA, 2014.

15 European Commission, *Final Report of the High-Level Panel of the European Decarbonisation Pathways Initiative*, Publications Office of the European Union, Luxembourg, 2018.

16 IPCC, in *Climate Change 2014: Mitigation of Climate Change. Contribution of Working Group III to the Fifth Assessment Report of the Intergovernmental Panel on Climate Change*, Cambridge University Press, Cambridge, U.K. and New York, NY, USA, 2014.

17 A. Berlin and M. Balakshin, *Bioenergy Res. Adv. Appl.*, 2014, 315–336.

18 P. C. A. Bruijnincx, R. Rinaldi and B. M. Weckhuysen, *Green Chem.*, 2015, **17**, 4860–4861.

19 P. Berg and O. Lingqvist, *McKinsey Co. Pap. For. Prod.*, 2017, 1–18.

20 C. P. J. M. Suhas and M. M. L. Ribeiro Carrott, *Bioresour. Technol.*, 2007, **98**, 2301–2312.

21 A. Duval and M. Lawoko, *React. Funct. Polym.*, 2014, **85**, 78–96.

22 W. Schutyser, T. Renders, S. Van den Bosch, S.-F. Koelewijn, G. T. Beckham and B. F. Sels, *Chem. Soc. Rev.*, 2018, **47**, 852–908.

23 R. Rinaldi, R. Jastrzebski, M. T. Clough, J. Ralph, M. Kennema, P. C. A. Bruijnincx and B. M. Weckhuysen, *Angew. Chemie - Int. Ed.*, 2016, **55**, 8164–8215.

24 R. Katahira, T. Elder and G. T. Beckham, in *Lignin Valorization: Emerging Approaches*, The Royal Society of Chemistry, 2018, pp. 1–9.

25 N. Giummarella, M. Balakshin, S. Koutaniemi, A. Kärkönen and M. Lawoko, *J. Exp. Bot.*, 2019, **70**, 5591–5601.

26 D. Tarasov, M. Leitch and P. Fatehi, *Biotechnol. Biofuels*, 2018, 1–28.

27 P. Kenrick and P. R. Crane, *Nature*, 1997, **389**, 33–39.

28 W. Boerjan, J. Ralph and M. Baucher, *Annu. Rev. Plant Biol.*, 2003, **54**, 519–546.

29 A. J. Ragauskas, G. T. Beckham, M. J. Biddy, R. Chandra, F. Chen, M. F. Davis, B. H. Davison, R. A. Dixon, P. Gilna, M. Keller, P. Langan, A. K. Naskar, J. N. Saddler, T. J. Tschaplinski, G. A. Tuskan and C. E. Wyman, *Science (80-.).*, 2014, **344**, 1246843.

30 K. David and A. J. Ragauskas, *Energy Environ. Sci.*, 2010, **3**, 1182–1190.

31 R. C. Pettersen, in *The chemistry of solid wood. Advances in chemistry series 207*, Washington DC, 1984, pp. 58–126.

32 F. Huang and A. Ragauskas, *Ind. Eng. Chem. Res.*, 2013, **52**, 1743–1749.

33 C. A. Nunes, C. F. Lima, L. C. De Almeida Barbosa, J. L. Colodette and P. H. Fidêncio, *Quim. Nova*, 2011, **34**, 279–283.

34 J. E. Jakes, X. Arzola, R. Bergman, P. Ciesielski, C. G. Hunt, N. Rahbar, M. Tshabalala, A. C. Wiedenhoeft and S. L. Zelinka, *Jom*, 2016, **68**, 2395–2404.

35 U. P. Agarwal, *Front. Plant Sci.*, 2014, **5**, 1–12.

36 R. M. Rowell, R. Pettersen, J. S. Han, J. S. Rowell and M. A. Tshabalala, in *Handbook of wood chemistry and wood composites*, 2005, pp. 37–74.

37 G. Daniel, in *Wood Chemistry and Biotechnology. Vol. 1.*, DeGruyter and Co, Berlin, 2009, pp. 45–71.

38 H. Zhu, W. Luo, P. N. Ciesielski, Z. Fang, J. Y. Zhu, G. Henriksson, M. E. Himmel and L. Hu, *Chem. Rev.*, 2016, 116, 9305–9374.

39 R. M. Rowell, R. Pettersen and M. A. Tshabalala, in *Handbook of Wood Chemistry and Wood Composites, Second Edition*, 2012, pp. 33–72.

40 L. Pereira Ramos, *Quim. Nova*, 2003, **26**, 863–871.

41 O. M. Terrett and P. Dupree, *Curr. Opin. Biotechnol.*, 2019, **56**, 97–104.

42 E. Sjöström, in *Wood Chemistry*, 1993, pp. 51–70.

43 N. Giummarella, Y. Pu, A. Ragauskas and M. Lawoko, *Green Chem.*, 2019, **21**, 1573–

1595.

44 Y. Tobimatsu and M. Schuetz, *Curr. Opin. Biotechnol.*, 2019, **56**, 75–81.

45 J. Ralph and L. L. Landucci, in *Lignin and Lignans*, 2010, pp. 137–243.

46 F. S. Chakar and A. J. Ragauskas, *Ind. Crops Prod.*, 2004, **20**, 131–141.

47 J. Ralph, K. Lundquist, G. Brunow, F. Lu, H. Kim, P. F. Schatz, J. M. Marita, R. D. Hatfield, S. A. Ralph, J. H. Christensen and W. Boerjan, *Phytochem. Rev.*, 2004, **3**, 29–60.

48 J. Ralph, C. Lapierre and W. Boerjan, *Curr. Opin. Biotechnol.*, 2019, **56**, 240–249.

49 G. C. Avgerinos and D. I. C. Wang, *Biotechnol. Bioeng.*, 1983, **25**, 67–83.

50 A. Brandt, J. Gräsvik, J. P. Hallett and T. Welton, *Green Chem.*, 2013, **15**, 550–583.

51 P. J. Crutzen, A. R. Mosier, K. A. Smith and W. Winiwarter, *Atmos. Chem. Phys.*, 2008, **8**, 389–395.

52 A. Johansson, O. Aaltonen and P. Ylinen, *Biomass*, 1987, **13**, 45–65.

53 S. Aziz and K. Sarkanen, *Tappi J.*, 1989, **72**, 169–175.

54 E. Sjöström, in *Wood Chemistry*, 1993, pp. 114–164.

55 C. Houtman, in *Lignin Valorization: Emerging Approaches*, 2018, pp. 62–73.

56 N. Mahmood, Z. Yuan, J. Schmidt and C. Xu, *Renew. Sustain. Energy Rev.*, 2016, **60**, 317–329.

57 G. Gellerstedt, *Ind. Crops Prod.*, 2015, **77**, 845–854.

58 J. Gierer, *Wood Sci. Technol.*, 1980, **14**, 241–266.

59 C. Crestini, H. Lange, M. Sette and D. S. Argyropoulos, *Green Chem.*, 2017, **19**, 4104–4121.

60 J. Fernández-Rodríguez, X. Erdocia, F. Hernández-Ramos, M. González Alriols and J. Labidi, in *Separation of Functional Molecules in Food by Memebrane Technology*, 2019, pp. 229–265.

61 J. E. Holladay, J. F. White, J. J. Bozell and D. Johnson, *Top value added chemicals from Biomass lignin*, 2007, vol. II.

62 P. Tomani, *Cellul. Chem. Technol.*, 2010, **44**, 53–58.

63 F. Cherubini, *Energy Convers. Manag.*, 2010, **51**, 1412–1421.

64 D. M. Alonso, S. H. Hakim, S. Zhou, W. Won, O. Hosseinaei, J. Tao, V. Garcia-Negron, A. H. Motagamwala, M. A. Mellmer, K. Huang, C. J. Houtman, N. Labbé, D. P. Harper, C. T. Maravelias, T. Runge and J. A. Dumesic, *Sci. Adv.*, 2017, **3**, 1–7.

65 E. Sjöström, in *Wood Chemistry*, 1993, pp. 225–248.

66 MetsäGroup, Bioproduct mill - Bioproducts, https://www.metsafibre.com/en/about-us/Production-units/Bioproduct-mill/Pages/Bioproducts.aspx.

67 T. Renders, S. Van den Bosch, S.-F. Koelewijn, W. Schutyser and B. F. Sels, *Energy Environ. Sci.*, 2017, **10**, 1551–1557.

68 J. Domínguez-Robles, T. Tamminen, T. Liitiä, M. S. Peresin, A. Rodríguez and A.-S. Jääskeläinen, *Int. J. Biol. Macromol.*, 2018, **106**, 979–987.

69 Q. Li, W. K. Serem, W. Dai, Y. Yue, M. T. Naik, S. Xie, P. Karki, L. Liu, H.-J. Sue, H. Liang, F. Zhou and J. S. Yuan, *J. Mater. Chem. A*, 2017, **5**, 12740–12746.

70 Q. Li, S. Xie, W. K. Serem, M. T. Naik, L. Liu and J. S. Yuan, *Green Chem.*, 2017, **19**, 1628–1634.

71 I. Brodin, E. Sjöholm and G. Gellerstedt, *Holzforschung*, 2009, **63**, 290–297.

72 E. L. Lovell and H. Hibbert, *J. Am. Chem. Soc.*, 1941, **63**, 2070–2073.

73 J. Jin, J. Ding, A. Klett, M. C. Thies and A. A. Ogale, *ACS Sustain. Chem. Eng.*, 2018, **6**, 14135–14142.

74 H. Liu, Z. Dai, Q. Cao, X. Shi, X. Wang, H. Li, Y. Han, Y. Li and J. Zhou, *ACS Sustain. Chem. Eng.*, 2018, **6**, 8554–8562.

75 S. Otani, Y. Fukuoka, B. Igarashi and K. Sasaki, *Method for Producing Carbonized Lignin Fiber*, 1969.

76 P. Bajpai, *Carbon Fibre from Lignin*, 2017.

77 A. Milbrandt and S. Booth, *Carbon Fiber from Biomass*, 2016.

78 H. Mainka, O. Täger, E. Körner, L. Hilfert, S. Busse, F. T. Edelmann and A. S. Herrmann, *J. Mater. Res. Technol.*, 2015, **4**, 283–296.

79 A. Jacob, *Reinf. Plast.*, 2010, **54**, 38–41.

80 E. Frank, L. M. Steudle, D. Ingildeev, J. M. Spörl and M. R. Buchmeiser, *Angew. Chemie - Int. Ed.*, 2014, 53, 5262–5298.

81 J. F. Brazdil, in *Ullmann's Encyclopedia of Industrial Chemistry, Vol. 24*, 2012, pp. 1–10.

82 E. Frank, F. Hermanutz and M. R. Buchmeiser, *Macromol. Mater. Eng.*, 2012, **297**, 493–501.

83 A. K. Naskar and R. M. Paul, *Low-Cost Bio-Based Carbon Fiber for High-Temperature Processing*, 2017.

84 D. A. Baker and T. G. Rials, *J. Appl. Polym. Sci.*, 2013, 130, 713–728.

85 D. J. Johnson, *J. Phys. D. Appl. Phys.*, 1987, **20**, 286–291.

86 D. D. L. Chung, in *Carbon Fiber Composites*, 1994, pp. 3–11.

87 R. A. Sullivan, *Jom*, 2006, **58**, 77–79.

88 D. D. L. Chung, in *Carbon Fiber Composites*, 1994, pp. 13–53.

89 S. O. Ismail and E. I. Akpan, in *Sustainable Lignin for Carbon Fibers: Principles, Techniques, and Applications*, 2019, pp. 365–426.

90 I. Brodin, M. Ernstsson, G. Gellerstedt and E. Sjöholm, *Holzforschung*, 2012, **66**, 141–147.

91 O. Hosseinaei, M. Åkerström, A. Uhlin, P. Tomani and S. Danielsson, in *NWBC 2018 Proceedings of the 8th Nordic Wood Biorefinery Conference*, 2018, pp. 157–163.

92 J. L. Braun, K. M. Holtman and J. F. Kadla, *Carbon*, 2005, **43**, 385–394.

93 D. J. Johnson, I. Tomizuka and O. Watanabe, *Carbon*, 1975, **13**, 321–325.

94 F. S. Baker, in *Frontiers in Biorefinery: Biobased Products from Renewable Carbon*, 2010.

95 O. Rios, S. K. Martha, M. A. McGuire, W. Tenhaeff, K. More, C. Daniel and J. Nanda, *Energy Technol.*, 2014, **2**, 773–777.

96 Y. Uraki, A. Nakatani, S. Kubo and Y. Sano, *J. Wood Sci.*, 2001, 465–469.

97 X. You, K. Koda, T. Yamada and Y. Uraki, *J. Wood Chem. Technol.*, 2016, **36**, 418–431.

98 W. Heschel and E. Klose, *Fuel*, 1995, **74**, 1786–1791.

99 W. M. N. S. M. Daud, S. Mustafa, S. R. Rahmadulla, S. A. bin C. Ghani and A. Hisyam, *Int. J. Supply Chain Manag.*, 2017, **6**, 127–132.

100 N. Arena, J. Lee and R. Clift, *J. Clean. Prod.*, 2016, **125**, 68–77.

101 Y. Uraki, S. Kubo, H. Kurakami and Y. Sano, *Holzforschung*, 1997, **51**, 188–192.

102 J. Rodríguez-Mirasol, T. Cordero and J. J. Rodríguez, *Carbon*, 1993, **31**, 87–95.

103 J.-W. Jeon, L. Zhang, J. L. Lutkenhaus, D. D. Laskar, J. P. Lemmon, D. Choi, M. I. Nandasiri, A. Hashmi, J. Xu, R. K. Motkuri, C. A. Fernandez, J. Liu, M. P. Tucker, P. B. McGrail, B. Yang and S. K. Nune, *ChemSusChem*, 2015, **8**, 428–432.

104 A. M. Navarro-Suárez, D. Saurel, P. Sánchez-Fontecoba, E. Castillo-Martínez, J. Carretero-González and T. Rojo, *J. Power Sources*, 2018, **397**, 296–306.

105 X.-F. Li, Q. Xu, Y. Fu and Q.-X. Guo, *Environ. Prog. Sustain. Energy*, 2014, 519–526.

106 R. Ruiz-Rosas, M. J. Valero-Romero, D. Salinas-Torres, J. Rodríguez-Mirasol, T. Cordero, E. Morallón and D. Cazorla-Amorós, *ChemSusChem*, 2014, **7**, 1458–1467.

107 J. M. Rosas, R. Berenguer, M. J. Valero-Romero, J. Rodríguez-Mirasol and T. Cordero, *Front. Mater.*, 2014, **1**, 1–17.

108 B. Yu, Z. Chang and C. Wang, *Mater. Chem. Phys.*, 2016, **181**, 187–193.

109 R. Ruiz-Rosas, J. Bedia, M. Lallave, I. G. Loscertales, A. Barrero, J. Rodríguez-Mirasol and T. Cordero, *Carbon*, 2010, **48**, 696–705.

110 W. E. Teo and S. Ramakrishna, *Nanotechnology*, 2006, **17**, 89–106.

111 P. H. S. Picciani, E. S. Medeiros, W. J. Orts and H. C. Mattoso, in *Nanofibers - Production, Properties and Functional Applications*, 2011, pp. 85–116.

112 G. Riboux, Á. G. Marnín., I. G. Loscertales and A. Barrero, *J. Fluid Mech.*, 2011, **671**, 226–253.

113 F. H. M. Graichen, W. J. Grigsby, S. J. Hill, L. G. Raymond, M. Sanglard, D. A. Smith, G. J. Thorlby, K. M. Torr and J. M. Warnes, *Ind. Crops Prod.*, 2017, **106**, 74–85.

114 U.S. Patent 20140271443 A1, 2014.

115 M. Lallave, J. Bedia, R. Ruiz-Rosas, J. Rodríguez-Mirasol, T. Cordero, J. C. Otero, M. Marquez, A. Barrero and I. G. Loscertales, *Adv. Mater.*, 2007, **19**, 4292–4296.

116 R. Berenguer, F. J. García-Mateos, R. Ruiz-Rosas, D. Cazorla-Amorós, E. Morallón, J. Rodríguez-Mirasol and T. Cordero, *Green Chem.*, 2016, **18**, 1506–1515.

117 F. J. García-Mateos, T. Cordero-Lanzac, R. Berenguer, E. Morallón, D. Cazorla-Amorós, J. Rodríguez-Mirasol and T. Cordero, *Appl. Catal. B Environ.*, 2017, **211**, 18–30.

118 R. Berenguer, J. Fornells, F. J. García-Mateos, M. O. Guerrero-Pérez, J. Rodríguez-Mirasol and T. Cordero, *Catal. Today*, 2016, **277**, 266–273.

119 F. J. García-Mateos, R. Berenguer, M. J. Valero-Romero, J. Rodríguez-Mirasol and T. Cordero, *J. Mater. Chem. A*, 2018, **6**, 1219–1233.

120 S. Kubo and J. F. Kadla, *Biomacromolecules*, 2003, **4**, 561–567.

121 J. F. Kadla, S. Kubo, R. A. Venditti, R. D. Gilbert, A. L. Compere and W. Griffith, *Carbon*, 2002, **40**, 2913–2920.

122 J. F. Kadla and S. Kubo, *Macromolecules*, 2003, **36**, 7803–7811.

123 S. Kubo and J. F. Kadla, *Macromolecules*, 2004, **37**, 6904–6911.

124 S. Kubo and J. F. Kadla, *J. Appl. Polym. Sci.*, 2005, **98**, 1437–1444.

125 S. Kubo and J. F. Kadla, *Biomacromolecules*, 2005, **6**, 2815–2821.

126 I. Dallmeyer, F. Ko and J. F. Kadla, *J. Wood Chem. Technol.*, 2010, **30**, 315–329.

127 S. Aslanzadeh, Z. Zhu, Q. Luo, B. Ahvazi, Y. Boluk and C. Ayranci, *Macromol. Mater. Eng.*, 2016, **301**, 401–413.

128 D. K. Seo, J. P. Jeun, H. Bin Kim and P. H. Kang, *Rev. Adv. Mater. Sci.*, 2011, **28**, 31–34.

129 M. Cho, M. Karaaslan, S. Chowdhury, F. Ko and S. Renneckar, *ACS Sustain. Chem. Eng.*, 2018, **6**, 6434–6444.

130 S. Hu and Y.-L. Hsieh, *J. Mater. Chem. A*, 2013, **1**, 11279–11288.

131 D. I. Choi, J.-N. Lee, J. Song, P.-H. Kang, J.-K. Park and Y. M. Lee, *J. Solid State Electrochem.*, 2013, **17**, 2471–2475.

132 S.-X. Wang, L. Yang, L. P. Stubbs, X. Li and C. He, *ACS Appl. Mater. Interfaces*, 2013, **5**, 12275–12282.

133 S. Hu, S. Zhang, N. Pan and Y.-L. Hsieh, *J. Power Sources*, 2014, **270**, 106–112.

134 C. Lai, Z. Zhou, L. Zhang, X. Wang, Q. Zhou, Y. Zhao, Y. Wang, X.-F. Wu, Z. Zhu and H. Fong, *J. Power Sources*, 2014, **247**, 134–141.

135 R. A. P. Jayawickramage, K. J. Balkus Jr and J. P. Ferraris, *Nanotechnology*, 2019, **30**, 355402.

136 J. Jin, B.-J. Yu, Z. Shi, C. Wang and C. Chong, *J. Power Sources*, 2014, **272**, 800–807.

137 A. Ma, L. Zhou and J. Chang, *NANO Br. Reports Rev.*, 2015, **10**, 1–9.

138 X. You, K. Koda, T. Yamada and Y. Uraki, *Holzforschung*, 2015, **69**, 1097–1106.

139 X. Shi, X. Wang, B. Tang, Z. Dai, K. Chen and J. Zhou, *J. Appl. Polym. Sci.*, 2017, **135**, 45580.

140 X. Ma, P. Kolla, Y. Zhao, A. L. Smirnova and H. Fong, *J. Power Sources*, 2016, **325**, 541–548.

141 J. Li, B. Michalkiewicz, J. Min, C. Ma, X. Chen, J. Gong, E. Mijowska and T. Tang, *Chem. Eng. J.*, 2019, **360**, 250–259.

142 M. Inagaki, Y. Yang and F. Kang, *Adv. Mater.*, 2012, **24**, 2547–2566.

143 F. Yao, D. T. Pham and Y. H. Lee, *ChemSusChem*, 2015, **8**, 2284–2311.

144 S. Biniak, A. Świątkowski and M. Pakuła, in *Chemistry and Physics of Carbon*, 2001, vol. 27, pp. 126–216.

145 T. Brousse, D. Bélanger, K. Chiba, M. Egashira, F. Favier, J. Long, J. R. Miller, M. Morita, K. Naoi, P. Simon and W. Sugimoto, in *Handbook of Electrochemical Energy*, 2017, pp. 495–561.

146 P. G. Bruce, B. Scrosati and J.-M. Tarascon, *Angew. Chemie - Int. Ed.*, 2008, **47**, 2930–2946.

147 N.-S. Choi, Z. Chen, S. A. Freunberger, X. Ji, Y.-K. Sun, K. Amine, G. Yushin, L. F.

Nazar, J. Cho and P. G. Bruce, *Angew. Chemie - Int. Ed.*, 2012, **51**, 9994–10024.

148 J. M. Tarascon and M. Armand, *Nature*, 2001, **414**, 359–367.

149 Z. Chen, D. Higgins, A. Yu, L. Zhang and J. Zhang, *Energy Environ. Sci.*, 2011, **4**, 3167–3192.

150 J.-S. Lee, S. T. Kim, R. Cao, N.-S. Choi, M. Liu, K. T. Lee and J. Cho, *Adv. Energy Mater.*, 2011, **1**, 34–50.

151 A. G. Pandolfo and A. F. Hollenkamp, *J. Power Sources*, 2006, **157**, 11–27.

152 T. Pandolfo, V. Ruiz, S. Sivakkumar and J. Nerkar, in *Supercapacitors Materials, Systems and Applications*, 2013, pp. 69–110.

153 P. Simon and Y. Gogotsi, *Nat. Mater.*, 2008, **7**, 845–854.

154 A. Burke, *Electrochim. Acta*, 2007, **53**, 1083–1091.

155 B. E. Conway, V. Birss and J. Wojtowicz, *J. Power Sources*, 1997, **66**, 1–14.

156 M. Born, *Zeitschrift fur Phys.*, 1920, **1**, 45–48.

157 U.S. Patent 2,800,616, 1957.

158 U.S. Patent 3536963, 1970.

159 Philipp Azais, in *Supercapacitors Materials, Systems and Applications*, 2013, pp. 307–372.

160 A. Burke and H. Zhao, in *5th European Symposium on Supercapacitor and Hybrid Solutions*, 2015.

161 R. Kötz and M. Carlen, *Electrochim. Acta*, 2000, **45**, 2483–2498.

162 AVX A KYOCERA GROUP COMPANY, *AVX BestCap ® Ultra-low ESR BestCap*, 2017.

163 ZapGo Ltd., *Carbon-Ion : a new , safer and faster charging category of rechargeable energy storage devices*, 2016.

164 J. Chmiola, C. Largeot, P.-L. Taberna, P. Simon and Y. Gogotsi, *Angew. Chemie - Int. Ed.*, 2008, **47**, 3392–3395.

165 C. Merlet, C. Péan, B. Rotenberg, P. A. Madden, B. Daffos, P.-L. Taberna, P. Simon and

M. Salanne, *Nat. Commun.*, 2013, **4**, 2–7.

166 O. Stern, *Zeitschrift für Elektrochemie und Angew. Phys. Chemie*, 1924, **30**, 508–516.

167 J. Huang, B. G. Sumpter and V. Meunier, *Angew. Chemie - Int. Ed.*, 2008, **47**, 520–524.

168 A. C. Forse, C. Merlet, J. M. Griffin and C. P. Grey, *J. Am. Chem. Soc.*, 2016, **138**, 5731–5744.

169 C. Prehal, D. Weingarth, E. Perre, R. T. Lechner, H. Amenitsch, O. Paris and V. Presser, *Energy Environ. Sci.*, 2015, **8**, 1725–1735.

170 X. Zheng, J. Luo, W. Lv, D.-W. Wang and Q.-H. Yang, *Adv. Mater.*, 2015, **27**, 5388–5395.

171 Z. Gao, Y. Zhang, N. Song and X. Li, *Mater. Res. Lett.*, 2017, **5**, 69–88.

172 F. Béguin, V. Presser, A. Balducci and E. Frackowiak, *Adv. Mater.*, 2014, **26**, 2219–2251.

173 Y. Zhang, X. Liu, S. Wang, L. Li and S. Dou, *Adv. Energy Mater.*, 2017, **7**, 1700592.

174 N. Pal and A. Bhaumik, *Adv. Colloid Interface Sci.*, 2013, **189**–**190**, 21–41.

175 M. M. Titirici, R. J. White, N. Brun, V. L. Budarin, D. S. Su, F. del Monte, J. H. Clark and M. J. MacLachlan, *Chem. Soc. Rev.*, 2015, **44**, 250–290.

176 L. Kong, M. Liu, Z. Diao, D. Chen, X. Chang and Y. Xiong, *Sci. Rep.*, 2016, **6**, 38176.

177 Donau Carbon, *Activated Carbon and its Applications*, 2017.

178 K. Koehlert, *Activated Carbon: Fundamentals and New Applications*, 2017.

179 C. Largeot, C. Portet, J. Chmiola, P.-L. Taberna, Y. Gogotsi and P. Simon, *J. Am. Chem. Soc.*, 2008, **130**, 2730–2731.

180 Y. Zhai, Y. Dou, D. Zhao, P. F. Fulvio, R. T. Mayes and S. Dai, *Adv. Mater.*, 2011, **23**, 4828–4850.

181 J. N. Barisci, G. G. Wallace, D. R. MacFarlane and R. H. Baughman, *Electrochem. Commun.*, 2004, **6**, 22–27.

182 R. Tang, K. Taguchi, H. Nishihara, T. Ishii, E. Morallón, D. Cazorla-Amorós, T. Asada, N. Kobayashi, Y. Muramatsu and T. Kyotani, *J. Mater. Chem. A*, 2019, **7**, 7480–7488.

183 K. Xu, M. S. Ding and T. R. Jow, *Electrochim. Acta*, 2001, **46**, 1823–1827.

184 E. Frackowiak and F. Béguin, *Carbon*, 2001, **39**, 937–950.

185 B. E. Conway, in *Electrochemical Supercapacitors: Scientific Fundamentals and Technological Applications*, New York, 1999, pp. 1–9.

186 E. Raymundo-Piñero, F. Leroux and F. Béguin, *Adv. Mater.*, 2006, **18**, 1877–1882.

187 H. A. Andreas and B. E. Conway, *Electrochim. Acta*, 2006, **51**, 6510–6520.

188 A. M. Navarro-Suárez, N. Casado, J. Carretero-González, D. Mecerreyes and T. Rojo, *J. Mater. Chem. A*, 2017, **5**, 7137–7143.

189 E. Fuente, J. A. Menéndez, D. Suárez and M. A. Montes-Morán, *Langmuir*, 2003, **19**, 3505–3511.

190 J. P. Chen and S. Wu, *Langmuir*, 2004, **20**, 2233–2242.

191 L. Guan, L. Yu and G. Z. Chen, *Electrochim. Acta*, 2016, **206**, 464–478.

192 H. Wang, C. Zhu, D. Chao, Q. Yan and H. J. Fan, *Adv. Mater.*, 2017, **29**, 1702093.

193 K. Naoi and Y. Nagano, in *Supercapacitors Materials, Systems and Applications*, 2013, pp. 239–256.

194 J. M. Miller, O. C. Onar, C. White, S. Campbell, C. Coomer, L. Seiber, R. Sepe Jr. and A. Steyerl, *IEEE Power Electron. Mag.*, 2014, **1**, 12–24.

195 K. Kuratani, M. Yao, H. Senoh, N. Takeichi, T. Sakai and T. Kiyobayashi, *Electrochim. Acta*, 2012, **76**, 320–325.

196 J. Ding, H. Wang, Z. Li, K. Cui, D. Karpuzov, X. Tan, A. Kohandehghan and D. Mitlin, *Energy Environ. Sci.*, 2015, **8**, 941–955.

197 S. R. Sivakkumar and A. G. Pandolfo, *Electrochim. Acta*, 2012, **65**, 280–287.

198 V. Khomenko, E. Raymundo-Piñero and F. Béguin, *J. Power Sources*, 2008, **177**, 643–651.

199 P. Simon and A. Burke, *Electrochem. Soc. Interface*, 2008, 38–43.

200 X. Lu, M. Yu, G. Wang, Y. Tong and Y. Li, *Energy Environ. Sci.*, 2014, **7**, 2160–2181.

201 C. S. Lancefield, G. M. M. Rashid, F. Bouxin, A. Wasak, W.-C. Tu, J. Hallett, S. Zein,

J. Rodríguez, S. D. Jackson, N. J. Westwood and T. D. H. Bugg, *ACS Sustain. Chem. Eng.*, 2016, **4**, 6921–6930.

202 C. S. Lancefield, H. L. J. Wienk, R. Boelens, B. M. Weckhuysen and P. C. A. Bruijnincx, *Chem. Sci.*, 2018, **9**, 6348–6360.

203 D. Ibarra, M. I. Chávez, J. Rencoret, J. C. Del Río, A. Gutiérrez, J. Romero, S. Camarero, M. J. Martínez, J. Jiménez-Barbero and A. T. Martínez, *J. Agric. Food Chem.*, 2007, **55**, 3477–3490.

204 Y. Lu, Y.-C. Lu, H.-Q. Hu, F.-J. Xie, X.-Y. Wei and X. Fan, *J. Spectrosc.*, 2017, 1–15.

205 J. Zakzeski, P. C. A. Bruijnincx, A. L. Jongerius and B. M. Weckhuysen, *Chem. Rev.*, 2010, **110**, 3552–3599.

206 M. V. Galkin, A. T. Smit, E. Subbotina, K. A. Artemenko, J. Bergquist, W. J. J. Huijgen and J. S. M. Samec, *ChemSusChem*, 2016, **9**, 3280–3287.

207 Z. Yue, A. Vakili, O. Hosseinaei and D. P. Harper, *J. Appl. Polym. Sci.*, 2017, 45507.

208 M. Foston, G. A. Nunnery, X. Meng, Q. Sun, F. S. Baker and A. Ragauskas, *Carbon*, 2013, **52**, 65–73.

209 R. Parthasarathi, R. A. Romero, A. Redondo and S. Gnanakaran, *J. Phys. Chem. Lett.*, 2011, **2**, 2660–2666.

210 P. F. Britt, A. C. Buchanan III, M. J. Cooney and D. R. Martineau, *J. Org. Chem.*, 2000, **65**, 1376–1389.

211 P. F. Britt, A. C. Buchanan III and E. A. Malcolm, *Energy & Fuels*, 2000, **14**, 1314–1322.

212 P. F. Britt, A. C. Buchanan III and E. A. Malcolm, *J. Org. Chem.*, 1995, **60**, 6523–6536.

213 A. Beste and A. C. Buchanan III, *J. Org. Chem.*, 2009, **74**, 2837–2841.

214 Z. Dai, X. Shi, H. Liu, H. Li, Y. Han and J. Zhou, *RSC Adv.*, 2018, **8**, 1218–1224.

215 J. L. Espinoza-Acosta, P. I. Torres-Chávez, J. L. Olmedo-Martínez, A. Vega-Rios, S. Flores-Gallardo and E. A. Zaragoza-Contreras, *J. Energy Chem.*, 2018, **27**, 1422–1438.

216 R. Mörck, H. Yoshida and K. P. Kringstad, *Holzforschung*, 1986, **40**, 51–60.

217 *Ash in wood, pulp, paper and paperboard: combustion at 525 °C*, 2012.

218 *TAPPI Standard T 222 om-11. Acid-insoluble lignin in wood and pulp*, 2011.

219 *TAPPI Useful Methods UM 250. Acid-soluble lignin in wood and pulp*, 2011.

220 *SCAN standard CM 71:09. Pulps – Carbohydrate content. Scandinavian Pulp, Paper and Board testing Committee*, 2009.

221 R. K. Patterson, *Anal. Chem.*, 1973, **45**, 605–609.

222 M. Sette, H. Lange and C. Crestini, *Comput. Struct. Biotechnol. J.*, 2013, **6**, e201303016.

223 H. Kim and J. Ralph, *Org. Biomol. Chem.*, 2010, **8**, 576–591.

224 A. Bax, B. L. Hawkins, G. E. Maciel and N. M. Szeverenyi, in *Magnetic Resonance. NATO ASI Series (Series C: Mathematical and Physical Sciences)*, 1984, pp. 137–145.

225 J. Ralph, G. Brunow and W. Boerjan, in *ENCYCLOPEDIA OF LIFE SCIENCES*, 2007, pp. 1–10.

226 O. Hosseinaei, D. P. Harper, J. J. Bozell and T. G. Rials, *ACS Sustain. Chem. Eng.*, 2016, **4**, 5785–5798.

227 Y. Uraki, Y. Sugiyama, K. Koda, S. Kubo, T. Kishimoto and J. F. Kadla, *Biomacromolecules*, 2012, **13**, 867–872.

228 A. Granata and D. S. Argyropoulos, *J. Agric. Food Chem.*, 1995, **43**, 1538–1544.

229 J. Rönnols, H. Schweinebarth, A. Jacobs, J. S. Stevanic, A.-M. Olsson, A. Reimann and F. Aldaeus, *Nord. Pulp Pap. Res. J.*, 2015, **30**, 550–561.

230 A. Guerra, I. Filpponen, L. A. Lucia, C. Saquing, S. Baumberger and D. S. Argyropoulos, *J. Agric. Food Chem.*, 2006, **54**, 5939–5947.

231 O. Hosseinaei, D. P. Harper, J. J. Bozell and T. G. Rials, *Int. J. Mol. Sci.*, 2017, **18**, 1410.

232 T. Faravelli, A. Frassoldati, G. Migliavacca and E. Ranzi, *Biomass and Bioenergy*, 2010, **34**, 290–301.

233 H. Yoshida, R. Mörck, K. P. Kringstad and H. Hatakeyama, *Holzforschung*, 1987, **41**, 171–176.

234 T. Elder, *Energy and Fuels*, 2014, **28**, 1175–1182.

235 C. M. Popescu, C. Vasile, M. C. Popescu, G. Singurel, V. I. Popa and B. S. Munteanu,

Cellul. Chem. Technol., 2006, **40**, 597–621.

236 C. G. Boeriu, D. Bravo, R. J. A. Gosselink and J. E. G. van Dam, *Ind. Crops Prod.*, 2004, **20**, 205–218.

237 C. S. Lancefield, S. Constant, P. de Peinder and P. C. A. Bruijnincx, *ChemSusChem*, 2019, **12**, 1139–1146.

238 A. C. Ferrari and D. M. Basko, *Nat. Nanotechnol.*, 2013, **8**, 235–246.

239 M. Cho, F. K. Ko and S. Renneckar, *ACS Omega*, 2019, **4**, 5345–5355.

240 C. Lian, H. Liu, D. Henderson and J. Wu, *J. Phys. Condens. Matter*, 2016, **28**, 414005.

241 M. J. Bleda-Martínez, J. A. Maciá-Agulló, D. Lozano-Castelló, E. Morallón, D. Cazorla-Amorós and A. Linares-Solano, *Carbon*, 2005, **43**, 2677–2684.

242 P. L. Taberna, P. Simon and J. F. Fauvarque, *J. Electrochem. Soc.*, 2003, **150**, A292–A300.

243 E. I. Akpan, in *Sustainable Lignin for Carbon Fibers: Principles, Techniques, and Applications*, 2019, pp. 353–394.

244 X.-J. Jin, Z.-M. Yu and Y. Wu, *Cellul. Chem. Technol.*, 2012, **46**, 79–85.

245 M. Sevilla and A. B. Fuertes, *ChemSusChem*, 2016, **9**, 1880–1888.

246 S. Ergun, *J. Phys. Chem.*, 1956, **60**, 480–485.

247 O. Boudouard, *C R Acad Sci.*, 1899, **128**, 1522–1525.

248 A. Mianowski, Z. Robak, M. Tomaszewicz and S. Stelmach, *J. Therm. Anal. Calorim.*, 2012, **110**, 93–102.

249 J. Hunt, A. Ferrari, A. Lita, M. Crosswhite, B. Ashley and A. E. Stiegman, *J. Phys. Chem. C*, 2013, **117**, 26871–26880.

250 C.-F. Chang, C.-Y. Chang and W.-T. Tsai, *J. Colloid Interface Sci.*, 2000, **232**, 45–49.

251 S. Chatterjee and T. Saito, *ChemSusChem*, 2015, **8**, 3941–3958.

252 J. Rodríguez-Mirasol, T. Cordero and J. J. Rodríguez, *Carbon*, 1993, **31**, 55–61.

253 J. Rodríguez-Mirasol, T. Cordero and J. J. Rodríguez, *Energy & Fuels*, 1993, **7**, 133–138.

254 D. Saha, Y. Li, Z. Bi, J. Chen, J. K. Keum, D. K. Hensley, H. A. Grappe, H. M. Meyer, S. Dai, M. P. Paranthaman and A. K. Naskar, *Langmuir*, 2014, **30**, 900–910.

255 F. K. Ko and Y. Wan, in *Introduction to Nanofiber Materials*, Cambridge University Press, 2014, pp. 13–43.

256 X. Zong, K. Kim, D. Fang, S. Ran, B. S. Hsiao and B. Chu, *Polymer (Guildf).*, 2002, **43**, 4403–4412.

257 C. Ma, Z. Li, J. Li, Q. Fan, L. Wu, J. Shi and Y. Song, *Appl. Surf. Sci.*, 2018, **456**, 568–576.

258 A. Haider, S. Haider and I.-K. Kang, *Arab. J. Chem.*, 2016, **11**, 1165–1188.

259 Z. Czigány and L. Hultman, *Ultramicroscopy*, 2010, **110**, 815–819.

260 J. D. Herdman, B. C. Connelly, M. D. Smooke, M. B. Long and J. H. Miller, *Carbon*, 2011, **49**, 5298–5311.

261 A. C. Ferrari and J. Robertson, *Phys. Rev. B*, 2000, **61**, 14095–14107.

262 J. Jagiello and M. Thommes, *Carbon*, 2004, **42**, 1227–1232.

263 J. Weber, Q. Su, M. Antonietti and A. Thomas, *Macromol. Rapid Commun.*, 2007, **28**, 1871–1876.

264 M. C. Román-Martínez, D. Cazorla-Amorós, A. Linares-Solano and C. Salinas-Martínez de Lecea, *Carbon*, 1993, **31**, 895–902.

265 J. L. Figueiredo, M. F. R. Pereira, M. M. A. Freitas and J. J. M. Órfão, *Carbon*, 1999, **37**, 1379–1389.

266 W. Laue, M. Thiemann, E. Scheibler and K. W. Wiegand, in *Ullmann's Encyclopedia of Industrial Chemistry, Vol. 24*, 2012, vol. 24, pp. 149–176.

267 E. S. Freeman, *J. Am. Chem. Soc.*, 1956, **60**, 1487–1493.

268 A. Mukhopadhyay, J. Hamel, R. Katahira and H. Zhu, *ACS Sustain. Chem. Eng.*, 2018, **6**, 5394–5400.

269 M. A. Lillo-Ródenas, D. Cazorla-Amorós and A. Linares-Solano, *Carbon*, 2003, **41**, 267–275.

270 A. Linares-Solano, M. A. Lillo-Ródenas, J. P. Marco-Lozar, M. Kunowsky and A. J.

Romero-Anaya, *Int. J. Energy, Environ. Econ.*, 2012, **20**, 59–91.

271 E. Raymundo-Piñero, P. Azais, T. Cacciaguerra, D. Cazorla-Amorós, A. Linares-Solano and F. Béguin, *Carbon*, 2005, **43**, 786–795.

272 A. E. Imel, A. K. Naskar and M. D. Dadmun, *ACS Appl. Mater. Interfaces*, 2016, **8**, 3200–3207.

273 K. H. Lee, H. Y. Kim, M. S. Khil, Y. M. Ra and D. R. Lee, *Polymer (Guildf).*, 2003, **44**, 1287–1294.

274 C. Ma, Y. Song, J. Shi, D. Zhang, X. Zhai, M. Zhong, Q. Guo and L. Liu, *Carbon*, 2013, **51**, 290–300.

275 C. Zhang, X. Yuan, L. Wu, Y. Han and J. Sheng, *Eur. Polym. J.*, 2005, **41**, 423–432.

276 L. G. Cançado, K. Takai, T. Enoki, M. Endo, Y. A. Kim, H. Mizusaki, A. Jorio, L. N. Coelho, R. Magalhães-Paniago and M. A. Pimenta, *Appl. Phys. Lett.*, 2006, **88**, 2–5.

277 F. Tuinstra and J. L. Koenig, *J. Chem. Phys.*, 1970, **53**, 1126–1130.

278 T. Tooming, T. Thomberg, H. Kurig, A. Jänes and E. Lust, *J. Power Sources*, 2015, **280**, 667–677.

279 E. Tee, I. Tallo, H. Kurig, T. Thomberg, A. Jänes and E. Lust, *Electrochim. Acta*, 2015, **161**, 364–370.

280 F. Xu, R. Cai, Q. Zeng, C. Zou, D. Wu, F. Li, X. Lu, Y. Liang and R. Fu, *J. Mater. Chem.*, 2011, **21**, 1970–1976.

281 C.-M. Chuang, C.-W. Huang, H. Teng and J.-M. Ting, *Energy & Fuels*, 2010, **24**, 6476–6482.

282 A. González, E. Goikolea, J. A. Barrena and R. Mysyk, *Renew. Sustain. Energy Rev.*, 2016, **58**, 1189–1206.

283 S.-B. Lai, M.-I. Jamesh, X.-C. Wu, Y.-L. Dong, J.-H. Wang, M. Gao, J.-F. Liu and X.-M. Sun, *Rare Met.*, 2017, **36**, 381–396.

284 F. Beck and P. Rüetschi, *Electrochim. Acta*, 2000, **45**, 2467–2482.

285 C. L. Berhaut, D. Lemordant, P. Porion, L. Timperman, G. Schmidt and M. Anouti, *RSC Adv.*, 2019, **9**, 4599–4608.

286 R. J. Gilliam, J. W. Graydon, D. W. Kirk and S. J. Thorpe, *Int. J. Hydrogen Energy*, 2007, **32**, 359–364.

287 A. J. Salkind and F. R. McLarnon, in *Proceedings of the Symposium on Rechargeable Zinc Batteries*, 1996, pp. 1–4.

288 L. Chen, X. Dong, Y. Wang and Y. Xia, *Nat. Commun.*, 2016, **7**, 1–8.

289 A. J. Salkind, E. Kantner and C. Grun, in *Proceedings of the Symposium on Rechargeable Zinc Batteries*, 1996, pp. 160–166.

290 Y. F. Yuan, J. P. Tu, H. M. Wu, Y. Li and D. Q. Shi, *Nanotechnology*, 2005, **16**, 803–808.

291 M. Ma, J. P. Tu, Y. F. Yuan, X. L. Wang, K. F. Li, F. Mao and Z. Y. Zeng, *J. Power Sources*, 2008, **179**, 395–400.

292 J. Jindra, *J. Power Sources*, 2000, **88**, 202–205.

293 M. Geng and D. O. Northwood, *Int. J. Hydrogen Energy*, 2003, **28**, 633–636.

294 T. C. Adler, F. R. Mclarnon and E. J. Cairns, *J. Electrochem. Soc.*, 1993, **140**, 289–294.

295 J. Phillips and S. Mohanta, *Electrolyte Composition For Nickel-Zinc batteries*, 2009.

296 J. F. Parker, C. N. Chervin, I. R. Pala, M. Machler, M. F. Burz, J. W. Long and D. R. Rolison, *Science (80-.).*, 2017, **365**, 415–418.

297 E. Frackowiak and K. Jurewicz, in *Electrochemical Engineering and Energy*, 1995, pp. 41–46.

298 J. L. Yang, Y. F. Yuan, H. M. Wu, Y. Li, Y. B. Chen and S. Y. Guo, *Electrochim. Acta*, 2010, **55**, 7050–7054.

299 J. Liu, C. Guan, C. Zhou, Z. Fan, Q. Ke, G. Zhang, C. Liu and J. Wang, *Adv. Mater.*, 2016, **28**, 8732–8739.

300 N. Alias and A. A. Mohamad, *J. King Saud Univ. - Eng. Sci.*, 2015, **27**, 43–48.

301 L. Wang, X. Li, T. Guo, X. Yan and B. K. Tay, *Int. J. Hydrogen Energy*, 2014, **39**, 7876–7884.

302 D. Floner and F. Geneste, *Electrochem. Commun.*, 2007, **9**, 2271–2275.

303 M. Gong, Y. Li, H. Zhang, B. Zhang, W. Zhou, J. Feng, H. Wang, Y. Liang, Z. Fan, J. Liu and H. Dai, *Energy Environ. Sci.*, 2014, **7**, 2025–2032.

304 H. H. Willard and N. K. Tang, *J. Am. Chem. Soc.*, 1937, **59**, 1190–1196.

305 B. Mavis and M. Akinc, *J. Am. Ceram. Soc.*, 2006, **89**, 471–477.

306 Merckmillipore, Zinc acetate dihydrate, https://www.sigmaaldrich.com/catalog/product/mm/108802?lang=en&region=GB&gclid=CjwKCAjw4pT1BRBUEiwAm5QuRwQiv2ksEzc_tPMXwdivNQtoeqYWCgT9EFLjH7OxxHE6qROtQN-loBoCJEwQAvD_BwE, (accessed 26 April 2020).

307 Merckmillipore, Nickel(II) chloride hexahydrate, https://www.merckmillipore.com/GB/en/product/NickelII-chloride-hexahydrate,MDA_CHEM-106717?ReferrerURL=https%3A%2F%2Fwww.google.com%2F, (accessed 26 April 2020).

308 P. Scherrer, *Nachrichten von der Gesellschaft der Wissenschaften zu Göttingen*, 1918, **1**, 98–100.

309 B. Mavis and M. Akinc, *Chem. Mater.*, 2006, **18**, 5317–5325.

310 G. J. de A. A. Soler-Illia, M. Jobbágy, A. E. Regazzoni and M. A. Blesa, *Chem. Mater.*, 1999, **11**, 3140–3146.

311 G. R. Dillip, A. N. Banerjee, V. C. Anitha, S. W. Joo, B. K. Min, S. Y. Sawant and M. H. Cho, *ChemPhysChem*, 2015, **16**, 3214–3232.

312 M. Technologies, *Datasheet - 2.7V 1F, 100 F, 150 F ultracapacitor cell*, 2018.

313 M. Horn, J. MacLeod, M. Liu, J. Webb and N. Motta, *Econ. Anal. Policy*, 2019, **61**, 93–103.

314 J. Rencoret, A. Gutiérrez, L. Nieto, J. Jiménez-Barbero, C. B. Faulds, H. Kim, J. Ralph, Á. T. Martínez and J. C. del Río, *Plant Physiol.*, 2011, **155**, 667–682.

315 S. Constant, H. L. J. Wienk, A. E. Frissen, P. de Peinder, R. Boelens, D. S. van Es, R. J. H. Grisel, B. M. Weckhuysen, W. J. J. Huijgen, R. J. A. Gosselink and P. C. A. Bruijnincx, *Green Chem.*, 2016, **18**, 2651–2665.

11. Appendix

11.1. List of publications

- Herou, S., Schlee, P., Belen Jorge, A. & Titirici, M., Biomass-derived electrodes for flexible supercapacitors. Curr. Opin. Green Sustain. Chem. 2452–2236 (2017). doi: https://doi.org/10.1016/j.cogsc.2017.10.005
- Schlee, P., Herou, S., Jervis, R., Shearing, P. R., Brett, D. J. L., Baker, D.; Hosseinaei, O., Tomani, P., Murshed, M. M., Li, Y., Mostazo-López, M. J., Cazorla-Amorós, D., Jorge Sobrido, A. B., Titirici, M. M., Free-standing supercapacitors from Kraft lignin nanofibers with remarkable volumetric energy density. Chem. Sci. 10, 2980–2988 (2019). doi: https://doi.org/10.1039/C8SC04936J
- Schlee, P., Hosseinaei, O., Baker, D., Landmér, A., Tomani, P., Mostazo-López, M. J., Cazorla-Amorós, D., Herou, S., Titirici, M. M., From Waste to Wealth: From Kraft Lignin to Free-standing Supercapacitors. Carbon 145, 470–480 (2019). doi: https://doi.org/10.1016/j.carbon.2019.01.035
- Herou, S., Ribadeneyra Crespo, M., Madhu, R., Araullo-Peters, V., Jensen, A., Schlee, P., Titirici, M.-M., Ordered mesoporous carbons from lignin: a new class of biobased electrodes for supercapacitors. Green Chem. 21, 550–559 (2019). doi: https://doi.org/10.1039/C8GC03497D
- Ribadeneyra, M. C., Grogan, L., Au, H., Schlee, P., Herou, S., Neville, T., Cullen, P. L., Kok, M. D. R., Hosseinaei, O., Danielsson, S., Tomani, P., Titirici, M. M., Brett, D. J. L., Shearing, P. R., Jervis, R., Jorge, A. B., Lignin-derived electrospun freestanding carbons as alternative electrodes for redox flow batteries. Carbon 157, 847–856 (2020). doi: https://doi.org/10.1016/j.carbon.2019.11.015
- Schlee, P., Hosseinaei, O., O' Keefe, C. A., Mostazo-López, M. J., Cazorla-Amorós, D., Herou, S., Tomani, P., Grey, C. P., Titirici, M. M., Hardwood versus softwood Kraft lignin – precursor-product relationships in the manufacture of porous carbon nanofibers for supercapacitors, (submitted)

11.2. List of oral presentations

13/10/2017	QMUL-UCL First Symposium: London Energy Materials and Devices Hub, London
12/06/2018	QMUL-NPU Summer School – Energy Nanomaterials, London
28/06/2018	First International Workshop on Multi-functional Nanocarbon Fibres, Madrid
01/07/2019	PhD symposium at Imperial College London, London
07/10/2019	Young Researchers Symposium organized by the Marcus Wallenberg Foundation, Stockholm
31/03/2020	CPE (Centre of Plastic Electronics) Sustainable Energy Materials online seminar, Imperial College London

11.3. The L(ignin) number

The concept of the L(ignin) number is still immature. However, it is worth mentioning it here. Lignin characterization and its representation are highly complex tasks, which has been described on numerous occasions in this thesis. A vast array of methods can be applied to lignins to gather data such as purity, chemical composition, molar mass, functional groups and thermal properties. The lignin property polygon (LPP) introduced in chapter 3 of this thesis is an attempt to depict the most important information for a specific context in a concise way

rather than in lengthy tables spanning several pages. To further facilitate the communication of the properties of a lignin precursor, the L(ignin) number has been developed by me. This integer number can be regarded as a means of transport for important information about the lignin precursor sent from a lignin seller to a lignin buyer - in a scenario where an active lignin market exists. This number is constructed based on the Gödel mapping established by one of the greatest mathematicians of the 20s century, Kurt Gödel. The mapping within the concept of the L(ignin) number works as follows:

- Each lignin property is mapped onto a prime number:
  $T_g \rightarrow 2$; D (dispersity) $\rightarrow 3$; M_w (weight average molar mass) $\rightarrow 5$ etc.
- Based on the value that the property has, a scale factor between 1 and 10 is assigned with the help of the table below:

Scale factor	Tg	M_w/ Da	D	carb+ash/%	Sulfur/%
1	90	500	1	0.1	1
2	100	1000	2	0.3	2
3	110	1500	3	0.5	3
4	120	2000	4	0.7	4
5	130	2500	5	0.9	5
6	140	3000	6	1.1	6
7	150	3500	7	1.3	7
8	160	4000	8	1.5	8
9	170	4500	9	1.7	9
10	180	5000	10	1.9	10

- The scale factor is then used to calculate a new unique prime factor (PF) by using it as the exponent of the prime number that represents the property. For example:
  The $T_g \rightarrow 2$ and the value of e.g. HKL in this thesis for the T_g was 154 °C. According to the table the scale factor is 8. Hence, the specific prime factor (PF) in this case is: $PF(T_g) = 2^8 = 256$.
  <u>This is then done for several other parameters:</u>
  - $D \rightarrow 3$, scale factor(D=1.5) = 2; $PF(D) = 3^2 = 9$
  - $Mw \rightarrow 5$, scale factor (M_w=1.9 kg/mol) = 4; $PF(M_w) = 5^4 = 625$
  - S (sulfur content) $\rightarrow 7$, scale factor (S=2.3%) = 3; $PF(S) = 7^3 = 343$

- Carbohydrate + ash content → 11 , scale factor (carb+ash=0.67%) = 4;
  PF(carb+ash) = $11^4 = 14641$

The L(ignin) number is defined as:

$L = PF(T_g) * PF(D) * PF(M_w) * PF(S) * PF(carb+ash)$

L = 256 * 9 * 625 * 343 * 14641 = 7231482720000

This is *per definitionem* a unique integer number assigned to this lignin precursor which bears a lot of information, that can be extracted easily by simple prime factorization for which applications are available online: e.g. https://www.wolframalpha.com/input/

One could ask: Is there any use for this L(ignin) number?

A lignin seller could print the number generated based on the procedure just explained on the package with the lignin batch that he/she sends to a buyer somewhere else. Once the buyer receives it, he/she can decompose the lignin number into its prime factor components with the help of the link above. By doing so, he/she gets a lot of information about the lignin batch just received assuming that there is a universal system in place that defines which property is mapped onto which prime number. This might also be a means of quality control of lignin properties from batch to batch. However, there is still a single flaw in this concept. The exponents, which are the specific values of the properties, have to be integers in order to generate an integer as L(ignin) number that is easily decomposable into its prime factors. Hence, a meaningful universal scale factor system (table shown above) needs to be found that is applicable to a wide range of lignins. This is a task which shall be performed in the future, hopefully.